Investigation of the s-Process Neutron Source ^{22}Ne+α

by
Richard Leigh Longland

A dissertation submitted to the faculty of the University of North Carolina at Chapel Hill in partial fulfillment of the requirements for the degree of Doctor of Philosophy in the Department of Physics and Astronomy.

Chapel Hill
2010

Approved by:

Dr. Christian Iliadis, Advisor

Dr. Arthur E. Champagne, Reader

Dr. Jonathan Engel, Reader

Dr. Reyco Henning, Reader

Dr. Daniel E. Reichart, Reader

ABSTRACT

Richard Leigh Longland: Investigation of the s-Process Neutron Source ^{22}Ne+α.
(Under the direction of Dr. Christian Iliadis.)

Neutron capture processes are associated with the production of most elements heavier than iron. The s-process is one such scenario for this nucleosynthesis, in which neutrons are captured at a slower rate than β-decay occurs, resulting in the enrichment of nuclei along the nuclear valley of stability. An important reaction that can produce these neutrons is ^{22}Ne(α,n)^{25}Mg. Uncertainties in the rate of this reaction and its competing ^{22}Ne(α,γ)^{26}Mg reaction hinder our understanding of nucleosynthesis in AGB stars and massive stars, the favoured sites for the s-process. Without improved nuclear physics input, constraints on the structure of these stars cannot be reliably applied from observational evidence.

In the present study, the ^{22}Ne+α reactions were investigated. A nuclear resonance fluorescence experiment was performed on the compound ^{26}Mg nucleus. The experiment used linearly polarised photons to excite ^{26}Mg and the emitted γ-rays were analysed to find the properties of excited states, thus improving our understanding of the resonance properties for the ^{22}Ne+α reactions. The findings of the experiment were incorporated into a re-evaluation of literature data, in which rates and their associated uncertainties were calculated with a novel Monte Carlo method. Rates on the order of 10 times lower than the literature values were obtained for the ^{22}Ne(α,γ)^{26}Mg reaction, while the ^{22}Ne(α,n)^{25}Mg was in agreement with the most recent results. The uncertainties of both reaction rates were reduced by an order of magnitude.

In order to further clarify the current literature data, direct measurements of both reactions should be performed in the future. In the present work, a novel method for determining the resonance strength for the $E_r^{\text{lab}} = 479$ keV resonance in ^{22}Ne(p,γ)^{23}Na was developed. This new strength of $\omega\gamma = 0.524(51)$ eV significantly reduces ^{22}Ne target stoichiometry uncertainty, which was one of the largest sources of uncertainty in direct ^{22}Ne+α cross section measurements.

ACKNOWLEDGMENTS

I would first like to thank my wonderful wife, Julie, without whom I wouldn't have been able to get to where I am today. She has been an inspiration to me in so many ways, and have helped me discover myself, both personally and academically. She is an excellent scientist, one in which I can always aspire to be like as I pursue my career in physics.

Christian Iliadis has been the best friend and mentor I could ever have hoped for in an advisor. Christian's guidance throughout my graduate studies has been invaluable, and I look forward to working closely with him in the future. I thank him, also, for taking me in for my undergraduate research placement. I consider myself very fortunate to have ended up at UNC under his guidance. Thanks for all the coffee, too, it always helps me get through Mondays!

I will always consider myself lucky to have had the pleasure of working closely with Art Champagne. Art, no matter how busy, always finds the time to explain a tricky problem, or describe how to maintain the lab equipment. I am always proud to show visitors around LENA, and Art's leadership is a big part of that. The rest of my committee, Reyco Henning, Jon Engel, and Dan Reichart also deserve a special thank you.

John Lattanzio, who welcomed me into his group for six weeks, really helped me understand AGB stars. The time I spent with him at Monash gave me an understanding of his field that I could not have reached otherwise. I would also like to acknowledge Anton Tonchev and Gencho Rusev for their help before, during and after my experiments at HIγS. Their work on the NRF program at TUNL has been a great contribution to nuclear physics.

The LENA group has become like a family to me. I am forever indebted to everyone in the lab, both past and present. I would especially like to thank Chris Fox for being so welcoming when I first arrived in this strange country. He was somebody to complain about the quality of American tea and American spelling with! I learnt so much about the computational side of the lab from Chris, things that I could never have learnt from a book. Bob Runkle and Johannes Pollanen taught me everything

about how the lab runs. In the years since they left, I have thanked my lucky stars countless times that they taught me so much. Johannes also deserves a special thank you because no matter how many things I broke, I never came close to his record! Ryan Fitzgerald has been central to my graduate career. Without his incredible ideas and understanding of physics, many of my projects over the years probably would never have happened. I'd also like to thank my senior graduate students, Peter Bertone and Joe Newton. Peter's interest in finding new and novel methods of doing things has inspired me to learn many new techniques for data analysis. Joe's dedication to getting everything right on the first attempt is something that has saved me many times. Joe deserves extra thanks for testing so much of my work when I was sick of looking at it! Of course, I should mention the guys I'll be leaving behind, especially Johnny and Stephen. They have been so much help to me, and I could never have finished without them. Johnny's skill with hardware is unsurpassed, and Stephen has helped me so much in developing many of the software tools we use in the lab. I wish them both the best of luck in the coming years. I'd also like to thank Paddy Finnerty for his impressive expertise in HPGe detectors and data analysis techniques. Discussions with him have lead to many breakthroughs in my research.

Anyone who does experiments at LENA knows how essential the TUNL technicians are to our work. Without Chris Westerfeldt in the lab, things would never run, and the lab probably would have fallen apart many years ago. Bret Carlin has also been a great help. He is always willing to drop everything to help us when disaster strikes! I would also like to thank John Dunham, Patrick Mulkey, and Jeff Addison for their help with everything. Of course, no discussion of the LENA technicians is complete without mentioning Richard O'Quinn. Richard's in depth knowledge of the lab has helped us many times. We have has many fruitful troubleshooting sessions with Richard, and I could not have finished without him. The UNC and TUNL shops have always been helpful and understanding when I've worked with them. They have built many things for me over the years, all manufactured to excellent standards.

At the University of Surrey, I would like to thank Paddy Regan for his leadership in the MPhys program, and who was responsible for my research placement at UNC. His excitement for physics is an inspiration, and I hope to work with him in the future. Outside the field of nuclear physics is Craig Underwood, who's broad depth of knowledge on satellite technology will always impress me. Although I no longer study the subject, I will always remember his fascinating lectures. I would

also like to thank the lab technicians at Surrey, where I had my first exposure to experimental physics, especially Jim Skinner. My classmates at Surrey also helped me get through many years of hard work. Richard Hughes deserves a special mention for always lightening the mood, especially during long lab write-ups and study sessions. Thanks, dude!

I'd like to thank my family, especially Mum, Dad, and Michael for raising me. I thank them for always being supportive of my studies, providing everything I need while allowing me the freedom to pursue my own interests. They are great parents, who have never failed to sacrifice for their children. Mum and Michael have been an inspiration, and have taught me the value of honest hard work. Dad has always taken a keen interest in my studies. He has never assumed that he would not understand something, which is very important to me, and something that has become a key part of my beliefs as a scientist. I would like to thank my siblings, Charlotte and Stephen, for our wonderful friendship. I will always be proud of their successes as they have grown into wonderful people!

Finally, I would like to thank the United States government, especially the Department of Energy, who provided much of the funding of my work.

TABLE OF CONTENTS

List of Tables

List of Figures

1 Introduction

1.1 The s-Process

GALACTIC abundances of elements heavier than iron are difficult to explain using charged particle reactions that fuel stars. Charged particle reaction cross sections at energies corresponding to hydrostatic stellar burning environments become prohibitively small for the creation of nuclei with masses larger than $A \approx 60$. At low temperatures, this is because the Coulomb barrier, which dominates the nuclear reaction cross sections, increases dramatically with proton number. At high temperatures, nucleosynthesis favours the nuclei residing around iron, which have the smallest binding energy per nucleon. How were nuclei heavier than $A \approx 60$ made? The answer to this question lies in neutral particle reactions. Reactions involving neutrons are not limited by a Coulomb barrier and therefore can have rather large cross sections, even at relatively low energies.

The seminal paper by Burbidge, Burbidge, Fowler and Hoyle [Bur57] envisioned two extreme scenarios when considering neutron capture in stellar environments: one in which neutrons are captured relatively slowly, and one in which they are captured rapidly. These are known as the s- and r-process, respectively. The s-process occurs when neutron capture occurs on a time scale that is slower than the β-decay rate of unstable nuclei, while the r-process occurs at neutron capture rates that are much larger than the β-decay rate, hence producing highly neutron rich nuclei. The r-process is thought to be responsible for the production of long-lived, high mass nuclei such as ^{235}U and ^{232}Th as well as the broad peaks visible in the solar system abundance distributions at masses of $A \approx 130$ and $A \approx 190$. For more discussion on the r-process, the reader is referred to Refs. [Bur57, Ili07] and references therein.

Nuclei are produced in the s-process by slow neutron capture and β-decay as illustrated in Fig.

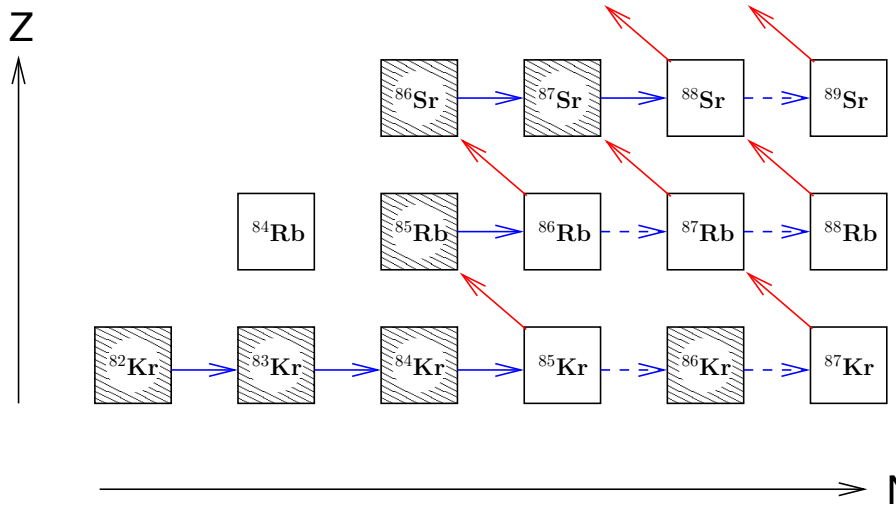

Figure 1.1: The s-process path near the rubidium isotopes. Also shown are possible branchings (dashed arrows) in the s-process path, which lead to differing abundance ratios between rubidium isotopes, depending on the neutron flux.

1.1. Starting from ^{83}Kr, for example, a neutron can be captured to produce the stable ^{84}Kr isotope. A further neutron capture produces ^{85}Kr, which can either β-decay to ^{85}Rb or capture another neutron to produce ^{86}Kr. Such locations are referred to as "branchings" in the s-process path. If a higher flux of neutrons is available, the branching to ^{86}Kr will be larger.

By considering solar system abundances of "s-only" nuclei (nuclei that can only be produced by the s-process), it can be shown that there are two main contributions to s-process nucleosynthesis; the "main" and the "weak" components. The main s-process component is responsible for the creation of nuclei in the mass range of $A \gtrsim 90$, which requires a relatively low flux of neutrons over a long time period. The weak component enhances abundances in the mass range of $A \lesssim 90$, which requires an efficient neutron capture process, but only for a short period of time. In the following section, the sites best describing these scenarios will be discussed.

1.2 Stellar Sites of the s-Process

1.2.1 AGB Stars

Asymptotic Giant Branch (AGB) stars are thought to produce the main component of the s-process. Moderate mass stars ($0.8M_{\odot} < M < 8M_{\odot}$), including the sun, will all eventually be-

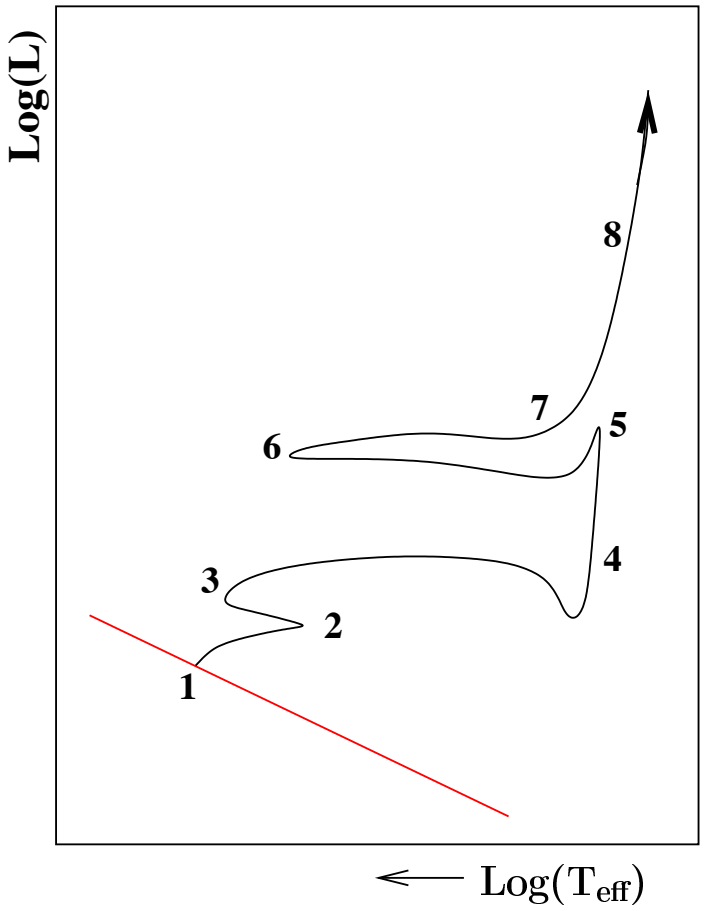

Figure 1.2: Hertzsprung-Russel diagram of the evolution of a $M = 5M_{\odot}$ star [Hab04]. Plotted are the luminosity of the star and the surface temperature, or colour. Note that temperature increases to the left of the x-axis. The thick line is the evolutionary track of the star. Refer to the text for details on the labels.

come AGB stars with ages depending on initial mass. In the following, the evolution of a typical $M = 5M_{\odot}$ star will be discussed by following the surface temperature and luminosity as the star evolves. A Hertzsprung-Russel (HR) diagram of this evolution, which plots the luminosity of the star against the surface temperature (colour) is shown in Fig. 1.2. Once the star has formed, and is burning hydrogen in the core, it will reside in a region on the HR diagram known as the main sequence (straight line in Fig. 1.2). At point (1), high temperatures in the core cause the convective envelope of the star to expand, leading to cooling on the surface. This happens because the stellar envelope is opaque, and radiation released from nuclear reactions is absorbed by the inner layers of the envelope, causing them to expand. Note that the star spends approximately 90% of its life on the main sequence. At point (2), after on the order of $10^9 - 10^{10}$ years hydrogen in the core will be exhausted, and the

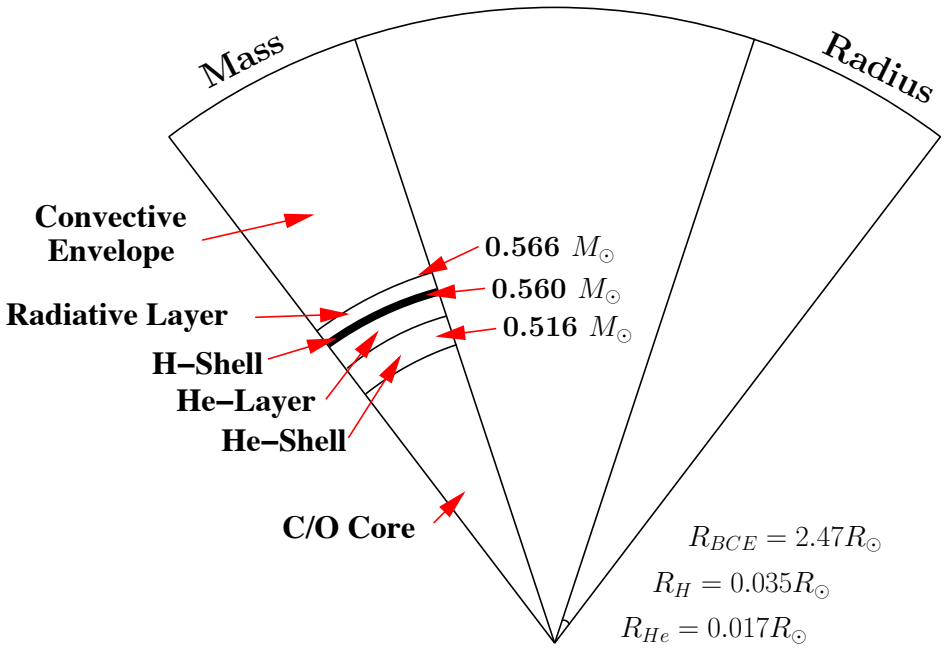

Figure 1.3: The internal structure of an AGB star. On the left side of the figure, the mass of the star is plotted. The right hand side plots the radius. Note that the core of the star contains 50% of the mass (in the present example), but only about 1% of the radius of the star as indicated by the small mark at $R = 0.017R_\odot$.

star will move towards point (3) on the diagram before hydrogen shell burning ignites, expanding the envelope once again. Between points (4) and (5) (the red giant branch), H-shell burning adds material (^{4}He) to the core, thereby increasing the temperature and pressure in the core until helium burning is ignited at point (5), causing a rapid surface temperature increase as energy is deposited into the envelope towards point (6). As helium is burned in the core, the envelope will expand once again to point (7), where helium is exhausted in the core. At this point in the evolution of the star, helium and hydrogen will burn intermittently in shells around a carbon-oxygen core through point (8). During this final stage of evolution, the star will lose mass rapidly in the form of stellar wind, eventually producing a planetary nebula. The carbon-oxygen core will remain as a white dwarf. In this pulsing stage, the star appears very close to the red giant branch, giving these stars their name of Asymptotic Giant Branch stars.

The internal structure of an AGB star is shown in Fig. 1.3. During this phase of the stars life, hydrogen and helium are burning intermittently in shells surrounding the C-O core, separated by a helium layer. The helium layer is the important region for the s-process. During the intermittent burning stage, known as the Thermally Pulsing (TP) stage, the helium shell will burn in short bursts,

followed by long quiescent hydrogen burning stages. During each pulse, a dredge-up episode occurs, which dredges processed material out of the helium shell and into the convective envelope of the star. Thermal pulses are shown schematically in Fig. 1.4.

During a thermal pulse, while helium is being converted into ^{12}C in the helium burning shell, a convective zone between the helium and hydrogen shell arises. The convective zone mixes ^{12}C and ^{16}O (He-burning ashes) into the helium layer, and adds protons from the hydrogen shell. The sequence ^{12}C(p,γ)^{13}N($\beta^+\nu$)^{13}C can occur, thus creating a ^{13}C rich pocket. The abundant helium can then react with ^{13}C to produce neutrons though the ^{13}C(α,n)^{16}O reaction. This reaction is one of the main sources of neutrons in AGB stars, and because of the long time period and repeated exposures, it is thought to be responsible for the majority of the main s-process component.

During the thermal pulse, temperatures in the base of the convective zone become high enough to ignite a second neutron source, ^{22}Ne$(\alpha, \mathrm{n})^{25}$Mg . The ^{22}Ne is produced from ^{14}N, which is in high abundance in the star, via ^{14}N(α,γ)^{18}F($\beta^+\nu$) ^{18}O(α,γ)^{22}Ne. This source is expected to produce a high flux of neutrons, but only for a fraction of the time of the ^{13}C source, especially for low mass AGB stars. The ^{22}Ne$(\alpha, \mathrm{n})^{25}$Mg reaction and its competing reaction ^{22}Ne$(\alpha, \gamma)^{26}$Mg are therefore thought to influence mainly the branchings in the s-process path. These branchings in the s-process track can be analysed very precisely in pre-solar grains. Note that recent studies [Gar06, Lug08] of rubidium enhancement in AGB stars suggest that in higher mass AGB stars, the ^{22}Ne$(\alpha, \mathrm{n})^{25}$Mg reaction could be the dominant s-process neutron source. Improved reaction rate estimates can help determine at what mass the ^{22}Ne+α reactions start to dominate the s-process neutron production.

1.2.2 Massive Stars

The lifetime of a massive star ($M \gtrsim 11M_\odot$) is considerably different than that of the lower mass stars discussed previously. The HR diagram for a $M = 25M_\odot$ star is shown in Fig. 1.5. The total lifespan of these stars is much shorter than that of lower mass stars ($10^6 - 10^7$ years [Ili07]), most of which is spent burning hydrogen on the main sequence (part (1) in Fig. 1.5). Following core hydrogen exhaustion, helium will be consumed in the core at point (2) until the star reaches point (3) in the figure. The star will then remain at point (3) as a supergiant star, undergoing core carbon, neon, oxygen, and finally silicon burning. Following silicon burning, the star will have a characteristic onion

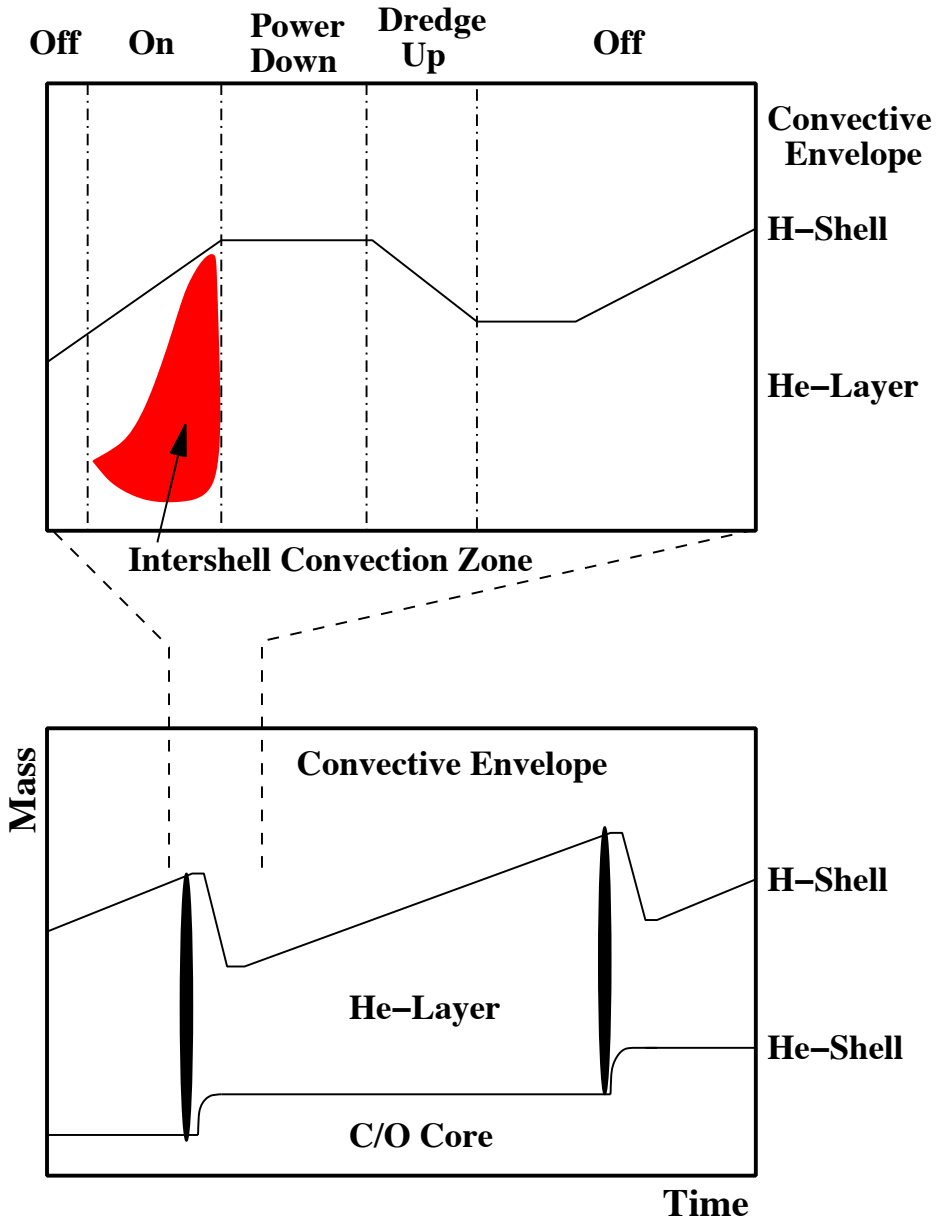

Figure 1.4: Details of a thermal pulse showing the hydrogen and helium burning shells as well as the dredge-up episode. During the "on" stage, the helium shell will ignite, setting up a convective zone in the helium layer (shown as a shaded region in the figure). Once the helium burning shell is extinguished, the convective envelope will expand into the helium layer, mixing material upwards to the surface of the star. In the "off" stage, the hydrogen shell will become active, adding material to the helium layer until the helium shell re-ignites, repeating the process.

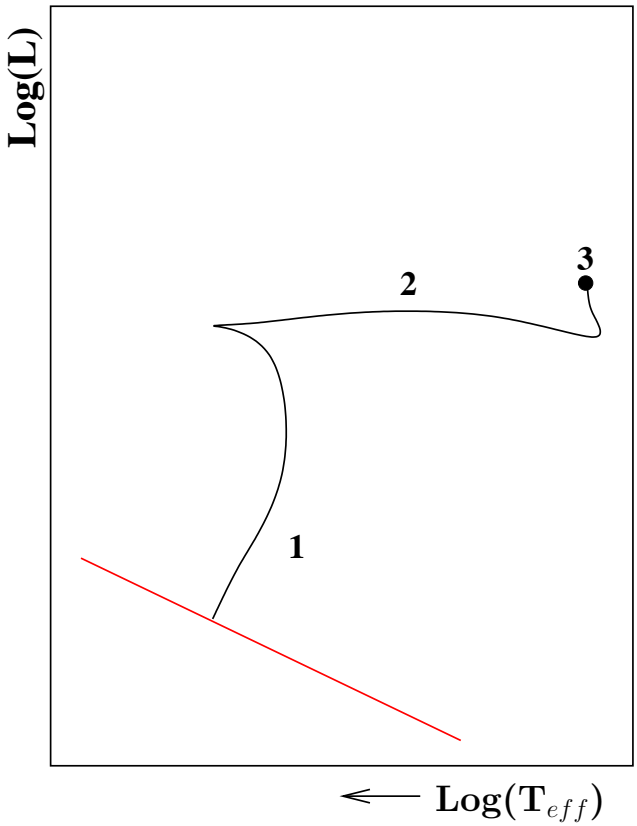

Figure 1.5: HR diagram for a $M = 25M_{\odot}$ star. The scale is not equal to that in Fig. 1.2. Massive stars are some of the most luminous stellar objects. See Fig. 1.2 for a description of HR diagrams.

structure, with an iron core surrounded by layers of increasingly lighter nuclei. Eventually, the star's core will collapse, resulting in a supernova.

During the core hydrogen burning stage of a massive star, hydrogen is processed into helium via the CNO-cycles. This process enriches the ^{14}N content in the core to a mass density on the order of 1% [Ili07, Arn96]. This enrichment occurs because ^{14}N is a bottleneck in the CNO cycle. Once core helium burning sets in, the ^{14}N is processed into ^{22}Ne through the reaction chain ^{14}N(α,γ)^{18}F ($\beta^{+}\nu$)^{18}O(α,γ)^{22}Ne. This chain will enrich the ^{22}Ne content of the star towards the end of the core helium burning phase to approximately ^{22}Ne:^{4}He$= 1 : 10$. As the core temperature increases to $T \approx 0.15$ GK, the ^{22}Ne$(\alpha, \mathrm{n})^{25}$Mg neutron source will start to produce neutrons, which drive the weak component of the s-process. Note that any remaining ^{22}Ne after core helium burning can produce a second flux of neutrons during carbon burning (which produces additional α-particles). Massive stars are thought to be responsible for the production of most ^{22}Ne, and over 50% of the ^{25}Mg and ^{26}Mg

in the universe [Arn96]. The s-process in massive stars is also thought to be a large contributor to relatively rare nuclides, such as ^{36}S, ^{37}Cl, and ^{40}Ar.

1.3 The ^{22}Ne(α,n)^{25}Mg s-Process Neutron Source

The ^{22}Ne$(\alpha, \mathrm{n})^{25}$Mg and ^{22}Ne$(\alpha, \gamma)^{26}$Mg reactions are important in s-process neutron production. While the ^{22}Ne$(\alpha, \mathrm{n})^{25}$Mg reaction is a neutron source, its competing ^{22}Ne$(\alpha, \gamma)^{26}$Mg reaction will serve to reduce the neutron flux available for the s-process, and is therefore equally important. In massive stars, the reaction rates determine the neutron flux available for the weak component of the s-process, while in AGB stars the reactions provide a high flux of neutrons for a short period of time, affecting mainly branchings in the s-process path.

Since the early 1980's, a number of studies have attempted to measure the cross sections of both reactions in the energy region of interest. Direct measurements of the ^{22}Ne$(\alpha, \mathrm{n})^{25}$Mg reaction were made by Refs. [Wol89, Har91, Dro93, Gie93, Jae01b]. All of those studies but one (Ref. [Gie93]) were performed using a gas target (the Rhinoceros system) at the Institut für Strahlenphysik in Stuttgart, Germany. The lowest measured resonance is located at $E_r^{\mathrm{lab}} = 832$ keV, which resides at the upper edge of the effective burning region for $T = 0.3$ GK. An additional $E_r^{\mathrm{lab}} = 633$ keV resonance was believed to have been seen [Dro91], which was later determined to be background from the ^{10}B(α,n)^{13}N reaction [Dro93]. This expected resonance has provided a fair about of controversy in the field (fuelled by the apparent need for a resonance in this energy region [The00]), and multiple studies (including the present work) have attempted a search for it [Gie93, Jae01b, Uga07].

Although the ^{22}Ne$(\alpha, \gamma)^{26}$Mg reaction plays an equally important role in neutron production, it has been studied significantly less. The only study close to the energy region relevant in stellar nucleosynthesis is that of Ref. [Wol89], which was performed in coincidence with an ^{22}Ne$(\alpha, \mathrm{n})^{25}$Mg measurement. The lowest measured resonance in this reaction was observed at $E_r^{\mathrm{lab}} = 828$ keV.

The ^{22}Ne$(\alpha, \mathrm{n})^{25}$Mg and ^{22}Ne$(\alpha, \gamma)^{26}$Mg reaction rates have significant uncertainties at the temperatures of interest in AGB stars and massive stars (T ~ 0.3 GK). The effects of these uncertainties on nucleosynthesis have been studied in AGB stars and massive stars by Pignarari *et al*. [Pig05] and The *et al*. [The00], respectively. Both studies find that the current uncertainties in these reactions

produce uncertainties of up to a factor of 10 in the abundances of key elements on the s-process path.

A recent re-evaluation of the rates of both reactions was made in Ref. [Kar06], which showed significant uncertainties at the temperatures relevant for s-process neutron production in AGB stars. Their result also showed that the uncertainties in the ^{22}Ne$(\alpha,\mathrm{n})^{25}$Mg and ^{22}Ne$(\alpha,\gamma)^{26}$Mg reaction rates affect the production ratios of ^{25}Mg and ^{26}Mg significantly. This is especially important because the magnesium isotopic ratios can be precisely measured in pre-solar grains [Zin05].

Observed branchings in the s-process path around rubidium [Bee89] from spectroscopic studies of AGB stars also suggests [Gar06] that our current understanding of the mechanics of AGB stars is incomplete. Their study showed that the ^{13}C neutron source cannot provide the flux of neutrons necessary to enhance rubidium. Constraints provided by those studies suggest that at lower metallicities, the ^{22}Ne$(\alpha,\mathrm{n})^{25}$Mg reaction could, indeed, be the main neutron source in AGB stars [Lug08]. With improved understanding of the ^{22}Ne$(\alpha,\mathrm{n})^{25}$Mg and ^{22}Ne$(\alpha,\gamma)^{26}$Mg reaction rates, AGB star models can be better constrained for calculation of the s-process.

In massive stars, the ^{22}Ne$(\alpha,\mathrm{n})^{25}$Mg and ^{22}Ne$(\alpha,\gamma)^{26}$Mg reactions directly influence the efficiency of the weak s-process component. Sensitivity studies by Ref. [The00] have shown that the rates of these reactions also influence the amount of ^{22}Ne remaining in the core following helium burning. Remaining ^{22}Ne will later produce neutrons during the carbon burning stage. However, in later stages, more neutron poisons will be present in the core, reducing the efficiency of the s-process [Woo03]. This s-process efficiency was found to depend on several other factors including convection models used in the calculations. Improvements in nuclear physics input can, therefore, help to constrain massive star models, and improve our understanding of these environments.

The neutron flux in stellar environments is an important factor influencing the amount of material that is produced in the s-process. Consequently, the reaction rate of the neutron producing ^{22}Ne$(\alpha,\mathrm{n})^{25}$Mg reaction and its competing ^{22}Ne$(\alpha,\gamma)^{26}$Mg reaction must be well known if comparisons between nucleosynthesis models and observations are to provide us with reliable information on the interior structure of stars. The goal of the current work is to improve our understanding of these reactions.

An overview of experimental methods used in the present work will be given in Ch. 4. Detector characterisation required to analyse cross section data reliably will be described. The production

of targets used for direct cross section measurements will be detailed as well as other experimental considerations relevant to the present work.

Studying excited states in the compound nucleus ^{26}Mg can improve our understanding of possible resonances that cannot be measured directly. A ^{26}Mg$(\gamma,\gamma)^{26}$Mg experiment performed to measure the quantum numbers of excited states in the compound ^{26}Mg nucleus will be described in Ch. 5.

Direct measurements of the ^{22}Ne$(\alpha,\gamma)^{26}$Mg and ^{22}Ne$(\alpha,\mathrm{n})^{25}$Mg reactions must be made to resolve inconsistencies in the data presented in the literature. In order to improve direct measurements, target stoichiometries must be known to high precision. The analysis of excitation functions arising from implanted targets, whose stoichiometry varies with depth in the target, is discussed in Ch. 3. Using this formalism, a new excitation function analysis technique used to find the stoichiometry of implanted ^{22}Ne targets is discussed in Ch. 6. This new technique is essential for determining the quantity of ^{22}Ne available for ^{22}Ne$+\alpha$ reaction cross section studies.

Improved statistical determination of reaction rates from measured quantities will improve the definition of reaction rates used in stellar models. These improvements will clarify constraints on processes occurring in these stars. The theoretical treatment of reaction rates in stellar environments will be discussed in Ch. 2, along with a new formalism for calculating statistically meaningful uncertainties on rates. This new formalism will then be applied to the calculation of the latest reaction rates for the ^{22}Ne$(\alpha,\gamma)^{26}$Mg and ^{22}Ne$(\alpha,\mathrm{n})^{25}$Mg reactions, which is discussed in detail in Ch. 7. Conclusions are formed in Ch. 8.

2 Reaction Rates

2.0.1 Introduction

THERMONUCLEAR reaction rates describe the rate at which a nuclear reaction occurs in stellar environments. Reaction rates are found by convoluting the cross section of a reaction with the energy distribution of particles in the star. This convolution results in an average reaction rate per particle pair for a given reaction, which is dependent on the temperature of the environment.

Reaction rate formalism is a well understood topic of nuclear astrophysics. The reader is referred to Ref. [Ili07] for a more detailed discussion than is presented here. The uncertainties of reaction rates, however, are poorly understood because of the complexity of the calculations involved. Prior to this work, the most statistically rigorous treatment of reaction rate uncertainties was performed by Ref. [Tho99]. Their method, however, was simplified to an analytical form by utilising statistical approximations, which are not valid in many cases. Their method also contained no statistically meaningful treatment of upper-limits on reaction rate parameters (e.g., resonance strengths). Most astrophysically important reactions occur at low bombarding energies. The Coulomb barrier at these energies causes the reaction cross section to be small, hence many cross sections have not been measured at the energies corresponding to nuclear burning. Upper limit cross sections have historically been incorrectly treated in reaction rate determination. In order to reliably predict reaction rates and their associated uncertainties, upper-limit cross sections must be correctly treated.

In this chapter, a new formalism will be presented for calculating reaction rates and their associated uncertainties. Statistically meaningful definitions for high and low uncertainty boundaries will be formed (in contrast to the old "upper limit" and "lower limit" reaction rates typically used by the nuclear astrophysics community), and upper-limit quantities in the cross section will be given a statistically meaningful treatment. All energies in this chapter will be given in the centre-of-mass frame

unless otherwise stated. Only laboratory thermonuclear reaction rates will be considered (i.e., thermal target excitations will be disregarded).

2.1 Reaction Rate Formalism

The reaction rate per particle pair in a medium of temperature, T, is given by

$$\langle \sigma v \rangle = \sqrt{\frac{8}{\pi \mu}} \frac{1}{(kT)^{3/2}} \int_0^\infty E \sigma(E) e^{-E/kT} dE \tag{2.1}$$

where μ is the reduced mass of the reacting particles, $\mu = M_0 M_1/(M_0 + M_1)$,; M_i refer to the masses of the particles; k is the Boltzmann constant; E is the centre-of-mass energy between the reacting particles; and $\sigma(E)$ is the reaction cross section at relative energy, E. Inspection of Eq. (2.1) reveals that the reaction rate is dependent on the cross section as a function of energy.

The strategy for determining reaction rates from Eq. (2.1) depends on the nature of the cross section. Under the assumption of non-interfering cross section contributions[1], the cross section can be separated into non-resonant and resonant parts. Each contribution will be discussed separately in the following sections.

2.1.1 Non-resonant Reaction Rates

Smoothly varying reaction cross sections can be written by

$$\sigma(E) = \frac{1}{E} e^{-2\pi\eta} S(E) \tag{2.2}$$

where η is the Sommerfeldt parameter, given by $2\pi\eta = \sqrt{\frac{2\mu}{E}} Z_0 Z_1 e^2/\hbar$ (Z_i is the atomic number of the nuclei); and $S(E)$ is the astrophysical S-factor. The S-factor is the slowly varying function of energy that remains once the $1/E$ and s-wave Coulomb barrier penetration energy dependence are

[1] In cases where this assumption is not valid (e.g., when interference between rate contributions is significant), other methods such as R-matrix theory must be used to calculate reaction rates.

removed from the cross section[2]. Substituting Eq. (2.2) into Eq. (2.1), we obtain

$$\langle \sigma v \rangle = \sqrt{\frac{8}{\pi \mu}} \frac{1}{(kT)^{3/2}} \int_0^\infty e^{-2\pi\eta} S(E) e^{-E/kT} dE \tag{2.3}$$

The integrand of this equation is dominated by two terms: the Gamow factor, $e^{-2\pi\eta}$, and the Boltzmann factor, $e^{-E/kT}$. The former of these increases with energy as $e^{-\sqrt{1/E}}$, while the latter decreases as e^{-E}. The overlap between the tails of these functions produces the Gamow peak, which determines the energy range at which reactions will occur in the stellar environment. The Gamow peak can be approximated by a Gaussian function with centroid (E_0) and $1/e$ width (ΔE_0) given by

$$E_0 = 0.1220 \left(Z_0^2 Z_1^2 \frac{M_0 M_1}{M_0 + M_1} T_9^2 \right)^{1/3} \tag{2.4}$$

$$\Delta E_0 = 0.2368 \left(Z_0^2 Z_1^2 \frac{M_0 M_1}{M_0 + M_1} T_9^5 \right)^{1/6} \tag{2.5}$$

where T_9 is the temperature in GK. The astrophysical s-factor can be approximated by a Taylor expansion around zero energy

$$S(E) \approx S(0) + S'(0)E + \frac{1}{2} S''(0) E^2 \tag{2.6}$$

where the derivatives ($S'(0)$ and $S''(0)$) are with respect to E. Following this approximation, Eqs. (2.2) and (2.6) can be substituted into Eq. (2.1) to provide an analytical expression for the reaction rate:

$$\langle \sigma v \rangle_{\text{nr}} = \frac{4.339 \times 10^8}{Z_0 Z_1} \frac{M_0 + M_1}{M_0 M_1} S_{\text{eff}} e^{-\tau} \tau^2 e^{(T_9/T_{9,\,\text{cutoff}})^2} \tag{2.7}$$

$$\tau = 4.2487 \left(Z_0^2 Z_1^2 \frac{M_0 M_1}{M_0 + M_1} \frac{1}{T_9} \right)^{1/3} \tag{2.8}$$

$$S_{\text{eff}} = S(0) \left[1 + \frac{5}{12\tau} + \frac{S'(0)}{S(0)} \left(E_0 + \frac{35}{36} kT \right) + \frac{1}{2} \frac{S''(0)}{S(0)} \left(E_0^2 + \frac{89}{36} E_0 kT \right) \right] \tag{2.9}$$

The last factor in Eq. (2.7) is an artificial addition to prevent this expression from becoming unphysical at high temperatures (i.e., where the Gamow peak assumption is no longer valid, or where resonances

[2]Note that the notion of an astrophysical S-factor is also applicable to resonant cross sections. In these cases, however, the S-factor will no longer be a smoothly varying function.

dominate the cross section).

2.1.2 Resonant Reaction Rates

The cross section arising from an isolated resonance is described by the Breit-Wigner formula [Bre36],

$$\sigma_{\mathrm{BW}}(E) = \frac{\lambda^2}{4\pi}\omega\frac{\Gamma_a(E)\Gamma_b(E)}{(E-E_r)^2+\Gamma(E)^2/4} \tag{2.10}$$

$\Gamma_a(E)$, $\Gamma_b(E)$, and $\Gamma(E)$ are the energy dependent entrance channel, exit channel, and total partial widths respectively. The factor ω is the spin factor,

$$\omega = \frac{2J+1}{(2J_0+1)(2J_1+1)} \tag{2.11}$$

where J and J_i are the resonance and particle spins, respectively; λ is the deBroglie wavelength at the resonance energy defined by,

$$\frac{\lambda^2}{2} = \frac{(\pi\hbar)^2}{\mu E} \tag{2.12}$$

Substituting the Breit-Wigner resonant cross section into Eq. (2.1), the reaction rate per particle pair becomes

$$\langle\sigma v\rangle = \frac{\sqrt{2\pi}\hbar^2}{(\mu kT)^{3/2}}\omega\int_0^\infty \frac{\Gamma_a(E)\Gamma_b(E)}{(E-E_r)^2+\Gamma(E)^2/4}e^{-E/kT}dE \tag{2.13}$$

Narrow Resonances

If the partial widths, Γ_i, and Boltzmann factor, $e^{-E/kT}$, do not vary significantly with energy over the width of the resonance, it can be considered to be narrow. The partial widths in Eq. (2.13) are then replaced with energy independent quantities

$$\langle\sigma v\rangle = \frac{\sqrt{2\pi}\hbar^2}{(\mu kT)^{3/2}}\omega\Gamma_a\Gamma_b\int_0^\infty \frac{e^{-E/kT}}{(E-E_r)^2+\Gamma(E)^2/4} \tag{2.14}$$

$$= \left(\frac{2\pi}{\mu kT}\right)^{3/2}\hbar^2\omega\frac{\Gamma_a\Gamma_b}{\Gamma}e^{-E_r/kT}, \tag{2.15}$$

where the resonance strength is defined by

$$\omega\gamma = \omega\frac{\Gamma_a\Gamma_b}{\Gamma} \tag{2.16}$$

Note that the resonance strength is proportional to the maximum cross section multiplied by the resonance width ($\omega\gamma \propto \sigma_{\max} \cdot \Gamma$). Furthermore, the reaction rate for an ensemble of narrow resonances can be summed incoherently,

$$\langle\sigma v\rangle = \left(\frac{2\pi}{\mu kT}\right)^{3/2}\hbar^2\sum_i(\omega\gamma)_i e^{-E_r/kT} \tag{2.17}$$

Wide Resonances

If the partial widths and Boltzmann factor vary significantly with energy, Eq. (2.13) must be integrated numerically. In the following discussion, a transition to a unique final state will be assumed. In reaction rate calculations, this assumption is a good approximation if the dominant transition is considered. The particle partial width for channel c is

$$\Gamma_c(E) = 2\frac{\hbar^2}{\mu R^2}P_c(E)\theta_c^2 \tag{2.18}$$

where the channel radius, R, is defined by $R = 1.25(A_0^{1/3} + A_1^{1/3})$; θ_c^2 is the dimensionless reduced width; and $P_c(E)$ is the penetration factor calculated from Coulomb wave functions by

$$P_c(E) = \frac{\rho}{(F^2(E) + G^2(E))} \tag{2.19}$$

where $\rho = 0.21874 \cdot R \cdot \sqrt{\mu E}$; and F and G are Coulomb wave functions. The dimensionless reduced width is proportional to a spectroscopic factor, S,

$$\theta_c^2 = C^2 S\theta_{pc}^2 \tag{2.20}$$

where C is an isospin Clebsch-Gordan coefficient and θ_{pc}^2 is the dimensionless single-particle reduced width, which can be calculated numerically. See Ref. [Ili97] for more details on calculating this

quantity.

From Eqs. (2.18)-(2.20), it becomes obvious that the energy dependence of charged particle cross sections arises from the Coulomb barrier, whose energy dependence is described by the penetration factor. The charged particle partial width can now be scaled with respect to the partial width at the resonance energy, E_r, by,

$$\Gamma_c(E) = \Gamma_c(E_r)\frac{P_c(E)}{P_c(E_r)} \tag{2.21}$$

It should be noted that these equations can also be applied to subthreshold resonances.

The energy dependent partial width for a γ-ray follows a similar procedure. The γ-ray partial width for a single transition is

$$\Gamma_\gamma(\bar{\omega}, E_\gamma) = \frac{8\pi(L+1)}{L[(2L+1)!!]^2}\left(\frac{E_\gamma}{\hbar c}\right)^{2L+1} B(\bar{\omega}L) \tag{2.22}$$

where $\bar{\omega}$ denotes either electric or magnetic radiation; L is the multipolarity of the γ-ray; E_γ is the transition energy; and the double factorial is defined as $(2L+1)!! = 1\cdot 3\cdot 5\ldots\cdot(2L+1)$. The γ-ray partial width as a function of the incoming particle energy, E, is therefore

$$\Gamma_\gamma(E) = \Gamma_\gamma(E_r)\left(\frac{E+Q-E_f}{E_r+Q-E_f}\right)^{2L+1} \tag{2.23}$$

where Q is the entrance particle separation energy (Q-value) and E_f is the final excitation energy of the γ-decay.

2.1.3 Interfering Resonances

If two or more broad resonances with the same spin and parity are close together in energy, their amplitudes may interfere. In the case of two interfering resonances with cross sections σ_1 and σ_2, respectively, the total cross section in the presence of interference is [Rol75]

$$\sigma(E) = \sigma_1(E) + \sigma_2(E) \pm 2\sqrt{\sigma_1(E)\sigma_2(E)}\cos(\delta_1 - \delta_2) \tag{2.24}$$

The phase shifts δ_i can be calculated by

$$\delta_i = \arctan\left[\frac{\Gamma_i(E)}{2(E - E_{ri})}\right] \tag{2.25}$$

The reaction rate arising from two interfering resonances is found by substituting Eq. (2.24) into Eq. (2.1) and integrating numerically. If interference is occurring between many resonances, (^{14}N(p,γ)^{15}O is a good example), other methods such as R-matrix theory, must be used to find the reaction rate.

2.2 Monte Carlo Reaction Rates

The equations outlined in Sec. 2 provide an array of tools for calculating thermonuclear reaction rates given estimates for the cross section parameters (E_r, $\omega\gamma$ etc.). A problem arises, however, when the uncertainties of the reaction rates are needed. With developments in computing power in the last decade or so, the demand for statistically meaningful reaction rate uncertainties is increasing greatly. It is becoming possible to perform stellar model calculations in relatively little time. This increase in modelling speed allows sensitivity studies to be performed, in which the reaction rates are varied within their uncertainties to find the influence on nucleosynthesis in stars.

In the present work, a Monte Carlo method is used to calculate the reaction rate uncertainties arising from uncertain input parameters. The general strategy of Monte Carlo uncertainty[3] propagation is the following: (i) Simultaneously sample from the probability density distribution for each uncertain parameter (these samples must be chosen independently to avoid correlations); (ii) Perform the calculation of the reaction rate using the sampled values and record it. (iii) Repeat steps (i)-(ii) many times (on the order of 5000). These three steps will result in a distribution of reaction rates, which can be interpreted as the probability distribution of the reaction rate. Extraction of uncertainties from the distribution will be discussed later. While input parameter sampling is being performed, care must be taken to consider correlations in parameters. For example, particle partial widths depend on the penetration factor through Eq. (2.18), which is an energy dependent quantity. The individual energy samples must, therefore, be propagated through the partial width calculation to fully account for the

[3]Throughout this work, care is taken to refer to the terms *uncertainty* and *error* correctly. The term *error* refers to a quantity that is believed to be incorrect, whereas *uncertainty* refers to the statistical spread of a parameter.

energy uncertainty correlation.

Note that Ref. [Tho99] states that a Monte Carlo method would take on the order of S^N calculations to calculate uncertainties in this way (where S and N are the number of random samples and uncertain parameters, respectively). However, this number of calculations is only necessary if the contribution of each input uncertainty needs to be known. In the present work, only final reaction rate uncertainties are desired, so the number of calculations needed is equal to the number of samples, S.

In order to proceed with using Monte Carlo sampling to calculate reaction rate uncertainties, the sampling distributions must be defined for each uncertain parameter. A brief overview of statistical distributions relevant to reaction rate calculation is in Appendix A. Once a reaction rate distribution has been determined, an appropriate mathematical description must be found to present the result. In the following, the statistical distributions used for each uncertain parameter will be discussed, followed by details on the mathematical description used for the final reaction rate uncertainties.

2.2.1 Statistical Distributions for Nuclear Physics Input

Resonance Energies

Resonance energies are assumed to have Gaussian distributed uncertainties. The reasons for this assumption are twofold. Firstly, most resonance energies are determined from the front edge of thick target yield curves. In this case, the resonance energy is determined from a sum of uncertain parameters such as individual magnet calibrations. The central limit theorem states that the sum of n independent continuous random variables x_i with means μ_i and uncertainties σ_i becomes a Gaussian random variable in the limit of $n \rightarrow \infty$. Secondly, for low energy resonances the energy can be found by measuring the excitation energy of the compound nucleus ($E = E_x - Q$). This case involves the subtraction of two Gaussian distributed variables, which is also expected to be Gaussian. Note that there is a finite probability of calculating a negative resonance energy. There is no contradiction in this situation, because the resonance can be treated as a subthreshold resonance.

Resonance Strengths

Resonance strengths are assigned lognormal uncertainties. To understand why this is, consider the experimental methods for determining these quantities. A resonance strength is estimated by one of two methods; (i) direct measurement, and (ii) estimation from partial widths determined in other experiments (such as particle transfer measurements). In the first case, a resonance strength is calculated from the product of many unknown quantities. An example of this is the resonance strength determination from the maximum yield of a thick target for a (p,γ) reaction,

$$\omega\gamma \sim \epsilon \frac{N_\gamma}{N_p \eta W(\theta) B} \tag{2.26}$$

where ϵ is the stopping power, N_γ and N_p are the number of measured γ-rays and incoming protons, respectively, η is the detector efficiency, B is the branching ratio, and W is the angular correlation for a detector at angle, θ. Each of these quantities are expected to have Gaussian uncertainties. The central limit theorem states that the product of normally distributed quantities results in a lognormally distributed quantity. The second case considered is also expected to have lognormally distributed uncertainties because partial widths are determined through similar means as those described above.

Once a lognormal distribution has been selected to describe the probability distribution of resonance strengths, an important question arises: how are quoted uncertainties converted into lognormal parameters? To answer this question, first consider the expectation value and variance of a lognormal distribution defined in Appendix A:

$$E[x] = e^{(2\mu+\sigma^2)/2}, \quad V[x] = e^{(2\mu+\sigma^2)} \left[e^{\sigma^2} - 1\right] \tag{2.27}$$

where the lognormal parameters μ and σ represent the mean and standard deviation of $\ln x$. The lognormal parameters are, therefore, defined by

$$\mu = \ln(E[x]) - \frac{1}{2}\ln\left(1 + \frac{V[x]}{E[x]^2}\right), \quad \sigma = \sqrt{\ln\left(1 + \frac{V[x]}{E[x]^2}\right)} \tag{2.28}$$

These parameters can now be found from literature values by associating quoted results with the

expectation value and the square root of the variance.

Note that a lognormal distribution is not defined for negative values of x. This feature is advantageous because it removes the finite probability of unphysical negative values that arise when Gaussian uncertainties are used. This is especially true for partial width measurements, which typically have uncertainties of close to 50% associated with them. A 50% Gaussian uncertainty results in a 5% probability of the partial width being below zero.

Nonresonant S-factors

Nonresonant S-factors are calculated following the parametrisation outlined in Eq. (2.6). A lognormal distribution is assumed for the effective S-factor, S_{eff}. Typical uncertainties of 40% to 50% are assumed for the nonresonant component of the cross section. Eq. (2.28) are used to convert these to lognormal parameters.

Interfering Resonances

Frequently, the sign of interference between wide resonances (see Eq. (2.24)) is not known. A binary distribution is sampled in this case, which will sample equally between signs of $+1$ and -1 as the number of samples approaches infinity. This will lead to a double-peaked reaction rate probability density function. Clearly, in these cases, the probability density function will not be described by a simple analytical function. However, in most cases, this effect will be convoluted with other cross section contributions, and the total reaction rate distribution will lose this double-peaked structure.

2.2.2 Upper Limits

The problem of calculating reaction rates using resonance strength upper limits will now be discussed. The standard practice in nuclear astrophysics is to assume that the best estimate of a resonance strength is 10% of a measured upper limit. The assumption is then made that the true value of the resonance strength has a uniform probability of residing between zero and the measured upper limit. Upper and lower bounds on the resonance strength are calculated using these limits. These assumptions imply a mean resonance strength value of exactly $1/2$ of the measured upper limit, which

contradicts the predictions of nuclear statistical models. In the present work, these models are taken as a starting point to construct a physically motivated treatment of upper limits for resonance strengths.

Resonance strength upper limits arise from two possible situations. Firstly, a direct measurement was performed with no observed signal above background. Secondly, an indirect measurement, such as a transfer measurement was performed to measure a particle partial width. The latter case will be discussed first.

Upper Limits of Partial Widths

Recall that particle partial widths are determined by the dimensionless reduced width, θ^2, in Eqs. (2.18) and (2.20). Similarly, γ-ray partial widths are determined from the reduced transition probability, B, in Eq. (2.22). These quantities are related to the square of nuclear Hamiltonian matrix elements, which in turn is an integral over the nuclear configuration space. For sufficiently complex wave functions, the matrix elements will arise from the sum over many contributions, each of which has a randomly distributed sign. The central limit theorem, therefore, dictates that a nuclear matrix element will have an expectation value of zero, with approximately Gaussian distributed uncertainties. The square of the nuclear matrix element is, therefore, expected to have a probability density function that follows a chi-squared distribution with one degree of freedom (See Apx. A). For a more detailed discussion of this issue (including verification studies), the reader is referred to Refs. [Por56, Lon10].

The probability density function describing observables that are related to the squares of nuclear matrix elements is known as a Porter-Thomas distribution, where the ratio of a variable to its local mean value is given by the chi-squared distribution with one degree of freedom. The dimensionless reduced width therefore, follows a probability density function given by

$$f(\theta^2) = \frac{c}{\sqrt{\theta^2}} e^{-\theta^2/(2\langle\theta^2\rangle)} \tag{2.29}$$

where c is a normalisation factor, and $\langle\theta^2\rangle$ is the average local mean value of the reduced width. That is, the mean value of the dimensionless reduced width for a specific nucleus, channel spin, orbital angular momentum etc. The problem in using the Porter-Thomas distribution for the calculation of partial width probability density functions now becomes one of collecting enough data to find $\langle\theta^2\rangle$

for every case needed. In the present work, the partial widths were obtained from the data presented in Ref. [Dra94] and references therein. The widths (1127 proton widths and 360 α-particle widths) were averaged globally because of the lack of available data for local fits of every l-value, nucleus and so on. More detail is presented in Refs. [New10a, Lon10]. The average values were found to be $\langle\theta_p^2\rangle = 0.0045$ and $\langle\theta_\alpha^2\rangle = 0.010$ for protons and α-particles, respectively.

Although, in principle, the same arguments can be made for γ-ray reduced transition probabilities, estimates for the mean value, $\langle B\rangle$, were more elusive. However, upper limits for γ-ray partial widths are less crucial in reaction rate calculations and were, therefore, omitted from the present work.

Now that a form for the probability density function of reduced widths has been defined, the question of including experimental upper limits can be addressed. Frequently, an experiment will measure an upper limit for a spectroscopic factor, which can be converted to a reduced width through Eq. (2.20). It should be clear that these upper limits, as with any experimental results, have some probability density function associated with them. However, probability density functions for upper limit measurements are rarely reported in the literature. In the absence of more information, the present work will use a sharp truncation of the Porter-Thomas distribution at the upper limit. That is

$$f(\theta) = \begin{cases} \frac{c}{\sqrt{\theta^2}} e^{-\theta^2/(2\langle\theta^2\rangle)} & \text{if } \theta^2 \leq \theta_{ul}^2 \\ 0 & \text{if } \theta^2 > \theta_{ul}^2 \end{cases} \tag{2.30}$$

where θ_{ul}^2 is the measured upper limit of the reduced width.

Upper Limits on Resonance Strengths

During a direct search for a resonance, an upper limit can also be reported if no signal is observed. The calculation of upper limits and their corresponding confidence limits is a well studied subject. The reader is referred to Refs. [Nar00, Zhu07, Cou08] and references therein for an introduction to the subject. In the field of nuclear astrophysics, however, confidence limits are rarely quoted. In the present work, the following strategy for incorporating upper limits from direct searches is used: (i) the upper limit, $\omega\gamma_{ul}$, is assumed to arise from the entrance particle partial width, $\Gamma_{a,ul}$ (this is a reasonable assumption for charged particle reactions at low energies, where cross sections are determined by the

Coulomb barrier); (ii) the partial width is used to calculate a reduced width upper limit, θ^2_{ul}; (iii) the probability density function used for sampling is calculated from Eq. (2.30).

At this point, all of the necessary probability density functions needed for Monte Carlo reaction rate calculations are described. The next step is to perform the calculations, and analyse the reaction rate distributions.

2.2.3 Monte Carlo Sampling and Analysis

The general strategy for Monte Carlo uncertainty propagation was outlined at the beginning of this section. In Sec. 2.2.1, the statistical distributions to be sampled for each input parameter were chosen. A computer code, `RatesMC`, was written to perform the Monte Carlo sampling over the distributions and to analyse the final rate distribution. The code is capable of calculating reaction rates through any of the methods described in Sec. 2.1, including integration of wide resonances and interfering pairs of resonances. Upper limits in resonance parameters are treated according to the method described in Sec. 2.2.2.

Once the reaction rate sampling has been performed, an ensemble of final reaction rates exits. It will have a probability density distribution that can be analysed to extract descriptive statistics (mean, median, variance etc.). An example of a reaction rate probability density distribution for 10,000 samples is shown in Fig. 2.1 for the reaction rate arising from a fictitious resonance in ^{22}Ne$(\alpha,\gamma)^{26}$Mg at $E_r = 300(15)$ keV with $\omega\gamma = 4.1 \pm 0.2$ eV at a temperature of $T = 0.45$ GK. Part (a) shows a histogram of the reaction rate probability density distribution and shows clearly a lognormal shape. Part (b) shows the cumulative distribution, which is obtained by summing each bin in part (a), and normalising to a maximum height of unity. Part (b) also illustrates the method utilised to obtain reaction rate uncertainties from the distribution. For the recommended reaction rate, the median reaction rate is used. The median is a useful statistic because exactly half of the calculated rates are lying above this value and half below. Note that the mean is not used for the final presentation of rates in the present work because it is strongly affected by outliers in the reaction rate distribution. Thus it was decided that the mean rate was not a good representation of the recommended rate. The low and high (not the "maximum" and "minimum" rates commonly used in nuclear astrophysics) reaction rates are obtained by considering a 68% coverage probability. There are several methods for

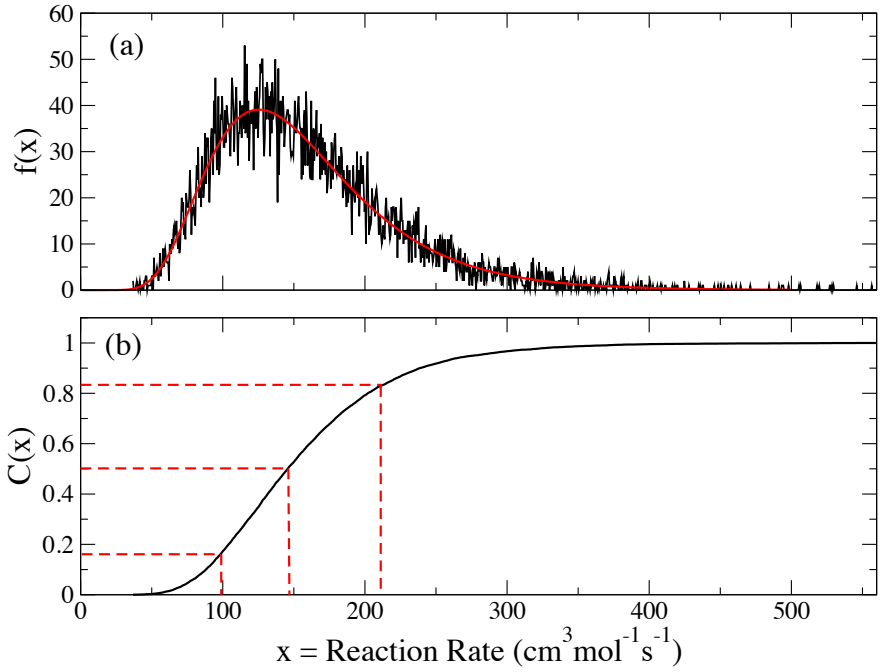

Figure 2.1: Reaction rate probability density distribution and corresponding cumulative distribution from the fictitious resonance described in the text. The dashed lines show the 16th, 50th, and 84th percentiles of the reaction rate.

obtaining these coverage probabilities, such as finding the coverage that minimises the range of the uncertainties, or one that is centred on the median. In the present work, the 16^{th} to 84^{th} percentiles are used. Note that in reality, the reaction rates are not initially binned when calculating a cumulative distribution to avoid the loss of information that arises from the binning process [Pre07].

Although a low, high and median rate are useful quantities, they do not necessarily contain all the information on the probability density. It was mentioned already that computational stellar modelling is becoming advanced enough that sensitivity studies on nuclear reaction rates are feasible. For these sensitivity studies to produce reliable results, the reaction rates should be sampled according to the probability density. It would be inconvenient, however, to publish histograms of the reaction rates (for every reaction, at each temperature, with 1000 bins each). A more convenient approach would be to approximate the reaction rate probability distribution with a simple analytical function. In order to find such a function, consider the following three examples: (i) the reaction rate is dominated by a non-resonant S-factor. Hence, the reaction rate is directly proportional to S_{eff} in Eq. (2.7), which in turn is described by lognormal uncertainties. (ii) the rate is dominated by a single resonance. If the resonance strength dominates the uncertainties, the reaction rate will be distributed according to a lognormal probability distribution. If the resonance energy (normally distributed) dominates the uncertainties, the rate will also be distributed lognormally. This is because the resonance energy enters through an e^{E_r} term; (iii) finally, consider the case where the rate has contributions from many resonances. The central limit theorem states that the sum of many uncertainties will be distributed according to a Gaussian. However, a lognormal distribution approximates a Gaussian well for uncertainties of less than about 20%. Although these examples do not offer proof that the reaction rate can be described by a lognormal distribution, they suggest that in most cases, it is a good approximation. The calculation of the lognormal parameters for the reaction rate distribution now becomes a trivial matter. The lognormal parameters are calculated by

$$\mu = E[\ln(x)], \qquad \sigma^2 = V[\ln(x)] \tag{2.31}$$

where $E[y]$ and $V[y]$ signify the expectation value and variance of their argument, y, respectively. The expressions in Eq. (2.31) were used to generate the smooth line in Fig. 2.1a, which shows excellent

T (GK)	Low rate	Median rate	High rate	lognormal μ	lognormal σ	A-D
0.100	4.23×10^{-10}	2.41×10^{-09}	1.37×10^{-08}	$-1.985\times10^{+01}$	$1.75\times10^{+00}$	2.77×10^{-01}
0.110	1.02×10^{-08}	4.95×10^{-08}	2.40×10^{-07}	$-1.682\times10^{+01}$	$1.59\times10^{+00}$	2.75×10^{-01}
0.120	1.43×10^{-07}	6.08×10^{-07}	2.59×10^{-06}	$-1.431\times10^{+01}$	$1.46\times10^{+00}$	2.73×10^{-01}
0.130	1.32×10^{-06}	5.02×10^{-06}	1.91×10^{-05}	$-1.220\times10^{+01}$	$1.34\times10^{+00}$	2.72×10^{-01}
0.140	8.79×10^{-06}	3.04×10^{-05}	1.05×10^{-04}	$-1.040\times10^{+01}$	$1.25\times10^{+00}$	2.70×10^{-01}
0.150	4.52×10^{-05}	1.44×10^{-04}	4.58×10^{-04}	$-8.845\times10^{+00}$	$1.17\times10^{+00}$	2.68×10^{-01}
0.160	1.88×10^{-04}	5.57×10^{-04}	1.65×10^{-03}	$-7.491\times10^{+00}$	$1.09\times10^{+00}$	2.65×10^{-01}
0.180	2.00×10^{-03}	5.23×10^{-03}	1.38×10^{-02}	$-5.250\times10^{+00}$	9.72×10^{-01}	2.61×10^{-01}
0.200	1.30×10^{-02}	3.10×10^{-02}	7.40×10^{-02}	$-3.473\times10^{+00}$	8.75×10^{-01}	2.57×10^{-01}
0.250	3.60×10^{-01}	7.20×10^{-01}	$1.45\times10^{+00}$	-3.254×10^{-01}	7.00×10^{-01}	2.49×10^{-01}
0.300	$3.13\times10^{+00}$	$5.59\times10^{+00}$	$10.00\times10^{+00}$	$1.723\times10^{+00}$	5.84×10^{-01}	2.47×10^{-01}
0.350	$1.41\times10^{+01}$	$2.33\times10^{+01}$	$3.84\times10^{+01}$	$3.150\times10^{+00}$	5.01×10^{-01}	2.48×10^{-01}
0.400	$4.27\times10^{+01}$	$6.62\times10^{+01}$	$1.03\times10^{+02}$	$4.193\times10^{+00}$	4.39×10^{-01}	2.51×10^{-01}

Table 2.1: Example reaction rates for the fictional ^{22}Ne(α,γ)^{26}Mg reaction described in the text.

agreement with the shape of the distribution (the reader should be aware that this is not a fit to the data, but the solid line is calculated directly from Eqs. (2.31)). A good measure of the applicability of a lognormal approximation is the Anderson-Darling statistic[4]. t_{AD}, is calculated by

$$t_{AD} = -n - \sum_{i=1}^{n} \frac{2i-1}{n} (\ln F(y_i) + \ln [1 - F(y_{n+1-i})] \tag{2.32}$$

where n is the number of samples, y_i are the samples (arranged in ascending order), and F is the cumulative distribution of a standard normal function (i.e., a Gaussian centred on zero). Although, statistically speaking, an A-D value greater than unity represents deviation from a lognormal distribution, in the present work it was found that the distribution does not *visibly* deviate from lognormal until A-D exceeds $t_{AD} \approx 30$. The A-D statistic is published along with all other values to provide a reference to the reader. An example reaction rate output table for the fictitious reaction discussed above is shown in Tab. 2.1. Note that t_{AD} is less that unity at all temperatures. This good agreement supports argument (ii) above.

[4]The Anderson-Darling statistic is more useful than a χ^2 statistic because it does not require binning of the data, which results in a loss of information as previously described.

2.3 Conclusions

A Monte Carlo reaction rate uncertainty propagation code, `RatesMC` has been written to compute reaction rates. The code is capable of calculating the reaction rate arising from non-resonant S-factors, narrow resonances, wide resonances, subthreshold resonances, and interfering resonance pairs. Upper limits in particle partial widths have been treated in a statistically meaningful manner for the first time. The code calculates a reaction rate distribution at a range of temperatures from $T = 0.01$ GK to 10 GK, which is suitable for all astrophysical situations. At each temperature, six parameters are output; the low, median, and high reaction rates; two parameters (μ and σ) describing the position and spread of a lognormal approximation; and an Anderson-Darling statistic to describe how well the lognormal approximation follows the rate distribution.

The code will be used as a specific example to calculate the reaction rates of ^{22}Ne$(\alpha,\gamma)^{26}$Mg and ^{22}Ne$(\alpha,\mathrm{n})^{25}$Mg in Ch. 7. For a more detailed discussion of the Monte Carlo method, which is outside the scope of this work, the reader is referred to Ref. [Lon10].

3 Yield Curve Analysis

3.1 Introduction

NUCLEAR reaction cross sections are needed to calculate thermonuclear reaction rates (see chapter 2). In an experiment, the quantity measured is a yield, not the cross section. The yield is a convolution of the cross section with other factors such as the beam energy spread and a finite target thickness. The study of yield curves is important for: (i) deriving an unknown cross section from a measured yield; and (ii) obtaining the depth concentration profile of a target if the cross section is well known.

The study of a target as a function of depth is known as depth profiling. Depth profiling with narrow nuclear resonances is a particularly useful non-destructive method of probing targets, which has become more powerful with improvements in computing power in the last few decades Ref. [Mau82]. Advanced deconvolution methods for obtaining the distribution of nuclei in a substrate are summarised in Ref. [McG91]. The depth profiling formalism will be discussed in the following. All energies are in the centre-of-mass frame unless otherwise stated.

3.2 Excitation Functions from Nuclear Resonances

An excitation function for a nuclear reaction is obtained by measuring the yield over a range of incident beam energies. The measured yield is defined as:

$$\text{Yield} = \frac{\text{Number of reactions}}{\text{Number of incident particles}} \tag{3.1}$$

For a radiative capture reaction, the experimental yield (Y) can be calculated by measuring the intensity of γ-rays with a germanium detector:

$$Y = \frac{e}{\varepsilon^p \, W(\theta) \, B} \frac{I}{Q}, \tag{3.2}$$

where e is the elementary charge; ε^p is the full-energy peak efficiency for the measured γ-ray; $W(\theta)$ is the angular correlation function at detector angle θ with respect to the beam direction; B is the cross section fraction that is carried by the observed γ-ray (e.g., the branching ratio for a primary transition); I is the number of counts observed in the full-energy peak; and Q is the measured beam charge accumulated on the target.

The yield depends on the measured cross section as well as on the nature of the target containing the reacting nuclei. Understanding the effect of the target on the measured yield is critical for extracting resonance strengths or cross sections from excitation functions. For a target with a varying atomic concentration with depth, the yield will depend on the location in the target where the reactions occur. For narrow resonances, most of the reactions will occur at a depth determined by the incident beam energy and the energy loss in the target. A finite beam resolution and energy straggling of the incident beam in the target serve to broaden the excitation function.

In the following, an implanted target will be considered. Implanted targets consist of a substrate ("target backing"), into which target nuclei have been implanted. This is usally performed by accelerating the ions of interest, and focusing them onto the substrate. The number of reactions originating from a nuclear reaction in an implanted target per incident beam particle is given by [Mau82]:

$$Y(E_0) = \int_0^\infty \mathrm{d}E \int_0^\infty \mathrm{d}x \, [C(x)\sigma(E)g_0(E; E_0; x)] \tag{3.3}$$

where $C(x)$ is the concentration profile of the target nuclei (cm^{-2}); $\sigma(E)$ is the cross section of the reaction at energy, E; and $g_0(E; E_0; x)$ is the energy spread law (i.e., the probability) of a beam particle having an energy of E, given an average incident energy, E_0, at depth x. The beam spread at the surface of the target ($x = 0$) is the beam spread of the incident beam, with the energy spread increasing due to straggling as the beam traverses the target. The beam energy spread in the target

can be expressed as a convolution of two functions: $h(E_0)$, which describes the beam spread of the incident beam; and $g(u;x)$, which describes the straggling of the beam energy (the probability density function of the beam particles having an energy u at depth x). Equation (3.3) can now be expressed as a set of convolution integrals:

$$Y(E_0) = \sigma(E_0) * h(E_0) * \int_0^\infty N(x) g(E_0; x) \mathrm{d}x \tag{3.4}$$

Convolution integrals are defined as:

$$a(x) * b(x) \equiv \int_{-\infty}^{\infty} a(x - x') b(x') \mathrm{d}x' \tag{3.5}$$

$$= \int_{-\infty}^{\infty} a(x') b(x - x') \mathrm{d}x' \tag{3.6}$$

The excitation function resulting from a varying ion concentration at different target depths can be described by dividing the target into many thin depth slices. Using this approximation, the yield from a nuclear reaction is obtained from a sum over the contributions of each layer, i, of the target [Mau82]:

$$Y(E_0) \approx \sum_i N_i F_i(E_0) \tag{3.7}$$

Here, E_0 is the mean beam energy; N_i is the target atom concentration in each layer (in units of nuclei per cm^2); and $F_i(E_0)$ is the convolution function of the cross section, $\sigma(E)$, beam energy profile, and energy straggling in the target [Mau82]:

$$F_i(E_0) = \int_{E'=0}^{E_0} g_i(E_0 - E')\, dE' \int_{E=-\infty}^{\infty} \sigma(E) h(E' - E)\, dE \tag{3.8}$$

The beam spread function, $h(E' - E)dE$, is expected to be Gaussian in shape, and describes the probability of a beam particle having an energy between E and dE at a depth corresponding to an energy of E'. The integral over negative energy E becomes truncated at $E = 0$ because the cross section at these energies is zero. The straggling function, $g_i(E_0 - E')dE'$ (defined at each layer, i), describes the probability of a beam particle having an energy between E' and dE' at a depth of x_i. Straggling effects can be computationally intensive to calculate [Pez08, Mau82]. However, beam

particles typically undergo many collisions with electrons, losing typically several keV of energy in the thick targets used in nuclear astrophysics experiments. In these cases, the central limit theorem of statistics states that energy straggling can be approximated by a Gaussian function [Pez08]. Thus:

$$h(E' - E) = \frac{1}{\sqrt{2\pi}\sigma_b} \exp\left[-\frac{(E' - E)^2}{2\sigma_b^2}\right] \tag{3.9}$$

$$g_i(E_0 - E') = \frac{1}{\sqrt{2\pi x_i}\sigma_s} \exp\left[-\frac{(E_0 - E' - \Delta_i)^2}{2\sigma_s^2 x_i}\right] \tag{3.10}$$

The adjustable parameters σ_b and σ_s define the beam energy width and straggling rate, respectively. The average energy loss of the beam particles at depth x_i is denoted by Δ_i, and is given by the integral (sum) of the total linear stopping power, dE/dx, up to that location:

$$\Delta_i = \sum_{j=1}^{i} (x_j - x_{j-1}) \frac{dE}{dx_j} \tag{3.11}$$

Previous work frequently assumed a constant total linear stopping power [Mau82]. This is only valid if (i) the beam does not lose too much energy in the target so that the stopping power for pure layers is nearly energy-independent, and (ii) the ion concentrations do not vary significantly over the depth of the target. For example, if a given species is implanted in high doses resulting in a strongly varying depth concentration, then the second assumption is not valid, and the total stopping power of the material cannot be assumed to be constant, even if the energy lost in the target is relatively small.

For a sample produced by implanting species p into a substrate of species q, the energy lost per unit path-length is given by:

$$\frac{dE}{dx} = N_q S_q + N_p S_p = N_A \left[\frac{\rho_q}{M_q} S_q + \frac{\rho_p}{M_p} S_p\right] \tag{3.12}$$

N is the number of atoms per cm^3; S is the stopping cross section (eV·cm^2/atom); N_A is Avogadro's number; M is the atomic mass in amu; and the mass density (in g/cm^3) of atoms is denoted by ρ. In general, the stopping cross sections depend on energy. In order to determine the densities ρ, the nature of the implanted region must be known. Here, the implanted atoms are assumed to be located

in inter-lattice spacings, resulting in an overall material density increase:

$$\rho_q(x_i) = \overline{\rho_q} = const \tag{3.13}$$

$$\rho_p(x_i) = \xi(x_i)\frac{\overline{\rho_q} M_p}{M_q} \tag{3.14}$$

where $\xi(x_i)$ is the stoichiometry (i.e., the number ratio of implanted to substrate atoms, N_p/N_q) at depth x_i; $\overline{\rho_q}$ is the mean density of the pure substrate material (without species p).

Depth profiling is usually performed with narrow nuclear resonances, whose peaked shapes provide sufficient depth resolution. As will be seen later, in the present work the measured resonances have total widths on the order of tens of eV. Narrow resonance cross sections, for which the partial widths can be assumed to be energy-independent over the total resonance width, can be described by the Breit-Wigner formula described in Sec. 2.1:

$$\sigma(E) = \frac{\lambda^2}{4\pi}\omega\frac{\Gamma_a\Gamma_b}{(E-E_r)^2 + \Gamma^2/4} \tag{3.15}$$

$$= \frac{\lambda^2}{4\pi}\omega\gamma\Gamma\frac{1}{(E-E_r)^2 + \Gamma^2/4}, \tag{3.16}$$

with

$$\omega = \frac{(2j+1)}{(2j_p+1)(2j_t+1)} \tag{3.17}$$

where Γ_a, Γ_b, and Γ are the entrance particle partial width, exit photon partial width, and the total width, respectively; E_r is the resonance energy; j, j_p and j_t are the spin of the resonance, projectile and target nucleus, respectively; and $\omega\gamma$ is the resonance strength:

$$\omega\gamma = \omega\frac{\Gamma_a\Gamma_b}{\Gamma} \tag{3.18}$$

If the resonance used for depth profiling is sufficiently narrow with respect to the beam energy spread (i.e., $\Gamma \ll \sigma_b$), the convolution of cross section and beam spread functions in Eq. (3.8) can be simpli-

fied:

$$\begin{aligned}\int_{E=-\infty}^{\infty} dE\,\sigma(E)h(E'-E) \\ =&\frac{\lambda^2}{4\pi}\omega\gamma\Gamma\int_{E=-\infty}^{\infty} dE\,\frac{h(E'-E)}{(E-E_r)^2+\Gamma^2/4} \\ =&\frac{\lambda^2}{2}\omega\gamma h(E'-E_r)\end{aligned} \tag{3.19}$$

For the assumption of a narrow resonance, the yield in Eqs. (3.7) and (3.8) can then be written as:

$$Y(E_0)=\frac{\lambda^2}{2}\omega\gamma\sum_i N_i\frac{1}{2\pi\sigma_b\sigma_s\sqrt{x_i}}\int_{E'=0}^{E_0} dE'\exp\left[-\frac{(E'-E_r)^2}{2\sigma_b^2}\right]\exp\left[-\frac{(E_0-E'-\Delta_i)^2}{2\sigma_s^2 x_i}\right] \tag{3.20}$$

This general equation for the yield curve arising from a target stoichiometry that varies as a function of depth can be used to analyse experimentally measured yield curves. This formalism is useful for extracting stoichiometry profiles of the implanted targets used in nuclear astrophysics experiments. More importantly, it allows for extracting absolute resonance strengths.

An example of using a simultaneous fit to both stoichiometry and resonance strength is given in Ch. 6. The formalism outlined above will be used to extract the $E_r^{\text{lab}} = 479$ keV strength in ^{22}Ne(p, n)^{23}Na by implanting ^{22}Ne into an aluminium and measuring the ^{27}Al+p yield curve.

If the implanted region of the target has a uniform depth profile, this treatment of excitation functions is changed somewhat. The general yield in Eq. (3.3) becomes

$$Y(\mathrm{E_0})=\int_{E_0-\Delta E}^{E_0}\mathrm{dE}'\int_{E_i=0}^{\infty}\mathrm{dE}_i\int_{E=0}^{E_i}\left[\frac{\sigma(\mathrm{E})}{\varepsilon(\mathrm{E})}f(\mathrm{E_0}-\mathrm{E}_i)g(\mathrm{E}_i-\mathrm{E},\mathrm{E}')\mathrm{dE}\right] \tag{3.21}$$

where ΔE is now the target thickness in units of energy. A beam particle will lose an average energy of ΔE as it traverses the implantation region of the target. By assuming an isolated narrow resonance (Breit-Wigner cross section) for σ, two useful quantities can be found from Eq. (3.21): (i) the maximum yield height, and (ii) the yield integral. The maximum yield height for a thick target ($\Delta E \to \infty$) is

$$Y_{\text{max}}=\frac{1}{\varepsilon_r}\frac{\lambda_r^2}{2}\omega\gamma \tag{3.22}$$

where ε_r is the effective stopping power in the target region (i.e., the total stopping power per target nucleus); λ_r is the deBroglie wavelength; and $\omega\gamma$ is the strength of the resonance. This equation is useful in determining a resonance strength if a target is sufficiently thick (usually $\Delta E > 15$ keV) and its stoichiometry is well known. If a target is not thick enough, Eq. (3.21) can be integrated to provide the expression

$$A_Y = \frac{\Delta E}{\varepsilon_r}\frac{\lambda_r^2}{2}\omega\gamma \tag{3.23}$$

A more detailed discussion of yield curves can be found in Ref. [Ili07].

4 Experimental Methods

4.1 Laboratory Equipment

EXPERIMENTS were performed at the Laboratory for Experimental Nuclear Astrophysics (LENA) at the Triangle Universities Nuclear Laboratory. A floor plan of the laboratory is shown in Fig. 4.1. LENA is dedicated to the measurement of low energy cross sections relevant in nuclear astrophysics.

The accelerator used in the present studies was a 1 MV Van de Graaff "JN" accelerator which is capable of accelerating protons and α-particles to energies of approximately $E = 150$ to 800 keV (assuming singly ionised atoms). The analysing magnet slit control system described in Sec. 4.3 constrains the beam energy, resulting in an energy uncertainty on the order of $\sigma_E = 0.5$ keV. The beam is focused onto a target thick enough to stop all incident particles. The targets usually consist of thin tantalum sheets with the reaction nuclei of interest implanted into them. Beam currents on target of up to $I = 150$ μA (approximately 10^{14} particles/s) are achievable with the JN accelerator (the other accelerator, an electron cyclotron resonance ion source, is capable of delivering beams of up to several mA to the target). The beam current is measured directly from the target chamber, which is electronically isolated. Secondary electron suppression allows for accurate beam current measurement. A liquid-nitrogen cooled copper cold trap serves to reduce contaminant buildup on the surface of the target, and de-ionised water is used for target cooling. The target chamber is shown in Fig. 4.2.

The main LENA detectors consist of a 135% high purity germanium (HPGe) detector and a NaI(Tl) scintillator annulus surrounding the target chamber. The HPGe detector is placed as close to the target as possible (1.1 cm from target to detector face) in order to cover the maximum possible

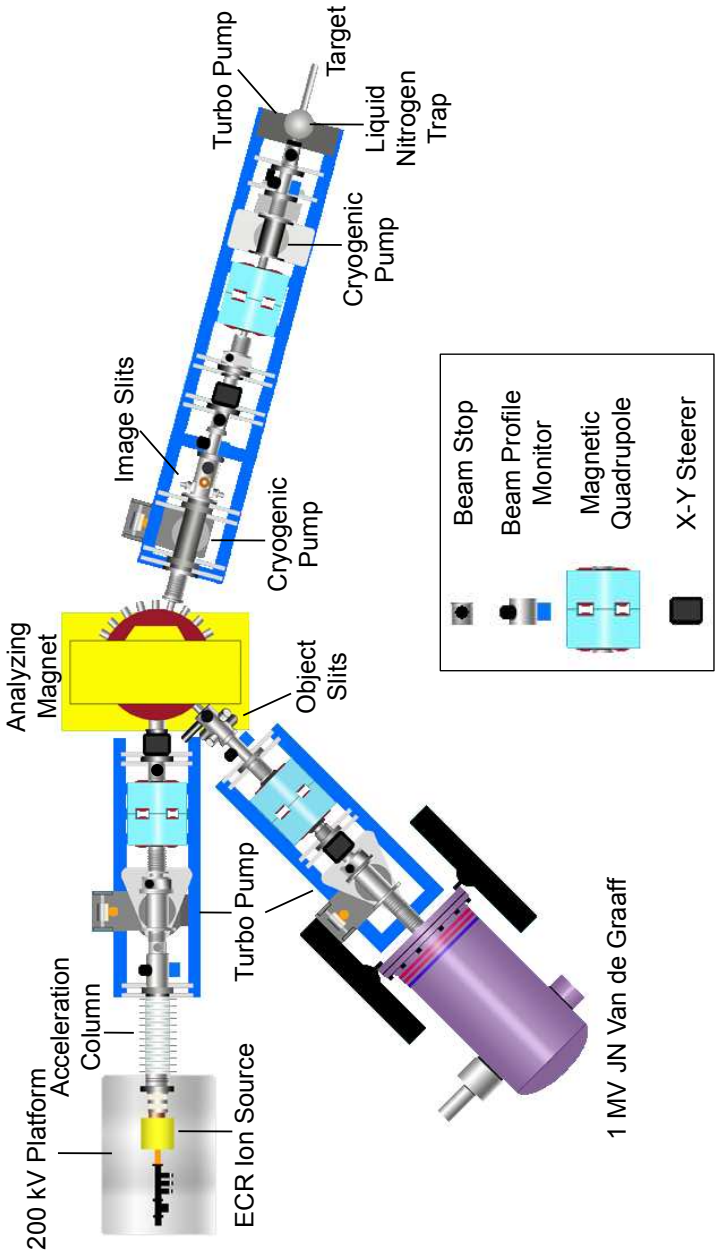

Figure 4.1: The Laboratory for Experimental Nuclear Astrophysics (LENA). Charged particles (usually protons or α-particles) are accelerated in one of the two accelerators, consisting of a 1 MV JN Van de Graaff and a 200 kV Electron Cyclotron Resonance (ECR) source. An analysing magnet is used to select the desired beam energy and particle species, which are focused onto the target situated at the far right of the figure.

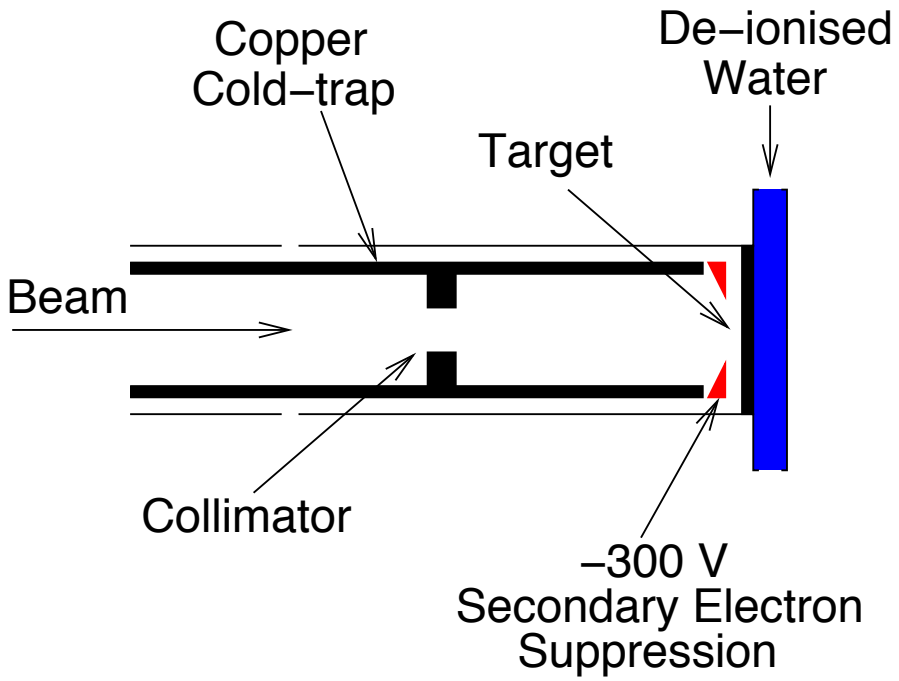

Figure 4.2: Schematic representation of the target chamber used in the experiment. A copper cold trap serves to reduce contaminant buildup on the surface of the target, and secondary electron suppression allows for accurate beam current measurement. Beam current is measured directly from the target chamber, which is electronically isolated. De-ionised water is used for target cooling.

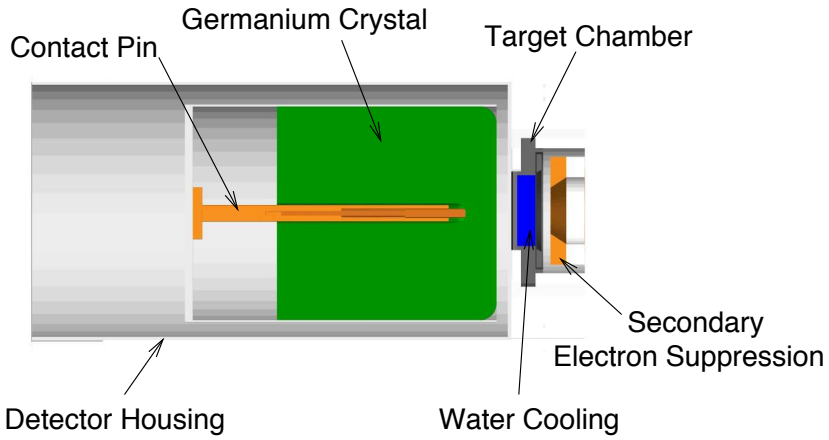

Figure 4.3: The HPGe detector, detailing the geometry of the detector crystal.

solid angle, thus maximising the detection efficiency. A scale image of the HPGe detector is shown in Fig. 4.3. A NaI(Tl) annulus surrounds the HPGe detector and covers a large solid angle to maximise coincidence efficiencies. It consists of 16 optically isolated NaI(Tl) segments, each with their own photomultiplier tube, arranged in an annulus of 35.7 cm outer diameter, 11.8 cm inner diameter, and 33.0 cm length. The target is located at the geometric centre of the annulus. The detectors are enclosed in a lead shield, which, in turn is surrounded by a five-sided anti-coincidence plastic scintillator shield. This setup is shown in Fig. 4.4.

The passive lead shield consists of a box of 25 mm thick lead, supported by 64 mm thick aluminium. A compromise is made between passive shield thickness and weight considerations. It should be noted that the NaI(Tl) annulus also provides some amount of passive shielding to the HPGe detector. The plastic scintillator muon shield, which reduces background counts originating from cosmic rays, consists of a five-sided shield of Bicron BC-408 plastic scintillator plates with optical fibre readouts. This readout method is used because the size and arrangement of the scintillators doesn't allow for practical use of light guides. The optical fibres used are Bicron BCF 91A multiclad wavelength shifting (WLS) fibres. This not only makes the apparatus much sturdier, but the attenuation coefficient in the WLS fibres is lower than for waveguides, giving better light yield. See Ref. [Lon06] for more details on the muon shield at LENA.

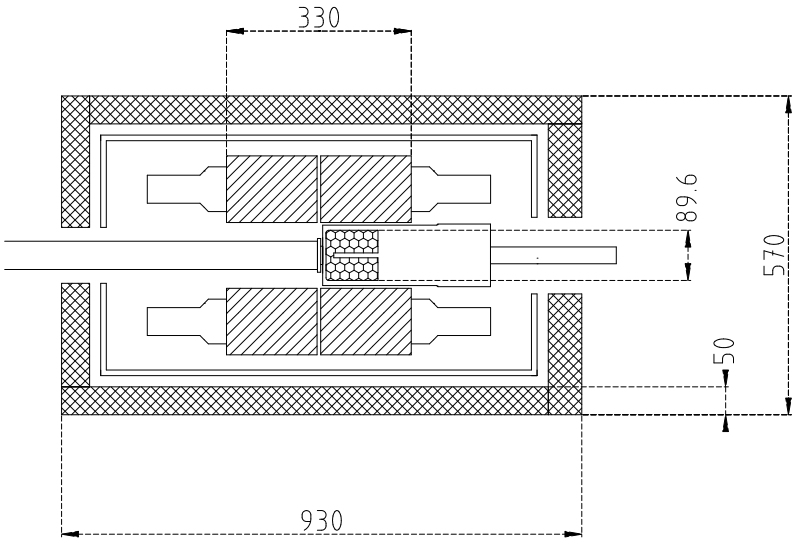

Figure 4.4: Experimental setup of detectors consisting of a 93 mm long by 90 mm diameter HPGe crystal, centred inside a NaI(Tl) annulus of inside and outside diameters of 118 mm and 357 mm, respectively. These are surrounded by a lead box, which is surrounded by 50 mm thick scintillator plates. Dimensions in the figure are given in mm.

4.2 HPGe Detectors

High Purity Germanium (HPGe) detectors are commonly used in nuclear physics experiments for the measurement of γ-rays. Although they typically have lower intrinsic efficiencies and costs more than scintillation detectors, the vast improvement in energy resolution over other detectors is essential when high precision data are needed .

In this section, the characterisation of a HPGe detector is described in detail. Absolute efficiency determination is described in Sec. 4.2.1. Determination of angular correlation coefficients for detector solid angle corrections is outlined in Sec. 4.2.2. Detector energy calibration is performed in Sec. 4.2.3, and the summing correction formalism, which must be considered carefully in large solid angle (high detection efficiency) situations, is provided in Sec. 4.2.4.

4.2.1 HPGe Detector Efficiencies

When analysing data to calculate cross sections of reactions, it is important to know the full energy peak efficiency of the detector in order to relate the number of detected photons to the number emitted in the reaction. The total efficiency of the detector is also important because it enters directly into calculations concerning the "summing out" of peaks (see below). This summing out correction affects the peak count rate considerably if the detector is placed in close geometry to a target (see Sec. 4.2.1 for more details on coincidence summing effects). It is possible to measure the peak and total efficiencies of a detector by using single line radioactive sources, but these measurements always rely on the activity of the source, which cannot always be known with certainty. The sum-peak method provides a technique for determining absolute efficiencies at a single energy. This efficiency data point can then be used to normalise efficiencies measured with other radioactive sources and reaction data.

The Sum-Peak Method for Determining Detector Efficiencies

The following method for calculating detector efficiencies from a two step cascade is named the sum-peak method [Kim03]. If a detector is placed in close geometry with a decaying nucleus, coincident summing can occur [Kno89]. This effect results when multiple γ-rays from the same decay are detected within the detector's resolving time. The result of this is a count, which is registered at

the energy sum of the individual γ-rays. If each of the γ-rays are fully detected, the registered count arrives in a peak known as the "sum-peak". This phenomenon is shown in Fig. 4.5.

The process of coincidence summing can be used to find analytical expressions for the full energy peak efficiencies arising from a simple two step decay. An example of a two step cascade is the decay of ^{60}Co to ^{60}Fe, which is nearly ideal for the sum-peak method. The nuclide ^{60}Co decays by emitting two γ-rays with equal intensity at $E_\gamma = 1173$ and 1332 keV (note that the ground state branching ratio is very small, $2 \cdot 10^{-8}$ [Bow74]). This decay provides a simple relationship between the counts in the full energy peaks and the detector efficiencies. The number of counts in the two full energy peaks, $\mathrm{N}_{\gamma 1}$ and $\mathrm{N}_{\gamma 2}$, in the sum peak, $\mathrm{N}_{\gamma 3}$, and the total number of counts, N_t in the spectrum, are:

$$\mathrm{N}_{\gamma 1} = \mathrm{N}_0 \varepsilon^p_{\gamma 1} \left[1 - \mathrm{W}_{tp}(\theta) \varepsilon^t_{\gamma 2}\right] \tag{4.1}$$

$$\mathrm{N}_{\gamma 2} = \mathrm{N}_0 \varepsilon^p_{\gamma 2} \left[1 - \mathrm{W}_{pt}(\theta) \varepsilon^t_{\gamma 1}\right] \tag{4.2}$$

$$\mathrm{N}_{\gamma 3} = \mathrm{N}_0 \varepsilon^p_{\gamma 1} \varepsilon^p_{\gamma 2} \mathrm{W}_{pp}(\theta) \tag{4.3}$$

$$\mathrm{N}_t = \mathrm{N}_0 \left[\varepsilon^t_{\gamma 1} + \varepsilon^t_{\gamma 2} - \varepsilon^t_{\gamma 1} \varepsilon^t_{\gamma 2} \mathrm{W}_{tt}(\theta)\right] \tag{4.4}$$

where N_0 is the total number of decays; ε^t_γ is the total efficiency (the probability that the γ-ray deposits any energy in the detector); ε^p_γ is the peak efficiency (the probability that the γ-ray is fully detected); and $\mathrm{W}_{pt}(\theta)$ is the solid angle corrected angular correlation coefficient calculated using the peak Q-coefficient for γ-ray 1, and the total Q-coefficient for γ-ray 2; W_{ij} (where i and j can be p for peak efficiency or t for total efficiency) is calculated by:

$$\mathrm{W}_{ij}(0^\circ) = 1 + \frac{5}{49} Q_2^{(1)i} Q_2^{(2)j} + \frac{4}{441} Q_4^{(1)i} Q_4^{(2)j} \tag{4.5}$$

The Q-coefficients are calculated from the geometry of the detectors. Here, $Q^{(1)}$ is the Q-coefficient for γ-ray 1 and $Q^{(2)}$ is the Q-coefficient for γ-ray 2. See Sec. 4.2.2 for more details on the calculation of Q-coefficients. The fractions in W are obtained from the direction-direction correlation for a cascade decay ($4^+ \rightarrow 2^+ \rightarrow 0^+$). The reader is referred to Ref. [Kim03] for more details. Simulations show that the angular correlation coefficient, $W_{ij}(0^\circ)$ is approximately equal for peak and total efficiencies, so $W_{ij}(0^\circ) \approx W(0^\circ)$.

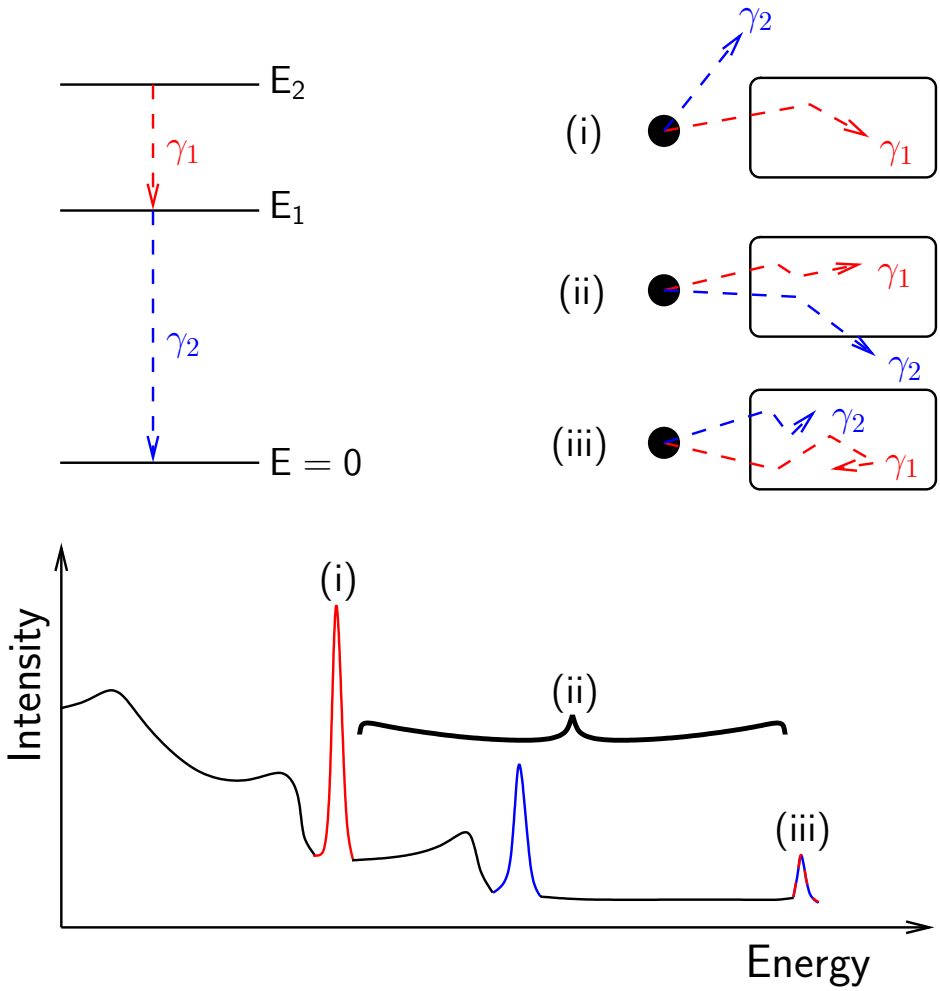

Figure 4.5: Schematic showing the concept of coincidence summing in a detector. Three possibilities are: (i) The first γ-ray (γ_1) is fully detected, while the second (γ_2) does not enter the detector, resulting in a count at the energy of γ_1 ($E_2 - E_1$). (ii) γ_1 is fully detected, and γ_2 also enters the detector, leaving a portion of its energy. This situation results in a count being removed from the peak at $E_2 - E_1$, and added into the Compton continuum at $E_2 - E_1 + \delta_2$ (δ_2 is the amount of energy that γ_2 deposited). (iii) Both γ-rays are fully detected by the counter. In this case, a count will be registered at the sum of their energies, E_2.

The peak and total efficiency can be found by solving Eqs. (4.1) - (4.4) and assuming that the total efficiencies are approximately equal at $E_\gamma = 1173$ and 1332 keV (i.e., $\varepsilon^t_{\gamma 1} \approx \varepsilon^t_{\gamma 2}$ for ^{60}Co). This assumption has been shown to be correct to within 3% with Monte Carlo simulations. The efficiencies are:

$$\varepsilon^p_{\gamma 1} = \frac{1}{W(\theta)} \sqrt{\frac{N_{\gamma 1} N^2_{\gamma 3}}{N_t N_{\gamma 2} N_{\gamma 3} + N_{\gamma 1} N^2_{\gamma 2}}} \tag{4.6}$$

$$\varepsilon^T_{\gamma 1} = \frac{1}{W(\theta)} - \frac{1}{W(\theta)} \sqrt{\frac{N_{\gamma 1} N_{\gamma 2}}{N_t N_{\gamma 3} + N_{\gamma 1} N_{\gamma 2}}} \tag{4.7}$$

To calculate the total number of counts in the spectrum, N_t, the room background contribution first needs to be subtracted. Once this has been performed, the spectrum needs to be extrapolated to zero energy, below the low-energy discriminator threshold. This is done by extrapolations from higher energies assuming that the Compton edge is relatively flat in this region. Although this is only an approximation, the fraction of counts in this region compared to the total number of counts in the spectrum is very small.

An additional correction must be made to the measured efficiencies to account for source geometry. When a source is placed on the face of the target backing (usually consisting of 1/2 mm thick tantalum), the source is further from the detector than a beam induced reaction occurring within the first few μm of the target face. This is shown schematically in Fig. 4.6. Reactions resulting from a beam hitting the target will also have a larger diameter, on the order of 1 cm. To correct for this geometrical effect, Monte Carlo simulations are performed for both situations to obtain a scaling factor between the two. This factor is then applied to the ^{60}Co sum-peak efficiencies.

In order to obtain good precision in the efficiencies using these methods, very good sum peak statistics need to be obtained. For example, in order to obtain uncertainties of less than 5% in the efficiency, sum peak statistics need to be known to less than 1%.

Peak Efficiencies at a Range of Energies for HPGe

Although the sum peak method is useful for finding peak efficiencies from two-line sources, other methods must be used to find efficiencies at a range of energies. Radioactive sources, such as ^{56}Co, emit a large range of high intensity γ-rays of energies between 263 keV and 3612 keV [Bow74]. These

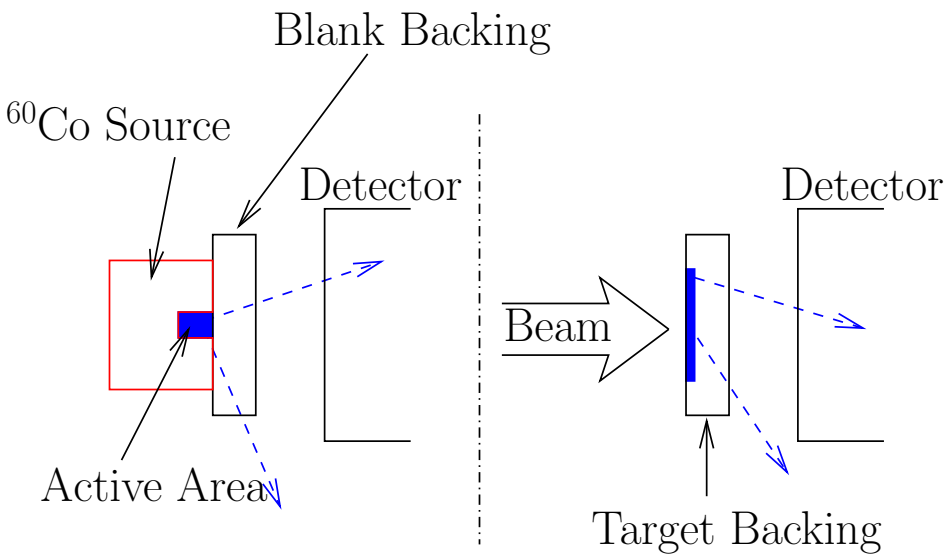

Figure 4.6: Geometry of (i) a ^{60}Co source on the face of a target backing and (ii) accelerated beam hitting an implanted target. In order to correct measured efficiencies to account for this difference in geometry, Monte-Carlo simulations of both situations are performed to obtain a scaling factor. The dimensions in this figure are not to scale.

radioactive sources are suitable for finding efficiencies at a range of energies without having to use multiple sources. However, coincidence summing becomes a concern and needs to be addressed. The summing correction codes described in Sec. 4.2.4 can be used to find peak efficiencies from measured intensities.

A summing correction computer code, `sump`, has been written in order to correct peak efficiencies for complicated decay schemes. The code is described in more detail in Sec. 4.2.4. For the electron capture decay of ^{56}Co to ^{56}Fe, there are 13 energy levels that need to be taken into account. A further complications arises because of an 18.1% β^+-decay creating 511 keV γ-rays. However, it is possible to add extra artificial levels in the decay scheme to produce 511 keV γ-rays for coincidence summing. These levels are populated with the feeding fraction known for the level (for example, the $E_x = 2481$ keV level has an 18.1% feeding fraction). The artificial levels decay with a branching ratio of 1.0 to the level they correspond to. For example, a artificial state at $E_x = 2992$ keV will decay (with $E_\gamma = 511$ keV) to the $E_x = 2481$ keV level 100% of the time. This has the result of 511 keV γ-rays being emitted in coincidence with decays from that level. Only γ-rays with good statistical uncertainties from an overnight acquisition should be used in the peak efficiency calculation, while the 1360 keV line is omitted because of strong contamination from summing of the 846 keV and 511 keV lines.

The summing correction code was also used with the $E_r^{\text{lab}} = 278$ keV resonance in ^{14}N(p,γ)^{15}O, which illustrates the effect of coincidence summing. This has the most influence on the ground state transition (summing-in), as shown in the peak efficiencies of Fig. 4.7 at $E_\gamma \approx 7.6$ MeV. Lower energy transitions also undergo more summing out because peak efficiencies for these γ-rays are higher.

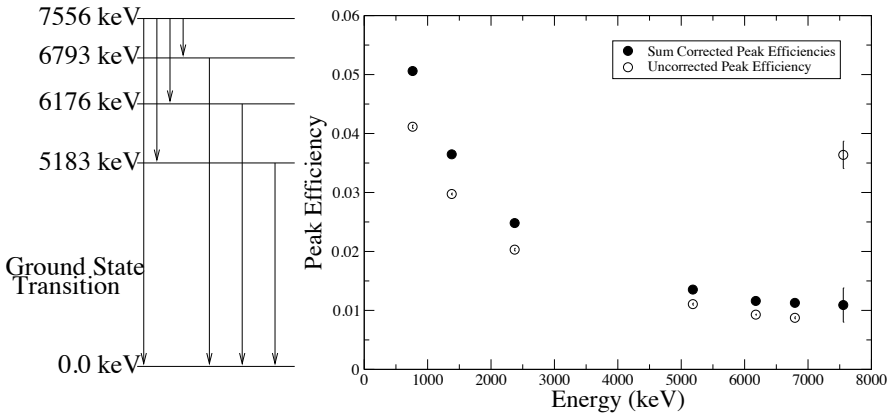

Figure 4.7: Peak efficiencies calculated from a measurement of the 278 keV resonance in ^{14}N(p,γ)^{15}O. This is a good example of the large effect of coincidence summing, where summing-in increases the perceived count rate in the ground state transition dramatically. The full and open symbols correspond to uncorrected, and corrected efficiencies, respectively.

There is a large dependence of the peak efficiencies on the disintegration rate supplied to the code. Energies that experience summing-in are affected more than those with summing-out effects. Therefore deviations in the disintegration rate create large fluctuations in the data points. Hence, the disintegration rate must be known to high accuracy. The same procedure used to calculate peak efficiencies from ^{14}N(p,γ)^{15}O was used with the $E_r^{\text{lab}} = 326$ keV resonance in ^{27}Al(p,γ)^{28}Si.

In order to normalise the peak efficiency curves to the absolute Sum-Peak efficiency from ^{60}Co, a bootstrapping method was applied. Initially, the peak efficiencies for ^{56}Co were fit with an analytical expression [Tra99]

$$\ln\left[\varepsilon^p(E)\right] = a + b\ln(E) + c(\ln(E))^2 \tag{4.8}$$

The fit is used to find the efficiencies at $E_\gamma = 1173$ and 1332 keV, which are used to normalise ^{56}Co efficiencies to the absolute ^{60}Co measurements. This procedure is then repeated with the ^{14}N(p,γ)^{15}O

data points, followed by ^{27}Al(p,γ)^{27}Si. This procedure yields reliable absolute peak efficiencies between a few hundred keV and about 10 MeV.

The peak efficiency curve obtained from the procedure described is shown in Fig. 4.8. There is some scatter in the efficiency data points, which is partially caused by the approximations used for treating 511 keV γ-rays from ^{56}Co decay. Contaminants such as ^{57}Co, which has a substantially longer half life than ^{56}Co, could also be contributing to this scatter through random summing effects. Random summing from the strongest lines can also contribute to this scatter if dead-time in the electronics is appreciable.

Monte Carlo simulations using `Geant4` are useful for finding efficiencies at energies between experimental data points, and for extrapolating to higher or lower energies. In order to produce an accurate Monte Carlo efficiency curve, minor adjustments are typically made to the detector geometry [Hel03, Lon06] to correct for small manufacturing uncertainties in the crystal position. In the present study, however, the detector dimensions are known through a Computed Tomography (CT) scan of the detector [Car10]. Following that procedure, the relative peak efficiency was found to be accurate to within a few percent when extrapolating between $E_\gamma = 4$ and 11 MeV. The Monte Carlo efficiency curve is represented by a solid line in Fig. 4.8. The geometry used in the `Geant4` efficiency calculations is shown in Figs. 4.9-4.10.

Total Efficiency Calculations for HPGe

Total efficiencies are important for the summing correction of spectra (see Sec. 4.2.4). Although Compton scattered γ-rays do not contribute to the full energy peak, they can give ride to the summing-out of other full energy peaks, thus lowering the number of counts observed. For this reason, it is important to know the total efficiency of the HPGe detector.

It is possible to calculate the total efficiency of the detector using the linear attenuation coefficients for germanium and integrating over the volume of the detector (see Figure 4.11). This has been performed for a cylindrical NaI(Tl) detector [Bol80], but it is a simple matter to improve the method to account for the contact pin hole in the HPGe crystal. This correction amounts to only 2% for the

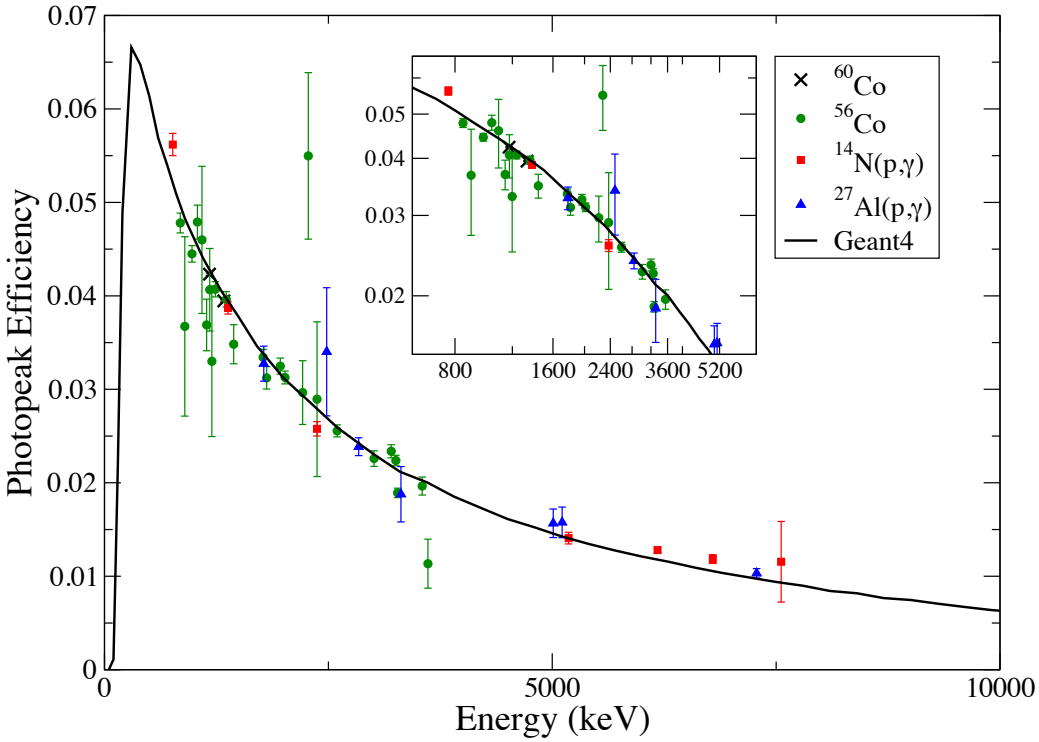

Figure 4.8: Peak efficiency curve for the LENA HPGe detector. For ^{56}Co, some scattered data points can be observed. This is probably caused by random summing with impurities in the source, as well as summing with 511 keV annihilation radiation. Statistical error bars in the `Geant4` calculations are smaller than the data points. Error bars in measured efficiencies arise from both statistical counting uncertainties and from the summing correction procedure, which includes branching ratio uncertainties.

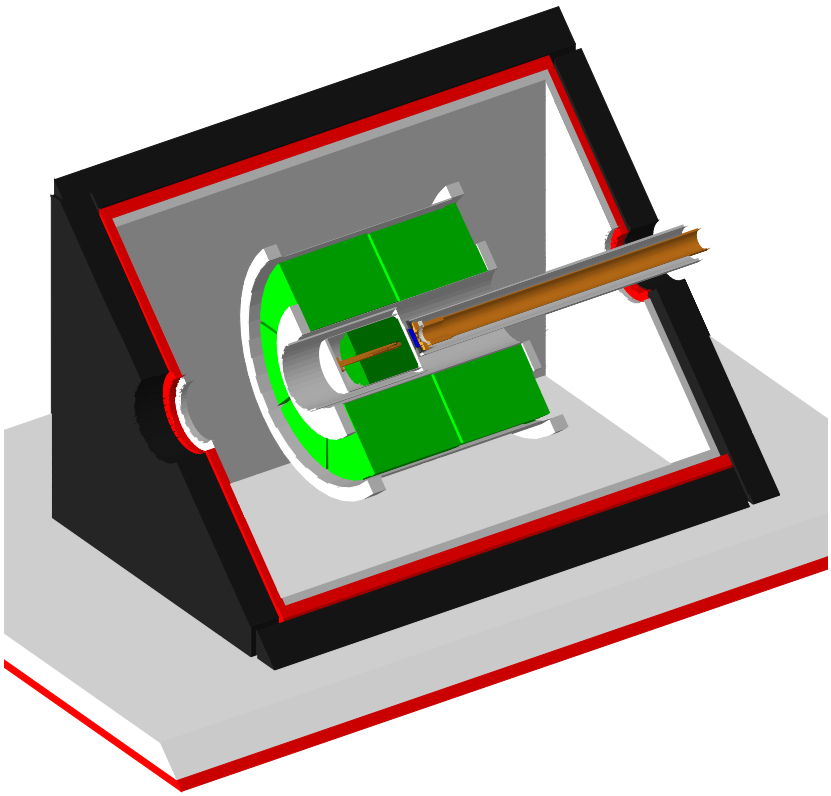

Figure 4.9: `Geant4` geometry used for the efficiency simulations of the HPGe detector at LENA. Shown is the entire geometry used. Green material represents detectors: HPGe and NaI(Tl). White represents structural material (detector housing, aluminium supports etc.); red signifies lead; and black material shows the plastic scintillator muon shield.

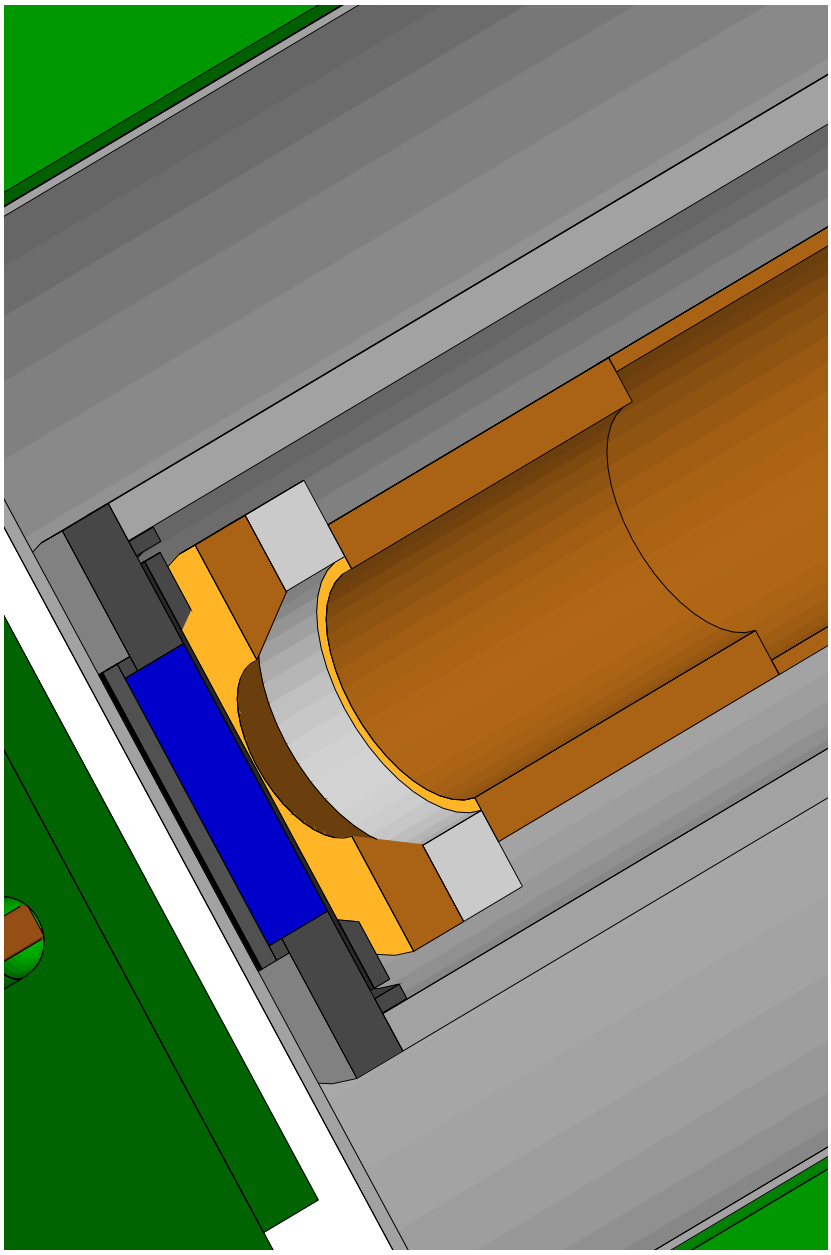

Figure 4.10: `Geant4` geometry used for the efficiency simulations of the HPGe detector at LENA. Shown in this figure is a close up of the target chamber assembly. This geometry is crucial in the determination for both peak and total efficiencies.

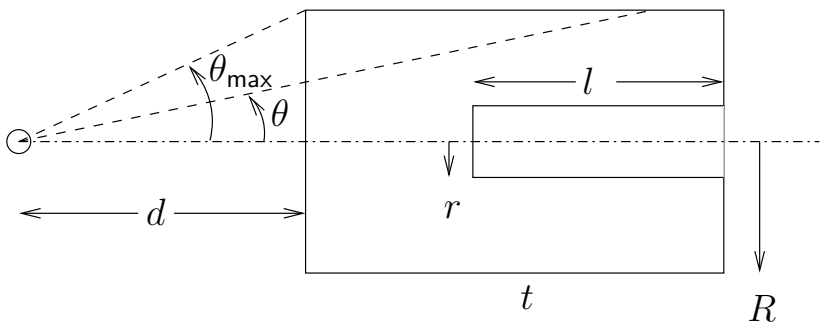

Figure 4.11: Determination of the Total Efficiency. Two separate integrals are required for the path lengths. One for the γ-rays passing through the back face of the detector, and one for the γ-rays passing through the sides.

LENA HPGe crystal. The equation for the total efficiency is:

$$\varepsilon_\gamma^T = \varepsilon_c - \alpha \tag{4.9}$$

where

$$\begin{aligned}\varepsilon_c = &\frac{1}{2}\left[\int_0^{\theta_1}\left(1-\exp\left(\frac{-\mu t}{\cos(\theta)}\right)\right)\sin(\theta)d\theta\right] \\ &+\frac{1}{2}\left[\int_{\theta_1}^{\theta_2}\left(1-\exp\left(\frac{-\mu R}{\sin(\theta)}+\frac{\mu d}{\cos(\theta)}\right)\right)\sin(\theta)d\theta\right] \qquad (4.10)\\ \alpha = &\frac{1}{2}\left[\int_0^{\theta_3}\left(1-\exp\left(\frac{-\mu l}{\cos(\theta)}\right)\right)\sin(\theta)d\theta\right] \\ &+\frac{1}{2}\left[\int_{\theta_3}^{\theta_4}\left(1-\exp\left(\frac{-\mu r}{\sin(\theta)}-\frac{\mu(t-l-d)}{\cos(\theta)}\right)\right)\sin(\theta)d\theta\right] \qquad (4.11)\end{aligned}$$

and μ is the linear attenuation coefficient for germanium, t is the thickness of the detector, R is the radius of the detector, and d is the distance of the source from the detector. In the contact pin hole correction term α, l is the length of the contact pin hole and r is its radius. Furthermore,

$$\theta_1 = \arctan\left(\frac{R}{d+t}\right) \qquad \theta_2 = \arctan\left(\frac{R}{d}\right) \tag{4.12}$$

This integral needs to be evaluated numerically and yields a good estimation for the total efficiency of the detector. The geometry for the angles used in this calculation is shown in Fig. 4.11.

This method is generalised to all energies by fitting a curve to attenuation coefficient data [Boo96]. This way, an expression for the linear attenuation coefficient μ as a function of energy can be obtained.

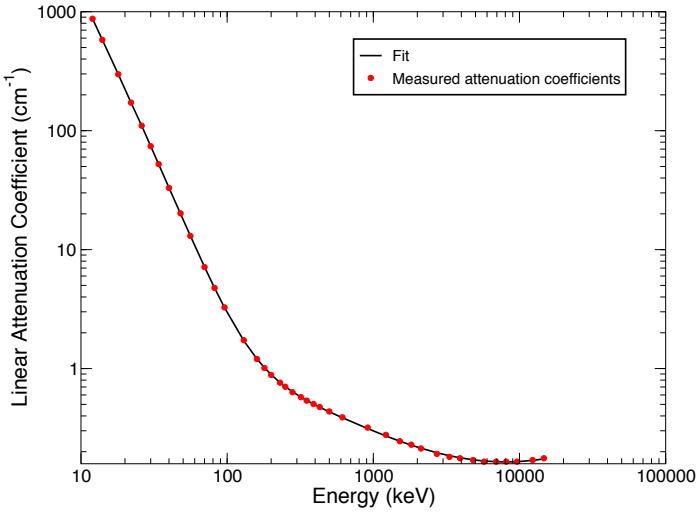

Figure 4.12: Curve fitted to attenuation coefficients for germanium

A 14 order polynomial fit to data acquired from Boone et al. [Boo96] is accurate between 15 keV and 15 MeV to within 3% (See Fig. 4.12). This fit is used with Eqs. (4.9)-(4.11) by replacing the coefficient μ with the energy-dependent fit. This method can also be adapted for NaI(Tl) detectors using the same fitting function.

As a test of these calculations, `Geant4` calculations can be performed in the same way as for the full energy peak efficiencies by only taking the HPGe crystal into account and removing all surrounding material. The results of this comparison are shown in Fig. 4.13. The agreement between calculations and simulations is remarkable. However, the efficiencies calculated with Eqs. (4.9)-(4.11) are consistently low owing to the fact that this method assumes that γ-rays travel in straight lines through the crystal with no scattering. Once the full detector geometry had been included (detector housing, target chamber etc.), the calculations outlined above are no longer adequate because they do not include scattering and absorption of photons in the surrounding material. This is an important effect, especially at high photon energies, where the photons can scatter into the HPGe detector from the surrounding material, thus increasing the total efficiency. The preferred method of obtaining total efficiencies is therefore to normalise the Monte Carlo total efficiencies to the experimental ^{60}Co sum-peak efficiency. After correction for dead-time in the electronics, the results yield the total efficiency curve seen in Fig. 4.14. The figure includes two sets of `Geant4` simulations, one with the full detec-

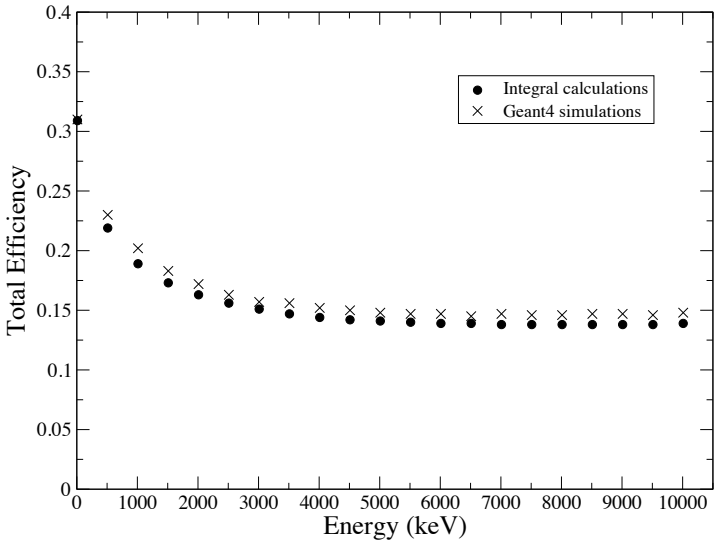

Figure 4.13: Total efficiency vs. energy for our Germanium detector. The integration method yields a curve that is very close to the GEANT4 simulations. The GEANT4 simulation is for the HPGe crystal only, i.e., it disregards surrounding material.

tor geometry, including the NaI(Tl) annulus and target chamber, the other of the HPGe crystal only. The effect of surrounding material on the total detection efficiencies is especially important at high and low energies. At high energies, for example, simulations including the full geometry are found to have a 50% higher efficiency than simulations of the crystal only. Both data sets have been adjusted to the experimental efficiency found from ^{60}Co.

4.2.2 Q-Coefficients for HPGe Detector

Angular correlation attenuation coefficients (Q-coefficients) are needed for the sum-peak method of efficiency calculations. They are used to correct theoretical angular correlation coefficients for solid angle detector effects. They are also important, therefore, for analysing measured angular correlations.

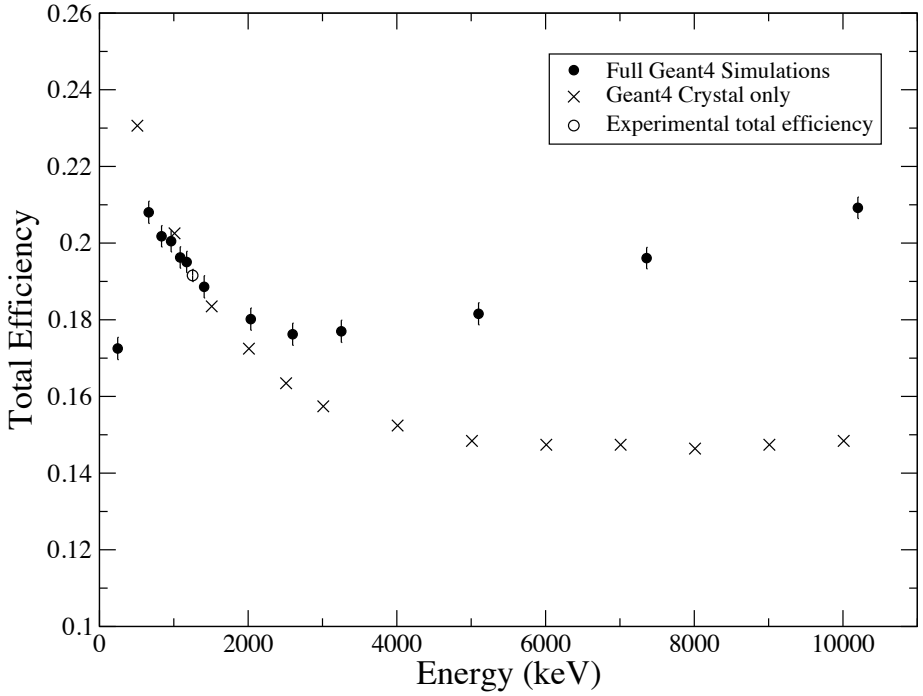

Figure 4.14: `Geant4` total efficiency curve for a HPGe detector adjusted to experimental data. Two simulations are included, one for the full detector geometry, and another for the crystal only.

Angular correlation coefficients are calculated from [Bol80, Kim03],

$$Q_k = J_k/J_0 \tag{4.13}$$

$$J_k = \int_0^{\theta_{max}} \sin(\theta) P_k(\cos\theta) \varepsilon_i(\theta) d\theta \tag{4.14}$$

where θ is the incident angle of the γ-ray with respect to the detector axis, θ_{max} is the maximum angle subtended by the detector from the source (see Fig. 4.11); $P_k(\cos\theta)$ is a k^{th} order Legendre polynomial; and $\varepsilon_i(\theta)$ is the efficiency of the detector for a highly collimated source at an angle θ. In sum-peak efficiency calculations, the Q-coefficients for both the peak and total efficiencies must be known in principle. For the total efficiency Q-coefficients, approximate numerical calculations such as those in Sec. 4.2.1 can be used. Q-coefficients are obtained with a code derived from Ref. [Kim03], where the coefficients are calculated from the geometry of the detector and the linear attenuation coefficient, μ, of germanium at that energy. The Q-coefficients for $k = 1, 2, 3, 4$ for a range of energies are shown in Fig. 4.15. However, for precision work, Monte Carlo methods should be used for the reasons outlined in Sec. 4.2.1.

In order to calculate the peak and total efficiency Q-coefficients using Monte Carlo simulations, several methods are availiable. One method is to find the efficiency of the detector as a function of incident angle using `Geant4` to simulate a collimated source at a range of energies. These efficiencies can then be used with Eq. (4.14) to calculate the Q-coefficients of the detector. This method, applied to peak effeiciency Q-coefficients, agrees with those quoted by Ref. [Yat63] to within 1%. Peak efficiency Q-coefficients have been calculated in the geometry shown in Fig. 4.11 for a range of energies. The results are presented in Fig. 4.16.

An alternative method for obtaining peak and total efficiency Q-coefficients is to use a post-processing analysis technique alongside a `Geant4` simulation. The simulation is used to produce a file with tracking information on every event that occurs in the detector. A post processing code written in `root` can analyse the file to calculate the Q-coefficients. Each time a full energy peak event (for peak Q-coefficients) is registered in the code, the initial angle of the γ-ray is recorded. The

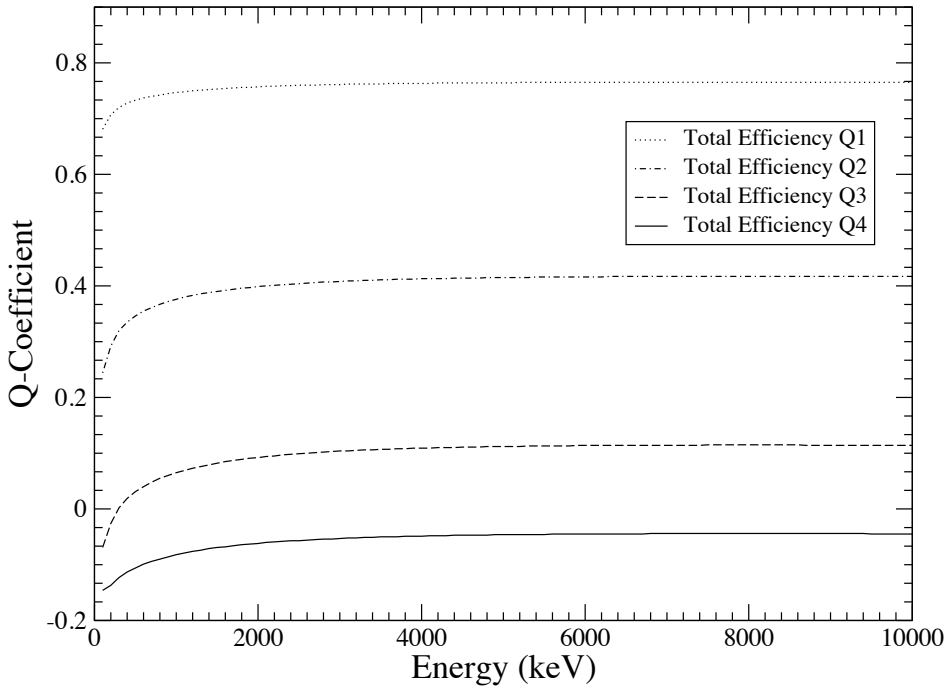

Figure 4.15: Total efficiency Q-coefficients for 135% Ge detector at a detector-source distance of 1.65 cm. The total efficiency coefficients were calculated numerically using linear attenuation coefficients.

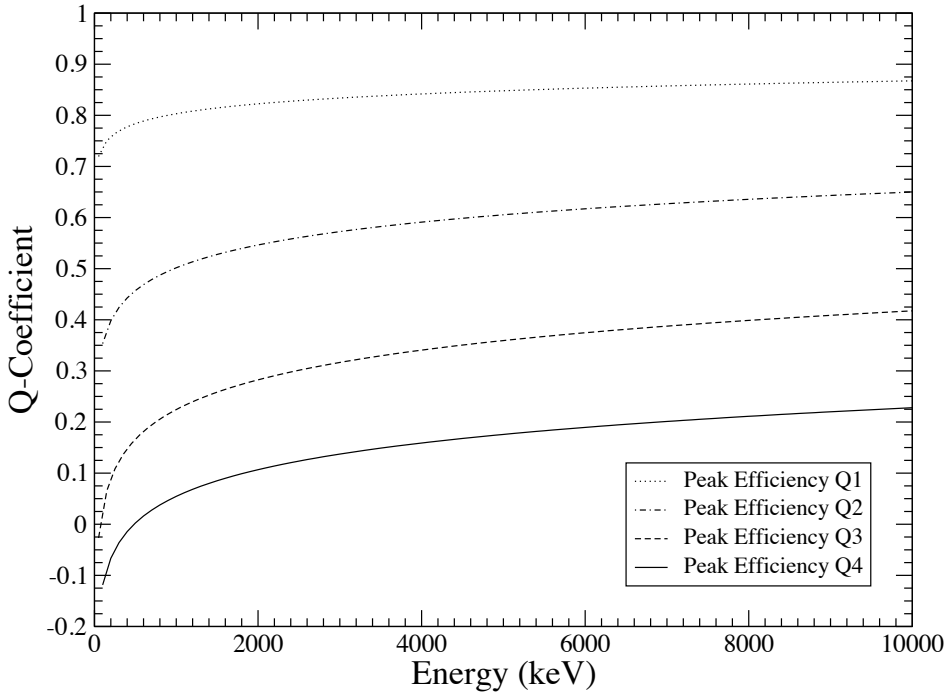

Figure 4.16: Peak efficiency Q-coefficients for 135% Ge detector at a detector-source distance of 1.65 cm. The peak efficiencies were calculated using `Geant4`.

Q-coefficient is calculated through,

$$Q_k = \frac{1}{N} \sum_{j=0}^{N} P_k \left(\cos \theta_j \right) \tag{4.15}$$

where N is the total number of full energy peak events; P_k is the k^{th} order Legendre polynomial; and θ_j is the initial angle of each fully detected γ-ray (i.e., the angle at which it was emitted from the source). This equation is equivalent to Eq. (4.13), and is also applicable to total efficiency Q-coefficients. The advantage of using this method is that it accounts for other material surrounding the detector without assuming spherical symmetry in the system.

4.2.3 Detector Energy Calibration

The HPGe pulse height spectrum is calibrated with radioactive sources and room background lines. The room background lines used are the ^{40}K and ^{208}Tl decay lines at $E_\gamma = 1460.822(6)$ keV [Cam04] and $E_\gamma = 2614.529(10)$ keV [Mar07], respectively. A ^{56}Co source provides energy calibration peaks at energies between $E_\gamma = 200$ and 3600 keV [Jun99] while a ^{137}Cs source provides an extra energy calibration point at $E_\gamma = 661.657(3)$ keV [Bro07]. The amplifier and ADC are known to be linear, so extrapolation of an energy calibration from these energies to those required in an experiment (usually on the order of about $E_\gamma = 10$ MeV) is justifiable. Additionally, the excitation energies of states in nuclei of interest in nuclear astrophysics are usually well known. If the energy of a state is required to better accuracy, extra energy calibration points close to the energy of interest are encouraged.

The energy calibration was performed by a least squares linear fit to the data. The calibration obtained is

$$E_\gamma = aC + b \tag{4.16}$$

where C is the channel number in the pulse height spectrum.

4.2.4 Summing Correction

Introduction

Numerical methods for treating coincidence summing were first developed in Refs. [McC75, Geh77, Deb79]. These methods were then generalised into matrix form in Ref. [Sem90], which is useful for integration into a code for simple and fast summing correction. For more details of this method, see Ref. [Sem90]. The following summing correction formalism can be used to correct measured spectra, for branching ratio determination, and for full-energy peak efficiency determination. Three codes: `sum`, `sumb`, and `sump` were written to perform these tasks.

Formalism

Consider a simple generalised decay scheme (Fig. 4.17) with n excited energy levels. In this example, a four level decay scheme ($n = 4$) for a radioactive source decay is considered. In radioactive decay the product is an excited nucleus, which can have a different energy. This distribution of initial excitated states is represented by the feeding fractions, f_n. The γ-ray branching ratios of each decay from level j to level i are denoted by x_{ji}.

In order to analyse the decay scheme in the presence of coincidence summing, these feeding fractions and branching ratios need to be converted into matrix form. The feeding fractions can be represented in the form of a row vector, **f**:

$$\mathbf{f} = (f_0\ f_1 \ldots f_n)\,, \tag{4.17}$$

The branching ratios are represented by an $(n+1) \times (n+1)$ matrix, **x**. The rows represent j, the starting level, and the columns represent i, the ending level. Following this convention, matrix element

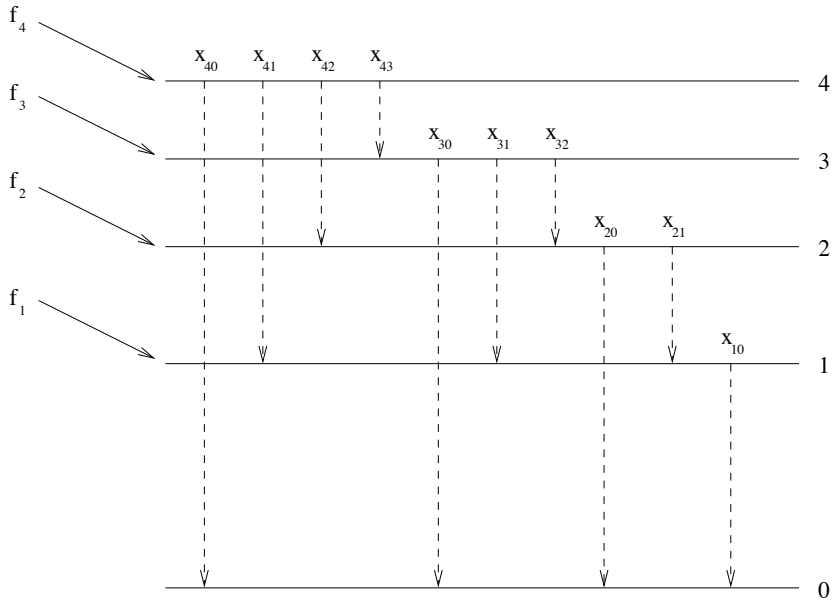

Figure 4.17: A simple decay scheme representing the possible decay routes of an excited nucleus. The feeding fractions, f_n, describe the population probability of each excited state, and x_{ji} are the branching ratios for the decay of state j to state i.

x_{ji} represents the γ-ray branching ratio from level j to level i:

$$\mathbf{x} = \begin{pmatrix} 0 & & & & \\ x_{10} & 0 & & & \\ x_{20} & x_{21} & 0 & & \\ \vdots & \vdots & \vdots & & \\ x_{n0} & x_{n1} & x_{n2} & \dots & 0 \end{pmatrix} \tag{4.18}$$

Now, three other matrices, **a**, **e** and **b**, which are functions of **x**, can be defined:

$$a_{ji} = x_{ji} \cdot \varepsilon_{ji}^{p} \tag{4.19}$$

$$e_{ji} = x_{ji} \cdot \varepsilon_{ji}^{T} \tag{4.20}$$

$$b_{ji} = x_{ji} - e_{ji} \tag{4.21}$$

where, ε_{ji}^{p} is the peak efficiency of the detector for measuring the γ-ray decay from level j to level i,

and ε_{ji}^{T} is the total efficiency. Using these matrices, two more can be defined:

$$\mathbf{A} = \sum_{k=1}^{n} \mathbf{a}^{k} \tag{4.22}$$

$$\mathbf{B} = \mathbf{E} + \sum_{k=1}^{n} \mathbf{b}^{k} \tag{4.23}$$

Where **E** is the unit matrix. Two more matrices can now be defined:

$$\mathbf{N} = diag\left([\mathbf{f} \cdot \mathbf{B}]_{i}\right) \tag{4.24}$$

$$\mathbf{M} = diag\left(B_{i0}\right) \tag{4.25}$$

The "$diag$" in Eq. (4.24) means that the row matrix obtained from the $\mathbf{f} \cdot \mathbf{B}$ calculation is converted into the diagonal elements of an $(n+1) \times (n+1)$ square matrix. Similarly, Eq. (4.25) converts the first column of the **B** matrix into an n+1 square matrix.

These matrices can now be combined to find the measured peak intensities of each γ-ray, **S**.

$$\mathbf{S} = R\mathbf{NAM} \tag{4.26}$$

where R is the disintegration rate (i.e., the total number of decaying nuclei). The matrix **A** contains information about the observed peak intensities including summing-in effects; **N** provides the feeding to a level both from the feeding fractions and from decays from higher lying states. Matrix **M** provides information about the γ-ray decay originating from each level. Together, **N** and **M** act on matrix **A** to provide the summing-out effects. This is all scaled by R to provide the observed intensities of each γ-ray.

The matrix **S** is not particularly useful in itself because it contains the observed peak intensities in the presence of coincidence summing. These values are the intensities that would be observed in an experimental spectrum. In order to *correct* for coincidence summing, Eq. (4.26) must be expanded into different orders of correction. For example, $\mathbf{S^{(0)}}$ is the matrix **S** with no summing correction and

$\mathbf{S^{(1)}}$ is $\mathbf{S}$ with summing corrections for only 2 coincident peaks. Using this expansion,

$$\mathbf{A^{(0)}} = \mathbf{a} \tag{4.27}$$

$$\mathbf{B^{(0)}} = \mathbf{E} + \sum_{k=1}^{n} \mathbf{x}^k \tag{4.28}$$

$$\mathbf{N^{(0)}} = diag\left(\left[\mathbf{f}\cdot\mathbf{B^{(0)}}\right]_i\right) \tag{4.29}$$

$$\mathbf{M^{(0)}} = \mathbf{E} \tag{4.30}$$

Eq. (4.26) can now be written as,

$$\mathbf{S} = R\left(\mathbf{N^{(0)}}\mathbf{A^{(0)}} + \mathbf{D}\right), \tag{4.31}$$

Where,

$$\mathbf{D} = \mathbf{N^{(0)}}\mathbf{A^{(0)}}\left(\mathbf{M} - \mathbf{M^{(0)}}\right) + \mathbf{N^{(0)}}\left(\mathbf{A} - \mathbf{A^{(0)}}\right)\mathbf{M} + \left(\mathbf{N} - \mathbf{N^{(0)}}\right)\mathbf{AM} \tag{4.32}$$

D is known as the correction matrix and contains all of the coincidence summing information. From this information several coincidence summing corrected quantities can be obtained. The sum corrected peak intensities, **I**, can be found using the branching ratio information (x_{ji}), the feeding fractions (f_j), the efficiencies of the detector (ε_{ji}^{p} and ε_{ji}^{T}) and the disintegration rate, R.

$$I_{ji} = R\left[\mathbf{N^{(0)}}\mathbf{c}\right]_{ji} \tag{4.33}$$

The disintegration rate can be found using the observed peak intensities in the presence of coincidence summing ($\mathbf{S}_{ji}$), the efficiencies, the feeding fractions and the branching ratios. Using Eq. (4.31),

$$S_{ji} = R_{ji}\left[\mathbf{N^{(0)}}\mathbf{A^{(0)}} + \mathbf{D}\right]_{ji} \tag{4.34}$$

A matrix of disintegration rates is obtained from this calculation, which vary because of statistical errors in the observed peak intensities. A value for R is obtained by averaging these values. The median of the rates is used for this purpose, because it is less affected by outliers in the rates.

If the observed peak intensities, branching ratios, feeding fractions, disintegration rate and total

efficiency of the detector are known, it is possible to calculate the sum corrected peak efficiency. Calculating the peak efficiency in this way is extremely useful because a single radioactive source with a range of γ-ray energies can be used to produce an efficiency curve. Eqs. (4.33) and (4.34) yield:

$$\varepsilon^{p}_{ji} = \frac{S_{ji}}{I_{ji}} - \frac{D_{ji}}{\left[\mathbf{N^{(0)}c}\right]_{ji}}, \tag{4.35}$$

where I_{ji} is calculated from Eq. (4.33). Unfortunately, the peak efficiencies are also contained in the correction matrix, **D**, so iterative methods are required. Initially, **D** is assumed to be zero so Eq. (4.35) becomes:

$$\varepsilon^{p}_{ji} = \frac{S_{ji}}{I_{ji}} \tag{4.36}$$

These values for the peak efficiency can then be used to calculate a new value for **D** from Eqs. (4.19) to (4.32) , which in turn can be used with Eq. (4.35) to recalculate the peak efficiencies. Desired accuracy of peak efficiencies can be obtained by repeating this procedure iteratively.

A similar method has been developed to calculate unknown branching ratios using the peak and total efficiencies, feeding fractions, observed values and disintegration rate. This method uses a form of Eq. (4.31):

$$A^{(0)}_{ji} = \frac{S_{ji}/R - D_{ji}}{N^{(0)}_{jj}} \tag{4.37}$$

where,

$$x_{ji} = \frac{A^{(0)}_{ji}}{\varepsilon^{p}_{ji}} \tag{4.38}$$

Once again, this method involves an iterative search where **D** is first assumed to be zero. Eq. (4.37) is used to find the uncorrected branching ratios, x_{ji}, which are then utilised to calculate values for **D**. These values can then be used to find the branching ratios and the iteration continues until a desired level of accuracy is achieved.

Summing Correction Codes

Several codes have been written to implement these methods. The first code corrects a spectrum for coincidence summing, corrects a single peak (useful for yield measurements) or calculates the

disintegration rate. The second code calculates the sum corrected peak efficiencies from the branching ratios, feeding fractions, observed peak intensities and a disintegration rate. The third code program is designed to calculate the branching ratios of a decay if the general structure of the level scheme is known. This latter code is designed to only be used for resonance reactions with 100% feeding to the top level. It requires an input of observed peak intensities, efficiencies and a disintegration. The code also has the feature of being able to hold known branching ratios constant and just calculate the unknown branches. The programs all use the same input file (See Fig. 4.18).

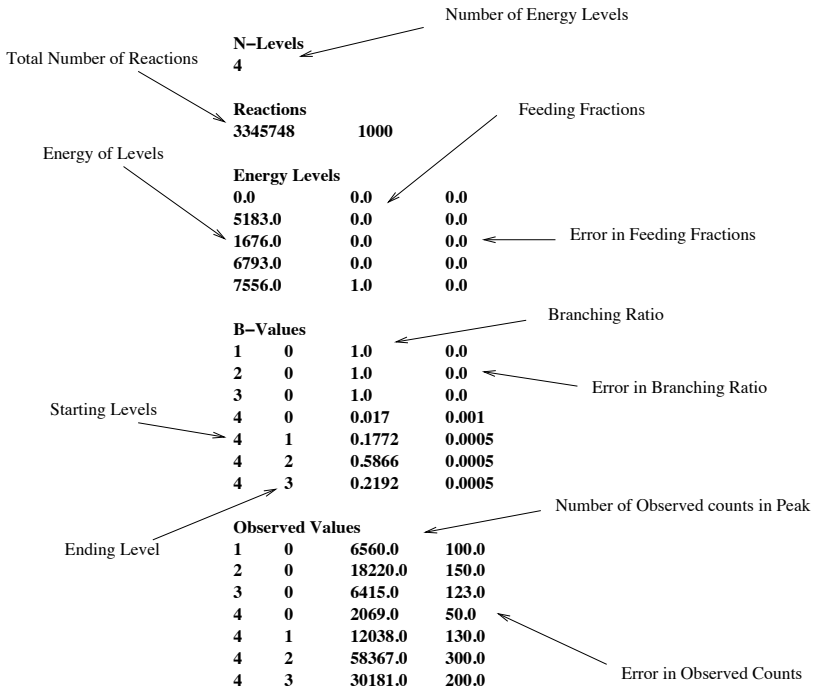

Figure 4.18: Sample input file for the decay of the ^{14}N(p,γ)^{15}O reaction.

The peak intensity correction program has been tested with a simple, theoretical four level decay scheme. The summing effects can also be calculated by hand by considering each γ-ray individually and accounting for every possible decay route that could lead to summing-in, or summing-out. This is relatively simple for a four level decay scheme and can be calculated with confidence. The results for calculation by hand were found to be identical to those obtained by running the program. This code can also be tested using the radioactive decay of ^{56}Co, which has a many level decay scheme and results in very complicated summing effects. Summing correction for this decay scheme would be

almost impossible without the aid of a sum correction code. This decay scheme is further complicated by β^+-decay, which can produce 511 keV annihilation radiation. These can sum with any of the decay γ-rays. The 511 keV annihilation radiation is assumed to originate from the target, and not from the surrounding material.

In order to account for summing effects involving annihilation radiation, it is possible to create a decay scheme for ^{56}Co by arbitrarily adding levels 511 keV above each of the levels that are fed by β^+-decay. These artificial levels are fed with the same feeding fraction as for the actual level. For example the $E_x = 2085$ keV excited state in ^{56}Fe is populated by β^+-decay with a feeding fraction of 18.1%. To account for coincident 511 keV summing effects, a level is added to the decay scheme at $E_x = 2085 + 511 = 2596$ keV with a feeding of 0.181. These extra states are then given a branching ratio of 1.0 to the level they represent (i.e., the $E_x = 2596$ keV state will decay to the $E_x = 2085$ keV state with a branching ratio of 1.0). This has the result of 511 keV γ-rays being emitted in coincidence with γ-ray decays from that level.

A decay scheme for ^{56}Co can be built in this manner using the branching ratios, feeding fractions, and energy levels found in Ref. [Jun99]. The calculated peak intensities in the presence of coincidence summing are then compared to the actual observed peak intensities (Fig. 4.19). Although some of the points do not agree with the observed values, most of the points agree within error. The points that disagree are mainly caused by summing with 511 keV γ-rays and impurities in the source (for example, the ^{56}Co source had a large ^{57}Co contamination).

A more complicated decay scheme was used to test the single peak correction function of the peak intensity correction program. The 519 keV resonance in ^{17}O(p,γ)^{18}F has a 13 level decay scheme, which would be extremely hard to correct by hand. The literature 519 keV resonance strength is $\omega\gamma = 1.37 \times 10^{-2} \pm 0.22 \times 10^{-2}$ [New10b]. With no summing correction, the 4975 keV peak contains 20821 ± 155 counts, which corresponds to a resonance strength of $\omega\gamma = 5.3 \times 10^{-2}$. When the peak was corrected for coincidence summing effects, the number of counts was 31837 ± 3728, 65% larger than the observed number of counts. This yielded a resonance strength of $\omega\gamma = 1.3 \times 10^{-2} \pm 0.2 \times 10^{-2}$, in excellent agreement with the literature. The large error in the corrected number of counts originates from uncertainties in the branching ratios of the decay scheme. This example highlights the large effect summing can have when using high efficiency detectors.

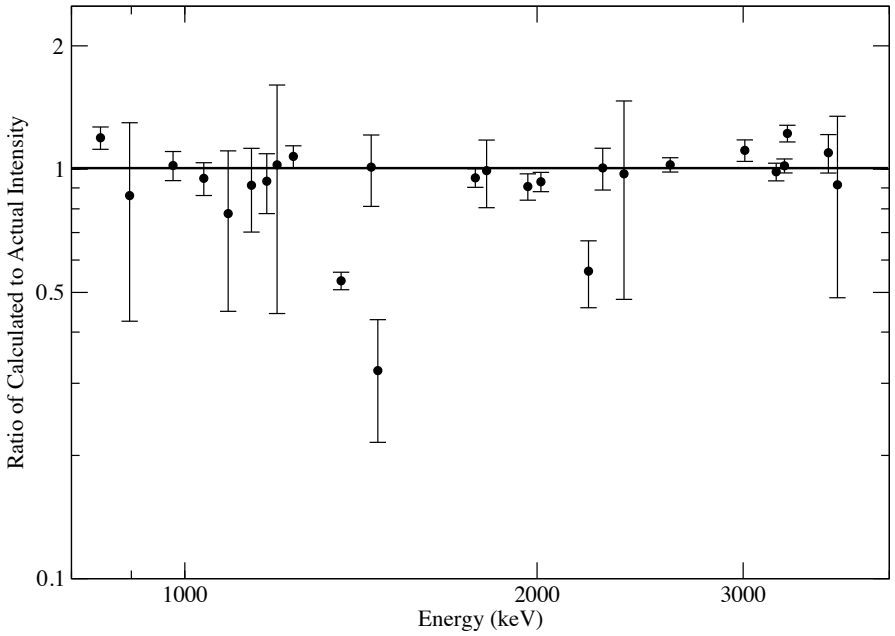

Figure 4.19: Ratio of calculated peak intensity to observed intensity in ^{56}Co decay. The peaks at 1360 keV, 1462 keV and 2212 keV appear considerably lower than expected. The 1360 keV peak is largely affected by 511 keV γ-rays.

The peak efficiency summing correction code is further described in Sec. 4.2.1. Hence the information will not be repeated in this discussion.

The third code calculates branching ratios of resonant reactions in the presence of coincidence summing. This program is not intended to be applied to radioactive sources, in which the levels are populated according to the feeding fractions; 100% feeding to the highest energy level is required, as in resonance reactions. The $E_r^{\mathrm{lab}} = 278$ keV resonance in ^{14}N(p,γ)^{15}O was used to test this code, owing to its simple decay scheme [AS91] for which the summing can also be calculated analytically. The code was developed so that well known branching ratios in the decay can be held constant and only unknown branches will be calculated. An ^{14}N(p,γ)^{15}O measurement was performed at LENA for the $E_r^{\mathrm{lab}} = 278$ keV resonance. After running the code with the observed intensities from the experiment, the branching ratios were compared with the literature values and experimental results.

Transition		Branching Ratio	Literature Value
E_i (keV)	E_f (keV)	Present	
5183	0	1.0 ± 0.0	1.0 ± 0.0
6176	0	1.0 ± 0.0	1.0 ± 0.0
6793	0	1.0 ± 0.0	1.0 ± 0.0
7556	0	0.0192 ± 0.0019	0.016 ± 0.001
7556	7583	0.1705 ± 0.0022	0.171 ± 0.002
7556	6176	0.5851 ± 0.0046	0.578 ± 0.003
7556	6793	0.2252 ± 0.0021	0.229 ± 0.003

Table 4.1: Branching Ratios calculated from the ^{14}N(p,γ)^{15}O resonance. The uncertainties in the present results to not include efficiency uncertainties, which amount to about 5%. The literature values are taken from Ref. [Imb05].

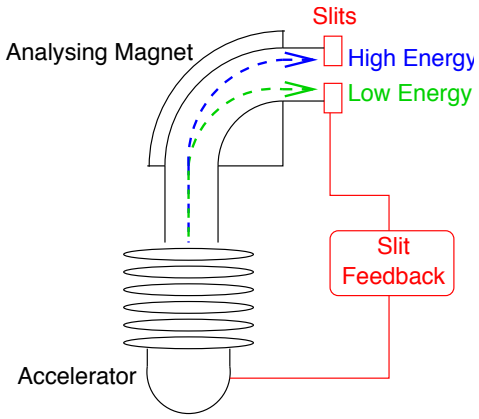

Figure 4.20: Schematic of the slit control system used to control the beam energy at LENA. If the beam energy becomes too low, for example, the beam will be deflected more by the magnet (whose field is precisely maintained). A current imbalance will be measured between the high and low energy slits causing the accelerator voltage to be increased.

Every decay branch agreed with the literature values within uncertainties (See Table 4.1).

4.3 Analysing Magnet Energy Calibrations

The beam energy delivered to a target in the LENA laboratory is selected with a horizontal slit system on the target side of an analysing magnet. The current measured on the slits is balanced with the aid of a feedback circuit, which controls the terminal voltage. This system is shown schematically in Fig. 4.20.

Prior to an experiment in which the beam energy must be known, the analysing magnet used to

Target	$E_r^{\text{lab}}(keV)$	E_x (keV)	$\omega\gamma$ (eV)
^{18}O	150.9 (2)	5789	$9.7 \times 10^{-}4$
^{27}Al	222.7 (4)	11719	$4.2(3) \times 10^{-}5$
^{26}Mg	292.12 (9)	8552	$7.0(12) \times 10^{-}3$
^{27}Al	292.6 (4)	11867	$2.33(13) \times 10^{-}4$
^{23}Na	308.75 (6)	11989	$0.105(19)$
^{27}Al	326.6 (4)	11899	$1.8(1) \times 10^{-}3$
^{27}Al	405.5 (3)	11976	$8.63(52) \times 10^{-}3$
^{26}Mg	462.6 (5)	8716	$0.035(11)$
^{27}Al	654.65 (4)	12216	$0.110(9)$

Table 4.2: Standard resonances used for analysing magnet calibration. All resonance energies and strengths are from Ref. [Ili10]

select the beam energy must be calibrated. The procedure for this is well established, and involves measuring several resonances with well-known resonance energies. Yield curves for each resonance listed in Tab. 4.2 were measured. A yield curve fitting code (see Sec. 3.2) was used to find the magnetic field that corresponded to the front edge of each resonance (an example is shown in Fig. 4.21). The field, B is related to beam energy, E, through [Ili07]

$$E = aB^2 \tag{4.39}$$

Fitting Eq. (4.39) provided the calibration constant for the magnet.

4.4 Target Implantation

Implanted targets are frequently used at LENA. They consist of a backing material (usually a thin tantalum sheet) with the nuclei of interest implanted into it. An Eaton ion implanter with a modified end station (located at the University of North Carolina at Chapel Hill) is used to implant ions into target backings. The ion implanter accelerates ions from pressurised gas bottles to implantation energies between $E_{\text{ion}} = 20$ keV and ≈ 100 keV (assuming singly ionised particles). A 90° analysing magnet (with a quoted selectivity of $1/100$) is used to mass separate the beam to ensure pure implantation of the ion of interest (see Fig. 4.22). The incident dose of particles is estimated by integrating the beam current on the backing, assuming singly charged incident ions.

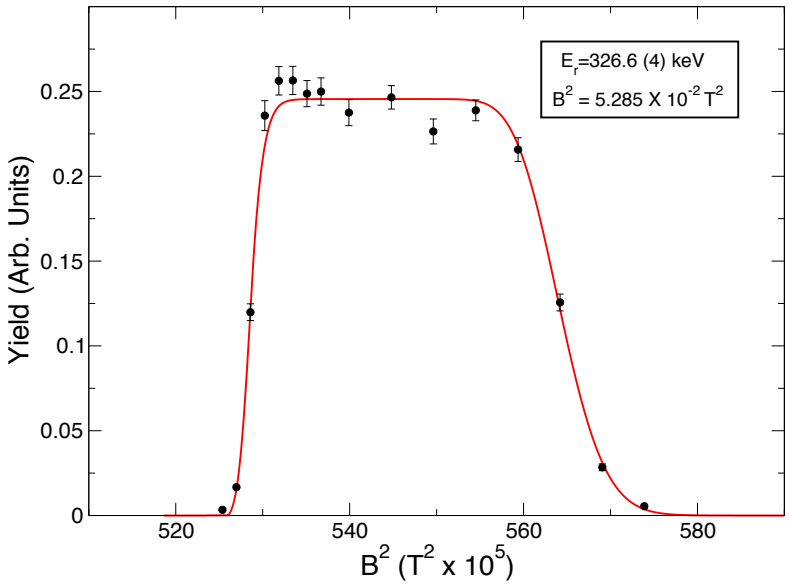

Figure 4.21: Sample yield curve for the $E_r^{\rm lab} = 326$ keV resonance in ^{27}Al(p,γ)^{28}Si. The front edge of the yield curve defines the magnetic field that corresponds to the resonance energy.

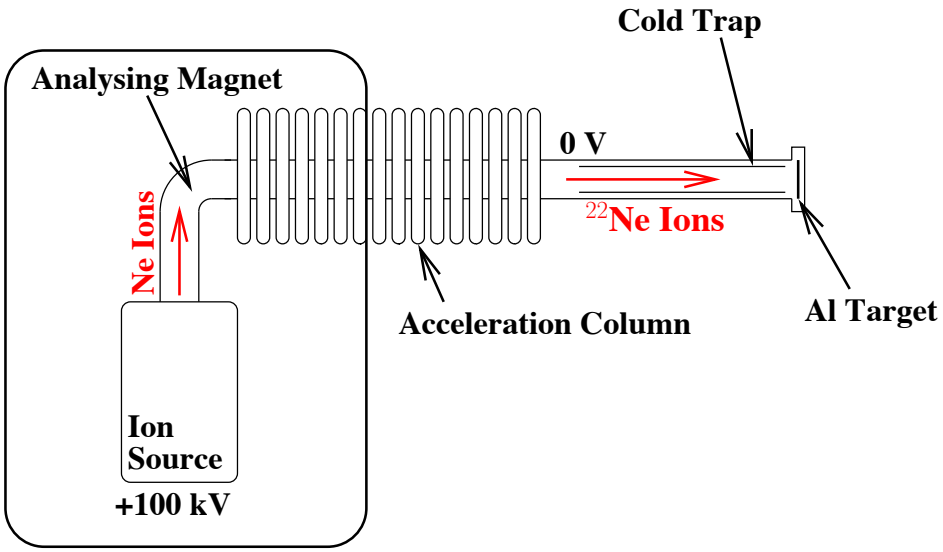

Figure 4.22: Schematic of the Eaton N200 ion implanter, which was used for implanting ions into target backings used for depth profiling. The ion source is held at a constant voltage of 20 kV above the acceleration voltage for beam extraction.

4.4.1 Target Thickness

The thickness of a target is usually quoted in units of energy, and corresponds to the amount of energy that will be lost as beam particles traverse the implanted region. The desired thickness of an implanted target depends on the experiment to be performed. Two situations are relevant for stopping targets (i.e., the beam will stop in the target backing) used at LENA: (i) narrow resonance strengths; a thick target ($\Delta E \approx 20$ keV) is required to ensure that all beam particles will interact in the target region; and (ii) a slowly varying cross section; a thin target ($\Delta E < 10$ keV) is required to measure the shape of the cross section accurately.

Once a target thickness (in units of energy) has been chosen to best suit the experiment, the implantation energy (energy of incident ions on a backing) needed to produce the target must be calculated. Estimates for implantation energies are best performed with the aid of the stopping power code `SRIM` [Zie04]. The user must first calculate the physical depth of a target that corresponds to the energy loss required. For example, if ^{22}Ne is to be implanted into a tantalum substrate to produce a $\Delta E = 15$ keV thick target at proton energies of $E_p^{\text{lab}} = 400$ keV, `SRIM` would be run for protons incident on a Ne-Ta compound at $E_p^{\text{lab}} = 400$ keV and $E_p^{\text{lab}} = 385$ keV. The difference in ranges is an approximate measure for how thick the implanted region must be (80 nm in this example). The next step is to calculate the implantation energy of ^{22}Ne incident on pure tantalum required to produce a target of the desired physical thickness. Once again, `SRIM` is used to find the beam energy of ^{22}Ne required to reproduce a range equal to that found in the first step. This implantation energy is $E^{\text{lab}} = 140$ keV for this example. Note that target thicknesses are not required to be an exact value, in general, so the approximate calculations outlined above are adequate for producing the targets used at LENA. The actual thickness of the targets are then found using narrow resonance yield curves (Ch. 3).

4.4.2 Dose Calculations

The number of ions implanted into a target depends on the beam current, implantation volume, implantation time and implantation efficiency. The required dose, D, is calculated using the simple geometry shown in Fig. 4.23. The implantation volume is constrained by a collimator placed approx-

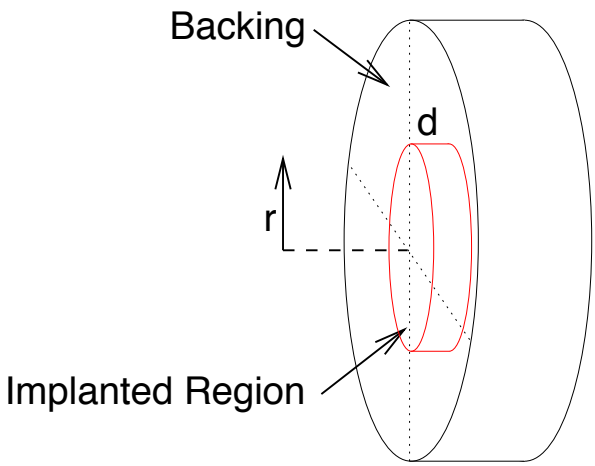

Figure 4.23: Geometry used to calculate required dose in implanted targets. The target ions are implanted into a thick target backing to a depth of d and a radius r defined by a collimator.

imately 20 cm away from the target, and by the thickness of target desired. For the present work, the implantation region diameter was 2.5 cm. The number of backing substrate atoms, N_b, in a volume, V, defined by $V = d \cdot r^2$ is given by:

$$N_b = \frac{\rho_b V N_A}{A_b} \tag{4.40}$$

where ρ_b is the backing substrate density (g cm^{-3}), A_b is the atomic mass of the backing atoms, and N_A is Avogadro's number. The number of required implanted ions, N_t, is therefore

$$N_t = \xi N_b \tag{4.41}$$

where ξ is the stoichiometry of the final implanted target. The stoichiometry achieved depends on the implanted ion as well as the backing substrate, which cannot typically be predicted. Examples of experimentally determined stoichiometries can be found in Ref. [Ili07]. For the case of ^{22}Ne ions implanted in tantalum, a stoichiometry of approximately Ne:Ta$= 1 : 3$ should be achievable. The required incident beam charge to implant N_t ions is given by

$$Q = \frac{N_t}{\eta} \tag{4.42}$$

where Q is the implanted charge as read from the target, and η is the sputtering ratio. Implantation efficiency is not typically known. However, all experiments performed at LENA require a saturated

target in order to maximise count rates of astrophysically important reactions. For this reason, the implantation efficiency is assumed to be a conservative 25%. For ^{22}Ne implanted into a tantalum backing to produce a $\Delta E = 15$ keV thick for protons at $E_p \approx 400$ keV, a dose of approximately 0.25 C is therefore required.

5 ^{26}Mg(γ,γ')^{26}Mg

5.1 Introduction

At a typical temperature near $T = 300$ MK, which is relevant for neutron production in massive stars and AGB stars, the Gamow peak for α-particle capture on ^{22}Ne occurs near $E_0 = 600$ keV. At these low bombarding energies, the Coulomb barrier dominates the α-particle partial width and, therefore, the reaction cross section decreases dramatically with decreasing energy. A consequence of the low cross section is the difficulty to measure ^{22}Ne+α reactions directly. The lowest measured resonance is located at $E_r^{\mathrm{lab}} = 830$ keV [Wol89, Jae01b]. Other methods must be utilised to obtain the properties of low energy resonances in order to estimate reliable neutron production rates in stellar environments.

Prior to the present work, the nuclear properties of levels between the α-particle threshold at $S_\alpha = 10615$ keV and the lowest directly observed resonance ($E_x = 11319$ keV) have been measured through neutron capture, α-particle transfer, and photo-neutron studies [Ber69, Gla86, Wal92, Gie93, KÖ2, Uga07]. In addition to these works, Nuclear Resonance Fluorescence (NRF) experiments using bremsstrahlung beams [Ber84, Sch09], and inelastic proton scattering experiments [Mos76, Cra89] have observed two states in the excitation energy region of interest at $E_x = 10649$ keV ($J^\pi = 1^+$) [Ber84, Sch09] and $E_x = 11154$ keV ($J = 1^{(+)}$) [Mos76, Cra89, Sch09]. The resolution of Ref. [Cra89] was approximately 60 keV. The 1^+ state observed in that experiment could therefore be attributed to a number of excited states in this energy region. Transfer measurements (^{22}Ne(^{6}Li, d)^{26}Mg) [Uga07, Gie93] have also studied low spin states between the α-particle and neutron thresholds in ^{26}Mg. Alpha-particle transfer studies typically yield excitation energy uncertainties in excess of several keV and, furthermore, do not provide unambiguous quantum numbers to excited

states. A ^{26}Mg$(\gamma,\gamma)^{26}$Mg measurement with a polarised, mono-energetic γ-ray beam can be useful for significantly improving uncertainties of the ^{22}Ne$(\alpha,\gamma)^{26}$Mg and ^{22}Ne$(\alpha,\mathrm{n})^{25}$Mg reaction rates. The High-Intensity γ-ray Source (HIγS) at the Triangle Universities Nuclear Laboratory (TUNL), utilising a linearly polarised γ-ray beam, is perfectly suited for this purpose.

Here, experimental results of the spin and parity measurements of dipole states in the photoexcitation ^{26}Mg$(\gamma,\gamma)^{26}$Mg reaction are presented. These measurements were made in the energy region important to astrophysical reaction rate calculations. The experimental setup is discussed in Section 5.2. Section 5.3 outlines the theory needed to interpret γ-ray angular correlation measurements. The results of the experiment are presented in Section 5.4. A discussion follows in Section 5.5, and conclusions are given in Section 5.6.

5.2 Experimental Setup

5.2.1 Photon Beam

The properties of excited states in a nucleus can be probed with high energy photons. A photon beam is used to excite the ground state nucleus to the desired energy, while the de-excitation γ-rays are observed. These beams can be produced in a variety of ways. Firstly, nuclear reactions can be used to produce mono-energetic γ-rays. However, only those energies allowed by the nuclear structure of the compound nucleus used will be available, hence tuning of γ-ray energies is not possible. This method therefore has very limited applicability. Secondly, the most common method is by using bremsstrahlung radiation[1] to excite the nucleus. Bremsstrahlung radiation is produced when a charged particle is accelerated in a high electric field, commonly an electron being deflected by the field of an atomic nucleus. Although this method can produce a high flux of radiation, the photon energy distribution is continuous. This creates complications in the analysis of γ-ray partial widths because the exact shape of the bremsstrahlung energy distribution must be known precisely. In addition, decays to other excited states are usually unresolvable because the continuous beam energy profile will excite lower lying states in the nucleus directly. A third method of producing photon beams is by Compton scattering laser photons from relativistic electrons. The present work was performed at the HIγS

[1] Originating from the German words *bremsen* (to brake) and *strahlung* (radiation)

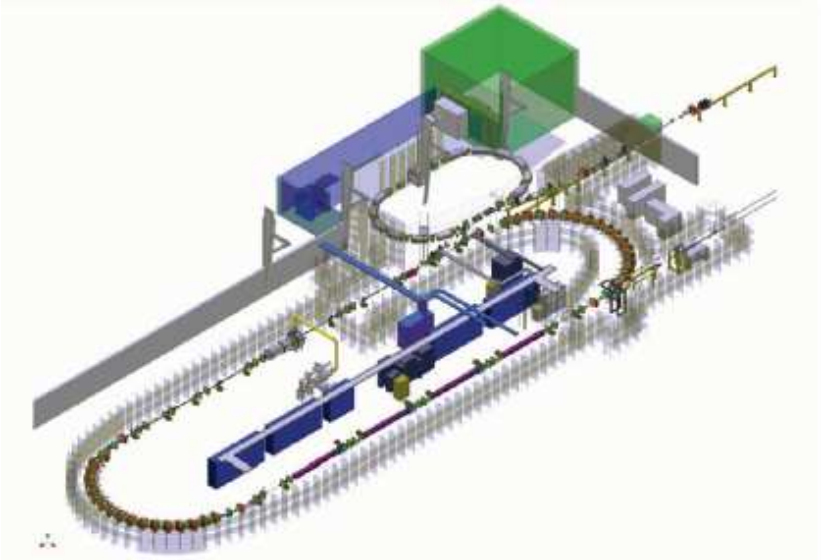

Figure 5.1: Design schematic of the DFEL facility. The HIγS target rooms are located to the right of the figure. Figure obtained from Ref. [Wel].

facility, which utilises the latter method. The advantages of using Compton scattering are as follows: (i) a mono-energetic beam (an energy spread of about 3% of the beam energy) can be produced; (ii) the beam can be highly (almost 100%) polarised; and (iii) a high intensity of photons (10^7 photons/s incident on the sample) can be achieved.

The photon beam at HIγS is produced using the Duke Free Electron Laser (DFEL). The beam production and transportation occurs in four main parts: an electron storage ring, a magnetic undulator, a resonating cavity, and the target area. An outline of the beam production follows, and more information can be found in Refs. [Car96, Lit97, Wel09] and references therein. A design schematic of the DFEL facility is shown in Fig. 5.1.

The Electron Storage Ring

The electron storage ring is a 107 m long "racetrack" shaped ring that is capable of accelerating electrons up to 1.2 GeV. The electron bunches are supplied by a 180-280 MeV S-band radio frequency linear accelerator. During HIγS operation, the storage ring contains two electron bunches, separated by half the ring length. An electron current of about 40 mA in the storage ring is sufficient to produce $10^7\gamma/s$ on the sample.

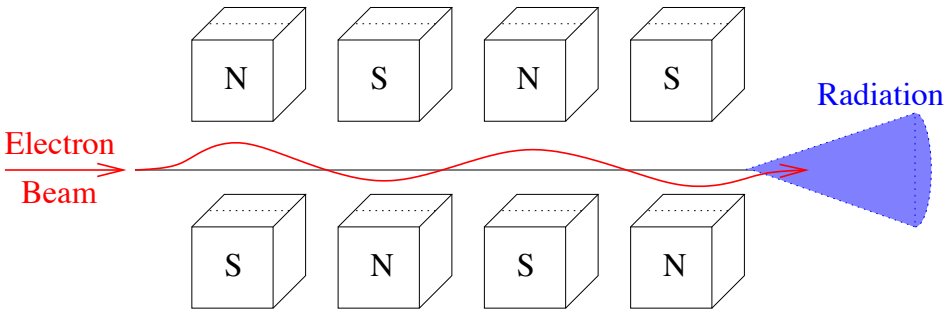

Figure 5.2: Schematic diagram of a wiggler system. The alternating magnetic field produces a characteristic photon beam in the downstream direction.

The Magnetic Undulator

The magnetic undulator, an optical klystron, produces a polarised photon beam. Commonly known as a "wiggler", the oscillator consists of a set of magnets that accelerate the electron bunches transverse to the beam direction. This motion transverse to the beam direction produces coherent light emission by the electrons. Unlike in conventional lasers, there is no lasing medium, hence the term "free electron laser". Figure 5.2 shows an example of the wiggler principle. The general equation governing the intensity, I, of radiation from an accelerating charged particle is given by [Jac98]:

$$\frac{\mathrm{d}^2 I}{\mathrm{d}\omega \mathrm{d}\Omega} = \frac{e^2\omega^2}{4\pi^2 c}\left|\int_{\infty}^{\infty} \mathbf{n}\times(\mathbf{n}\times\beta)\, e^{i\omega(t-\mathbf{n}\cdot\mathbf{r}(t)/c)}\mathrm{d}t\right|^2 \tag{5.1}$$

where: ω is the frequency of emitted radiation; Ω is the solid angle; $\mathbf{n}$ is a unit vector towards the emission direction; $\beta = \mathbf{v}/c$, where $\mathbf{v}$ is the velocity of the particle; and $\mathbf{r}(t)$ is the position of the particle as a function of time.

If the electron is relativistic, the radiation is emitted in a narrow cone in the direction of motion. Provided the angle of motion is less than that of the light cone, an observer situated "downstream" will observe a continuous beam of photons. This photon beam will have a typical energy, E, depending on the electron energy and wiggler magnetic field properties [Car96]:

$$E \approx \frac{chk_w\gamma^2}{\pi}\left(1+a_w^2\right) \tag{5.2}$$

where: c is the speed of light; h is Planck's Constant; k_w is the undulator wave number, which is

obtained from the magnet spacing; γ is the relativistic Doppler shift of the electrons; and a_w is the normalised rms vector potential of the undulator, which is related to the strength of the magnetic field. The DFEL undulator has $k_w = 62.8\ \mathrm{m}^{-1}$, and a_w is variable from zero to 4.1 by varying the magnetic field. The photon energy spread depends on the number of magnetic periods in the undulator, N, and is given by: $\Delta E/E \sim 1/N$. The transverse motion of the electrons will produce linearly polarised photons, with the polarisation vector transverse to the magnetic field and beam direction [Car96].

The Resonating Cavity

The resonating cavity is an optical cavity that captures the photons produced in the undulator. Fig. 5.3 shows the cavity arrangement in relation to the electron storage ring and undulator. The cavity consists of two mirrors on either end of the undulator section of the storage ring. These mirrors are separated by one half of the storage ring length. Therefore, the photons will pass back through the undulator when the electron bunch has made a full circuit. The mirrors can be moved to ensure an even number of wavelengths in the cavity so that the electric field of the photons provides additional force on the electrons, further stimulating emission. These photons will be referred to as the laser photons. The number of laser photons stored in the resonating cavity can reach about 10^{13} photons [Car96], which corresponds to about 15 W beam power.

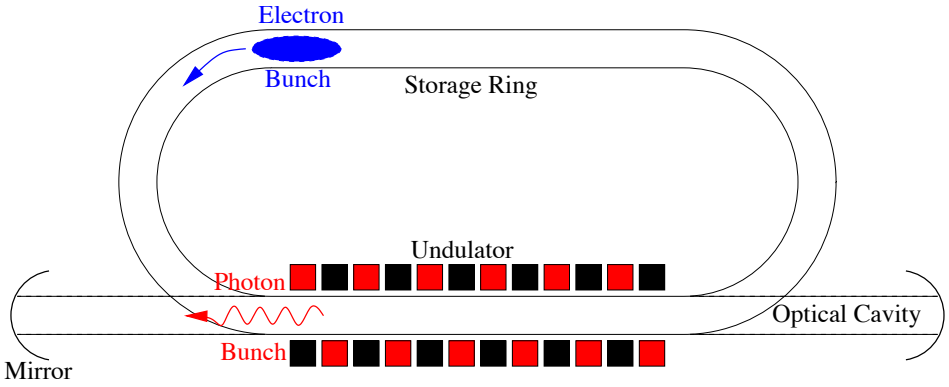

Figure 5.3: Representation of the resonating cavity in the DFEL. The optical cavity is tuned so that the electron and photon bunches reach the undulator simultaneously. This creates lasing as the photon electric fields stimulate coherent photon emission from the electrons.

If a second electron bunch is added to the storage ring, separated from the first by half the ring length, high energy photons can be produced. As the second electron bunch reaches the undulator, it

will meet the laser photon bunch travelling in the opposite direction. The Compton scattering of laser photons off these relativistic electrons produces high energy photons, which are polarised in the same plane as the laser photons. In an electron's rest frame, the energy, E', of a scattered photon is:

$$E' = \frac{m_e c^2 E}{m_e c^2 + E\,(1 + \cos\theta)}, \tag{5.3}$$

where: E is the incoming laser photon energy; m_e is the electron rest mass; and θ is the scattering energy. The differential cross section of scattering is given by the Klein-Nishina Eqn. ([Kle29]):

$$\frac{\mathrm{d}\sigma}{\mathrm{d}\Omega} = r_e^2 \left(\frac{E'}{E}\right)^2 \left(\left|\varepsilon^* \cdot \varepsilon_0\right|^2 + \frac{(E - E')^2}{4EE'}\right), \tag{5.4}$$

where: r_e is the electron radius ($r_e = 2.8 \times 10^{-15}$ m); E and E' are the incoming and outgoing photon energies; ε^* and ε_0 are the polarisation vectors of the incoming laser photons and outgoing photons, respectively. Applying these equations to the situation of low energy photons scattering from relativistic electrons results in a high energy photon beam. Neglecting recoil effects, the photon beam will have an energy of about $(2\gamma^2)E^{\text{lab}}$. Consider, for example, an electron energy of about 500 MeV and photon energy of 3 eV. In this case, photons will be produced with energies on the order of 11 MeV. The photon beam will be concentrated to a narrow cone aligned with the electron bunch direction. An example can be seen in Fig. 7 of [Kle29], where most of the beam is within one thousandth of a radian of the electron beam direction. Equation (5.3) shows that the photon energy depends on the scatter angle. Consequently, placing collimators downstream can tune the beam energy width desired on the sample.

The Target Area

The target area is located about fifty metres downstream of where the γ-rays are produced in the undulator. It is split into two main rooms: the "collimator hut", and the "gamma vault". The collimators are used to select the width of the beam. Selecting a narrower beam profile restricts the energy width and intensity of the beam. The gamma vault, situated downstream from the collimator hut, is where experimental setups are placed. A sensitive beam imager can be placed in the gamma

vault for accurate alignment of the beam to within a few millimetres. Accurate photon beam alignment enables the use of smaller samples because it can be ensured that the entire beam travels through the active area of the sample.

Parameters used in the Experiment

The storage ring of the HIγS facility was operated with two electron bunches at an energy of $E_{e^-} = 515 - 530$ MeV and a current of $I_{e^-} \approx 45$ mA. The collimator size used, which defines the diameter of the beam incident on the sample, amounts to 1.91 cm, resulting in a beam energy spread of about 200 keV at a beam energy of 11.0 MeV. The intensity of the 100% linearly polarised photon beam at the sample was about 10^7 s^{-1}. Four incident γ-ray beam energies were used throughout the experiment: 10.8, 11.0, 11.2 and 11.4 MeV. A beam dump downstream from the sample reduced Compton scattering into the detectors.

5.2.2 Samples

The sample consisted of magnesium-oxide (MgO) powder, enriched to 99.41(6)% in ^{26}Mg. The ^{24}Mg and ^{25}Mg compositions were 0.41(2)% and 0.18(4)%, respectively. In addition, a spectroscopic analysis of the sample, performed at Oak Ridge National Laboratory who provided the sample, revealed only small impurities with a concentration in excess of 10 parts per million: iron (10 ppm); and zinc (20 ppm). Impurities of less than 10 ppm could not be detected in that analysis, and are irrelevant for the present work. The total sample mass amounted to 16418.5 mg, corresponding to a ^{26}Mg mass of 10162.5 mg. The sample was contained in a polycarbonate cylindrical container with 0.16 cm thick walls and end caps, with an inner cavity of 2.30 cm in diameter and 3.10 cm in length. The sample container was suspended in a sample holder consisting of a plastic ring with a fishing line lattice as shown in Fig. 5.4. The fishing line held the sample in place in the centre of the beam line while minimising material that could create scattering events. In addition, a natural magnesium oxide ($^{\text{nat}}$MgO) sample (79% ^{24}Mg, 11% ^{25}Mg, 10% ^{26}Mg), housed in an identical polycarbonate container, was used for background measurements and energy calibrations. This $^{\text{nat}}$MgO sample had a mass of 4.3 g.

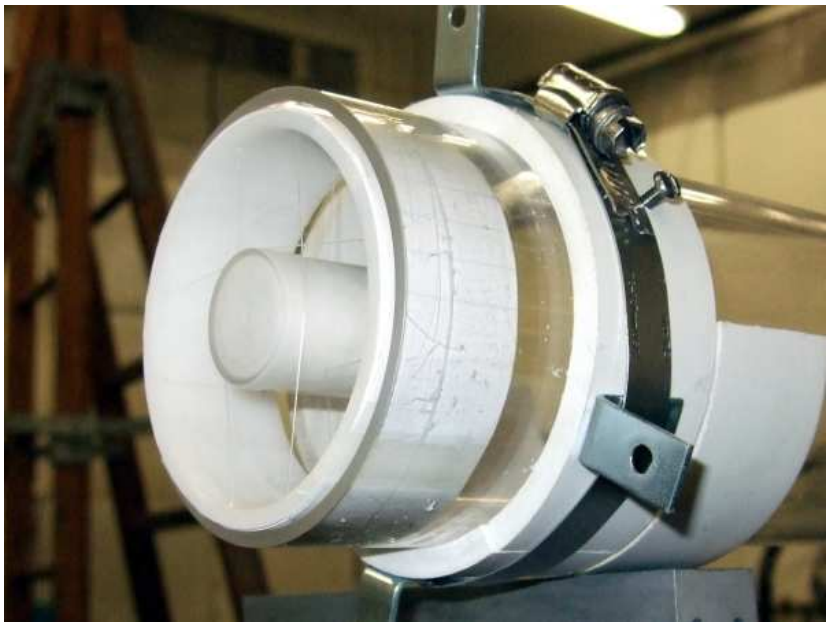

Figure 5.4: The ^{26}MgO sample suspended in the sample holder. The sample holder consists of a ring with fishing line to suspend the sample. This reduces the amount of material available for Compton scattering, which would produce background in the detectors.

5.2.3 Detectors

Four High Purity Germanium (HPGe) detectors with relative efficiencies of 60% were used in the measurements. The detectors were arranged around the sample as shown in Fig. 5.5. Three detectors, two vertical and one horizontal, were positioned perpendicular to the incident beam, while one detector, the "out-of-plane" detector, was located outside the vertical plane. These positions were chosen in order to determine the spins and parities of ^{26}Mg excited states unambiguously, as will be discussed in Section 5.3.

Each detector was placed at a distance of about 10 cm from the centre of the sample. After positioning, the γ-ray beam was aligned with a high resolution beam imager to ensure homogeneous beam intensity across the sample. Small detector geometry differences were later accounted for by using Monte-Carlo simulations and radioactive source measurements and will be discussed in Sec. 5.4.1. The internal geometry of the detectors is shown in Fig. 5.6, and dimensions provided by the manufacturer are tabulated in Tab. 5.1. Each detector had a passive shield and absorber comprised of lead and copper. The purpose of the absorbers was to reduce contributions from low energy background and 511 keV annihilation γ-rays produced in the sample. A copper plate, approximately 1 m

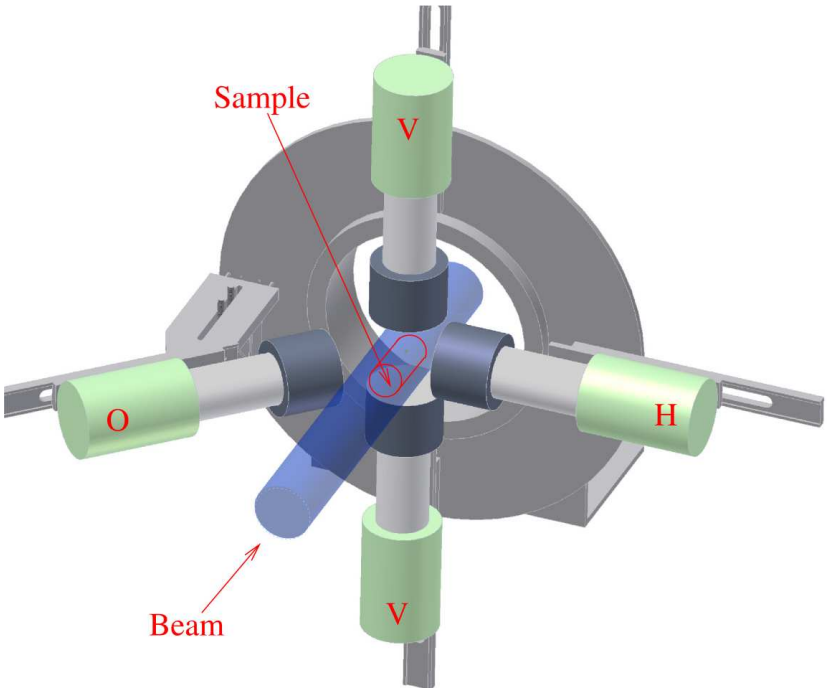

Figure 5.5: The detector setup used for energy and spin-parity measurements of ^{26}Mg excited states. The sample was placed at the centre of the array consisting of four 60% HPGe detectors, where the labels "V", "H", and "O" represent the vertical, horizontal and out-of-plane detectors, respectively. The dark grey cylinders shown on the detector front faces are passive lead and copper shields. The detector labels correspond to the indicies referred to in the text.

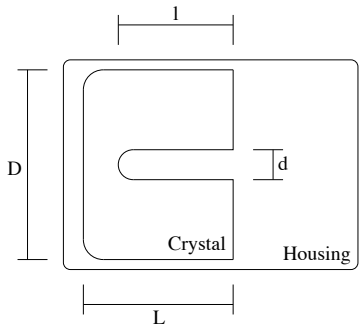

Figure 5.6: Schematic of the internal HPGe geometry. Shown is the HPGe crystal (of length L and diameter D) mounted in an aluminium end cap. The crystal has a contact pin (length l and diameter d).

Detector	L (cm)	D (cm)	l (cm)	d (cm)
1	8.90	6.46	7.27	1.12
2	7.75	6.82	7.09	1.17
3	6.83	6.97	6.00	0.99
4	8.05	6.80	7.31	0.93

Table 5.1: HPGe crystal geometries as shown in Fig. 5.6.

downstream of the sample was used to Compton scatter beam photons into an additional 135% HPGe detector, which was placed 4 m downstream of the sample. This detector is about 5° out of the beam so that it cannot be reached directly by the incident beam. A lead shield behind the sample prevents scattering from the sample into the 5° detector. Through Monte-Carlo simulations, the photon flux can be reconstructed by matching the Compton scattering spectrum measured in the 135% HPGe detector. This detector can also be moved into the beam to measure the beam energy profile (low fluxes must be used for this to avoid overloading the detector).

5.3 Nuclear Resonance Fluorescence

A linearly polarised photon beam incident on a $J^\pi = 0^+$ target nucleus, such as ^{26}Mg, gives rise to a distinct radiation pattern depending on the quantum numbers of the excited states [Bie53]. The observed intensity pattern is referred to as polarisation-direction correlation. This type of angular correlation is described in detail in Ref. [Bie53]. The detector geometry was similar to the one used in earlier experiments at the HIγS facility (see Ref. [Wel09] and references therein). The only change

performed in the present work was to move one of the horizontal detectors out of the vertical plane to a backward angle. This change was necessary to unambiguously distinguish between radiation from $J = 1$ and $J = 2$ excited states (see below).

For an incident linearly polarised γ-ray beam, the angular correlation function, which is proportional to the probability of de-excitation in a particular direction, for pure transitions (i.e., those involving unique quantum numbers) is given by [Bie53]:

$$\begin{aligned} W_{\text{theory}}(\theta,\phi) &= \sum_n F_n(L_1,L_1,j_1,j)F_n(L_2,L_2,j_2,j) \\ &\quad \times \left[P_n(\cos(\theta)) + (-1)^{\sigma_1}\frac{\langle L_1 1 L_1 1|n2\rangle}{\langle L_1 1 L_1 -1|n0\rangle}\left(\frac{(n-2)!}{(n+2)!}\right)^{1/2}\cos(2\phi)P_n^{(2)}(\cos(\theta))\right] \\ F_n(L_a,L_a',j_a,j) &= (-1)^{j_a-j-1}\sqrt{(2j+1)(2L_a+1)(2L_a')} \quad \langle L_a 1 L_a' -1|n0\rangle W(jjL_aL_a';nj_a) \end{aligned} \tag{5.5}$$

where n is an even integer ranging from 0 to $n_{\text{max}} = \min(2j+1, 2L_1+1, 2L_2+1)$; the subscripts '1' and '2' refer to the first (incident beam) and second (detected photons) radiations (the incident beam has known polarisation); $\langle L_a 1 L_a' -1|n0\rangle$ is a Clebsch-Gordan coefficient; $W(jjL_aL_a';nj_a)$ is a Racah coefficient; $P_n(\cos\theta)$ is an n^{th} order Legendre polynomial; and $P_n^{(2)}(\cos(\theta))$ is an n^{th} order associated Legendre polynomial; j_1, j and j_2 correspond to the initial, intermediate and final state spin, respectively; L_1 and L_2 are the excitation and de-excitation γ-ray multipolarities, respectively; and $\sigma_1 = 0$ for electric transitions, $\sigma_1 = 1$ for magnetic transitions. The angles in Eq. (5.5) are defined as follows: (i) θ is the angle of the emitted radiation with respect to the direction of the incoming photon ray beam. (ii) ϕ is the angle between the polarisation plane of the incoming radiation (the horizontal plane in our experiment), and the plane defined by the direction of the incoming γ-ray beam and the normal to the plane defined by the incoming γ-ray beam and the emitted radiation direction. A sample decay scheme and the angles θ and ϕ are shown in Fig. 5.7.

The angular correlations for the most important spin sequences of relevance in the present work are given below (the three J^π values refer to the sample ground state (0^+), the intermediate excited

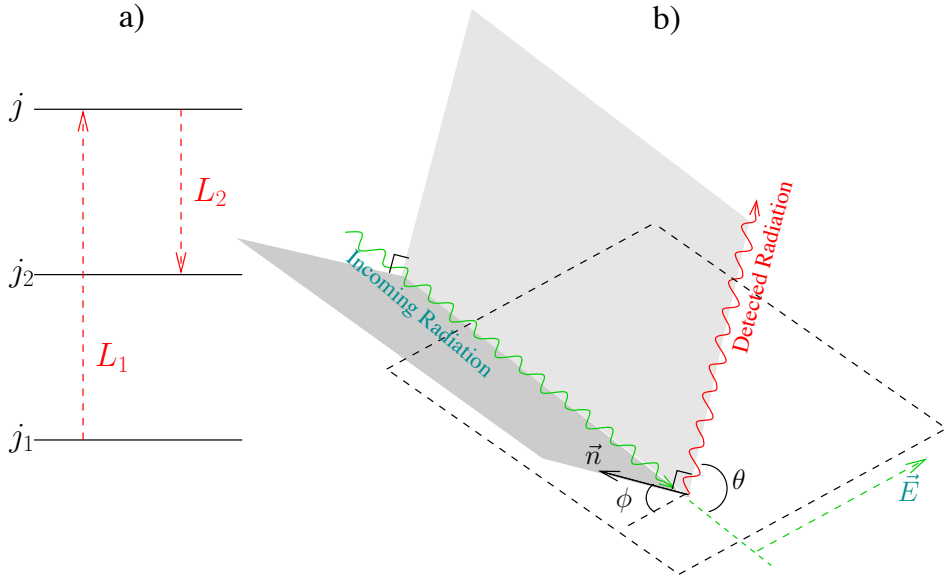

Figure 5.7: (a) Sample level scheme, showing excitation and de-excitation of a nucleus. (b) Definition of the coordinate system used in Eq. (5.5). The angle θ is defined as the angle between the emitted radiation and the incoming γ-ray beam. Angle ϕ is the angle between the polarisation plane of the incoming γ-ray beam, and the plane defined by the direction of the incoming γ-ray beam and the normal to the plane defined by the incoming γ-ray beam and the emitted radiation direction. For example, if the emitted γ-ray is detected in a counter located in the horizontal plane, $\phi = 90°$.

state, and the final state, respectively):

$$0^+ \to 1^\pm \to 0^+ : \qquad W_{\text{theory}}(\theta,\phi) = 1 + \frac{1}{2}\left[P_2(\cos\theta) + \frac{1}{2}(-1)^{\sigma_1} P_2^{(2)}(\cos\theta)\cos(2\phi)\right] \tag{5.6}$$

$$\begin{aligned} 0^+ \to 2^\pm \to 0^+ : \qquad W_{\text{theory}}(\theta,\phi) =& 1 + \left[\frac{5}{14}P_2(\cos\theta) + \frac{8}{7}P_4(\cos\theta)\right] \\ & - (-1)^{\sigma_1}\left[\frac{5}{28}P_2^{(2)}(\cos\theta) - \frac{2}{21}P_4^{(2)}(\cos\theta)\right]\cos(2\phi) \end{aligned} \tag{5.7}$$

$$0^+ \to 1^\pm \to 2^+ : \qquad W_{\text{theory}}(\theta,\phi) = 1 + \frac{1}{20}\left[\frac{1}{10}P_2(\cos\theta) + \frac{1}{\sqrt{2}}(-1)^{\sigma_1} P_2^{(2)}(\cos\theta)\cos(2\phi)\right] \tag{5.8}$$

For the detector positions shown in Fig. 5.7, Eqs. (5.6)–(5.8) yield values for $W_{\text{theory}}(\theta,\phi)$ that are listed in Tab. 5.2. Finite solid angle effects were accounted for using Monte Carlo simulations. The adjusted, experimentally expected, angular correlations $W_{\text{adj}}(\theta,\phi)$ are also listed in Tab. 5.2.

Sequence	$W_{\text{theory}}(\theta,\phi)$			$W_{\text{adj}}(\theta,\phi)$		
	H	V	O	H	V	O
$0^+ \rightarrow 1^+ \rightarrow 0^+$	1.50	0	1.50	1.47	0.04	1.47
$0^+ \rightarrow 1^- \rightarrow 0^+$	0	1.50	0.75	0.04	1.47	0.75
$0^+ \rightarrow 2^+ \rightarrow 0^+$	2.50	0	0	2.36	0.07	0.08
$0^+ \rightarrow 2^- \rightarrow 0^+$	0	2.50	1.25	0.06	2.31	1.22
$0^+ \rightarrow 1^+ \rightarrow 2^+$	1.05	0.90	1.05	1.05	0.90	1.05
$0^+ \rightarrow 1^- \rightarrow 2^+$	0.90	1.05	0.975	0.90	1.05	0.97

Table 5.2: Angular correlations for spin sequences that are relevant for the present analysis. The detectors were placed as follows: the horizontal detector ("H") at $(\theta,\phi) = (90°, 90°)$; the two vertical detectors ("V") at $(\theta,\phi) = (90°, 0°)$; and the out-of-plane detector ("O") at $(\theta,\phi) = (135°, 90°)$ (see Fig. 5.7). Columns 2, 3, and 4 list the theoretical angular correlations, calculated using Eq. (5.5). Columns 5, 6, and 7 show the adjusted angular correlations, $W_{\text{adj}}(\theta,\phi)$, accounting for finite detector and sample solid angle effects.

In order to better visualise the angular correlations, expected radiation patterns for sample spin sequences are shown in Fig. 5.8. Consider first the sequence $0^+ \rightarrow 1^- \rightarrow 0^+$, shown in the upper left panel of Fig. 5.8. No intensity is observed by the horizontal detector (H), maximum intensity is observed by the vertical detector (V), and some intensity is observed by the out-of-plane detector (O). A very different radiation pattern is observed for the spin sequence $0^+ \rightarrow 1^+ \rightarrow 0^+$ (upper right panel). Maximum intensity is now observed in both the horizontal and out-of-plane detectors, and no intensity is observed in the vertical detector. Consider now, the $0^+ \rightarrow 2^+ \rightarrow 0^+$ sequence (lower left panel). The vertical and horizontal detectors observe the same intensity ratios as for the $0^+ \rightarrow 1^+ \rightarrow 0^+$ spin sequence, and thus could not distinguish the excitation of a $J^\pi = 1^+$ or 2^+ intermediate state based on these two detectors alone. This was the reason why a detector was placed out of the vertical plane: it detects no intensity for a 2^+ intermediate state, whereas maximum intensity is observed for a 1^+ intermediate state. The radiation patterns are distinct, and lead to unambiguous spin-parity assignments for the intermediate (excited ^{26}Mg) state.

5.4 Procedure and Results

Incident beam energies of $E_\gamma = 10.8$, 11.0, 11.2 and 11.4 MeV were used to populate excited states in ^{26}Mg. For each energy, the beam was incident on the sample for approximately 11 hours. Additionally, measurements were performed on a natural $^{\text{nat}}$MgO sample at the same incident photon

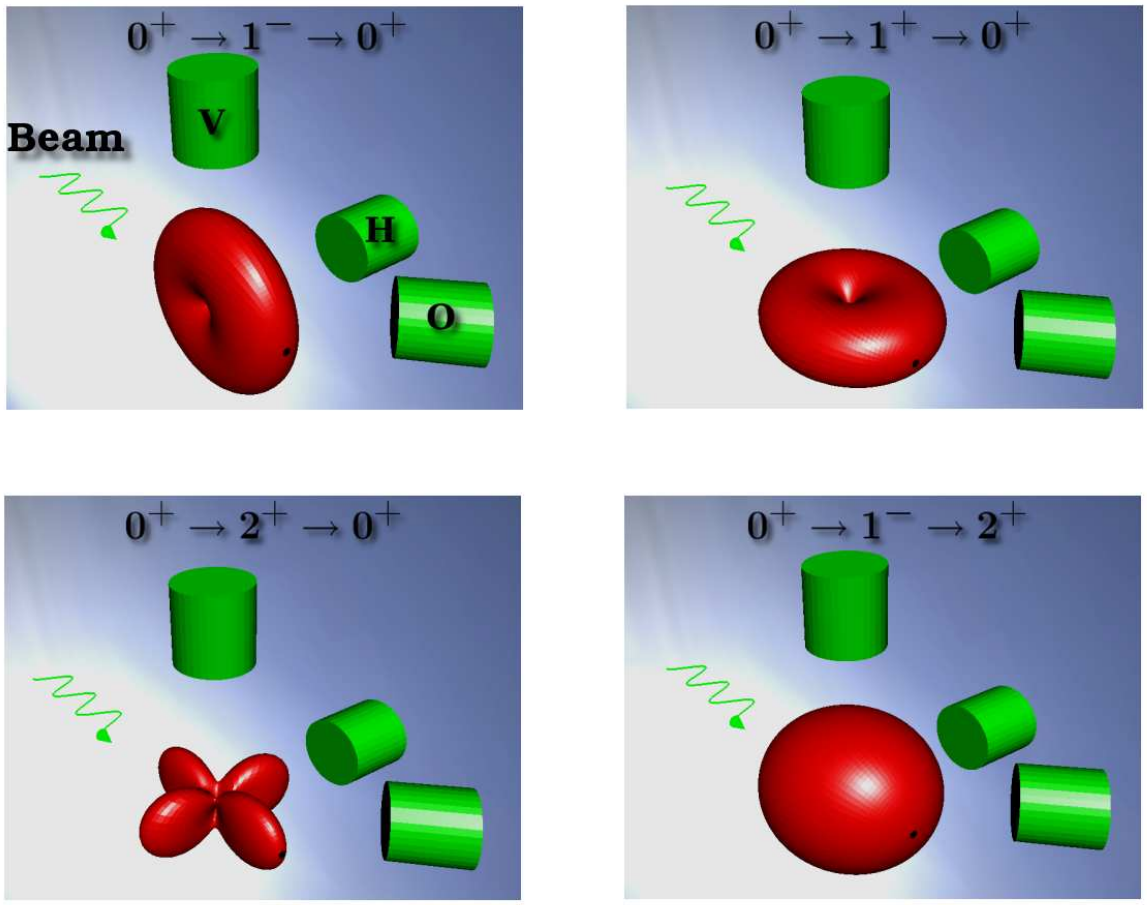

Figure 5.8: The angular correlation distributions for sample spin sequences: $0^+ \rightarrow 1^- \rightarrow 0^+$, $0^+ \rightarrow 1^+ \rightarrow 0^+$, $0^+ \rightarrow 2^+ \rightarrow 0^+$, and $0^+ \rightarrow 1^- \rightarrow 2^+$. The labels refer to the detector position ("V": vertical plane; "H": horizontal plane; and "O": out-of-plane). The out-of-plane detector is shown at $\theta = 45°$ rather than $\theta = 135°$ for reasons of clarity (the distributions are symmetric around $\theta = 90°$).

beam energies as for the ^{26}MgO sample, but for only half of the acquisition time. These data are important for two purposes: (i) for background peak identification from sample impurities, particularly from ^{24}Mg, as well as from the container; and (ii) for the detector energy calibration. The background runs helped us to unambiguously assign observed transitions to ^{26}Mg. The beam energy spread had a full width at half maximum of about 2%, corresponding to 200 keV at $E_\gamma = 11.0$ MeV. This resolution was determined by first inserting beam attenuators into the photon beam to reduce the flux to acceptable limits, and then inserting the 135% HPGe detector. The beam energy spread could be extracted from the high-energy part of the detected spectrum, which was least affected by the detector response (that is, from Compton scattered events and pair-production γ-rays).

5.4.1 Detector Calibrations

Energy calibrations of the HPGe detectors were performed using room background lines and with nuclear reactions. Well-known room background lines below 3 MeV (^{40}K, ^{208}Tl) were used as low energy calibration points. In addition, spectra using $^{\text{nat}}$MgO were recorded by populating the well-known ^{24}Mg excited state at $E_x = 9967.8(3)$ keV, which decays to the first excited state at $E_x = 1368.675(6)$ keV [End90] with the emission of nearly isotropic radiation. This isotropic radiation yields a further energy calibration point.

During the experiment, gain instabilities caused peaks to shift in the spectrum several times. Fig. 5.9 shows an example of this gain shift. These shifts meant that the calibration from ^{24}Mg could not be used without first applying a correction to the spectra recorded each day. In the experiment, there were two sets of runs: the calibration run in which decays from ^{24}Mg were observed, and the data runs containing room background lines. The data runs could initially be calibrated so that all background peak channels (C_i, where i refers to the run number) coincide with the calibration run channels (C_{cal}). The second energy calibration using room background and ^{24}Mg could then be applied.

The initial calibration between data runs, i, and calibration run was performed according to

$$C_{\text{cal}} = a_i C_i + b_i, \tag{5.9}$$

where a_i and b_i are the calibration coefficients needed to shift the channels of each run, i, to those of the calibration run. The energy, E, is related to the calibration run through:

$$E = aC_{\text{cal}} + b \tag{5.10}$$

Combining these equations gives an expression with which each run can be individually calibrated:

$$E = a_i a C_i + (ab_i + b) \tag{5.11}$$

The parameters are obtained through separate linear model least-squares fits of known background γ-ray lines and the one γ-ray observed in ^{24}Mg(γ,γ'). The known background lines used were from

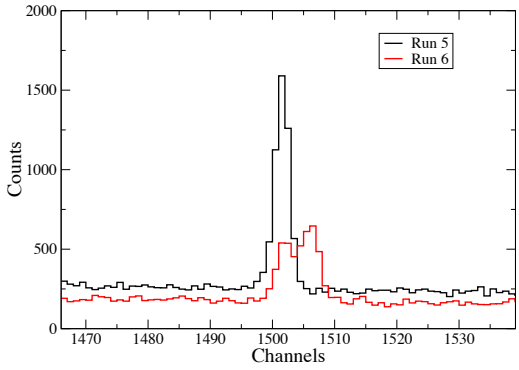

Figure 5.9: Effect of gain shift on detected peaks. The shift occurred during run number 6, and occurred suddenly because two distinct peaks are visible for that run. This shift appears in all detectors. The cause of such shifts has not been found.

^{208}Tl at $E_\gamma = 1460.851(6)$ keV [Cam04], and from ^{40}K at $E_\gamma = 2614.529(10)$ keV [Mar07].

Detector efficiencies must be known in order to obtain spin-parity assignments and decay branching ratios. A combination of radioactive source measurements and Monte-Carlo simulations was used to obtain the full-energy peak efficiencies of the detectors (escape peaks were not used in the analysis). The radioactive sources used were ^{60}Co and ^{56}Co, which yield efficiencies up to about $E_\gamma = 3.5$ MeV. The sum-peak method [Kim03] was used with ^{60}Co to obtain absolute efficiencies, independent of source activities.

Coincidence summing also occurs in the efficiency measurement of decays from ^{56}Co. In this case, however, the effect can be assumed to be negligible because the decay is highly fragmented and the solid angles of the detectors are relatively small. For example, in the ^{60}Co spectrum for detector 1, the number of counts observed in the sum-peak ($E_\gamma = 1173 + 1332$ keV) was 0.2% of the number of counts in the $E_\gamma = 1173$ keV peak. Any summing out effects, where counts are lost from a peak caused by coincidence summing, will therefore be negligible. The ^{56}Co full energy peak efficiencies were then normalised to those measured with ^{60}Co. The photo-peak efficiency of a detector can be approximated by [Tra99]:

$$\ln\left(\varepsilon_\gamma^p\right) = a + b\ln(E_\gamma) + c\ln(E_\gamma)^2, \tag{5.12}$$

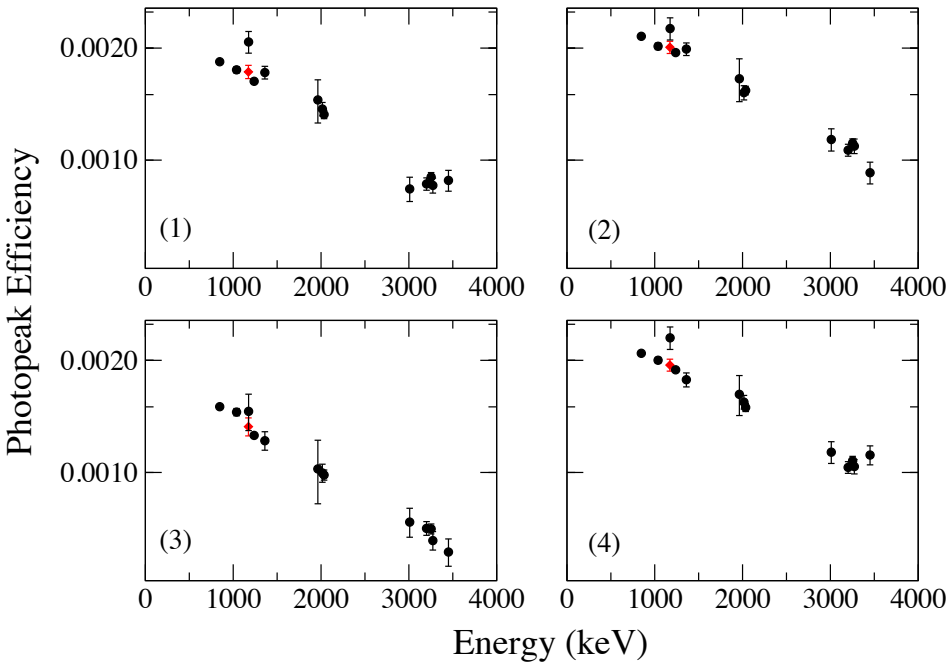

Figure 5.10: The full energy peak efficiencies of the four detectors used for the quantum number assignments of excited states in ^{26}Mg. Detector 3 has consistently lower efficiencies because of its 45° placement; the diameter of the beam pipe requires that the detector is moved to a further distance from the sample.

This approximation for the photo-peak efficiency is fit to the ^{56}Co data. The value of the fit at $E_{\gamma} = 1173$ keV was used to normalise the ^{56}Co efficiencies to the ^{60}Co data. The normalised photo-peak efficiencies of the four detectors are shown in Fig. 5.10.

Monte Carlo simulations were then used to extrapolate full-energy peak efficiencies to higher energies covered in the present experiment. The Monte-Carlo code used for this experiment was Geant4 [Ago03]. A schematic of the geometry used in the simulation is shown in Fig. 5.11. The entire setup, including all four detectors was included in the simulations. This accounted for Compton scattered γ-rays from one detector to another. The beam pipe was also included in the simulations to account for scattering of beam photons into the detectors. The effect of atomic absorption of γ-rays in the sample was accounted for by including an extended MgO source, which emitted γ-ray s isotropically.

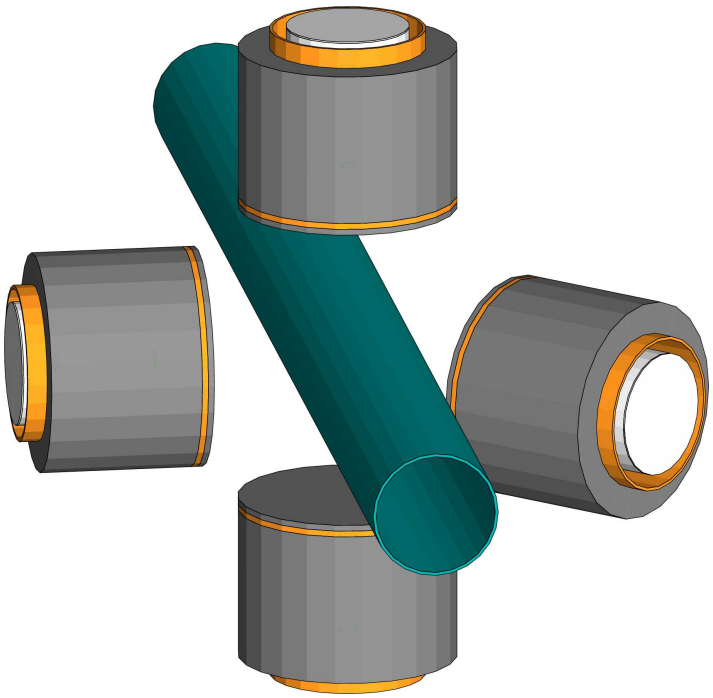

Figure 5.11: Geometry used in the Geant4 efficiency simulations. See text for details.

Simulations were performed at a variety of energies, up to about 12 MeV. Two separate simulations for ^{60}Co were also performed. One using an extended source, and one for a point source, to simulate the radioactive source measurements. This enables the correction of the source measurements to allow for a finite sample size. The simulated efficiencies can then be normalised to the radioactive source measurements. The normalisation factors needed to match simulated efficiencies with experimental efficiencies are shown in table 5.3. In addition to an absolute normalisation of simulated efficiencies, the normalisation as a function of energy was calculated. If the normalisation is not constant over the energy range covered by radioactive sources, the geometry used in the simulation does not accurately reflect that of the true detector setup and efficiencies cannot be reliably extrapolated to high energies. Figure 5.12 shows the ratio of simulated and experimental photo-peak efficiencies for ^{56}Co as a function of energy, which shows a slope consistent with unity. The simulated efficiencies, therefore, agree with experimental efficiencies. To reduce the uncertainties in the fit, a more extensive study would be required, which is outside the scope of the current project.

The results of the simulations are shown in figure 5.13. Detection efficiencies for individual full-

Detector	Normalisation	
	ε^p	ε^T
1	1.0157	1.0538
2	1.0668	1.0730
3	1.0368	1.1556
4	0.9513	1.0299

Table 5.3: The normalisation factors needed to match simulated and experimental efficiencies.

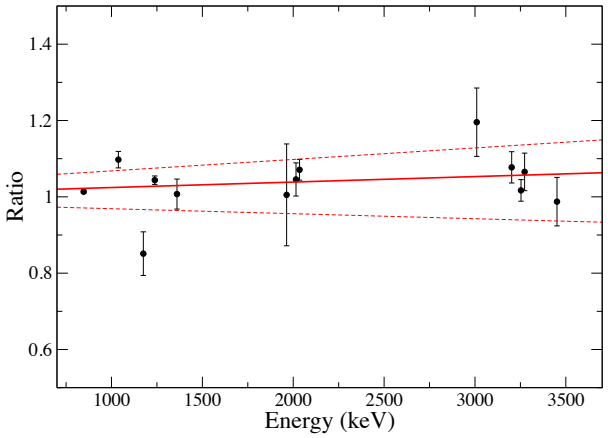

Figure 5.12: Ratio of simulated and experimental peak efficiencies versus energy. The solid line represents a linear fit to the ratios, while the dotted lines represent the uncertainties of the fit. The fit parameters for the equation $R = aE + b$ are $a = 1.4(1.6) \times 10^{-5}$ and $b = 1.010(20)$.

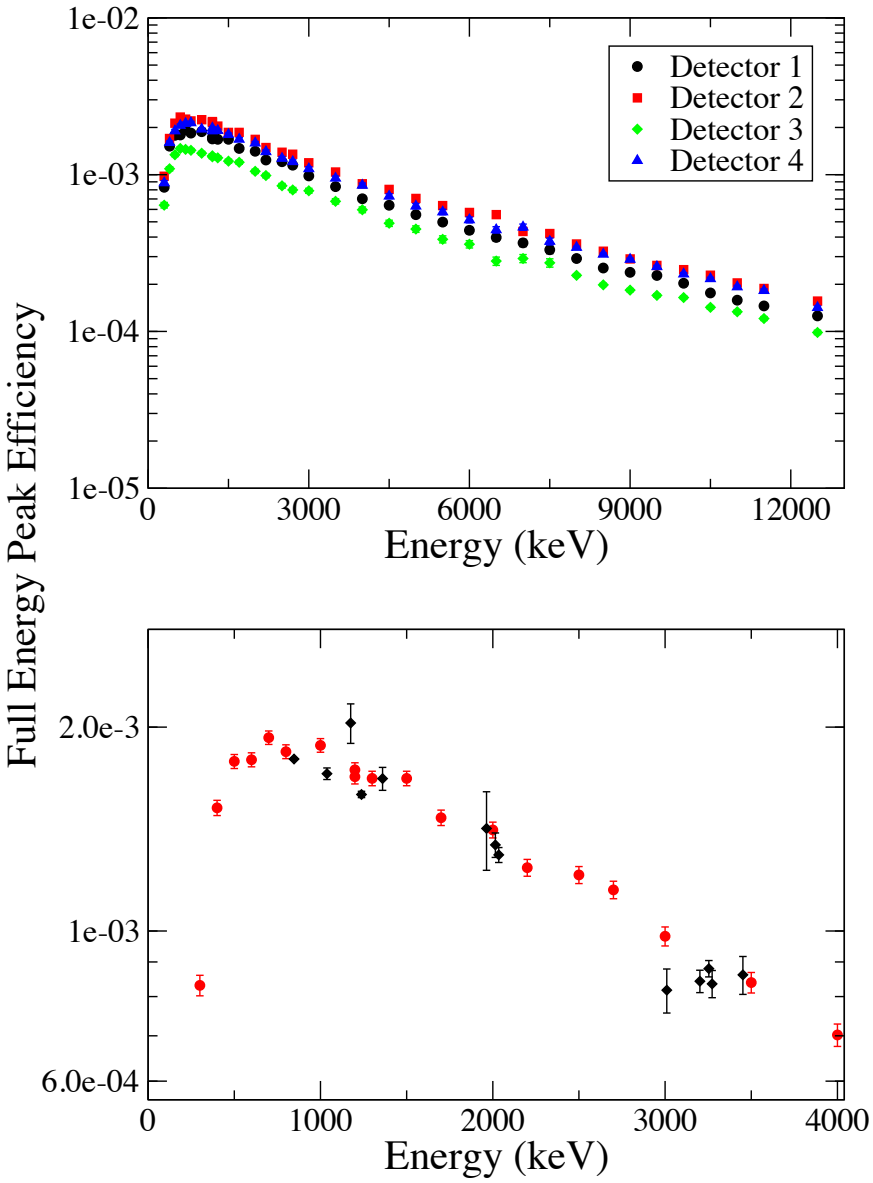

Figure 5.13: Peak efficiencies for the four 60% HPGe detectors, as simulated in Geant4 (upper panel). These efficiencies have been normalised to the ^{60}Co experimental point at $E_\gamma = 1173$ keV, which in turn is corrected for finite sample size. Differences in absolute magnitude of efficiency are because of differences in detector sizes, as shown in table 5.1. The lower panel shows the agreement of simulated efficiencies with measured ^{56}Co photo-peak efficiencies for detector 1.

energy peaks were obtained by cubic spline interpolation between simulated full-energy peak efficiencies. The uncertainty of full-energy peak efficiencies near $E_\gamma = 11$ MeV, arising from uncertainties in both detector geometry and other experimental uncertainties were assumed to be 5%.

5.4.2 Excitation Energies

All γ-ray energies measured in the experiment were corrected for both recoil shift and Doppler shift. The recoil shift reduces the energy of an emitted γ-ray because momentum and energy conservation dictates that as an excited nucleus decays, it must recoil in the opposite direction to the γ-ray emission with some share of the decay energy. By considering the centre of mass before and after the decay, one obtains for energy and momentum:

$$E_x = E_B + E_\gamma \tag{5.13}$$

$$0 = \frac{E_\gamma}{2} + \sqrt{2 m_B E_B}, \tag{5.14}$$

where $E_x = E_i - E_f$ is the energy difference between initial, E_i, and final, E_f, states; E_γ is the detected γ-ray energy; m_B is the mass of the decaying nucleus; and E_B is the energy of the recoiling nucleus. Solving these equations, the transition energy is:

$$E_x = E_\gamma + \frac{E_\gamma^2}{2 m_B c^2} \tag{5.15}$$

For calibration purposes, γ-ray energy is required and Eqn. (5.15) can be rearranged into a Taylor series, with the result

$$E_\gamma \approx E_x - \frac{E_x^2}{2 m_B c^2} \tag{5.16}$$

The Doppler shift of emitted γ-rays occurs because the excited nucleus will have momentum in the direction of the photon beam (provided that is does not slow down before decaying). The out-of-plane detector will therefore measure a smaller γ-ray energy. The Doppler shift of a γ-ray with energy E_γ, detected at angle θ is given by:

$$\Delta E_D = \frac{v}{c} E_\gamma \cos\theta, \tag{5.17}$$

where v is the velocity of the recoiling nucleus. Using the momentum conservation in Eqn. (5.14), the Doppler shift becomes:

$$\Delta E_D = \frac{E_\gamma}{m_B c^2} \cos\theta \tag{5.18}$$

Peak energies were obtained from the centre-of-mass (first moment) of each peak in the spectra. This method is preferable to fitting a Gaussian because of the low number of counts in the peaks. The peaks are not normally distributed for low count rates, so the centroid of a peak and its uncertainty are defined by:

$$C = \frac{\sum_{i=1}^{n} x_i y_i}{\sum_{i=1}^{n} y_i} \tag{5.19}$$

$$\sigma_c = \sqrt{\frac{\sum_{i=1}^{n} y_i (x_i - C)^2}{(n-1)\sum_{i=1}^{n} y_i}} \tag{5.20}$$

where x_i is the energy of channel i ($i = 1$ corresponds to the first channel of the peak), and y_i is the number of counts in that channel.

To obtain the excitation energy, a weighted average of the excitation energies obtained from all detectors was performed. The uncertainties in observed γ-ray energies arise from statistical uncertainties and uncertainties in the energy calibration. Almost every ground state transition that was observed was accompanied by one or more de-excitations to intermediate states. The excitation energy uncertainties could be reduced by including the energies of these intermediate state transitions. For each transition observed, the γ-ray energy was corrected for the recoil and Doppler shifts. Table 5.4 shows the comparison between the presently derived excitation energies and the literature values. It can be seen the the new E_x values agree with previous results, but the uncertainties are significantly smaller.

5.4.3 Quantum Numbers and Branching Ratios

Quantum numbers of the observed states were assigned by analysing the observed radiation pattern. Note that intensity was was observed at the locations where the theoretical angular correlation $W(\theta, \phi)$ is zero because of finite solid angle effects. Such effects were modelled using Monte Carlo simulations (Sec. 5.4.1) and could be accounted for.

The efficiency corrected measured full energy peak intensities, normalised to the theoretical angu-

Excitation Energy (keV)				
Present	[End98]	[KÖ2]	[Uga07]	[Sch09]
10573.3 (8)	10567 (3)			
10647.3 (8)	10646 (2)			10648.8 (5)
10805.7 (7)	10805.9 (4)		10808 (20)	
10949.1 (8)	10945 (3)		10953 (25)	
11153.5 (10)	11153.2 (2)	11153.386 (86)		11153.8 (12)

Table 5.4: Excitation energies in ^{26}Mg for states populated in the present experiment. Shown also are the excitation energies reported in the literature. Excitation energies from Ref. [End98] are compiled from original sources.

lar correlations for each ground state transition are shown in Tab. 5.5. Comparison to the $W_{\text{adj}}(\theta, \phi)$ values listed in Tab. 5.2 was performed by normalising the highest observed intensity to the adjusted theoretical angular correlation expected in that detector. The normalisation was performed in this way because $W_{\text{adj}}(\theta, \phi)$ describes the theoretical scaling of detected intensities between detectors for a chosen spin-sequence. After normalisation, comparison of observed intensities with the theoretical angular correlations in Tab. 5.2 immediately reveals the spin sequence that gives rise to the observed intensities. These comparisons are shown in Fig. 5.14 for four of the ground state transitions listed in Tab. 5.5. The unambiguous J^π assignments are consistent with previous J^π assignments or restrictions, except for one case (see below). Branching ratios were calculated from the observed peak intensities and corrected for angular correlations and detector efficiencies. Table 5.6 shows the branching ratios observed in the experiment. They agree with previous measurements [Ber84, Wal92], with one exception that is discussed below. In addition, the relatively low background from the monoenergetic γ-ray beam allowed for resolving additional, weaker decay branches of populated states. The observed decay schemes for each incident beam energy are shown in Figs. 5.16-5.19.

Sample spectra, which were recorded at a beam energy of 11.2 MeV for approximately 11 hours, are shown in Fig. 5.15. The decay of two states at $E_x = 11154$ keV and $E_x = 10949$ keV is observed, which will be used to illustrate the assignment of quantum numbers to excited states. Decay of the populated state at $E_x = 11154$ keV is observed to the ground state (0^+) as well as the excited state at $E_x = 3589$ keV (0^+). Approximately equal intensity (after proper efficiency corrections) is found in the horizontal and out-of-plane detectors, and no intensity in the vertical detectors. According to the

Present Results					Literature J^π Assignments			
E_x	I_H	I_V	I_O	J^π	[End98]	[Gla86]	[Uga07]	[Sch09]
10573	≤ 1.2	1.47 (3)	≤ 1.3	1^-				
10647	1.45 (3)	0.044 (9)	1.47 (3)	1^+	1^+			1^+
10805	≤ 0.5	1.47 (4)	≤ 0.9	1^-	$(0^+ - 4^+)$		N	
10949	≤ 0.4	1.47 (1)	0.6 (3)	1^-		$(4-7)$	N	
11154	1.47 (9)	0.015 (7)	1.44 (9)	1^+	1^-			1

Table 5.5: Observed ground state transition intensities (efficiency corrected) and resulting quantum numbers for excited states in ^{26}Mg; $I_{H,V,O}$ refers to the relative intensity (normalised to the angular correlations) observed in the horizontal, vertical and out-of-plane detector, respectively; the label, "N", refers to natural parity (i.e., $J^\pi = 0^+, 1^-, 2^+, \ldots$). The upper limits listed here correspond to 90% Gaussian confidence limits.

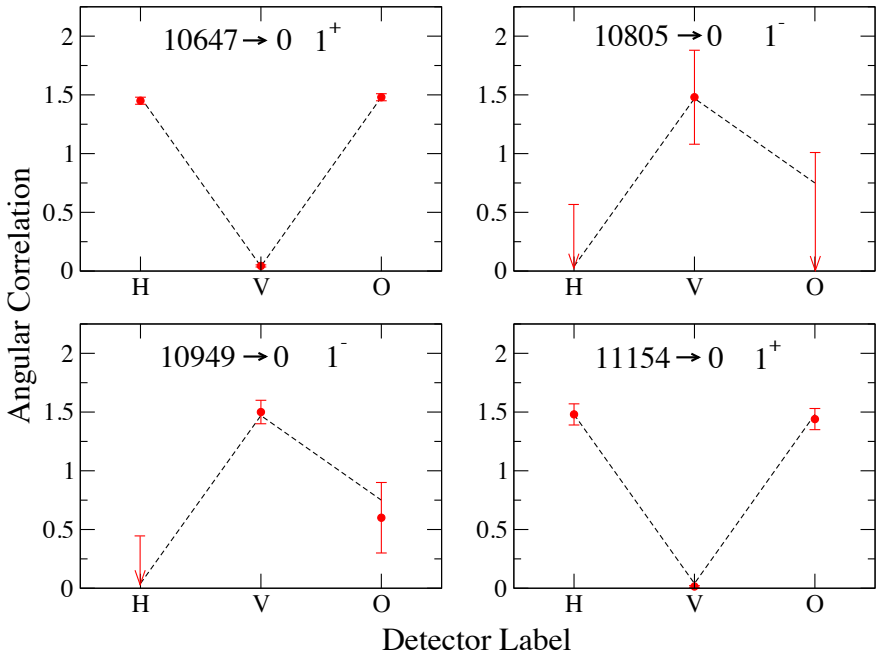

Figure 5.14: Efficiency corrected, measured intensities (circles) for the four ground state transitions listed in Tab. 5.5 compared to the adjusted theoretical angular correlations (dashed lines) from columns 5, 6, and 7 in Tab. 5.2 for the assigned spin-parities. The measured intensities are normalised so that the highest intensity for each transition equals the maximum adjusted theoretical angular correlation. Upper limit assignments are indicated with arrows.

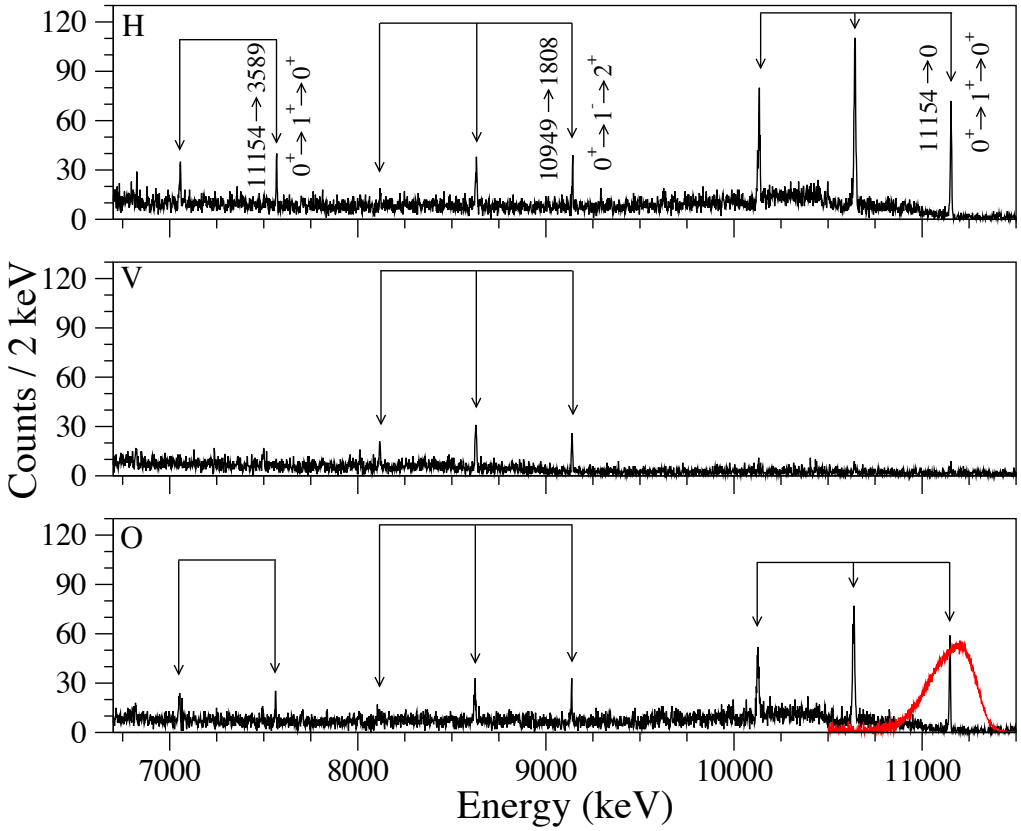

Figure 5.15: Observed spectra in the horizontal ("H"), vertical ("V"), and out-of-plane ("O") detectors, recorded with a γ-ray beam energy of $E_\gamma = 11.2$ MeV. Decays to the ground state and excited states are shown from the $E_x = 11154$ keV (1^+) and $E_x = 10949$ keV (1^-) states. The broad peak in the lower panel is the beam profile obtained from the zero degree detector (arbitrary scale). See the text for more discussion.

		Initial Excited State, E_{x_i} (keV), J_i^π				
		10573	10647	10806	10949	11154
E_{x_f} (keV)	J_f^π	1^-	1^+	1^-	1^-	1^+
0	0^+	0.47 (10)	0.876 (27)	0.218 (61)	0.138 (19)	0.688 (81)
1809	2^+		0.0155 (18)	0.782 (87)	0.572 (29)	0.029 (4)
2938	2^+		0.0636 (30)		0.135 (13)	
3589	0^+				0.047 (7)	0.110 (22)
4333	2^+				0.108 (96)	0.077 (11)
4972	0^+	0.528 (91)	0.0162 (13)			0.096 (24)
5292	2^+		0.0163 (13)			
7100	2^+		0.0124 (12)			

Table 5.6: Observed branching ratios from excited states in ^{26}Mg. The initial excitation energy, E_{x_i}, spin-parity, J_i^π, and branching ratio, B_γ, are from the present work. The final excitation energy, E_{x_f}, and spin-parity, J_f^π, are from Ref. [End90].

expected angular correlations, summarised in Tab. 5.2 and shown in Fig. 5.8, both of these observed γ-rays must arise from a $0^+ \rightarrow 1^+ \rightarrow 0^+$ spin sequence and the state is thus assigned $J^\pi = 1^+$. Decay from the $E_x = 10949$ keV excited state to the first excited state at $E_x = 1809$ keV ($J^\pi = 2^+$) can also be seen in Fig. 5.15. This decay is observed with similar intensity in all detectors. The radiation pattern is consistent with an expected pattern for a $0^+ \rightarrow 1^- \rightarrow 2^+$ spin sequence (Tab. 5.2 and Fig. 5.8). Thus, this state can be assigned an unambiguous spin-parity of $J^\pi = 1^-$.

5.5 Discussion

Five excited states were observed in this experiment. The relatively low beam induced background at the HIγS facility, coupled with good separation of states, allowed for observation of very weak branching ratios (Tab. 5.6) and for the assignment of unambiguous quantum numbers for every excited state observed in the study. Previously, two of the states had unknown quantum numbers, and large energy uncertainties, which have now been determined with significantly improved precision. One additional state had previously assigned quantum numbers, which are shown to be inconsistent with the current results. A detailed discussion of individual states follows below.

The state observed at $E_x = 10573$ keV was previously been observed at $E_x = 10567(3)$ keV in inelastic proton scattering [Mos76]. The quantum numbers of the state have been determined to be

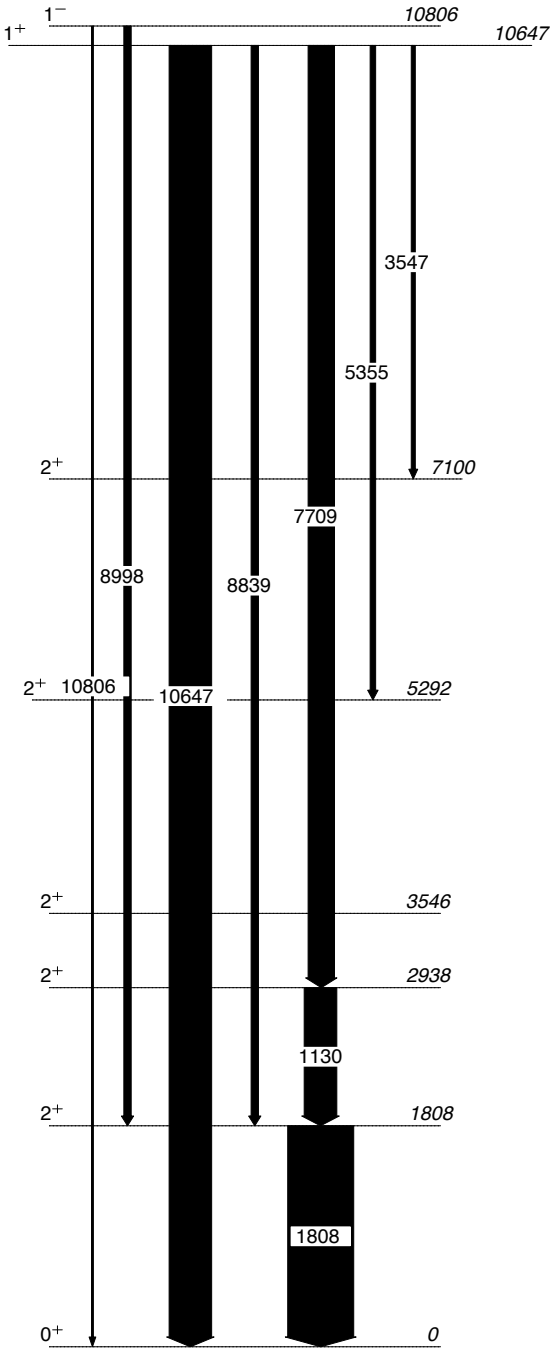

Figure 5.16: The observed decay scheme of ^{26}Mg obtained with an incident γ-ray beam energy of $E_\gamma = 10.8$ MeV. The observed intensities (corrected for detector efficiencies) are proportional to the displayed arrow widths. For clarity, the 10647 keV γ-ray is displayed with one tenth of its true intensity. The displayed γ-ray energies are approximate in this figure.

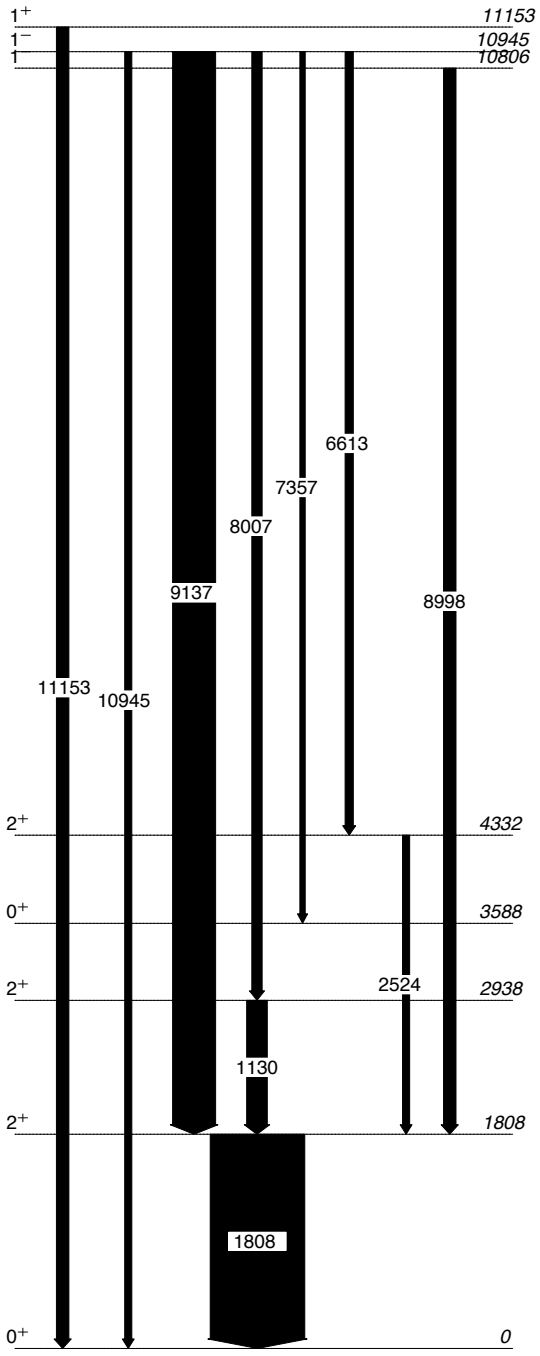

Figure 5.17: The observed decay scheme of ^{26}Mg obtained with an incident γ-ray beam energy of $E_\gamma = 11.0$ MeV. The observed intensities (corrected for detector efficiencies) are proportional to the displayed arrow widths. The displayed γ-ray energies are approximate in this figure.

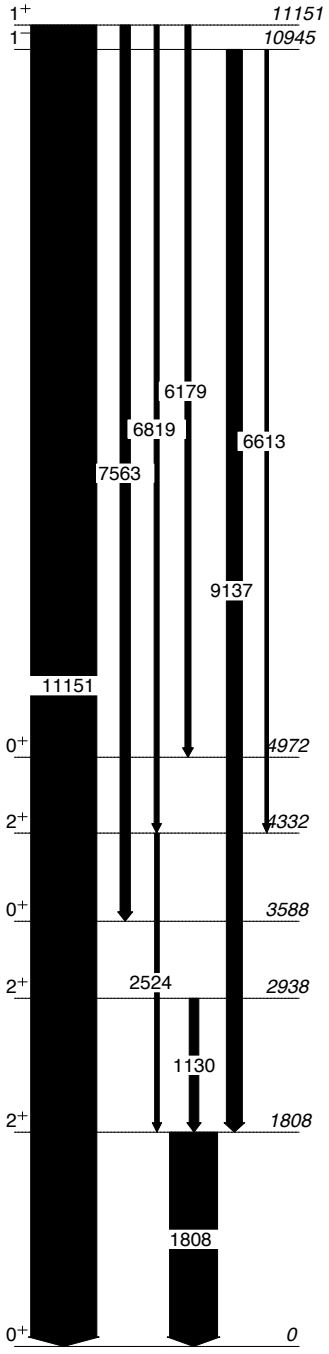

Figure 5.18: The observed decay scheme of ^{26}Mg obtained with an incident γ-ray beam energy of $E_\gamma = 11.2$ MeV. The observed intensities (corrected for detector efficiencies) are proportional to the displayed arrow widths. The displayed γ-ray energies are approximate in this figure.

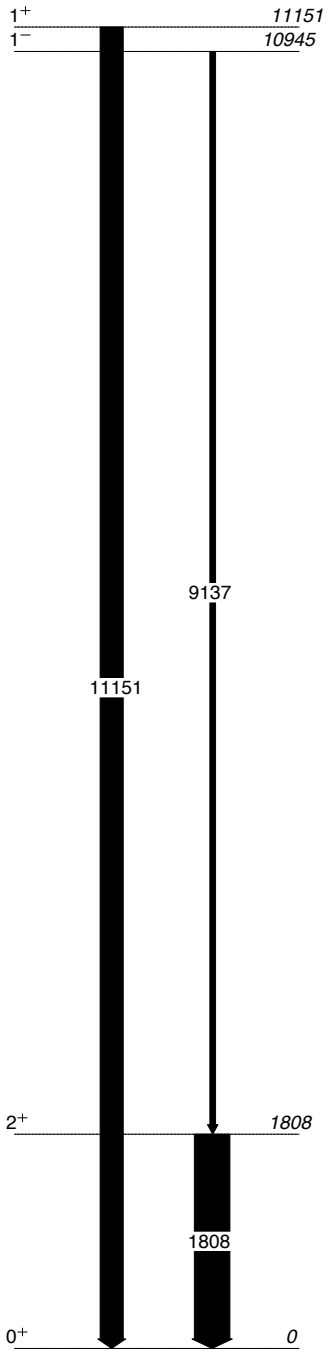

Figure 5.19: The observed decay scheme of ^{26}Mg obtained with an incident γ-ray beam energy of $E_\gamma = 11.4$ MeV. The observed intensities (corrected for detector efficiencies) are proportional to the displayed arrow widths. The displayed γ-ray energies are approximate in this figure.

$J^\pi = 1^-$ in the present experiment, where none were assigned previously. Branching to the ground state and to the excited state at $E_x = 4972$ keV were observed for the first time in the present work.

The state at $E_x = 10647$ keV has previously been observed at $E_x = 10646(2)$ keV with $J^\pi = 1^+$ and a mean lifetime of $\tau_m = 110(30)$ [End98], and by Ref. [Sch09] at $E_x = 10648.8(5)$ keV. The current analysis agrees with the energy and quantum number assignments for this state. Only the ground state transition has previously been measured by Berg *et al*. [Ber84]. In total, five decays from this level were resolved, the strongest of which is the ground state transition, with a branching ratio of 87.6 (27)%.

The state at $E_x = 10806$ keV was previously observed in a thermal neutron capture experiment on ^{25}Mg at $E_x = 10805.9(4)$ keV [Wal92] and in α-particle transfer measurements on ^{22}Ne at $E_x = 10808(20)$ keV [Uga07]. The neutron capture experiment placed restrictions on this state's quantum numbers by observing the decay to the first excited state. The α-particle transfer work assigned natural parity. In the present work, an unambiguous $J^\pi = 1^-$ assignment is obtained, consistent with the literature restrictions. The observed decay scheme agrees with that of Ref. [Wal92], but resolves an additional weak branch to the ground state.

Levels near the $E_x = 10950$ keV state have previously been observed in three experiments: ^{26}Mg(p,p′)^{26}Mg at $E_x = 10950$ keV [Mos76], ^{22}Ne(^{6}Li,d)^{26}Mg at $E_x = 10953(25)$ keV [Uga07], and ^{23}Na(α,pγ)^{26}Mg at $E_x = 10943(2)$ keV [Gla86]. The current unambiguous assignment of $J^\pi = 1^-$ is consistent with the natural parity assignment made in the α-particle transfer measurement, but is inconsistent with the decay observed in Ref. [Gla86]. That work reports secondary decays to $E_x = 7953$ keV ($J^\pi = 5^-$) with a branching ratio of 64.5%, and to $E_x = 9169$ keV ($J^\pi = 6^-$) with a branching ratio of 36.5%. Empirical rules [End90] lead to $J^\pi = (4^+ - 7^-)$ for the decaying state. Giesen *et al*. [Gie93] also observed a state at 10.95 MeV, and assigned J$^\pi = (2^+, 3^-, 4^+)$. The most likely explanation for the disagreement to the present J^π assignment is the presence of a doublet at this energy, as suggested by Ref. [Uga07]. Since there is not enough information to determine which of these states has the large α-particle width seen by Ref. [Uga07], ^{22}Ne+α thermonuclear reaction rate calculations should be performed using the observed α-particle width as an upper limit for both states.

The excited state observed at $E_x = 11154$ keV corresponds to a ^{22}Ne(α,n)^{25}Mg resonance at

$E_r(\text{lab}) \approx 630$ keV, believed to have been seen by Refs. [Dro91, Har91], but later proven to be caused by background from ^{11}B [Dro93]. An expected resonance at this location has since been treated as the most important expected contribution to the ^{22}Ne(α,n)^{25}Mg reaction rate, and has been searched for repeatedly [Gie93, Jae01b, Dro93, Uga07]. A state near this energy has also been observed through inelastic proton scattering at $E_x = 11156$ keV [Mos76] and $E_x = 11150$ keV [Cra89], photo-neutron studies at $E_x = 11153.8$ keV [Ber69], neutron capture on ^{25}Mg at $E_x = 11153.387(86)$ keV [KÖ2], and photo-excitation experiments [Ber84, Sch09]. The proton scattering experiment of Ref. [Mos76] and photo-excitation experiments did not assign quantum numbers, but the work of Ref. [Ber69] suggested a spin-parity of $J^\pi = 1^-$. Ref. [Cra89] made a spin-parity assignment of $J^\pi = 1^+$. However, excitation energy uncertainties of about 60 keV in that experiment lead to ambiguity regarding which excited state was observed. In the current work, this state was observed with very good statistics and energy resolution, as shown in Fig. 5.15. The present angular correlation measurements using 100% linearly polarised photon beam assign an unambiguous $J^\pi = 1^+$ value to this level. This finding is significant since it rules out any contributions of this unnatural parity level to the ^{22}Ne+α reaction rates. No branchings to secondary excited states were observed in other experiments. A total of four branchings were observed from this level (Tab. 5.6).

5.6 Conclusion

The ^{22}Ne(α,γ)^{26}Mg and ^{22}Ne(α,n)^{25}Mg reactions, which are important for s-process neutron production, proceed through excited states in the compound nucleus: ^{26}Mg. The important excitation energy region in ^{26}Mg, corresponding to relevant resonances in ^{22}Ne+α, ranges from the α-particle threshold at $S_\alpha = 10615$ keV to $E_x \approx 11600$ keV. Many of the states in this energy region have uncertain excitation energies and quantum numbers, which are essential ingredients for reaction rate calculations.

A ^{26}Mg$(\gamma,\gamma)^{26}$Mg experiment was performed at the HIγS facility with γ-ray beam energies of $E_\gamma = 10.8, 11.0, 11.2$ and 11.4 MeV to determine the quantum numbers of excited states in ^{26}Mg. In total, five excited states were identified, with $E_x = 10573.3(8)$ keV ($J^\pi = 1^-$), $E_x = 10647.3(8)$ keV ($J^\pi = 1^+$), $E_x = 10805.7(7)$ keV ($J^\pi = 1^-$), $E_x = 10949.1(8)$ keV ($J^\pi = 1^-$), and

$E_x = 11153.5(10)$ keV ($J^\pi = 1^+$). The excited states at $E_x = 10806$ keV and $E_x = 10949$ keV have previously been observed in α-particle transfer studies with undetermined quantum numbers. The present results for these states, which are located below the neutron threshold, are expected to significantly influence the ^{22}Ne(α,γ)^{26}Mg reaction rate. The unnatural parity state observed at $E_x = 11154$ keV was previously believed to be an important resonance in the ^{22}Ne+α reactions. However, the present results show that this state is irrelevant for neutron production in the s-process.

6 ^{22}Ne(p,γ)^{23}Na Resonance Strength

6.1 Introduction

NUCLEAR reaction rates of many important stellar burning processes are dominated by resonances in the reaction cross section. Many resonance strengths for capture reactions involving noble gases have been measured previously using implanted targets, where in most cases, the target backing was a thin (≈ 0.5 mm thick) tantalum sheet. In such cases, it is notoriously difficult to obtain absolute strengths since the stoichiometry of the implanted region must be known in order to extract a strength from a thick-target excitation function.

Measurements of astrophysically important reactions are typically performed at low beam energies, corresponding to low nuclear burning temperatures in stellar environments. However, the only absolutely measured strength in ^{22}Ne(p,γ)^{23}Na corresponds to the $E_r^{\text{lab}} = 1278$ keV resonance [Kei77], which is beyond the reach of most low energy accelerators. For this resonance, the stoichiometry of the implanted ^{22}Ne targets was obtained with Rutherford back-scattering, requiring specialised equipment not widely available in low-energy accelerator laboratories. Here a novel method is presented for extracting absolute resonance strengths at low bombarding energies from measured excitation functions.

This new method, based on material depth profiling, is applied to the measurement of the $E_r^{\text{lab}} = 479$ keV resonance in ^{22}Ne(p,γ)^{23}Na. The experiment utilises a target composed of ^{22}Ne ions implanted into an aluminium substrate. By measuring the well-known $E_r^{\text{lab}} = 406$ keV resonance in ^{27}Al(p,γ)^{28}Si and the $E_r^{\text{lab}} = 479$ keV resonance in ^{22}Ne(p,γ)^{23}Na simultaneously, the absolute strength of the latter resonance can be obtained independently from the knowledge of absolute beam currents, absolute detector efficiencies, or the stoichiometry of the target. Obtaining a resonance

strength independently of the target stoichiometry, which introduces systematic uncertainties that are difficult to quantify, is a significant advantage of this method.

For more information on the theory of depth profiling of an implanted substrate, see chapter 3. Throughout this work, kinematic quantities are given in the centre-of-mass reference frame, unless stated otherwise.

6.2 Excitation Functions from an Implanted Aluminium Substrate

In the present work, ^{22}Ne ions were implanted into a thick aluminium sheet yields of the narrow resonances at $E_r^{\text{lab}} = 406$ keV in ^{27}Al(p,γ)^{28}Si and at $E_r^{\text{lab}} = 479$ keV resonance in ^{22}Ne(p,γ)^{23}Na were measured simultaneously. For both resonances, the yield is given by Eq. (3.20). In the following, the implanted species ($p =^{22}$Ne) will be denoted by the subscript 22, and the substrate species ($q =^{27}$Al) by the subscript 27.

Since the implanted ^{22}Ne ions are concentrated near the surface of the aluminium sheet, a well-defined peak-shape is expected for the ^{22}Ne+p yield curve. On the other hand, the ^{27}Al+p yield curve will reveal an interesting structure. In the pure aluminium region, beyond the implanted ^{22}Ne depth, the ^{27}Al+p yield will be at a maximum ($\rho_{22} = 0$ in Eq. (3.12)). However, in the ^{22}Ne implanted region, $\rho_{22} \neq 0$ and thus the energy loss, Δ_i, in Eq. (3.20) increases, resulting in a smaller yield. Therefore, a step in the excitation function is expected caused by the implanted region near the surface of the target. The situation is shown schematically in Fig. 6.1.

The general strategy was the following: (i) fit Eq. (3.20) to the measured ^{27}Al+p yield curve, including the step on the front edge; this allowed the extraction of the stoichiometry, $\xi(x) = N_{22}/N_{27}$, which enters through Eqs. (3.11)-(3.14) together with the absolute normalisation of the yield. (ii) with the stoichiometry $\xi(x)$ and the absolute yield normalisation factor determined from the previous step, Eq. (3.20) was fit to the measured ^{22}Ne+p yield curve. The resonance strength in ^{22}Ne+p is left as a free parameter to be extracted from the fit.

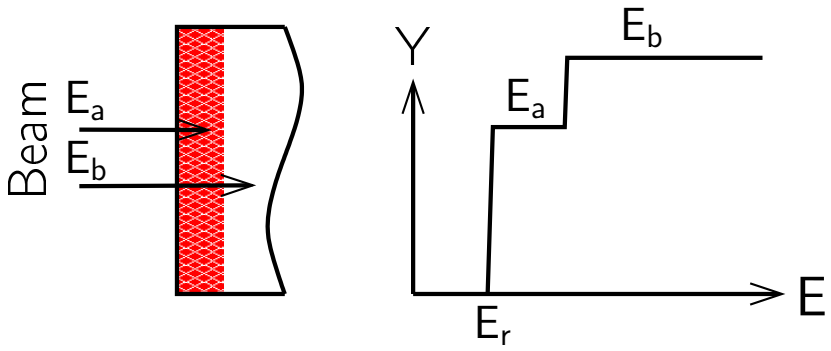

Figure 6.1: Schematic showing the effect of implanting neon ions into an aluminium substrate. Incident protons with energies E_a are captured by ^{27}Al nuclei in the implanted region, which is close to the surface of the target. The increased total stopping cross section in this region leads to a decreased yield (Eq. (3.20)). Beams with energies of E_b react deeper inside the target in a region of pure aluminium. The yield at these energies is higher compared to the implanted region. Note, however, that for a given incident energy the depth of a reaction occurring in a region of pure aluminium will be affected by the energy loss (or total stopping power) in the implanted region.

6.3 Experimental Equipment

6.3.1 Implanted Target

The backing used for the experiment was a 1 mm thick aluminium sheet (99% purity). The backing was cleaned thoroughly with acetone and ethanol before implantation. The ^{22}Ne ions were implanted into the backing using the implanter described in Sec. 4.4. The ion implanter accelerated neon ions from a pressurised natural neon ($9.25\% \pm 0.03\%$ molar fraction of ^{22}Ne) gas bottle to an energy of 100 keV. The incident dose of ^{22}Ne was estimated by integrating the beam current on the backing, assuming singly charged incident ^{22}Ne ions. The beam current on the backing amounted to about 20 μA on average. The total accumulated charge was 0.26 C (corresponding to 1.6×10^{18} incident ^{22}Ne ions) over a circular implantation region of 2.5 cm diameter. A liquid nitrogen cooled trap reduced contamination buildup (such as carbon and fluorine) on the backing.

6.3.2 Setup

Depth profiling of the implanted aluminium backing was conducted at the Laboratory for Experimental Nuclear Astrophysics (LENA), located at the Triangle Universities Nuclear Laboratory. The 1 MV Van de Graaff accelerator described in Sec. 4.1 was used to accelerate proton beams to energies in the range of $E_p^{\text{lab}} = 400 - 505$ keV with a total integrated beam charge on target of ≈ 0.13 C over a

beam spot of about 1 cm diameter. Secondary electron suppression was applied for the beam current measurement as shown in Fig. 4.2. In addition, a liquid nitrogen-cooled trap reduced contaminant buildup on the target surface. The beam current was kept to a minimum (≈ 5 μA) to ensure that the target did not degrade.

6.3.3 Detector

Capture γ-rays from the excited compound nuclei (^{28}Si and ^{23}Na) were detected using a 135 % relative efficiency HPGe detector. The detector was located at 55° with respect to the beam direction at a distance of 3.0 cm from the centre of the target. The target and detector were surrounded by at least 5 cm of lead in all directions to reduce background caused by environmental sources and from x-rays produced by the accelerator.

The energy signals from the detector were amplified with an Ortec 572 spectroscopy amplifier and recorded with a CAEN 785 ADC. Detector dead times were monitored with an Ortec 448 precision pulse generator throughout the experiment and were kept below 3%.

The detector efficiencies, used both for peak intensity normalisation and for summing corrections, were obtained by three methods: radioactive source measurements, resonant (p,γ) reactions, and Monte-Carlo simulations using `Geant4` [Ago03]. First, the Sum-Peak method [Kim03] was used with ^{60}Co to find the absolute full-energy peak and total efficiencies at $E_\gamma = 1173$ and 1332 keV that do not depend on knowledge of the absolute source activity. Subsequently, other radioactive sources (^{56}Co, ^{152}Eu) were used to obtain relative full-energy peak efficiencies up to $E_\gamma = 3.5$ MeV. The $E_r^{\text{lab}} = 278$ keV resonance in ^{14}N(p,γ)^{15}O was used to extend the full-energy peak efficiency curve up to $E_\gamma = 7.5$ MeV. It is important to note that because of the close detector geometry, all experimental full-energy peak efficiencies had to be corrected for coincidence summing effects. The corrections were performed using the code `LENASum` [Lon06], which is based on the formulation described in Ref. [Sem90]. Following the experimental determination of full-energy peak efficiencies, the experimental data points were interpolated using `Geant4` simulations. Total detection efficiencies, which were needed for coincidence summing corrections, were also obtained with `Geant4` and normalised to the ^{60}Co data. More details on detector characterisation can be found in Ch. 4.

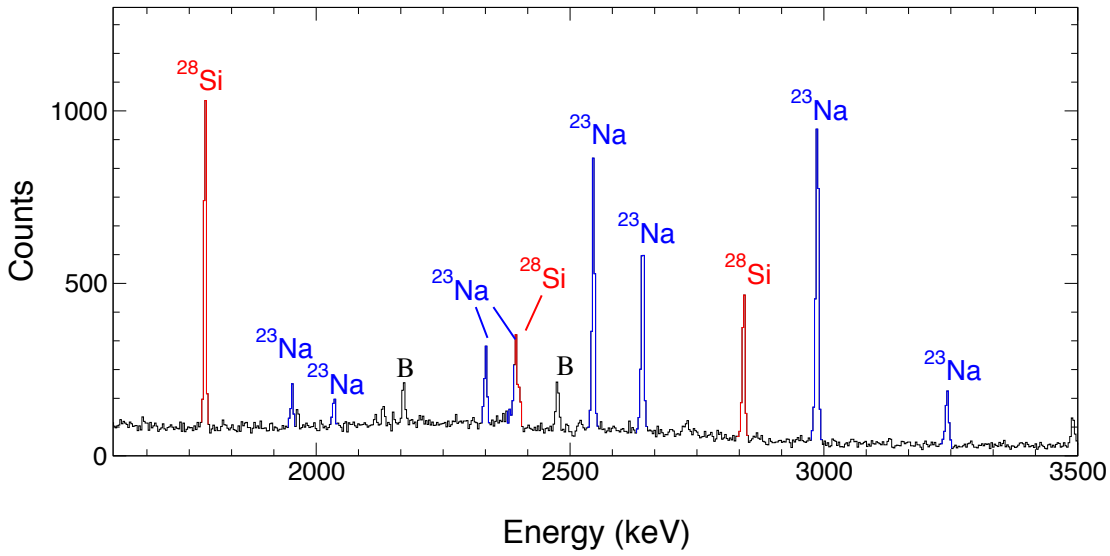

Figure 6.2: Sample γ-ray spectrum, obtained at a beam energy of 490 keV with an accumulated charge of 2×10^{-3} C on target. The target consisted of ^{22}Ne ions implanted into aluminium and thus resonances in the ^{27}Al(p,γ)^{28}Si and ^{22}Ne(p,γ)^{23}Na reactions were excited simultaneously. Major peaks are labelled by the decaying nucleus (^{23}Na in blue; ^{28}Si in red), while the label "B" denotes background.

6.4 Procedure and Analysis

6.4.1 Yield Curves

Yield curves were measured simultaneously for the ^{27}Al(p,γ)^{28}Si and ^{22}Ne(p,γ)^{23}Na reactions at incident proton energies of $E_p^{\text{lab}} = 400$ – 505 keV. A sample γ-ray spectrum, obtained at an incident beam energy of $E_r^{\text{lab}} = 490$ keV, is shown in Fig. 6.2. The observed in-beam γ-rays arise from the narrow resonances at $E_r^{\text{lab}} = 406$ keV in ^{27}Al+p and at $E_r^{\text{lab}} = 479$ keV in ^{22}Ne+p .

The ^{27}Al+p resonance has a target spin of $j = 5/2$ and thus the angular correlation is expected to be approximately isotropic. Considering, in addition, that the detector was located at $\theta_\gamma = 55°$, where the Legendre polynomial $\mathrm{P}_2(\cos\theta) = 0$, an angular correlation factor of $W_{27}(\theta) = 1$ can safely be adopted in Eq. (3.2). Additionally, the ^{22}Ne+p resonance at $E_r^{\text{lab}} = 479$ keV has a spin of $j = 1/2$ and thus $W_{22}(\theta)$ is unity in Eq. (3.2).

^{27}Al(p,γ)^{28}Si

The $E_r^{\rm lab} = 405.5(3)$ keV resonance ($\omega\gamma = 8.63(52)\times10^{-3}$ eV) [Pow98] was used to measure the ^{27}Al(p,γ)^{28}Si yield curve. Relatively small beam currents (≈ 5 μA) were required to avoid damage to the target. The resulting low counting statistics for the primary transitions was insufficient for reliable depth profiling. Thus the much stronger secondary decay from the first excited state (1779 keV$\rightarrow$0), which carries 98% of the decay strength, was used for this purpose. The disadvantage of monitoring secondary decays in a measurement with an infinitely thick target (i.e., all beam particles stop in the aluminium) is that lower energy resonances in ^{27}Al+p may contaminate the measured yield. The $E_r^{\rm lab} = 326$ keV resonance in ^{27}Al+p resonance ($\omega\gamma = 1.8(1) \times 10^{-3}$ eV [Ili10]) is of particular importance and had to be accounted for. This was achieved by calculating the expected maximum yield for an infinitely thick target using Eq. (3.2). The expected contribution to the total 1779 keV$\rightarrow$ 0 intensity was then estimated using the branching ratios from Ref. [Ili90] and amounted to about 16% of the maximum yield. This contribution to the decay strength was subtracted from the measured intensities. Note that the first data point in the ^{27}Al+p yield curve is consistent with zero, validating this method of subtracting contamination from other resonances. Another resonance in ^{27}Al+p at $E_r^{\rm lab} = 447$ keV ($\omega\gamma = 1.50(13) \times 10^{-3}$ eV [Ili10]) had to be considered as well. To avoid fitting the cumulative yield from two ^{27}Al+p resonances ($E_r^{\rm lab} = 406$ keV and $E_r^{\rm lab} = 447$ keV) simultaneously, data points near the higher energy resonance from $E_p^{\rm lab} = 445$ to 475 keV were removed from the analysis. The expected yield of the $E_r^{\rm lab} = 447$ keV resonance was then subtracted from data points above $E^{\rm lab} = 475$ keV. The resulting yield curve, after these corrections have been applied, is shown in Fig. 6.3a and will be discussed later.

^{22}Ne(p,γ)^{23}Na

The primary ground state transition of the $E_r^{\rm lab} = 479.3(8)$ keV resonance in ^{22}Ne(p,γ)^{23}Na [End90] was used to measure the yield curve shown in Fig. 6.3b. The yield was calculated with Eq. (3.2). For the branching ratio of the ground state transition (9253 keV$\rightarrow$ 0) a weighted average of the literature results which are in mutual agreement ($B_{22} = 0.46$ and $B_{22} = 0.48$ respectively) [Mey73, Pii71] was adopted.

Yield Curve Analysis

The predicted step close to the front edge of the ^{27}Al+p yield curve (Fig. 6.3a), resulting from the ^{22}Ne concentration near the target surface, is clearly observed. The ^{22}Ne+p yield curve (Fig. 6.3b), on the other hand, shows a smooth peak, consistent with expectations (Sec. 3.2). Deviation from the expected step shape (Fig. 6.1) in Fig. 6.3a and from a sharp front edge at $E^{\text{lab}} = 479$ keV in Fig. 6.3b is because the ^{22}Ne was not implanted in a uniform layer at the front of the target, but rather in a varying concentration with depth, as shown in Fig. 6.4. It should be noted that an approximately 40 nm thick layer of aluminium oxide [JJ91] will affect the shape of the yield curve. A `SRIM` calculation reveals that the energy loss difference with and without the aluminium oxide layer is less that 0.5 keV and, therefore, outside the resolution of the present experiment. The effect of the oxide layer is lessened because of the low ^{22}Ne density close to the surface of the aluminium substrate (see Fig. 6.4).

Two codes were written to analyse the yield curves obtained in the experiment. The first code assumed an implantation profile that varied with depth according to a Gaussian distribution. This code was used for proof-of-concept purposes since the analytical form required less fitting parameters and hence less computation time. The second code was written to fit Eq. (3.20) to the measured yield curves. The least-squares fitting method of McGlone *et al*. [McG91] was used to determine the depth profile of ^{22}Ne implanted into Al. The concentration profile of implanted atoms was constrained to a smoothly varying function by adding corrections to the log–likelihood function. The log-likelihood function for a profile grid of M slices, which are fit to N data points, is given by,

$$\chi^2 = \chi^2_{\text{data}} + \sum_{j=N+1}^{N+M+1-B} \left[W_{j-N} \sum_{b=1}^{B} N_{22_{j-N+b-1}} P_b \right] \tag{6.1}$$

where,

$$\chi^2_{\text{data}} = \sum_i \frac{(x_i - \overline{x})^2}{\sigma_i^2}$$

Here, χ^2_{data} is the log-likelihood function calculated from the deviation of fitted points, $\overline{x}$, to experimental points, x_i, assuming uncertainties of σ_i in the data; N_{22_k} denotes the ^{22}Ne ion concentration at each grid point; B and P_k are fixed parameters for controlling the smoothness of the profile; and W_k

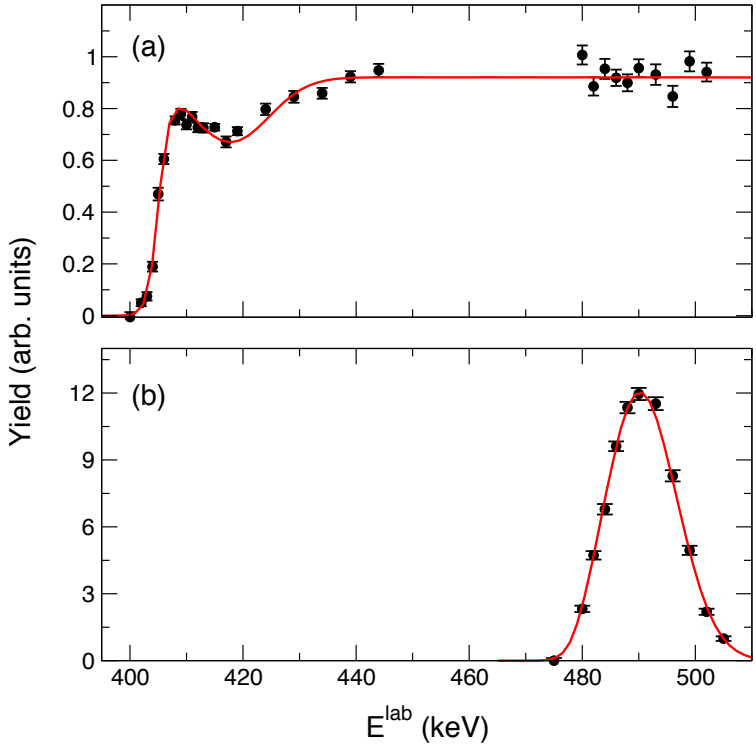

Figure 6.3: Best fits to the ^{27}Al+p and ^{22}Ne+p yields. (a) Best fit to the $E_r^{\rm lab} = 406$ keV resonance in ^{27}Al(p,γ)^{28}Si. The absolute yield height has been corrected for other contaminant resonances as discussed in Sec. 6.4.1. The yield normalisation A in Eq. (6.2) is extracted from the measured yield points above $E^{\rm lab} = 480$ keV. (b) Best fit to the $E_r^{\rm lab} = 479$ keV resonance in ^{22}Ne(p,γ)^{23}Na. The absolute height of the yield curve is left as a free parameter in the fit, which determines the resonance strength. Note that there are more high energy data points in the ^{22}Ne+p yield curve than in the ^{27}Al+p yield curve. This is because some ^{27}Al+p data points were removed because of contamination from other resonances (see Sec. 6.4.1). These contaminants do not affect the ^{22}Ne+p yield.

are weights, which were adjusted manually in order to control the smoothness of the profile. As in Ref. [McG91], $B = 4$ and $P_b = -1, 3, -3, 1$ were chosen to obtain a quadratic smoothness between every four points with $W = 20$ [1].

The strength of the $E_r^{\rm lab} = 479$ keV resonance in ^{22}Ne(p,γ)^{23}Na was determined from the following procedure (outlined already in Sec. 3.2). Initially, the yield for the ^{27}Al+p reaction was calculated,

[1] A two-step minimisation was employed to find the best fit depth profile. The Broyden–Fletcher–Goldfarb–Shanno (BFGS) method [Nas90] was used for the initial parameter search, while the Nelder-Mead gradient based search [Nel65] was adopted to finely tune the minimisation. Finite difference second derivatives were employed to estimate uncertainties in the fit parameters.

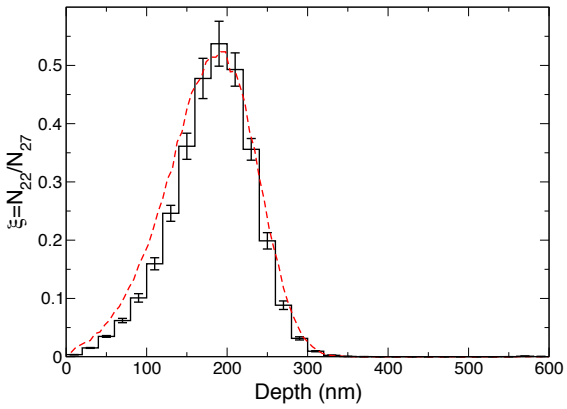

Figure 6.4: Stoichiometry profile, $\xi(x)$, of implanted ^{22}Ne ions in the aluminium backing as obtained from a fit to the ^{27}Al+p yield curve in Fig. 6.3a. The concentration profile simulated with `SRIM`, which is normalised to the maximum height of the data points, is shown as a dashed line.

which is given by Eqs. (3.2) and (3.20) as:

$$\begin{aligned} Y_{27}(E_0) =& A \left(\frac{1}{\varepsilon_{27}^{p} Q_{27}} \right)_{\text{rel}} \frac{e}{B_{27}} I_{27}(E_0) \\ =& \omega\gamma_{27} \frac{\lambda_r^2}{2\pi\sigma_b\sigma_s} \sum_i N_{27_i} \frac{1}{\sqrt{x_i}} \int_{E'=0}^{E_0} dE' \exp\left[-\frac{(E'-E_r)^2}{2\sigma_b^2} \right] \exp\left[-\frac{(E_0-E'-\Delta_i)^2}{2\sigma_s^2 x_i} \right] \end{aligned} \tag{6.2}$$

where $(\varepsilon_{27}^{p} Q_{27})_{\text{rel}}$ is the product of the relative peak efficiency and relative accumulated charge, and A denotes their combined absolute normalisation factor. The absolute strength of the $E_r^{\text{lab}} = 406$ keV resonance is labelled by $\omega\gamma_{27}$. From the measured ^{27}Al+p yield curve (Fig. 6.3a), the fitting parameters A and $\xi(x)$ (affecting the energy loss Δ_i according to Eq. 3.11) were extracted.

The stoichiometry, $\xi = N_{22}/N_{27}$, as a function of depth that was extracted by fitting the ^{27}Al+p yield is shown in Fig. 6.4. The stoichiometry profile is overlaid with the simulated profile (dashed line) of 100 keV ^{22}Ne ions implanted into an aluminium substrate, as obtained from the Monte-Carlo ion transport code `SRIM` [Zie04]. There is reasonable agreement between measured and simulated ^{22}Ne depth profiles. Note that the maximum stoichiometry amounts to a number ratio of Ne : Al$= 1 : 2$.

Once the stoichiometry profile, ξ, and constant, A, were extracted from the ^{27}Al+p yield curve,

the ^{22}Ne+p yield curve was fit. The ^{22}Ne+p yield is given by:

$$\begin{aligned} Y_{22}(E_0) =& A\left(\frac{e}{\varepsilon_{22}^{p} B_{22} Q_{22}}\right)_{\text{rel}} I_{22}(E_0) \\ =& \omega\gamma_{22}\frac{\lambda_r^2}{2\pi\sigma_b\sigma_s}\sum_i N_{22_i}\frac{1}{\sqrt{x_i}}\int_{E'=0}^{E_0} dE' \exp\left[-\frac{(E'-E_r)^2}{2\sigma_b^2}\right]\exp\left[-\frac{(E_0-E'-\Delta_i)^2}{2\sigma_s^2 x_i}\right] \end{aligned} \tag{6.3}$$

At this stage, the only fitting parameter is the strength of the ^{22}Ne+p resonance, $\omega\gamma_{22}$. There are several advantages of using the method outlined above. Firstly, only relative detector efficiencies need to be known. These relative efficiencies have been shown in Ref. [Car10] to be accurate to within a few percent. Secondly, only the relative accumulated charge needs to be known. Note that above $E^{\text{lab}} = 480$ keV the same runs were used to analyse the ^{22}Ne+p and ^{27}Al+p yields, and thus the beam charge, Q, cancels completely. Fitting Eq. (6.3) to the measured yield shown in Fig. 6.3b gave the strength of the $E_r^{\text{lab}} = 479$ keV resonance in ^{22}Ne+p , for which a value of $\omega\gamma = 0.524(51)$ eV was found.

The uncertainty budget for the extracted strength of the $E_r^{\text{lab}} = 479$ keV resonance in ^{22}Ne+p is presented in Tab. 6.1. The uncertainty in the reference resonance strength ($E_r^{\text{lab}} = 406$ keV in ^{27}Al+p) is 6% [Pow98]. The `Geant4` simulations used to derive relative detector efficiencies are shown to be accurate to within a few percent for extrapolation in the energy range of $E_\gamma = 4-11$ MeV [Car10]. Relative uncertainties of 2% were therefore assigned to detection efficiencies. Literature values for the primary branching ratios in ^{22}Ne+p contribute 5% to the resonance strength uncertainty. Stopping power uncertainties in the energy regions of interest were estimated from the data compiled on the SRIM website [Zie04]. The stopping power uncertainties for ^{27}Al+p and ^{22}Ne+p were estimated to be 4% and 3%, respectively. The stopping powers affect the yield of both ^{27}Al+p and ^{22}Ne+p yield curves through Eq. (3.11). Since the energy loss enters in the exponential of both Eqs. (6.2) and (6.3), the importance of the stopping power uncertainties is lessened, resulting in resonance strength uncertainty contributions of just 2% and 1%, respectively. In addition to uncertainties affecting the resonance strength, the effect of a different implantation model was investigated. In this model, the implanted ^{22}Ne atoms replaced aluminium atoms during implantation, resulting in a constant number

Source	Uncertainty in $\omega\gamma_{22}$ (%)
Reference ^{27}Al+p Strength	6
Relative Efficiencies	2
Branching Ratios	5
Stopping Powers (Al)	2
Stopping Powers (Ne)	1
Fitting	5
Total	10

Table 6.1: Uncertainty budget for the extracted $E_r^{\text{lab}} = 479$ keV resonance strength in ^{22}Ne+p .

density for the implanted material. Equations (3.13) and (3.14) are then replaced by,

$$\rho_{27}(x_i) = \overline{\rho_{27}}(1 - \xi(x)) \tag{6.4}$$

$$\rho_{22}(x_i) = \xi(x_i)\frac{\overline{\rho_{27}}M_{22}}{M_{27}} \tag{6.5}$$

This model was found to only affect the width of the extracted profile, while the total number of implanted nuclei and hence the resonance strength $\omega\gamma_{22}$ remains approximately constant. All uncertainties were summed in quadrature. The total uncertainty in the extracted $E_r^{\text{lab}} = 479$ keV resonance strength in ^{22}Ne(p,γ)^{23}Na amounted to 10%.

6.5 Discussion

All previously measured strengths for the $E_r^{\text{lab}} = 479$ keV resonance in ^{22}Ne+p were normalised relative to higher lying resonances in the ^{22}Ne+p reaction. In the present work, the resonance strength has been determined independently of other resonances in ^{22}Ne+p, with no dependence on absolute detector efficiencies or absolute beam charge integration. A comparison of the new result with values derived from the literature is shown in Fig. 6.5.

The value obtained by Meyer *et al*. [Mey73] was normalised to the ^{22}Ne+p , $E_r^{\text{lab}} = 640$ keV resonance strength from Ref. [Du 71]. The rather large uncertainty is dominated by the uncertainty of that reference resonance. The value of $\omega\gamma = 0.45(10)$ eV ($\pm$20%) in Endt [End90], on the other hand, was obtained by normalising the resonance strengths from Meyer *et al*. [Mey73] to the absolute strength of the ^{22}Ne+p $E_r^{\text{lab}} = 1278$ keV resonance reported by Keinonen *et al*. [Kei77]. Another

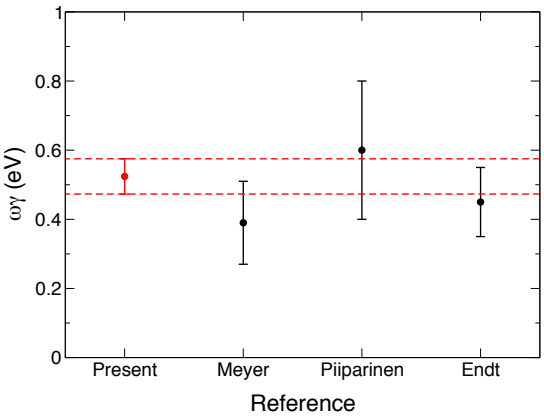

Figure 6.5: Comparison of present result (shown in red) for the $E_r^{\rm lab} = 479$ keV resonance strength in ^{22}Ne(p,γ)^{23}Na to previously published results. The labels Meyer, Piiparinen, and Endt refer to Refs. [Mey73], [Pii71], and [End90], respectively.

relative measurement was performed by Piiparinen *et al*. [Pii71], but unfortunately, no uncertainties are quoted for the relative yield of the $E_r^{\rm lab} = 479$ keV resonance. For comparison, a relative yield uncertainty of 30% was used (by considering their statement that relative yield uncertainties were between 10% and 50%), and their strength was normalised to the result from Keinonen *et al*. [Kei77]. As is apparent from Fig. 6.5, the present result has significantly improved the uncertainty of the $E_r^{\rm lab} = 479$ keV resonance strength in ^{22}Ne+p , from a previous value near 30% to 10%. The new technique removes any systematic uncertainty caused by the target stoichiometry, which is difficult to quantify using traditional methods.

It was already mentioned in the introduction that the new value for the $E_r^{\rm lab} = 479$ keV resonance strength in ^{22}Ne+p is important in two respects. Firstly, it will reduce the rate uncertainties of the ^{22}Ne(p,γ)^{23}Na reaction since the strengths of the low-energy resonances can be re-normalised relative to the present precisely measured strength for $E_r^{\rm lab} = 479$ keV, and thus improve predictions of hydrogen burning nucleosynthesis. Secondly, the present strength can be used to determine more reliable stoichiometries for implanted ^{22}Ne -Ta targets that have been employed in measurements of the important ^{22}Ne(α,γ)^{26}Mg and ^{22}Ne(α,n)^{25}Mg s-process neutron source reactions. New thermonuclear reaction rates for ^{22}Ne+p and ^{22}Ne+α will be published elsewhere.

6.6 Summary

A novel method for measuring reliable resonance strengths has been employed. By implanting ^{22}Ne ions into a thick aluminium backing, and simultaneously measuring the ^{22}Ne +p and ^{27}Al+p reactions, the strength of the $E_r^{\text{lab}} = 479$ keV resonance in ^{22}Ne(p,γ)^{23}Na was determined to be $\omega\gamma = 0.524(51)$ eV. The new formalism allows for finding the implantation profile of ^{22}Ne in a thick aluminium target backing. This novel approach significantly reduced uncertainties in the desired resonance strength arising from the cancellation of several systematic experimental uncertainties. The well known $E_r^{\text{lab}} = 406$ keV resonance in ^{27}Al(p,γ)^{28}Si was used as a reference. The new precise value for the ^{22}Ne+p resonance strength is important for estimating reliable thermonuclear reaction rates for the hydrogen burning of ^{22}Ne and for the normalisation of the ^{22}Ne+p s-process reaction rates.

7 ^{22}Ne+α Rates

7.1 Introduction

NUCLEI heavier than $A \approx 60$ can be produced through neutron capture in stars. The s-process is one mechanism for this production, where the neutron flux is an important factor to the amount of material that is produced. Consequently, the reaction rates of the neutron producing reactions must be well known if comparisons between nucleosynthesis models and observations are ever to provide us with reliable information on the interior structure of stars. For the case of the ^{22}Ne(α,n)^{25}Mg reaction, its competing reaction ^{22}Ne(α,γ)^{26}Mg also plays an indirect role in the production of neutrons. Both of these reactions have significant uncertainties at the temperatures of interest in these stars (T $\sim$ $0.1 - 0.3$ GK). The effects of these uncertainties have been studied in AGB stars and massive stars by Pignarari *et al*. [Pig05] and The *et al*. [The00], respectively. Both studies find that the current uncertainties in the ^{22}Ne+α reactions produce variations of up to a factor of 10 in the abundances of key elements in the s-process.

In the present work, the two ^{22}Ne+α reactions are analysed carefully to find the best estimates for the current uncertainties in the reactions. Throughout this section, significant problems in the experimental data will be highlighted as they are encountered. In addition to information from direct measurements of the reactions, data from α-particle transfer reactions [Gie93, Uga07] and neutron capture data on ^{25}Mg [Wei76, KÖ2] will be considered. The separation energies from the compound ^{26}Mg nucleus used in the following analysis are $S_\alpha = 10614.787(33)$ keV and $Q_n = 11093.083(83)$ keV.

The derived reaction rates will be compared with previous results. Many different estimates of the ^{22}Ne+α rates can be found in the literature. Thus to avoid confusion, the present work will

concentrate on reaction rate comparisons to (i) the latest *experimental* reaction rates (i.e., the latest studies that presented reaction rates along with a new cross section measurement; and (ii) the NACRE compiled reaction rates [Ang99]. The reason for this is that most nucleosynthesis modelling codes use the NACRE rates as input. Note that the reaction rates of Karakas *et. al* [Kar06] will not be discussed in the present work because they add little new information.

Throughout this chapter, all energies are presented in the centre-of-mass frame unless otherwise stated.

7.2 Excited States in ^{26}Mg

In order to take the tails of wide resonances into account at low temperatures, the NACRE compilation [Ang99] used the total width upper limits of the resonances as measured in Refs. [Wol89, Dro93]. In the present analysis, total widths as measured by Refs. [Wei76, KÖ2] are used when available. In order to integrate wide resonances in the ^{22}Ne$(\alpha,\gamma)^{26}$Mg and ^{22}Ne$(\alpha,\mathrm{n})^{25}$Mg reactions, their corresponding excited states in the ^{26}Mg compound nucleus must be identified. In this section, these identifications will be discussed. Following this identification, the specific cases of each reaction will be discussed separately.

The directly measured resonance strengths in the ^{22}Ne$(\alpha,\gamma)^{26}$Mg reaction are adopted from Wolke *et al*. [Wol89]. Direct measurements of resonances in the ^{22}Ne(α,n)^{25}Mg reaction have been made by Refs. [Wol89, Har91, Dro93, Jae01b]. All of these measurements were made at the same facility, with variations of the same target and detector system. In the present analysis, it is assumed that with each subsequent measurement, the techniques were improved upon, so the work of Jaeger *et al*. [Jae01b] supersedes the work of all others.

$E_x = 11315$ keV, $E_r^{\mathrm{lab}} = 830$ keV

Köhler [KÖ2] argued that this state cannot correspond to the resonances observed by Jaeger *et al*. [Jae01b] at $E_r = 832(2)$ keV and Wolke *et al*. [Wol89] at $E_r^{\mathrm{lab}} = 828(5)$ keV. He argues that the value for Γ_γ would be far too large (assuming Γ reported in [Jae01b] is correct). The calculation is a

follows:

$$\omega\gamma_{\alpha\gamma} = \omega\frac{\Gamma_\alpha\Gamma_\gamma}{\Gamma_\alpha+\Gamma_\gamma+\Gamma_n}, \qquad \omega\gamma_{\alpha n} = \omega\frac{\Gamma_\alpha\Gamma_n}{\Gamma_\alpha+\Gamma_\gamma+\Gamma_n} \tag{7.1}$$

where Γ_α, Γ_n, and Γ_γ are the α-particle, neutron, and γ-ray partial widths, respectively; $\omega\gamma_{\alpha n}$ and $\omega\gamma_{\alpha\gamma}$ are the ^{22}Ne$(\alpha,\mathrm{n})^{25}$Mg and ^{22}Ne$(\alpha,\gamma)^{26}$Mg resonance strengths, respectively;and ω is a spin factor calculated by:

$$\omega = \frac{2J+1}{(2j_a+1)(2j_A+1)} \tag{7.2}$$

J, j_a and j_A are the spin of the compound state, the spin of the projectile and the target, respectively. The ratio of Eqs. (7.1) is:

$$\frac{\omega\gamma_{\alpha\gamma}}{\omega\gamma_{\alpha n}} = \frac{\Gamma_\gamma}{\Gamma_n} \tag{7.3}$$

Therefore, for the state in question,

$$\Gamma_\gamma = \Gamma_n\frac{\omega\gamma_{\alpha\gamma}}{\omega\gamma_{\alpha n}} = 250(170)\times\frac{3.6(4)\times10^{-5}}{1.18(11)\times10^{-4}} = 76(53)\text{eV}$$

The mean value of Γ_γ in this energy range is reported to be 3 eV [KÖ2], 25 times smaller than that calculated in Eq (7.1). However, once the rather large uncertainties are considered, it only differs by 1.4σ. Upon inspection of the PhD thesis of Jaeger [Jae01a], it is apparent that the ^{22}Ne$(\alpha,\gamma)^{26}$Mg reaction was measured simultaneously with the ^{22}Ne$(\alpha,\mathrm{n})^{25}$Mg reaction. In that measurement, a resonance was found at $E_r = 833(3)$ keV in ^{22}Ne$(\alpha,\gamma)^{26}$Mg , in very good agreement with the resonance found at $E_r = 832(2)$ keV in the ^{22}Ne$(\alpha,\mathrm{n})^{25}$Mg reaction. The excitation function fit to the ^{22}Ne$(\alpha,\mathrm{n})^{25}$Mg data that produced the total width of $\Gamma = 250(170)$ eV shows a rather ambiguous fit, which could easily explain the discrepancy in partial widths discussed above.

Jaeger *et al*. [Jae01b] assign this state with $J^\pi = 2^+$, originating from the assignment made by Giesen *et al*. [Gie93]. There are no states observed in other studies in this energy region that closely match this resonance, but there are several possibilities for which state it could correspond to: (a) The state at $\mathrm{E}_x = 11328.2(1)$ keV with $J^\pi = 1^-$ and $\Gamma_T = 427(86)$ eV, (b) The state at $\mathrm{E}_x = 11310.7(3)$ keV with $J^\pi = 1^-$ and $\Gamma_T = 4.1(16)$ eV, (c) The state at $\mathrm{E}_x = 11286.4(1)$ keV with $J^\pi = 2^+$ and $\Gamma_T = 17.1(61)$ eV or (d) a state that has not been observed in other works. State (c) is the only 2^+ state in this energy region, but is 16σ outside the energy uncertainties, and 1.5σ

outside the width uncertainties. Similarly, state (b) is 4σ outside the energy uncertainties and 1.4σ outside the width uncertainties. State (a) still doesn't agree in energy, being 5σ outside the uncertainty (corresponding to 10 keV as mentioned in Ref. [Kar06]), but agrees well in total width (0.9σ).

Following these arguments the resonances are assumed to arise from the same excited state in the present analysis, and a weighted average between Refs. [Wol89] and [Jae01b] is used for the resonance energy. Although the DWBA fits from Giesen *et al*. [Gie93] do not rule out a $J^\pi = 1^-$ state, to avoid ambiguities in the state assignments, it will be treated as a new state with resonance energy $E_r = 831.9(24)$ keV, a total with of $\Gamma_T = 250(170)$ eV, and $J^\pi = 2^+$.

$E_x = 11440$ keV, $E_r^{\text{lab}} = 976$ keV Resonance

The $E_r^{\text{lab}} = 976$ keV resonance has only been observed in the ^{22}Ne$(\alpha, \text{n})^{25}$Mg reaction [Jae01b]. There is one excited state in this energy region with similar energy and total width to the observed resonance at $E_r^{\text{lab}} = 976$ keV. However, the J^π assignments disagree. Jaeger *et al*. assume a $J^\pi = 1^-$ whereas the assignment from Köhler is $J^\pi = 4^+$. The PhD thesis of Jaeger [Jae01a] states that $J^\pi = 1^-$ was used if no assignment could been made. Thus, in the present analysis a $J^\pi = 4^+$ assignment is assumed for this state. The weighted average of the energy and total width of this resonance are $\text{E}_x = 11440.8(2)$ keV and $\Gamma_T = 1475(80)$ eV, respectively.

$E_x = 11461$ keV, $E_r = 1000$ keV Resonance

The $E_r^{\text{lab}} = 1000$ keV resonance has only been observed in the ^{22}Ne$(\alpha, \text{n})^{25}$Mg reaction [Jae01b]. There are two possible states in this energy region that could correspond to the $E_r = 1000$ keV resonance ($\text{E}_x = 11461(2)$ keV with $\Gamma_T = 9300(2500)$ eV). The first is located at an excitation energy of $\text{E}_x = 11457(2)$ keV and was observed by Ref. [Gla86]. The state was not analysed in their experiment. The other possible state was analysed by Ref. [KÖ2], and is located at an excitation energy of $\text{E}_x = 11465.3(2)$ keV with a total width of $\Gamma_T = 6553(90)$ eV. Once again, this state has been assigned different quantum numbers by the two studies: $J^\pi = 5^-$ by Koehler and $J^\pi = 1^-$ by Jaeger. As with the $E_r = 976$ keV resonance, the Koehler assignment was adopted in the present study. The weighted average energy and total width of this resonance are $\text{E}_x = 11465.2(2)$ keV and $\Gamma_T = 6554(90)$ eV, respectively.

$E_x = 11828$ keV, $E_r = 1434$ keV

This state most likely corresponds to the resonances observed in the ^{22}Ne(α,n)^{25}Mg data of Ref. [Jae01b] at 1434(2) keV and in the ^{22}Ne$(\alpha,\gamma)^{26}$Mg data of Wolke *et al*. [Wol89]. The weighted average resonance energy is therefore $E_r = 1434(3)$ keV. Jaeger *et al*. [Jae01b] measured the total width of this state to be $\Gamma = 1100(250)$ eV. At these excitation energies in this mass range, Ref. [KÖ2] claims that the average γ-ray partial width is 3 eV. The width of this state is therefore most likely due to the neutron partial width. With an assumed value of $\Gamma_\gamma = 3$ eV, the α-particle partial width can be calculated by:

$$\omega\gamma_{\alpha\gamma} = \omega\frac{\Gamma_\alpha\Gamma_\gamma}{\Gamma_T} \tag{7.4}$$

$$\text{Therefore,} \qquad \Gamma_\alpha = \frac{\omega\gamma_{\alpha\gamma}}{\omega\Gamma_\gamma}\Gamma_T \approx \frac{\omega\gamma_{\alpha\gamma}}{\omega\Gamma_\gamma}(\Gamma_n + \Gamma_\gamma)$$

$$= \frac{2.5\times10^{-3}}{3\times3}1100 = 1.8(10)\times10^{-1}\text{eV}$$

7.3 The ^{22}Ne$(\alpha,\gamma)^{26}$Mg Reaction

Directly Observed Resonances

For resonances with laboratory energies below $E_r^{\text{lab}} = 1434$ keV, the parameters from Sec. 7.2 were used. Resonances strengths and energies above $E_r^{\text{lab}} = 1434$ keV were adopted from Ref. [Wol89]. For resonances that have an upper limit total width, the calculations were performed assuming narrow resonances. The rates for resonances with a measured total width can be integrated numerically to take their tails into account. Resonances with widths this high above the neutron threshold will be dominated by the neutron partial width, and an average γ-ray partial width of $\Gamma_\gamma = 3$ eV is assumed. The α-particle partial width is then calculated using Eq. (7.4).

E_x (keV)	E^{cm} (keV)	E^{lab} (keV)	J^π	$\omega\gamma$ (eV)	Partial Widths (eV) Γ_α	Γ_γ [c]	Γ_n	Γ_T	Int
11319	704	831.9(25)	2^+	$3.6(4)\times10^{-5}$	$7.20(44)\times10^{-6}$	3	250 (170)	250 (170)	✓
11441	826	976.39(23)[d]	4^+	- - - -	$1.13(13)\times10^{-5}$	3	1470 (80)	1470 (80)	✓
11465	850	1005.23(25)[d]	5^-	- - - -	$1.60(33)\times10^{-5}$	3	6550 (90)	6550 (90)	✓
11508	893	1055.9(11)[d]	1^-	- - - -	$1.17(20)\times10^{-4}$	3	$1.27\ (25)\times10^4$	$1.27\ (25)\times10^4$	✓
11526	911	1077(2)[d]	1^-	- - - -	$2.77(23)\times10^{-4}$	3	$1.8\ (9)\times10^3$	$1.8\ (9)\times10^3$	✓
11630	1015	1200(2)[d]	1^-	- - - -	$2.83(33)\times10^{-3}$	3	$1.35\ (17)\times10^4$	$1.35\ (17)\times10^4$	✓
11748	1134	1340(10)[d]	1^-	- - - -	$2.0(3)\times10^{-2}$	3	$6.35\ (85)\times10^4$	$6.35\ (85)\times10^4$	✓
11787	1172	1385(4)[d]	1^-	- - - -	$1.67(23)\times10^{-2}$	3	$2.45\ (24)\times10^4$	$2.45\ (24)\times10^4$	✓
11828	1213	1434(3)	2^+	$2.5(3)\times10^{-4}$	$1.84(10)\times10^{-1}$	3	1100 (250)[b]	1100 (250)[b]	✓
11895	1280	1513(5)	1^- [a]	$2.0(2)\times10^{-3}$	$8.9(45)\times10^{-1}$	3	- - - -	< 3000	
11912	1297	1533(3)	1^- [a]	$3.4(4)\times10^{-3}$	$1.89(79)\times10^{+0}$	3	$5\ (2)\times10^3$	$5\ (2)\times10^3$	✓
11953	1338	1582(3)	3^- [a]	$3.4(4)\times10^{-3}$	$6.5(33)\times10^{-1}$	3	$2\ (1)\times10^3$	$2\ (1)\times10^3$	✓
12051	1437	1698(3)	3^- [a]	$6.0(7)\times10^{-3}$	$8.6(58)\times10^{-1}$	3	$4\ (2)\times10^3$	$4\ (2)\times10^3$	✓
12139	1525	1802(3)	1^- [a]	$1.0(2)\times10^{-3}$	$1.67(40)\times10^{+0}$	3	$15\ (3)\times10^3$	$15\ (3)\times10^3$	✓
12184	1569	1855(8)	(0^+)	$1.1(2)\times10^{-3}$	$1.21(29)\times10^{+1}$	3	$33\ (5)\times10^3$	$33\ (5)\times10^3$	✓
12273	1658	1960(8)	(0^+)	$8.9(1)\times10^{-3}$	$1.63(35)\times10^{+2}$	3	$73\ (9)\times10^3$	$73\ (9)\times10^3$	✓
12343	1728	2043(5)	0^+	$5.4(7)\times10^{-2}$	$6.3(12)\times10^{+2}$	3	$35\ (5)\times10^3$	$35\ (5)\times10^3$	✓

Table 7.1: Directly measured resonances in the ^{22}Ne(α,γ)^{26}Mg reaction. Total partial widths are from Ref. [Wol89] unless stated otherwise.
[a] J^π from Ref. [Har91]
[b] From Ref. [KÖ2]
[c] See text for details
[d] Γ_α from ^{22}Ne(α,n)^{25}Mg measurements

7.3.1 Upper Limit Resonances

States With Measured Partial Widths

For resonances with one or more measured partial widths and are located below $E_r = 1005$ keV, their neutron and γ-ray partial widths have been measured by R-matrix analysis of neutron capture data [KÖ2]. For each of these states, measured partial widths are adopted from Ref. [KÖ2] and upper limits for $\omega\gamma_{\alpha\gamma}$ are taken from Fig. 7 in Ref. [Wol89]. That figure displays the reaction cross section, assuming broad resonances (the resonance width is much larger than the target width), so the resonance strength is given by (see Sec. 2.1.2),

$$\omega\gamma = \frac{\pi\Gamma_T}{\lambda^2}\sigma \tag{7.5}$$

By using the resonance at $E_r = 1434$ keV as a reference, the upper limit resonance strengths can be found from the known widths and upper limit cross sections. See Appendix B.2 for more details on the calculation of these upper limits. The α-particle partial width at these energies is several orders

of magnitude smaller than the total width. Thus the width will either be dominated by the neutron partial width or the γ-ray partial width. In the former case, numerical integration of the rate can be performed by assuming an average γ-ray partial width of $\Gamma_\gamma = 3$ eV (see Sec. 7.2). In the latter case, the resonance cannot be safely integrated, so a narrow resonance is assumed. The α-particle partial width can be calculated following the same procedure as in Sec. 7.2.

States Without Measured Partial Widths

These states, mostly above $E_r = 883$ keV, have been observed in the ^{25}Mg(n,γ)^{26}Mg data of Weigmann *et al*. [Wei76] and in ^{23}Na(α,pγ)^{26}Mg measurements by Glatz *et al*. [Gla86]. In both of these cases the resonance parameters were not measured. In this situation, it is not practical to use upper limits or average values for all of the partial widths. Consequently, such states have been omitted in the present calculations. Fortunately, all but one of these levels occur at high energies, where the directly observed resonances will dominate the total reaction rate.

					Partial Widths (eV)				
E_x (keV)	E^{cm} (keV)	E^{lab} (keV)	J^π	$\omega\gamma_{UL}$ (eV)	$\Gamma_{\alpha,UL}$	Γ_γ	Γ_n	Γ_T	Int
11112	497	587.90(10)	2^+	3.8×10^{-08}	7.7×10^{-09}	1.732(31)	2578(180))	2580(24)	✓
11163	548	647.93(11)	2^+	4.3×10^{-07}	8.7×10^{-08}	4.56(29)	4644(100)	4649(100)	✓
11171	556	657.53(19)	(2^+)	6.2×10^{-07}	1.2×10^{-07}	3	1.44(16)	4.4(15)	
11183	568	671.70(21)	(1^-)	1.0×10^{-06}	2.0×10^{-07}	3	0.540(88)	3.5(15)	
11243	628	742.81(12)	$2^{(-)}$	4.7×10^{-06}	9.4×10^{-07}	7.42(60)	4511(107)	4518(110)	✓
11274	659	779.32(14)	$(2)^+$	4.9×10^{-06}	9.9×10^{-07}	3.24(35)	540(54)	543(54)	✓
11280	665	786.17(13)	$4^{(-)}$	8.2×10^{-07}	9.1×10^{-08}	0.59(24)	1513(34)	1514(34)	✓
11286	671	792.90(15)	1^-	5.0×10^{-06}	1.6×10^{-06}	0.79(46)	1256(100)	1260(100)	✓
11286	672	793.83(14)	(2^+)	5.0×10^{-06}	1.0×10^{-06}	4.26(60)	12.80(60)	17.1(60)	✓
11289	674	797.10(29)	(2^-)	5.1×10^{-06}	1.0×10^{-06}	3	1.54(46)	4.5(16)	
11296	681	805.19(16)	(3^-)	5.1×10^{-06}	7.3×10^{-07}	3.31(73)	8060(120)	8060(120)	✓
11311	696	822.62(41)	(1^-)	5.2×10^{-06}	1.7×10^{-06}	3	1.12(40)	4.1(16)	
11326	711	840.81(63)	(1^-)	5.4×10^{-06}	1.8×10^{-06}	3	0.60(32)	3.6(15)	
11328	713	843.24(17)	1^-	5.4×10^{-06}	1.8×10^{-06}	3.63(47)	424(86)	428(86)	✓
11329	714	844.35(64)	(1^-)	5.4×10^{-06}	1.8×10^{-06}	3	2.8(10)	5.8(18)	
11337	722	853.55(67)	(1^-)	5.4×10^{-06}	1.8×10^{-06}	3	1.42(56)	4.4(18)	
11344	729	861.86(18)	(2^+)	5.5×10^{-06}	1.1×10^{-06}	1.18(27)	153(42)	154(42)	✓
11345	730	862.91(19)	$4^{(-)}$	5.5×10^{-06}	6.1×10^{-07}	1.82(38)	4130(190)	4130(190)	✓
11393	778	919.34(19)	$5^{(+)}$	1.6×10^{-06}	1.5×10^{-07}	3	290(19)	293(19)	✓
11441	826	976.40(23)	4^+	6.2×10^{-06}	2.0×10^{-06}	3	1470(80)	1473(80)	✓
11465	851	1005.30(25)	5^-	6.4×10^{-06}	5.8×10^{-07}	3	6550(90)	6553(90)	✓

Table 7.2: Upper limit resonances in the ^{22}Ne(α,γ)^{26}Mg reaction; γ-ray and neutron partial widths are taken from the R-matrix fit of Ref. [KÖ2].

7.3.2 Transfer Measurements

Indirect α-particle transfer measurements have been performed below the neutron threshold by Giesen *et al*. [Gie93] and Ugalde *at al*. [Uga07]. In both of these measurements, a ^{6}Li beam was incident on a ^{22}Ne target to populate states in ^{26}Mg. The deuteron momentum was subsequently measured to obtain the ^{26}Mg excitation energy.

Between the α-particle threshold at $S_\alpha = 10615$ keV and the excitation energy of the lowest measured resonance by Ref. [Wol89] at $E_x = 12346$ keV, Ref. [Gie93] observed two α-particle clusters at $E_x = 10694(20)$ keV and $E_x = 10949(20)$ keV. The first state is assumed to be the same one as that measured in Refs. [Gla86, Mos76] and the weighted average of these excitation energies will be used. Ugalde *et al*. suggest that this state is most likely a 4^+ state as it has been observed by Ref. [Gla86] to decay to the 5^+ state at $E_x = 7395(1)$ keV.

The second state measured by Ref. [Gie93] has also been resolved into two separate states by Ref. [Uga07] at the excitation energies of $E_x = 10808(20)$ keV and $E_x = 10953(25)$ keV. For this state, the work of Ugalde *et al*. [Uga07] is assumed to supersede that of Giesen *et al*. [Gie93]. These states most closely agree with those of Walkiewicz *et al*. [Wal92] at $E_x = 10805.9(4)$ keV and those seen by Refs. [Gla86, Mos76] at $E_x = 10943(2)$ keV and $E_x = 10950(3)$ keV respectively. The weighted averages of these energies have been used in our analysis.

These measurements yield spectroscopic factors, which are obtained through DWBA fitting of angular distributions of the data. The work of Ref. [Uga07] did not deduce angular distributions. Thus their spectroscopic factors for the observed states were estimated by normalising to the state observed by Ref. [Gie93] at $E_x = 10949(25)$ keV. Their analysis consisted of taking the area of the peak observed by Ref. [Gie93] and splitting it into two parts corresponding to the areas of the newly observed peaks. The results of that analysis are shown in Tab. 7.3. In the present work, the spectroscopic factors from Ugalde *et al*. will be treated as upper limits because the ambiguities associated with estimating spectroscopic factors in this way. The larger of the three values calculated in Tab. 7.3 were used for the upper limits.

Partial widths can be calculated from the spectroscopic factors by

$$\Gamma_\alpha = \frac{2\hbar^2}{\mu R^2} P C^2 S_\alpha \tag{7.6}$$

where P is the penetration factor; C is the isospin Clebsch-Gordan coefficient; R is the nuclear radius calculated from $R = R_0(A_t^{1/3} + A_\alpha^{1/3})$, where $R_0 = 1.25$ fm and A_t is the target nucleon number ($A_t = 22$); μ is the reduced mass and S_α is the measured spectroscopic factor.

7.3.3 Quantum Number Measurements at HIγS

Measurements of ^{26}Mg(γ,γ')^{26}Mg are discussed in Chapter 5. The assignments, and how they affect the reaction rate calculations are discussed below:

$\mathbf{E_x = 10647.3(8)}$ keV, $\boldsymbol{J^\pi = 1^+}$

This state is a well known $J^\pi = 1^+$ state [End90]. The present result reduces the uncertainties in resonance energy considerably. However, the close proximity of this state to the α-particle threshold means that its influence on the on the ^{22}Ne+α reaction rates is low.

$\mathbf{E_x = 10805.7(7)}$ keV, $\boldsymbol{J^\pi = 1^-}$

This state was seen previously in ^{22}Ne(^{6}Li,d)^{26}Mg measurements by Ugalde *et al*. [Uga07] at $E_x = 10808(20)$ keV, and in ^{25}Mg(n$_t$,γ)^{26}Mg measurements (thermal neutron capture) by Walkiewicz *et al*. [Wal92] at $E_x = 10805.9(4)$ keV. The previous measurements assigned $J^\pi = (0^+ - 4^+)$, while the present result shows it to have $J^\pi = 1^-$. This unambiguous quantum number assignment is expected to reduce the reaction rate uncertainties arising from this state significantly.

$\mathbf{E_x = 10949.1(8)}$ keV, $\boldsymbol{J^\pi = 1^-}$

This state has been observed previously in ^{26}Mg(p,p$'$)^{26}Mg measurements by Moss *et al*. [Mos76] at $E_x = 10950(3)$ keV. It was also observed in ^{22}Ne(^{6}Li,d)^{26}Mg transfer measurements by Ugalde *et al*. [Uga07] at $E_x = 10953(25)$ keV. The latter measurements could only assign the state with natural parity, although the (p,p$'$) measurements suggest a $J^\pi = 1^-$ state, which agrees with the present

result. One important point to note is that Ugalde *et al.* assumed this state is the same one as that observed in the ^{23}Na(α,pγ)^{26}Mg measurements by Glatz *et al.* [Gla86] at $E_x = 10943(2)$ keV with $J^\pi = (4^\pm - 7^\pm)$. With no further information, it is impossible to know which state was observed by Ugalde *et al.* [Uga07]. Consequently, in the present analysis, the spectroscopic factor that was measured by Ugalde *et al.* is treated as an upper limit, and the same upper limit was used for both states. This is shown is Tab. 7.3.

$\mathbf{E_x = 11153.5(10)\ keV, J^\pi = 1^+}$

This state corresponds to the presumed astrophysically important 630 keV resonance [Dro91, Dro93, Jae01b, Gie93]. The results in chapter 5 show that the state can be assigned with a definite spin-parity of $J^\pi = 1^+$. This unnatural parity state cannot be formed by an α-particle and ^{22}Ne without breaking angular momentum conservation laws, and therefore, cannot contribute to the reaction rate. A previous assignment by Koehler [KÖ2] of $J^\pi = 1^-$ was motivated by erroneous results (background from ^{11}B) in Ref. [Har91], although it could not be assigned without ambiguity.

					Partial Widths (eV)		
E_x (keV)	E_{cm} (keV)	E_{lab} (keV)	J^π	S_α	Γ_α	$\Gamma_\gamma{}^a$	Γ_T
10693 (2)	79	93 (2)	4^+	2.4×10^{-2}	$1.5(12) \times 10^{-46}$	3	3
10805.7 (7)	191	225.9 (5)	1^-	1.9×10^{-2}	1.25×10^{-23}	3	3
10945 (2)	331	391 (2)	$(5^- - 7^-)$	2.8×10^{-3}	$< 370(180) \times 10^{-27}$	3	3
10949.1 (8)	334	395.15 (18)	1^-	2.8×10^{-3}	$< 1.20 \times 10^{-9}$	3	3

Table 7.3: Resonance parameters for states observed in ^{22}Ne(^{6}Li,d)^{26}Mg. These results include the additional quantum number assignments from chapter 5.
[a] Assumed average γ-ray partial width (see Sec. 7.2)

7.3.4 Normalisation of Hauser-Feshbach Reaction Rates at Higher Temperatures

Theoretical Hauser-Feshbach reaction rates are needed at higher temperatures because resonances are only measured up to a finite energy, E_{max}^{exp}. If the effective burning window extends above this energy, the rate will not accurately reflect reality. Statistical techniques must, therefore, be used to calculate a theoretical reaction rate above this temperature. The method used is described in detail in Ref. [New08]. The method uses the following strategy: (i) an *effective thermonuclear energy range*

is defined using the 8^{th}, 50^{th}, and 92^{nd} percentiles of the fractional reaction rate contributions at each temperature (i.e., the reaction rate arising from a single reonance at temperature, T divided by the total reaction rate at T); (ii) the temperature, $T^{\text{ETER}}_{\text{match}}$, at which Hauser-Feshbach reaction rates will be adopted is calculated by

$$E(T^{\text{ETER}}_{\text{match}}) + \Delta E(T^{\text{ETER}}_{\text{match}}) = E^{\text{exp}}_{\text{max}} \tag{7.7}$$

where $\Delta E(T^{\text{ETER}}_{\text{match}})$ is the width of the ETER calculated from the 8^{th} and 92^{nd} rate percentiles. At this point, Hauser-Feshbach reaction rates are normalised to the experimentally determined rates, and extrapolated to higher temperatures. The matching temperature for the $^{22}\text{Ne}(\alpha,\gamma)^{26}\text{Mg}$ reaction is calculated to be $T = 1.33$ GK.

7.3.5 Results

The input file used to calculate the $^{22}\text{Ne}(\alpha,\gamma)^{26}\text{Mg}$ reaction rate with the `RatesMC` code is shown in Fig. 7.1. The reaction rates parameters discussed in Sec. 2.2.3 are tabulated in Tab. 7.4 at a range of temperatures from $T = 0.01$ to 10 GK. The low and high rates should be interpreted as the 0.16 and 0.84 quantiles of the reaction rate distributions. Also tabulated are the lognormal parameters needed to describe the reaction rate probability density function, where μ and σ represent the lognormal parameters of the distribution. A quantitative measure for the agreement between the theoretical lognormal shape and the actual reaction rate distribution is presented in the final column, A-D. A value of $A - D > 30$ means that the lognormal approximation is considered to deviate visibly from the actual distribution. The reaction rate distributions for six sample temperatures are shown in Fig. 7.2. Note that the reaction rate is dominated by upper limits in resonances below $T \approx 0.1$ GK, giving rise to reaction rate distributions that resemble chi-squared distributions (Appendix. A).

The uncertainty bands in Tab. 7.4 are shown in the upper panel of Fig. 7.3 as solid lines. The dashed lines represent the uncertainty bands of the previous reaction rate compilation (NACRE [Ang99]). The lower panel plots the ratio of the present results to the NACRE rates. The present results deviate significantly from the literature reaction rates. This deviation is mostly because of the treatment of upper limits by using a Porter-Thomas probability distribution in the present work. The literature followed the procedure discussed in Sec. 2.2. Another explanation for the large discrepancy in reaction

```
22Ne(a,g)26Mg
************************************************************************************************************************
2               ! Zproj
10              ! Ztarget
0               ! Zexitparticle (=0 when only 2 channels open)
4.003           ! Aproj
21.991          ! Atarget
1.009           ! Aexitparticle (=0 when only 2 channels open)
0.0             ! Jproj
0.0             ! Jtarget
0.5             ! Jexitparticle (=0 when only 2 channels open)
10614.79        ! projectile separation energy (keV)
11093.08        ! exit particle separation energy (=0 when only 2 channels open)
1.25            ! Radius parameter R0 (fm)
2               ! Gamma-ray channel number (=2 if ejectile is a g-ray; =3 otherwise)
************************************************************************************************************************
1.0             ! Minimum energy for numerical integration (keV)
5000            ! Number of random samples (>5000 for better statistics)
0               ! =0 for rate output at all temperatures; =NT for rate output at selected temperatures
************************************************************************************************************************ ********
Nonresonant Contribution
S(keVb)  S'(b)   S''(b/keV)   fracErr   Cutoff Energy (keV)
0.0      0.0     0.0          0.0       0.0
0.0      0.0     0.0          0.0       0.0
************************************************************************************************************************
Resonant Contribution
Note: G1 = entrance channel, G2 = exit channel, G3 = spectator channel !! Ecm, Exf in (keV); wg, Gx in (eV) !!
Note: if Er<0, theta^2=C2S*theta_sp^2 must be entered instead of entrance channel partial width
Ecm      DEcm   wg       Dwg      J   G1         DG1        L1   G2   DG2   L2   G3        DG3      L3   Exf   Int
  78.37  1.7    0        0        4   1.5e-46    1.2e-46    4    3.0  1.5   1    0         0        0    0.0   0
 703.78  2.11   0        0        2   7.2e-6     4.4e-7     2    3.0  1.5   1    2.5e2     1.7e2    1    0.0   1
 826.04  0.19   0        0        4   3.78e-6    4.44e-7    4    3.0  1.5   1    1.47e3    8.0e1    2    0.0   1
 850.44  0.21   0        0        5   4.36e-6    9.09e-7    5    3.0  1.5   1    6.55e3    9.0e1    3    0.0   1
 893.31  0.90   0        0        1   1.17e-4    2.0e-5     1    3.0  1.5   1    1.27e4    2.5e3    1    0.0   1
 911.16  1.69   0        0        1   2.77e-4    2.33e-5    1    3.0  1.5   1    1.80e3    9.0e2    1    0.0   1
1015.22  1.69   0        0        1   2.83e-3    3.33e-4    1    3.0  1.5   1    1.35e4    1.7e3    1    0.0   1
1133.66  8.46   0        0        1   2.0e-2     3.0e-3     1    3.0  1.5   1    6.35e4    8.5e3    1    0.0   1
1171.74  3.38   0        0        1   1.67e-2    2.33e-3    1    3.0  1.5   1    2.45e4    2.4e3    1    0.0   1
1213.0   2.0    0        0        2   1.84e-1    1.03e-1    2    3.0  1.5   1    1.10e3    2.5e2    0    0.0   1
1280.0   4.0    2.0e-3   2.0e-4   1   0          0          0    0    0     0    0         0        1    0.0   0
1297.0   3.0    0        0        1   1.89       7.88e-1    1    3.0  1.5   1    5.0e3     2.0e3    1    0.0   1
1338.0   3.0    0        0        3   6.48e-1    3.33e-1    3    3.0  1.5   1    4.0e3     2.0e3    0    0.0   1
1437.0   3.0    0        0        3   8.58e-1    5.81e-1    3    3.0  1.5   1    3.0e3     2.0e3    0    0.0   1
1525.0   3.0    0        0        1   1.67       4.01e-1    1    3.0  1.5   1    1.5e4     2.0e3    1    0.0   1
1569.0   7.0    0        0        0   1.21e1     2.86       0    3.0  1.5   1    3.3e4     5.0e3    2    0.0   1
1658.0   7.0    0        0        0   1.63e2     3.49e1     0    3.0  1.5   1    5.5e4     1.0e4    2    0.0   1
1728.0   4.0    0        0        0   6.30e2     1.22e2     0    3.0  1.5   1    3.5e4     5.0e3    2    0.0   1
************************************************************************************************************************
Upper Limits of Resonances
Note: enter partial width upper limit by chosing non-zero value for PT, where PT=<theta^2> for particles and...
Note: ...PT=<B> for g-rays [enter: "upper_limit 0.0"]; for each resonance: # upper limits < # open channels!
Ecm      DEcm   Jr  G1         DG1  L1  PT     G2       DG2      L2  PT  G3        DG3      L3  PT   Exf   Int
191.08   0.15   1   1.25e-23   0    1   0.01   3.0      1.5      1   0   0         0        0   0    0.0   0
334.31   0.1    1   1.20e-9    0    1   0.01   3.0      1.5      1   0   0         0        0   0    0.0   0
328.21   2.0    7   3.70e-23   0    7   0.01   3.0      1.5      1   0   0         0        0   0    0.0   0
497.38   0.08   2   9.28e-12   0    2   0.01   1.73     3.1e-2   1   0   2.58e3    2.40e1   0   0    0.0   1
548.16   0.10   2   8.74e-8    0    2   0.01   4.56     2.9e-1   1   0   4.64e3    1.00e2   1   0    0.0   1
556.28   0.16   2   1.25e-7    0    2   0.01   3.0      1.5      1   0   1.44      1.6e-1   2   0    0.0   0
568.27   0.19   1   2.08e-7    0    1   0.01   3.0      1.5      1   0   5.4e-1    8.8e-2   1   0    0.0   0
628.43   0.10   2   9.46e-7    0    2   0.01   7.42     6.0e-1   1   0   4.51e3    1.07e2   1   0    0.0   1
659.32   0.12   2   9.97e-7    0    2   0.01   3.24     3.5e-1   1   0   5.4e2     5.4e1    0   0    0.0   1
665.11   0.11   4   9.16e-8    0    4   0.01   5.9e-1   2.4e-1   1   0   1.51e3    3.4e1    1   0    0.0   1
670.81   0.13   1   1.69e-6    0    1   0.01   7.9e-1   4.6e-1   1   0   1.26e3    1.0e2    1   0    0.0   1
671.59   0.12   2   1.02e-6    0    2   0.01   4.26     6.0e-1   1   0   1.28e1    6.0      2   0    0.0   1
674.36   0.25   2   1.02e-6    0    2   0.01   3.0      1.5      1   0   1.54      4.6e-1   1   0    0.0   0
681.21   0.13   3   7.37e-7    0    3   0.01   3.31     7.3e-1   1   0   8.06e3    1.2e2    1   0    0.0   1
695.95   0.35   1   1.76e-6    0    1   0.01   3.0      1.5      1   0   1.12      4.0e-1   1   0    0.0   0
711.34   0.54   1   1.80e-6    0    1   0.01   3.0      1.5      1   0   6.0e-1    3.2e-1   1   0    0.0   0
713.40   0.14   1   1.81e-6    0    1   0.01   3.63     4.7e-1   1   0   4.2e2     8.6e1    1   0    0.0   1
714.34   0.55   1   1.81e-6    0    1   0.01   3.0      1.5      1   0   2.8       1.0      1   0    0.0   0
722.12   0.56   1   1.83e-6    0    1   0.01   3.0      1.5      1   0   1.42      5.6e-1   1   0    0.0   0
729.15   0.15   2   1.11e-6    0    2   0.01   1.18     2.7e-1   1   0   1.53e2    4.2e1    1   0    0.0   1
730.03   0.16   4   6.16e-7    0    4   0.01   1.82     3.8e-1   1   0   4.13e3    1.9e2    3   0    0.0   1
777.78   0.16   5   1.51e-7    0    5   0.01   3.0      1.5      1   0   2.9e2     1.9e1    2   0    0.0   1
************************************************************************************************************************
Interference between Resonances [numerical integration only]
Note: + for positive, - for negative interference; +- if interference sign is unknown
Ecm    DEcm   Jr    G1      DG1   L1   PT      G2      DG2      L2  PT   G3     DG3    L3  PT   Exf  Int
!+-
0.0    0.0    0.0   0.0     0.0   0    0       0.0     0.0      0   0    0.0    0.0    0   0    0.0  0
0.0    0.0    0.0   0.0     0.0   0    0       0.0     0.0      0   0    0.0    0.0    0   0    0.0  0
************************************************************************************************************************
Reaction Rate and PDF at NT selected temperatures only
Note: default values are used for reaction rate range if Min=Max=0.0
T9    Min   Max
0.01  0.0   0.0
0.1   0.0   0.0
************************************************************************************************************************
Comments:
Reaction Rates using recent FEL results
The doublet state at ~330 keV has been included twice as upper limits for the spectroscopic factor
The 703 keV resonance is treated as the same as seen in 22Ne(a,n)
```

Figure 7.1: RatesMC input file for ^{22}Ne(α,γ)^{26}Mg reaction rates.

T (GK)	Low rate	Median rate	High rate	lognormal μ	lognormal σ	A-D
0.010	3.26×10^{-78}	7.98×10^{-78}	1.93×10^{-77}	$-1.775\times10^{+02}$	8.89×10^{-01}	4.15×10^{-01}
0.011	1.24×10^{-74}	2.74×10^{-74}	6.02×10^{-74}	$-1.694\times10^{+02}$	7.94×10^{-01}	3.55×10^{-01}
0.012	1.11×10^{-71}	2.34×10^{-71}	4.93×10^{-71}	$-1.626\times10^{+02}$	7.38×10^{-01}	2.91×10^{-01}
0.013	3.47×10^{-69}	7.08×10^{-69}	1.45×10^{-68}	$-1.569\times10^{+02}$	7.12×10^{-01}	3.16×10^{-01}
0.014	4.66×10^{-67}	9.43×10^{-67}	1.91×10^{-66}	$-1.520\times10^{+02}$	7.06×10^{-01}	2.93×10^{-01}
0.015	3.18×10^{-65}	6.48×10^{-65}	1.32×10^{-64}	$-1.478\times10^{+02}$	7.14×10^{-01}	3.59×10^{-01}
0.016	1.25×10^{-63}	2.61×10^{-63}	5.39×10^{-63}	$-1.441\times10^{+02}$	7.31×10^{-01}	3.43×10^{-01}
0.018	5.54×10^{-61}	1.21×10^{-60}	2.64×10^{-60}	$-1.380\times10^{+02}$	7.77×10^{-01}	2.38×10^{-01}
0.020	7.04×10^{-59}	1.63×10^{-58}	3.72×10^{-58}	$-1.331\times10^{+02}$	8.27×10^{-01}	2.56×10^{-01}
0.025	6.11×10^{-55}	1.28×10^{-54}	2.93×10^{-54}	$-1.241\times10^{+02}$	7.94×10^{-01}	$1.83\times10^{+00}$
0.030	2.16×10^{-50}	2.17×10^{-49}	7.94×10^{-49}	$-1.125\times10^{+02}$	$1.79\times10^{+00}$	$1.22\times10^{+02}$
0.040	1.41×10^{-42}	1.49×10^{-41}	5.46×10^{-41}	$-9.454\times10^{+01}$	$2.04\times10^{+00}$	$1.60\times10^{+02}$
0.050	6.58×10^{-38}	6.98×10^{-37}	2.56×10^{-36}	$-8.379\times10^{+01}$	$2.05\times10^{+00}$	$1.61\times10^{+02}$
0.060	8.28×10^{-35}	8.62×10^{-34}	3.16×10^{-33}	$-7.662\times10^{+01}$	$1.91\times10^{+00}$	$1.39\times10^{+02}$
0.070	2.64×10^{-32}	1.49×10^{-31}	5.05×10^{-31}	$-7.125\times10^{+01}$	$1.49\times10^{+00}$	$7.29\times10^{+01}$
0.080	4.50×10^{-30}	1.63×10^{-29}	3.76×10^{-29}	$-6.652\times10^{+01}$	$1.20\times10^{+00}$	$8.01\times10^{+01}$
0.090	2.54×10^{-28}	1.16×10^{-27}	4.41×10^{-27}	$-6.214\times10^{+01}$	$1.46\times10^{+00}$	$2.11\times10^{+01}$
0.100	7.38×10^{-27}	6.43×10^{-26}	2.71×10^{-25}	$-5.830\times10^{+01}$	$1.75\times10^{+00}$	$4.59\times10^{+01}$
0.110	1.76×10^{-25}	1.84×10^{-24}	7.94×10^{-24}	$-5.503\times10^{+01}$	$1.93\times10^{+00}$	$7.43\times10^{+01}$
0.120	2.80×10^{-24}	3.05×10^{-23}	1.32×10^{-22}	$-5.226\times10^{+01}$	$1.99\times10^{+00}$	$8.68\times10^{+01}$
0.130	3.06×10^{-23}	3.26×10^{-22}	1.41×10^{-21}	$-4.986\times10^{+01}$	$1.93\times10^{+00}$	$7.67\times10^{+01}$
0.140	2.66×10^{-22}	2.50×10^{-21}	1.06×10^{-20}	$-4.774\times10^{+01}$	$1.77\times10^{+00}$	$5.20\times10^{+01}$
0.150	2.39×10^{-21}	1.52×10^{-20}	6.15×10^{-20}	$-4.583\times10^{+01}$	$1.56\times10^{+00}$	$2.69\times10^{+01}$
0.160	1.89×10^{-20}	8.09×10^{-20}	2.89×10^{-19}	$-4.406\times10^{+01}$	$1.34\times10^{+00}$	$1.23\times10^{+01}$
0.180	7.20×10^{-19}	2.08×10^{-18}	5.14×10^{-18}	$-4.081\times10^{+01}$	9.99×10^{-01}	$1.81\times10^{+01}$
0.200	1.56×10^{-17}	3.98×10^{-17}	8.78×10^{-17}	$-3.782\times10^{+01}$	8.62×10^{-01}	$9.51\times10^{+00}$
0.250	9.78×10^{-15}	1.94×10^{-14}	4.22×10^{-14}	$-3.154\times10^{+01}$	7.15×10^{-01}	$3.69\times10^{+00}$
0.300	1.14×10^{-12}	1.96×10^{-12}	3.44×10^{-12}	$-2.695\times10^{+01}$	5.54×10^{-01}	5.65×10^{-01}
0.350	3.65×10^{-11}	5.92×10^{-11}	9.26×10^{-11}	$-2.357\times10^{+01}$	4.74×10^{-01}	$5.04\times10^{+00}$
0.400	4.89×10^{-10}	7.88×10^{-10}	1.18×10^{-09}	$-2.100\times10^{+01}$	4.45×10^{-01}	$1.38\times10^{+01}$
0.450	3.72×10^{-09}	5.95×10^{-09}	8.73×10^{-09}	$-1.898\times10^{+01}$	4.36×10^{-01}	$1.92\times10^{+01}$
0.500	1.89×10^{-08}	3.00×10^{-08}	4.38×10^{-08}	$-1.737\times10^{+01}$	4.34×10^{-01}	$2.15\times10^{+01}$
0.600	2.21×10^{-07}	3.46×10^{-07}	4.98×10^{-07}	$-1.492\times10^{+01}$	4.17×10^{-01}	$2.06\times10^{+01}$
0.700	1.49×10^{-06}	2.21×10^{-06}	3.04×10^{-06}	$-1.306\times10^{+01}$	3.63×10^{-01}	$1.58\times10^{+01}$
0.800	7.75×10^{-06}	1.07×10^{-05}	1.43×10^{-05}	$-1.146\times10^{+01}$	3.06×10^{-01}	$6.45\times10^{+00}$
0.900	3.34×10^{-05}	4.41×10^{-05}	5.84×10^{-05}	$-1.002\times10^{+01}$	2.92×10^{-01}	$2.01\times10^{+00}$
1.000	1.19×10^{-04}	1.56×10^{-04}	2.14×10^{-04}	$-8.742\times10^{+00}$	3.04×10^{-01}	$9.64\times10^{+00}$
1.250	1.45×10^{-03}	1.92×10^{-03}	2.73×10^{-03}	$-6.229\times10^{+00}$	3.23×10^{-01}	$1.33\times10^{+01}$
1.500	(9.69×10^{-03})	(1.34×10^{-02})	(1.85×10^{-02})	$(-4.314\times10^{+00})$	(3.22×10^{-01})	
1.750	(5.05×10^{-02})	(6.96×10^{-02})	(9.61×10^{-02})	$(-2.664\times10^{+00})$	(3.22×10^{-01})	
2.000	(2.01×10^{-01})	(2.77×10^{-01})	(3.83×10^{-01})	$(-1.283\times10^{+00})$	(3.22×10^{-01})	
2.500	$(1.71\times10^{+00})$	$(2.36\times10^{+00})$	$(3.25\times10^{+00})$	(8.570×10^{-01})	(3.22×10^{-01})	
3.000	$(8.30\times10^{+00})$	$(1.15\times10^{+01})$	$(1.58\times10^{+01})$	$(2.439\times10^{+00})$	(3.22×10^{-01})	
3.500	$(2.80\times10^{+01})$	$(3.87\times10^{+01})$	$(5.34\times10^{+01})$	$(3.655\times10^{+00})$	(3.22×10^{-01})	
4.000	$(7.38\times10^{+01})$	$(1.02\times10^{+02})$	$(1.41\times10^{+02})$	$(4.623\times10^{+00})$	(3.22×10^{-01})	
5.000	$(3.15\times10^{+02})$	$(4.35\times10^{+02})$	$(6.01\times10^{+02})$	$(6.076\times10^{+00})$	(3.22×10^{-01})	
6.000	$(8.91\times10^{+02})$	$(1.23\times10^{+03})$	$(1.70\times10^{+03})$	$(7.115\times10^{+00})$	(3.22×10^{-01})	
7.000	$(1.95\times10^{+03})$	$(2.69\times10^{+03})$	$(3.71\times10^{+03})$	$(7.896\times10^{+00})$	(3.22×10^{-01})	
8.000	$(3.59\times10^{+03})$	$(4.95\times10^{+03})$	$(6.83\times10^{+03})$	$(8.508\times10^{+00})$	(3.22×10^{-01})	
9.000	$(5.82\times10^{+03})$	$(8.03\times10^{+03})$	$(1.11\times10^{+04})$	$(8.991\times10^{+00})$	(3.22×10^{-01})	
10.000	$(8.68\times10^{+03})$	$(1.20\times10^{+04})$	$(1.65\times10^{+04})$	$(9.391\times10^{+00})$	(3.22×10^{-01})	

Table 7.4: Monte Carlo reaction rates for the ^{22}Ne(α,γ)^{26}Mg reaction. Numbers in parentheses indicate rates that have been normalised to Hauser-Feshbach rates from Ref. [Rau01].

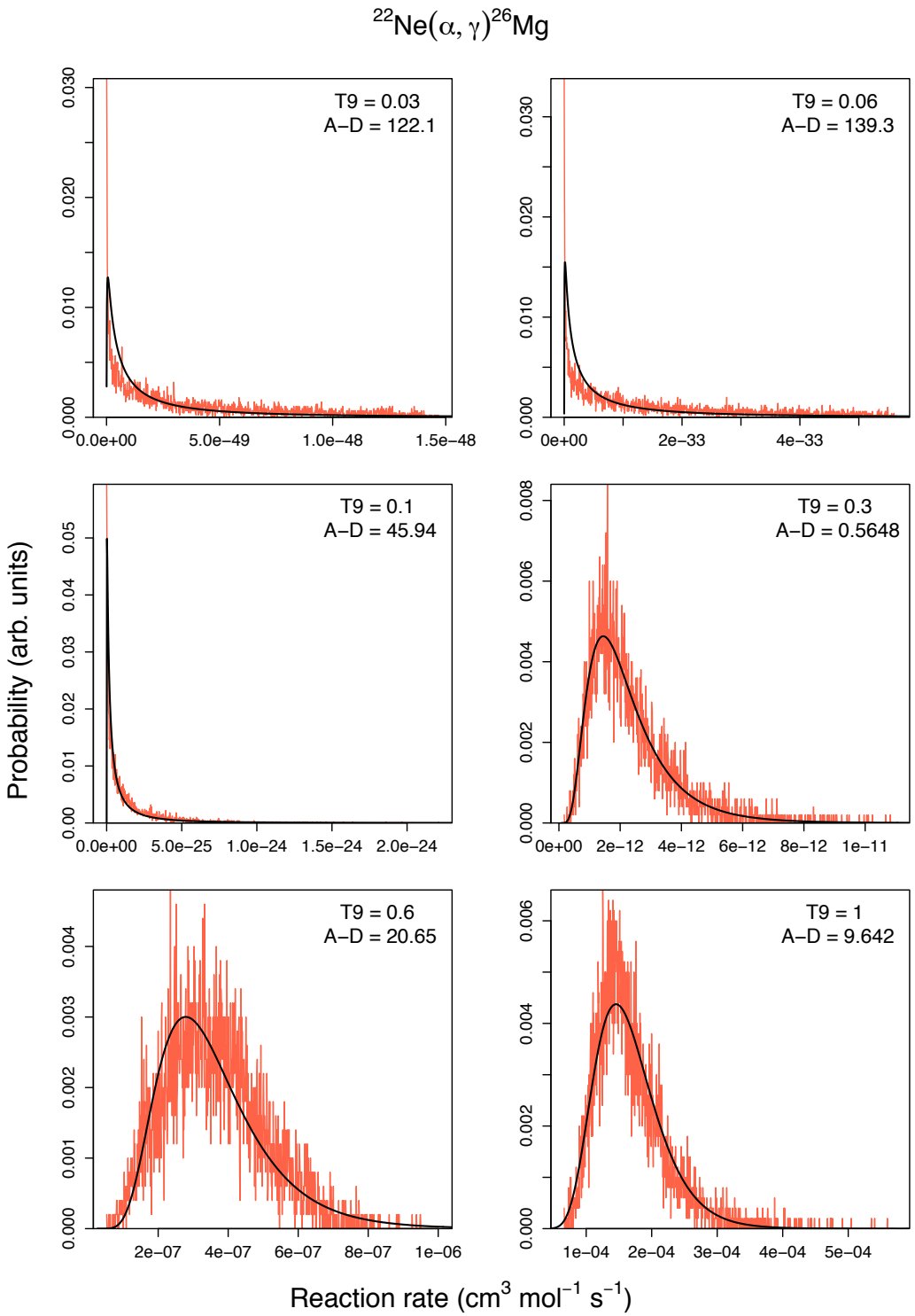

Figure 7.2: Reaction rate probability densities for the ^{22}Ne(α,γ)^{26}Mg reaction. Shown are histograms of the reaction rates and the associated lognormal function used to approximate the rates.

rates between the present results and the NACRE rates could be their treatment of resonance widths. In the NACRE rate calculation, the cross sections were integrated assuming wide resonances by using upper limit total widths ($\Gamma = 4 - 10$ keV) that are considerably larger than the widths used in the present analysis.

Several studies of the compound nucleus ^{26}Mg have been performed since the NACRE rates were published. Directly measured ^{22}Ne$(\alpha, \mathrm{n})^{25}$Mg measurements [Jae01b] and an R-matrix analysis of ^{25}Mg(n,γ)^{26}Mg [KÖ2] have provided improved estimates for the parameters of excited states. A comparison of the reaction rates before and after the measurement described in Ch. 5 is shown in Fig. 7.4.

The upper panel in Fig. 7.4 shows clearly that the reaction rate uncertainties have been reduced significantly between $T = 0.03$ and 0.1 GK. This is because of the unique quantum number assignment for the excited state at $E_x = 10805$ keV (Sec. 5.4.3). The lower panel shows a sharp peak in the reaction rate ratio, corresponding to a rate approximately 1000 times larger at $T = 0.1$ GK. This spike results from the spin-parity assignment of $J^\pi = 1^-$ to the excited state at $E_x = 10949$ keV. This state was previously believed to have a spin of $J = 4 - 7$. In the present analysis, this state was split into a doublet, and each was assigned an upper limit spectroscopic factor that was measured by Ref. [Uga07]. The lack of resonance information in this energy region means that an upper limit partial width will have a significant effect on the reaction rates.

7.3.6 Influence of 832 keV Resonance Assignments

The resonance at $E_r^{\mathrm{lab}} = 832$ keV was assumed to correspond to the same state as the resonance measured in ^{22}Ne(α,n)^{25}Mg [Wol89, Dro93, Jae01b]. This state has been assumed to be a $J^\pi = 2^+$ state. The other possibility is that these two states are, indeed, distinct as suggested by Ref. [KÖ2].

Figure 7.5 shows the effect of separating this resonance into two levels on the ^{22}Ne(α,γ)^{25}Mg reaction rate. In separating this state, the only known level that is close in energy is located at $\mathrm{E}_x = 11310.50(49)$ keV (compared with $\mathrm{E}_x = 11315(5)$ measured by Wolke). This state has $J^\pi = 1^-$ (a spin assignment couldn't be made by Wolke *et al.* [Wol89]), which results in a higher reaction rate for the separate state assumption. See Sec. 7.2 for more discussion on the procedure used in the present study. The difference between the rather arbitrary choice of assignments clearly shows that

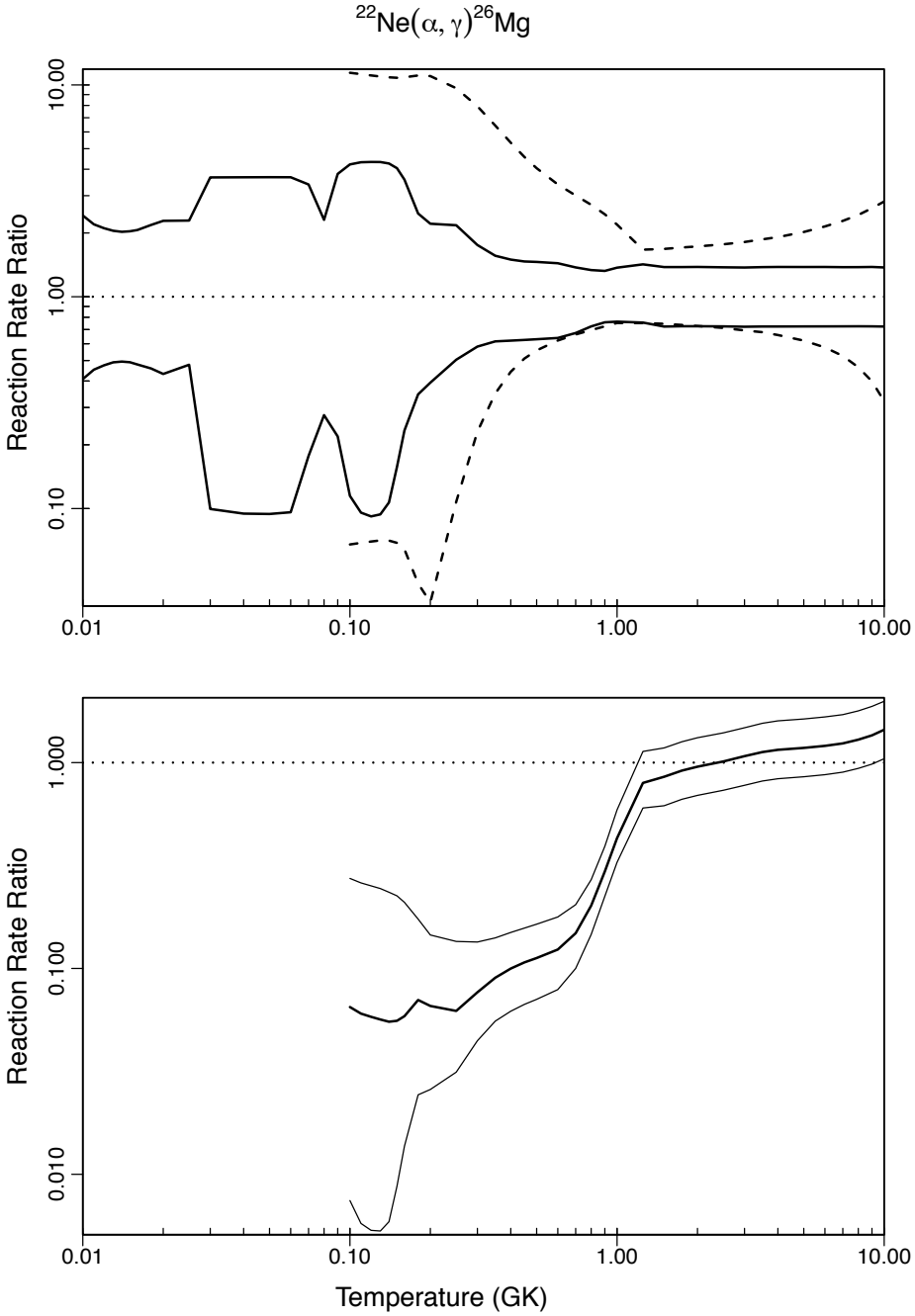

Figure 7.3: The uncertainty bands for the ^{22}Ne(α,γ)^{26}Mg reaction. The largest uncertainties are caused by upper limit resonances, and uncertainties in the strengths of the lower measured resonances. The lower panel is a comparison to the NACRE rates. In the upper figure, the solid lines represent the present high and low reaction rates normalised to the recommended rate. The dashed lines represent the literature upper and lower reaction rates normalised to the literature recommended rate. In the lower panel, the present results are normalised to the literature rates (the thick line represents the recommended rate and the thinner lines show the high and low rates). Points below unity show that the present rates are lower than the literature rates.

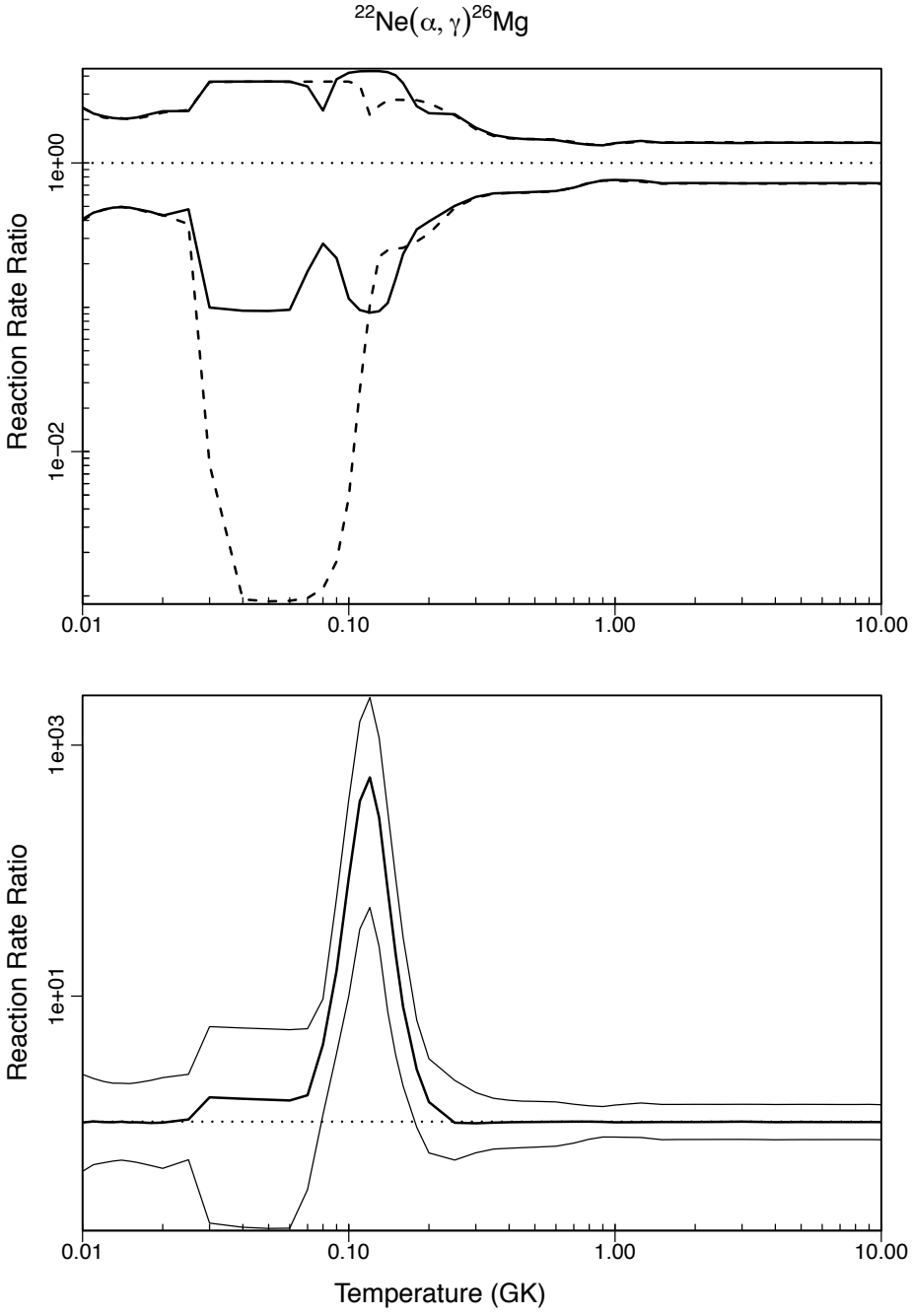

Figure 7.4: Comparison of the present results to the reaction rates calculated prior to the measurements in Ch. 5. See Fig. 7.3 for a description of the plot.

the parameters of these resonances must be measured carefully for both the ^{22}Ne$(\alpha,\gamma)^{26}$Mg and the ^{22}Ne$(\alpha,\mathrm{n})^{25}$Mg reactions to resolve this issue.

7.4 The ^{22}Ne$(\alpha$,n$)^{26}$Mg Reaction

The ^{22}Ne$(\alpha,\mathrm{n})^{25}$Mg reaction is the s-process neutron source thought to be active in AGB stars and during the helium burning stage of massive stars. It has been studied more extensively than the competing ^{22}Ne(α,γ)^{26}Mg reaction. The lowest measured resonance is located at $E_r = 832$ keV [Jae01b], at the upper edge of the Gamow peak (for $T = 0.3$ GK, the Gamow peak is located at $E_0 = 600$ keV with $\Delta E = 290$ keV). A resonance was thought to have been observed at $E_r = 633$ keV, but was later found to be caused by background from ^{10}B [Dro93], and gave rise to some controversy [Jae01b, Gie93, Uga07]. Significant rate uncertainties still exist in this reaction as outlined in the following analysis.

7.4.1 Directly Measured Resonances

Resonance parameters below $E_r^{\mathrm{lab}} = 1434$ keV were adopted according to the discussion in Sec. 7.2. Above the highest energy measured resonance of Ref. [Jae01b] at $E_r = 1434(2)$ keV, the work of Drotleff *et al*. [Dro93] is used for resonances in the ^{22}Ne$(\alpha,\mathrm{n})^{25}$Mg reaction from $E_r = 1475(3)$ keV to $E_r = 2289(15)$ keV. No normalisation in the studies is performed in the present analysis because the few resonances that coincide between the studies did not have a consistent magnitude shift and any normalisation would therefore be arbitrary.

$\mathbf{E_r > 1000}$ keV Resonances

Excited states above $\mathrm{E}_x = 11465$ keV have not been analysed by any other experiments. For these resonances, the energy and total width of Ref. [Jae01b] have been used. In order to numerically integrate the cross sections of these resonances, the α-particle, γ-ray and neutron partial widths must be known. For the γ-ray partial width, an average of $\Gamma_\gamma = 3$ eV is used. Note that if $\omega\gamma$ is small compared to the width of the resonance, at these energies the neutron partial width will dominate the

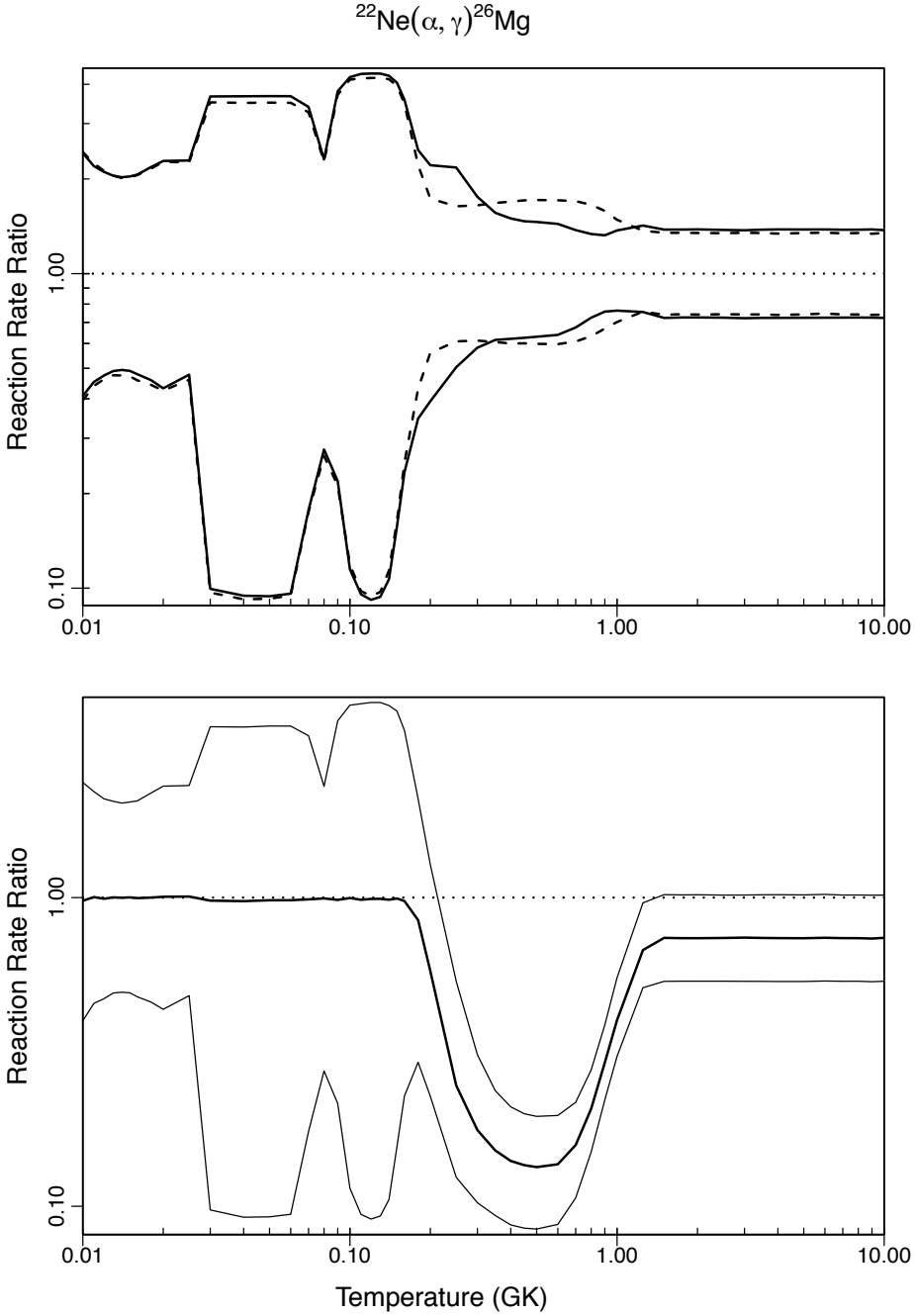

Figure 7.5: The effect on the reaction rate of separating the 832 keV resonance into two states as discussed in the text. The top panel shows that the uncertainty bands remain approximately constant between the two calculations (solid lines correspond to the single state assumption). The lower panel shows the ratio of recommended reaction rates for the single state assumption and that of the doublet. A ratio larger than unity means that the single state assumption produces a larger rate. The lower panel shows a significantly lower reaction rate for the single state assumption between $T = 0.2$ and 1.0 GK.

total width of the resonance. Thus, the α-particle partial width is calculated as follows.

$$\begin{aligned}\omega\gamma =& \omega\frac{\Gamma_\alpha\Gamma_n}{\Gamma_\alpha+\Gamma_n+\Gamma_\gamma} \\ \approx& \omega\frac{\Gamma_\alpha\Gamma_n}{\Gamma_n}\end{aligned} \tag{7.8}$$

$$\omega\gamma \approx \omega\Gamma_\alpha \tag{7.9}$$

As the resonance strength becomes comparable to the total width of the resonance, this approximation is not valid because $\Gamma_\alpha \sim \Gamma_n$, and the resonance cross section cannot be integrated numerically.

					Partial Widths (eV)				
E_x (keV)	E_{cm} (keV)	E_{lab} (keV)[a]	J^π	$\omega\gamma$ (eV)[a]	Γ_α[b]	Γ_γ[e]	Γ_n[c]	Γ_T	Int
11319	704	831.9(24)	2^+	$1.18(11)\times10^{-4}$	$2.36(22)\times10^{-5}$	3	250 (170)	250 (170)	✓
11441	826	976.39(23)	4^+	$3.4(4)\times10^{-5}$	$1.13(13)\times10^{-5}$	3	$1.475\ (80)\times10^{3}$	$1.475\ (80)\times10^{3}$	✓
11465	850	1005.23(25)	5^-	$4.8(10)\times10^{-5}$	$1.60(33)\times10^{-5}$	3	$6.554\ (90)\times10^{3}$	$6.554\ (90)\times10^{3}$	✓
11506	891	1053(2)	1^-	$3.5(6)\times10^{-4}$	$1.17(20)\times10^{-4}$	3	$1.27\ (25)\times10^{4}$	$1.27\ (25)\times10^{4}$	✓
11526	911	1077(2)	1^-	$8.3(7)\times10^{-4}$	$2.77(23)\times10^{-4}$	3	$1.8\ (9)\times10^{3}$	$1.8\ (9)\times10^{3}$	✓
11630	1015	1200(2)	1^-	$8.5(10)\times10^{-3}$	$2.83(33)\times10^{-3}$	3	$1.35\ (17)\times10^{4}$	$1.35\ (17)\times10^{4}$	✓
11748	1134	1340(10)	1^-	$6.0(9)\times10^{-2}$	$2.00(30)\times10^{-2}$	3	$6.35\ (85)\times10^{4}$	$6.35\ (85)\times10^{4}$	✓
11787	1172	1385(4)	1^-	$5.0(7)\times10^{-2}$	$1.67(23)\times10^{-2}$	3	$2.45\ (34)\times10^{4}$	$2.45\ (34)\times10^{4}$	✓
11828	1213	1434(3)	2^+	$1.067(42)\times10^{+0}$	$2.134(84)\times10^{-1}$	3	$1.10\ (25)\times10^{3}$	$1.10\ (25)\times10^{3}$	✓
11863	1248	1475(3)	1^-	$4.5(30)\times10^{+1}$	$4.5(30)\times10^{+1}$	3	$1.4\ (5)\times10^{4}$	$1.4\ (5)\times10^{4}$	✓
11880	1265	1495(3)	1^-	$3.88(57)\times10^{+2}$	----	3	----	----	
11891	1276	1508(3)	1^-	$5.60(60)\times10^{+2}$	----	3	----	----	
11910	1295	1531(3)	$1^-, 2^+$ [d]	$1.445(160)\times10^{+3}$	----	3	----	----	
11951	1337	1580(3)	$2^+, 3^-, 4^+$ [d]	$2.90(30)\times10^{+3}$	----	3	----	----	
12052	1437	1699(3)	$2^+, 3^-$ [d]	$6.035(770)\times10^{+3}$	----	3	----	----	
12115	1500	1773(5)	1^-	$1.00(24)\times10^{+3}$	----	3	----	----	
12141	1526	1804(3)	1^-	$3.010(335)\times10^{+3}$	----	3	----	----	
12184	1569	1855(8)	(0^+) [d]	$8.95(210)\times10^{+2}$	----	3	----	----	
12265	1650	1950(10)	(0^+) [d]	$3.10(85)\times10^{+4}$	----	3	----	----	
12346	1731	2046(8)	0^+ [d]	$1.97(33)\times10^{+5}$	----	3	----	----	
12435	1821	2152(10)	1^-	$2.76(70)\times10^{+4}$	----	3	----	----	
12551	1937	2289(15)	1^-	$1.21(45)\times10^{+5}$	----	3	----	----	

Table 7.5: Directly measured resonances in the ^{22}Ne(α,n)^{25}Mg reaction.
[a] See text for details.
[b] Calculated using Eq. (7.9).
[c] Assuming Γ_T is dominated by Γ_n.
[d] From Ref. [Wol89].
[e] See text for details.

7.4.2 Upper Limit Resonances

The resonance strength upper limits of resonances in the ^{22}Ne(α,n)^{25}Mg reaction have been calculated in a similar way to those in the ^{22}Ne(α,γ)^{26}Mg case (Section 7.3.1). In this case, Fig. 1 of

Ref. [Jae01b] was used to extract the upper limits from the measured yield.

In addition to this method, the PhD thesis of Jaeger [Jae01a] contains calculated upper limits. This method is preferable to the methods above as they do not rely on reading yield values off a graph.

					Partial Widths (eV)				
E_x (keV)	E_{cm} (keV)	E_{cm} (keV)[a]	J^π	$\omega\gamma_{UL}$ (eV)	$\Gamma_{\alpha,UL}$	Γ_n	Γ_γ	Γ_T	Int
11112	497	587.90(10)	2^+	5.8×10^{-8}	7.7×10^{-9}	2578(180))	1.732(31)	2580(24)	✓
11163	548	647.93(11)	2^+	1.9×10^{-7}	3.8×10^{-8}	4644(100)	4.56(29)	4649(100)	✓
11171	556	657.53(19)	(2^+)	7.5×10^{-8}	1.5×10^{-8}	1.44(16)	3	4.4(15)	
11183	568	671.70(21)	(1^-)	7.7×10^{-5}	2.1×10^{-7}	0.540(88)	3	3.5(15)	
11243	628	742.81(12)	$2^{(-)}$	1.2×10^{-7}	2.4×10^{-8}	4511(107)	7.42(60)	4518(110)	✓
11274	659	779.32(14)	$(2)^+$	1.1×10^{-7}	2.2×10^{-8}	540(54)	3.24(35)	543(54)	✓
11280	665	786.17(13)	$4^{(-)}$	1.3×10^{-7}	1.4×10^{-8}	1513(34)	0.59(24)	1514(34)	✓
11286	671	792.90(15)	1^-	7.7×10^{-8}	2.6×10^{-8}	1256(100)	0.79(46)	1260(100)	✓
11286	672	793.83(14)	(2^+)	7.7×10^{-8}	1.5×10^{-8}	12.80(60)	4.26(60)	17.1(60)	✓
11289	674	797.10(29)	(2^-)	7.7×10^{-8}	1.5×10^{-8}	1.54(46)	3	4.5(16)	
11296	681	805.19(16)	(3^-)	1.0×10^{-7}	1.4×10^{-8}	8060(120)	3.31(73)	8060(120)	✓
11311	696	822.62(41)	(1^-)	1.6×10^{-8}	5.3×10^{-9}	1.12(40)	3	4.1(16)	
11326	711	840.81(63)	(1^-)	1.2×10^{-7}	4.1×10^{-8}	0.60(32)	3	3.6(15)	
11328	713	843.24(17)	1^-	5.0×10^{-7}	1.7×10^{-7}	424(86)	3.63(47)	428(86)	✓
11329	714	844.35(64)	(1^-)	1.2×10^{-7}	4.1×10^{-8}	2.8(10)	3	5.8(18)	
11337	722	853.55(67)	(1^-)	1.3×10^{-7}	4.2×10^{-8}	1.42(56)	3	4.4(18)	
11344	729	861.86(18)	(2^+)	2.0×10^{-7}	4.0×10^{-8}	153(42)	1.18(27)	154(42)	✓
11345	730	862.91(19)	$4^{(-)}$	4.2×10^{-8}	4.7×10^{-9}	4130(190)	1.82(38)	4130(190)	✓
11393	778	919.34(19)	$5^{(+)}$	3.7×10^{-8}	3.3×10^{-9}	290(19)	3	293(19)	✓

Table 7.6: Upper limit resonances in the ^{22}Ne(α,n)^{25}Mg reaction; γ-ray and neutron partial widths are taken from the R-matrix fit of Ref. [KÖ2].
[a] Weighted averages from Refs. [Mos76, Wei76, Gla86, Wol89, KÖ2].

7.4.3 Normalisation of Hauser-Feshbach Reaction Rates at Higher Temperatures.

The method used for matching Hauser-Feshbach reaction rates to experimental rates is the same as that outlined in section 7.3.4. In the process of matching the ^{22}Ne(α,n)^{26}Mg reaction rates, it was found that at low temperatures, the only strongly contributing resonance was the lowest measured one at $E_r^{\text{lab}} = 843$ keV. A single contributing resonance does not agree with the statistical assumptions of Ref. [New08] and consequently, the reaction rates were matched at an erroneous temperature. Visual inspection of the resonance contributions in Fig. 7.6 shows that the true matching temperature should be at approximately 1.0 GK, where the $E_{lab} = 823$ keV resonance has a negligible contribution to the total reaction rate. For this reason, it is safe to remove that resonance, and match the Hauser-Feshbach

rates with a truncated set of resonances. This truncated set yields a matching temperature of $T = 1.37$ GK.

7.4.4 Results

The input file used to calculate the rate of the ^{22}Ne$(\alpha, \mathrm{n})^{25}$Mg reaction with the `RatesMC` Monte Carlo code is shown in Fig. 7.7. The resulting reaction rates are tabulated in Tab. 7.7. Note that for this reaction, the Anderson-Darling statistic begins at higher temperatures to show agreement between the lognormal approximation to the rate distribution and the actual distribution. This agreement is for two reasons: (i) experiments have focused on measuring this reaction directly, resulting in a more complete data set for resonance parameters; and (ii) Lower lying states in ^{26}Mg no longer contribute to the rate because they are below the neutron threshold. This effect can also be seen in Fig. 7.8, where the reaction rate distributions better resemble lognormal shapes. Note the effect of an upper limit cutoff on the reaction rate distributions at $T = 0.06$ GK.

The uncertainty bands in Tab. 7.7 are shown in Fig. 7.9 as solid lines. The upper panel shows the current uncertainty bands in comparison to those from NACRE [Ang99]. The first thing to note is the dramatic reduction in uncertainties in the present rates. This reduction results partially from improved measurements of resonance parameters by Refs. [Jae01b, KÖ2]. The lower panel in Fig. 7.9 shows that the present reaction rates are up to a factor of 10 smaller than those presented in NACRE [Ang99]. Once again, this is mostly a result of the treatment of upper limits in the present study. The determination of unnatural parity for the previously assumed natural parity $E_x = 11154$ keV excited state in ^{26}Mg ($E_r^{\mathrm{lab}} \approx 630$ keV) also serves to lower the reaction rate. Additionally, the NACRE reaction rate analysis assumed wide resonances, with resonance widths given by the measured upper limits, which are a factor of 100 larger than those used in the present analysis.

A comparison with the most recent reaction rate calculations by Ref. [Jae01b] is shown in Fig. 7.10. The top panel shows a significant reduction in uncertainties in the present rate calculations from a factor of ten to a factor of two between $T = 0.1$ and 0.2 GK. This reduction in uncertainties is partially based on the present result for the $E_x = 11154$ keV state, and also partially arises from the improved resonance parameter measurements from Ref. [KÖ2]. The lower panel shows that the current recommended reaction rates agree well with the previous results between $T = 0.1$ and 1.0

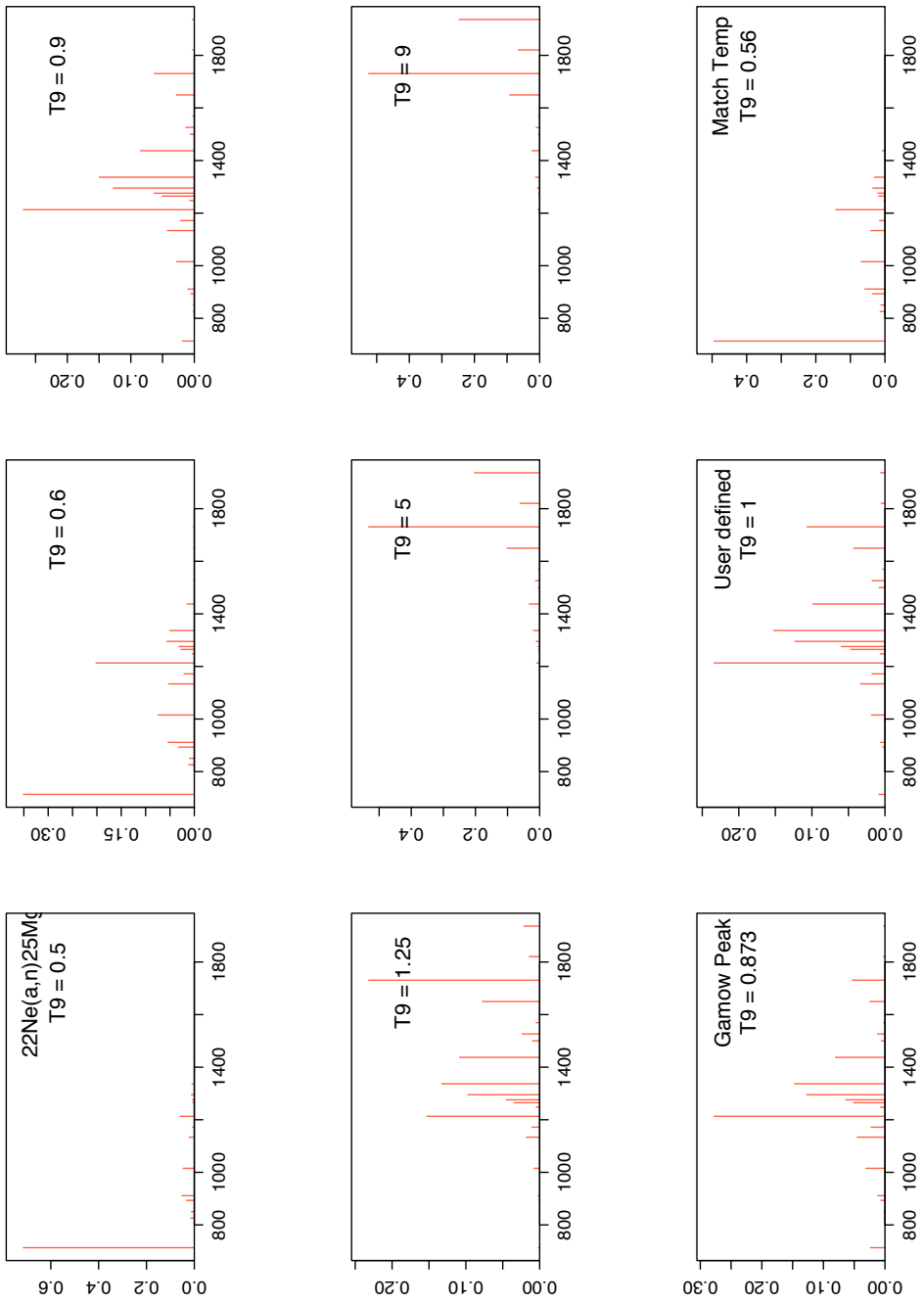

Figure 7.6: Resonance contributions to the ^{22}Ne(α,n)^{26}Mg reaction rate. The strong resonance at $E_{lab} = 843$ keV dominates the rate at low temperatures, giving rise to an unreasonable Hauser-Feshbach matching temperature. The figure clearly shows that the true matching temperature should be at $T_9 \approx 1$. A similar method of using the Gamow peak defined in Sec. 2.1 to normalise Hauser-Feshbach rates is also shown (see Ref. [New08]).

```
22Ne(a,n)25Mg
************************************************************************************************************************
2               ! Zproj
10              ! Ztarget
0               ! Zexitparticle (=0 when only 2 channels open)
4.003           ! Aproj
21.991          ! Atarget
1.009           ! Aexitparticle (=0 when only 2 channels open)
0.0             ! Jproj
0.0             ! Jtarget
0.5             ! Jexitparticle (=0 when only 2 channels open)
10614.79        ! projectile separation energy (keV)
11093.08        ! exit particle separation energy (=0 when only 2 channels open)
1.25            ! Radius parameter R0 (fm)
3               ! Gamma-ray channel number (=2 if ejectile is a g-ray; =3 otherwise)
************************************************************************************************************************
1.0             ! Minimum energy for numerical integration (keV)
5000            ! Number of random samples (>5000 for better statistics)
0               ! =0 for rate output at all temperatures; =NT for rate output at selected temperatures
************************************************************************************************************************
Nonresonant Contribution
S(keVb)  S'(b)   S''(b/keV)   fracErr   Cutoff Energy (keV)
0.0      0.0     0.0          0.0       0.0
0.0      0.0     0.0          0.0       0.0
************************************************************************************************************************
Resonant Contribution
Note: G1 = entrance channel, G2 = exit channel, G3 = spectator channel !! Ecm, Exf in (keV); wg, Gx in (eV) !!
Note: if Er<0, theta^2=C2S*theta_sp^2 must be entered instead of entrance channel partial width
Ecm      DEcm   wg      Dwg      J   G1        DG1       L1  G2        DG2       L2  G3  DG3   L3  Exf   Int
703.78   2.11   0       0        2   2.36e-5   2.2e-6    2   2.5e2     1.7e2     2   3   1.5   1   0.0   1
826.04   0.19   0       0        4   3.78e-6   4.4e-7    4   1.47e3    8.0e1     4   3   1.5   1   0.0   1
850.44   0.21   0       0        5   4.36e-6   9.1e-7    5   6.55e3    9.0e1     5   3   1.5   1   0.0   1
893.31   0.90   0       0        1   1.17e-4   2.0e-5    1   1.27e4    2.5e3     1   3   1.5   1   0.0   1
911.16   1.69   0       0        1   2.77e-4   2.3e-5    1   1.80e3    9.0e2     1   3   1.5   1   0.0   1
1015.22  1.69   0       0        1   2.83e-3   3.3e-4    1   1.35e4    1.7e3     1   3   1.5   1   0.0   1
1133.66  8.46   0       0        1   2.0e-2    3.0e-3    1   6.35e4    8.5e3     1   3   1.5   1   0.0   1
1171.74  3.38   0       0        1   1.67e-2   2.3e-3    1   2.45e4    2.4e3     1   3   1.5   1   0.0   1
1213.19  2.34   0       0        2   2.13e-1   8.4e-3    2   1.10e3    2.5e2     2   3   1.5   1   0.0   1
1247.88  2.54   0       0        1   1.5e-2    1.0e-2    1   2.45e4    3.4e3     1   3   1.5   1   0.0   1
1264.80  2.54   3.9e-1  5.7e-2   1   0         0         1   0         0         1   0   0     1   0.0   0
1275.80  2.54   5.6e-1  6.0e-2   1   0         0         1   0         0         1   0   0     1   0.0   0
1295.25  2.54   1.5     1.6e-1   1   0         0         1   0         0         1   0   0     1   0.0   0
1336.71  2.54   2.9     3.0e-1   1   0         0         1   0         0         1   0   0     1   0.0   0
1437.38  2.54   6.0     7.7e-1   1   0         0         1   0         0         1   0   0     1   0.0   0
1499.99  4.23   1.0     2.4e-1   1   0         0         1   0         0         1   0   0     1   0.0   0
1526.22  2.54   3.0     3.4e-1   1   0         0         1   0         0         1   0   0     1   0.0   0
1569.36  6.77   9.0e-1  2.1e-1   1   0         0         1   0         0         1   0   0     1   0.0   0
1649.74  8.46   3.1e+1  8.5      1   0         0         1   0         0         1   0   0     1   0.0   0
1730.95  6.77   2.0e+2  3.3e+1   1   0         0         1   0         0         1   0   0     1   0.0   0
1820.63  8.46   2.8e+1  7.0      1   0         0         1   0         0         1   0   0     1   0.0   0
1936.54  12.69  1.2e+2  4.5e+1   1   0         0         1   0         0         1   0   0     1   0.0   0
************************************************************************************************************************
Upper Limits of Resonances
Note: enter partial width upper limit by chosing non-zero value for PT, where PT=<theta^2> for particles and...
Note: ...PT=<B> for g-rays [enter: "upper_limit 0.0"]; for each resonance: # upper limits < # open channels!
Ecm      DEcm   Jr  G1        DG1 L1  PT     G2       DG2      L2   PT   G3       DG3       L3  PT  Exf   Int
497.38   0.08   2   9.28e-12  0   2   0.01   2.58e3   2.4e1    0    0    1.73     3e-2      1   0   0.0   1
548.16   0.10   2   3.80e-8   0   2   0.01   4.64e3   1.0e2    1    0    4.56     0.29      1   0   0.0   1
556.28   0.16   2   1.50e-8   0   2   0.01   1.44     1.6e-1   2    0    3.0      1.5       1   0   0.0   0
568.27   0.19   1   2.08e-7   0   1   0.01   5.40e-1  8.8e-2   1    0    3.0      1.5       1   0   0.0   0
628.43   0.10   2   2.40e-8   0   2   0.01   4.51e3   1.1e2    1    0    7.42     0.60      1   0   0.0   1
659.32   0.12   2   2.20e-8   0   2   0.01   5.40e2   5.4e1    0    0    3.24     0.35      1   0   0.0   1
665.11   0.11   4   1.44e-8   0   4   0.01   1.51e3   3.4e1    1    0    5.9e-1   2.4e-1    1   0   0.0   1
670.81   0.13   1   2.57e-8   0   1   0.01   1.26e3   1.0e2    1    0    7.9e-1   4.6e-1    1   0   0.0   1
671.59   0.12   2   1.54e-8   0   2   0.01   1.28e1   6.0      2    0    4.26     0.60      1   0   0.0   1
674.36   0.25   2   1.54e-8   0   2   0.01   1.54     0.46     1    0    3.0      1.5       1   0   0.0   0
681.21   0.13   3   1.43e-8   0   3   0.01   8.06e3   1.2e2    1    0    3.31     0.73      1   0   0.0   1
695.95   0.35   1   5.34e-9   0   1   0.01   1.12     0.40     1    0    3.0      1.5       1   0   0.0   0
711.34   0.54   1   4.11e-8   0   1   0.01   6.0e-1   3.2e-1   1    0    3.0      1.5       1   0   0.0   0
713.40   0.14   1   1.67e-7   0   1   0.01   4.24e2   8.6e1    1    0    3.63     0.47      1   0   0.0   1
714.34   0.55   1   4.12e-8   0   1   0.01   2.8      1.0      1    0    3.0      1.5       1   0   0.0   0
722.12   0.56   1   4.17e-8   0   1   0.01   1.42     0.56     1    0    3.0      1.5       1   0   0.0   0
729.15   0.15   2   4.00e-8   0   2   0.01   1.53e2   4.2e1    1    0    1.18     0.27      1   0   0.0   1
730.03   0.16   4   4.68e-9   0   4   0.01   4.13e3   1.9e2    3    0    1.82     0.38      1   0   0.0   1
777.78   0.16   5   3.34e-9   0   5   0.01   2.90e2   1.9e1    2    0    3.0      1.5       1   0   0.0   1
************************************************************************************************************************
Interference between Resonances [numerical integration only]
Note: + for positive, - for negative interference; +- if interference sign is unknown
Ecm    DEcm   Jr    G1      DG1   L1   PT      G2      DG2      L2  PT   G3    DG3    L3  PT   Exf   Int
!+-
0.0    0.0    0.0   0.0     0.0   0    0       0.0     0.0      0   0    0.0   0.0    0   0    0.0   0
0.0    0.0    0.0   0.0     0.0   0    0       0.0     0.0      0   0    0.0   0.0    0   0    0.0   0
************************************************************************************************************************
Reaction Rate and PDF at NT selected temperatures only
Note: default values are used for reaction rate range if Min=Max=0.0
T9    Min   Max
0.01  0.0   0.0
0.1   0.0   0.0
************************************************************************************************************************
Comments:
a,n measurements including results from recent FEL run
The 703 keV resonance is treated as the same as seen in 22Ne(a,g)
```

Figure 7.7: RatesMC input file for ^{22}Ne(α,n)^{26}Mg reaction rates.

T (GK)	Low rate	Median rate	High rate	lognormal μ	lognormal σ	A-D
0.010	2.16×10^{-250}	1.25×10^{-249}	3.39×10^{-249}	$-5.734\times10^{+02}$	$1.32\times10^{+00}$	$1.08\times10^{+02}$
0.011	2.00×10^{-228}	1.14×10^{-227}	3.09×10^{-227}	$-5.229\times10^{+02}$	$1.31\times10^{+00}$	$1.07\times10^{+02}$
0.012	4.07×10^{-210}	2.29×10^{-209}	6.20×10^{-209}	$-4.807\times10^{+02}$	$1.31\times10^{+00}$	$1.06\times10^{+02}$
0.013	1.26×10^{-194}	7.06×10^{-194}	1.91×10^{-193}	$-4.450\times10^{+02}$	$1.30\times10^{+00}$	$1.05\times10^{+02}$
0.014	2.41×10^{-181}	1.34×10^{-180}	3.62×10^{-180}	$-4.145\times10^{+02}$	$1.30\times10^{+00}$	$1.05\times10^{+02}$
0.015	7.88×10^{-170}	4.34×10^{-169}	1.17×10^{-168}	$-3.880\times10^{+02}$	$1.29\times10^{+00}$	$1.04\times10^{+02}$
0.016	9.44×10^{-160}	5.17×10^{-159}	1.39×10^{-158}	$-3.648\times10^{+02}$	$1.29\times10^{+00}$	$1.04\times10^{+02}$
0.018	6.02×10^{-143}	3.28×10^{-142}	8.80×10^{-142}	$-3.261\times10^{+02}$	$1.28\times10^{+00}$	$1.03\times10^{+02}$
0.020	1.73×10^{-129}	9.40×10^{-129}	2.52×10^{-128}	$-2.951\times10^{+02}$	$1.28\times10^{+00}$	$1.03\times10^{+02}$
0.025	3.30×10^{-105}	1.85×10^{-104}	4.97×10^{-104}	$-2.392\times10^{+02}$	$1.30\times10^{+00}$	$1.05\times10^{+02}$
0.030	5.97×10^{-89}	3.51×10^{-88}	9.60×10^{-88}	$-2.017\times10^{+02}$	$1.34\times10^{+00}$	$1.10\times10^{+02}$
0.040	1.58×10^{-68}	1.01×10^{-67}	2.80×10^{-67}	$-1.546\times10^{+02}$	$1.41\times10^{+00}$	$1.19\times10^{+02}$
0.050	3.21×10^{-56}	2.07×10^{-55}	5.75×10^{-55}	$-1.263\times10^{+02}$	$1.41\times10^{+00}$	$1.20\times10^{+02}$
0.060	5.90×10^{-48}	3.43×10^{-47}	9.30×10^{-47}	$-1.073\times10^{+02}$	$1.34\times10^{+00}$	$1.10\times10^{+02}$
0.070	5.75×10^{-42}	2.69×10^{-41}	6.83×10^{-41}	$-9.368\times10^{+01}$	$1.20\times10^{+00}$	$9.41\times10^{+01}$
0.080	2.13×10^{-37}	7.85×10^{-37}	1.77×10^{-36}	$-8.335\times10^{+01}$	$1.04\times10^{+00}$	$8.28\times10^{+01}$
0.090	8.32×10^{-34}	2.56×10^{-33}	5.13×10^{-33}	$-7.523\times10^{+01}$	9.20×10^{-01}	$7.02\times10^{+01}$
0.100	6.69×10^{-31}	1.74×10^{-30}	3.28×10^{-30}	$-6.866\times10^{+01}$	8.52×10^{-01}	$4.90\times10^{+01}$
0.110	1.61×10^{-28}	3.84×10^{-28}	7.31×10^{-28}	$-6.323\times10^{+01}$	8.25×10^{-01}	$2.82\times10^{+01}$
0.120	1.59×10^{-26}	3.49×10^{-26}	7.13×10^{-26}	$-5.867\times10^{+01}$	8.17×10^{-01}	$1.40\times10^{+01}$
0.130	7.77×10^{-25}	1.67×10^{-24}	3.57×10^{-24}	$-5.477\times10^{+01}$	8.08×10^{-01}	$5.16\times10^{+00}$
0.140	2.30×10^{-23}	4.84×10^{-23}	1.05×10^{-22}	$-5.138\times10^{+01}$	7.79×10^{-01}	8.79×10^{-01}
0.150	4.73×10^{-22}	9.56×10^{-22}	2.01×10^{-21}	$-4.838\times10^{+01}$	7.22×10^{-01}	$2.28\times10^{+00}$
0.160	7.57×10^{-21}	1.39×10^{-20}	2.77×10^{-20}	$-4.568\times10^{+01}$	6.37×10^{-01}	$1.09\times10^{+01}$
0.180	1.06×10^{-18}	1.52×10^{-18}	2.49×10^{-18}	$-4.096\times10^{+01}$	4.36×10^{-01}	$4.34\times10^{+01}$
0.200	6.82×10^{-17}	8.39×10^{-17}	1.13×10^{-16}	$-3.697\times10^{+01}$	2.73×10^{-01}	$6.07\times10^{+01}$
0.250	1.46×10^{-13}	1.63×10^{-13}	1.82×10^{-13}	$-2.944\times10^{+01}$	1.15×10^{-01}	$3.85\times10^{+00}$
0.300	2.48×10^{-11}	2.73×10^{-11}	2.99×10^{-11}	$-2.433\times10^{+01}$	9.40×10^{-02}	1.97×10^{-01}
0.350	9.67×10^{-10}	1.06×10^{-09}	1.16×10^{-09}	$-2.067\times10^{+01}$	9.01×10^{-02}	1.81×10^{-01}
0.400	1.51×10^{-08}	1.65×10^{-08}	1.79×10^{-08}	$-1.792\times10^{+01}$	8.70×10^{-02}	2.54×10^{-01}
0.450	1.32×10^{-07}	1.43×10^{-07}	1.55×10^{-07}	$-1.576\times10^{+01}$	8.15×10^{-02}	2.77×10^{-01}
0.500	8.07×10^{-07}	8.66×10^{-07}	9.30×10^{-07}	$-1.396\times10^{+01}$	7.15×10^{-02}	3.78×10^{-01}
0.600	1.85×10^{-05}	1.92×10^{-05}	2.01×10^{-05}	$-1.086\times10^{+01}$	4.23×10^{-02}	$1.10\times10^{+00}$
0.700	2.83×10^{-04}	2.91×10^{-04}	3.00×10^{-04}	$-8.141\times10^{+00}$	2.99×10^{-02}	4.32×10^{-01}
0.800	2.76×10^{-03}	2.84×10^{-03}	2.93×10^{-03}	$-5.862\times10^{+00}$	3.08×10^{-02}	4.14×10^{-01}
0.900	1.79×10^{-02}	1.85×10^{-02}	1.91×10^{-02}	$-3.992\times10^{+00}$	3.35×10^{-02}	3.75×10^{-01}
1.000	8.37×10^{-02}	8.68×10^{-02}	9.02×10^{-02}	$-2.443\times10^{+00}$	3.76×10^{-02}	4.61×10^{-01}
1.250	$1.51\times10^{+00}$	$1.59\times10^{+00}$	$1.68\times10^{+00}$	4.676×10^{-01}	5.32×10^{-02}	$1.57\times10^{+00}$
1.500	$(1.33\times10^{+01})$	$(1.41\times10^{+01})$	$(1.50\times10^{+01})$	$(2.649\times10^{+00})$	(5.99×10^{-02})	
1.750	$(8.18\times10^{+01})$	$(8.68\times10^{+01})$	$(9.22\times10^{+01})$	$(4.464\times10^{+00})$	(5.99×10^{-02})	
2.000	$(3.56\times10^{+02})$	$(3.78\times10^{+02})$	$(4.01\times10^{+02})$	$(5.935\times10^{+00})$	(5.99×10^{-02})	
2.500	$(3.33\times10^{+03})$	$(3.54\times10^{+03})$	$(3.76\times10^{+03})$	$(8.171\times10^{+00})$	(5.99×10^{-02})	
3.000	$(1.71\times10^{+04})$	$(1.82\times10^{+04})$	$(1.93\times10^{+04})$	$(9.808\times10^{+00})$	(5.99×10^{-02})	
3.500	$(6.04\times10^{+04})$	$(6.42\times10^{+04})$	$(6.81\times10^{+04})$	$(1.107\times10^{+01})$	(5.99×10^{-02})	
4.000	$(1.65\times10^{+05})$	$(1.75\times10^{+05})$	$(1.86\times10^{+05})$	$(1.207\times10^{+01})$	(5.99×10^{-02})	
5.000	$(7.42\times10^{+05})$	$(7.88\times10^{+05})$	$(8.37\times10^{+05})$	$(1.358\times10^{+01})$	(5.99×10^{-02})	
6.000	$(2.20\times10^{+06})$	$(2.33\times10^{+06})$	$(2.48\times10^{+06})$	$(1.466\times10^{+01})$	(5.99×10^{-02})	
7.000	$(4.95\times10^{+06})$	$(5.26\times10^{+06})$	$(5.58\times10^{+06})$	$(1.548\times10^{+01})$	(5.99×10^{-02})	
8.000	$(9.38\times10^{+06})$	$(9.96\times10^{+06})$	$(1.06\times10^{+07})$	$(1.611\times10^{+01})$	(5.99×10^{-02})	
9.000	$(1.56\times10^{+07})$	$(1.66\times10^{+07})$	$(1.76\times10^{+07})$	$(1.662\times10^{+01})$	(5.99×10^{-02})	
10.000	$(2.39\times10^{+07})$	$(2.54\times10^{+07})$	$(2.70\times10^{+07})$	$(1.705\times10^{+01})$	(5.99×10^{-02})	

Table 7.7: Monte Carlo reaction rates for the ^{22}Ne(α,n)^{26}Mg reaction. See Tab. 7.4 for a description of the table.

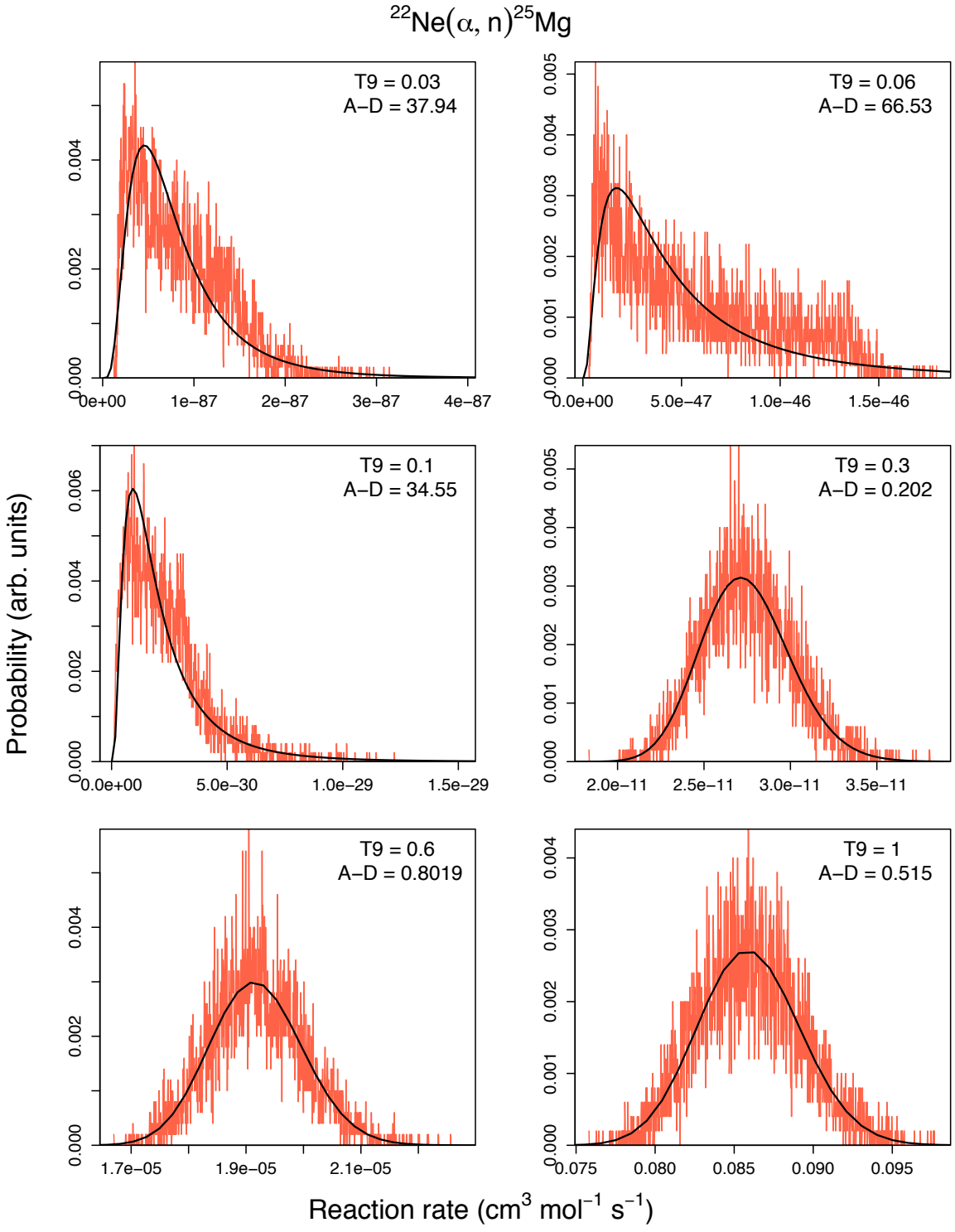

Figure 7.8: Reaction rate probability densities for the ^{22}Ne(α,n)^{25}Mg reaction. Shown are histograms of the Monte Carlo reaction rates, as well as the lognormal approximation calculated from Eq. (2.28).

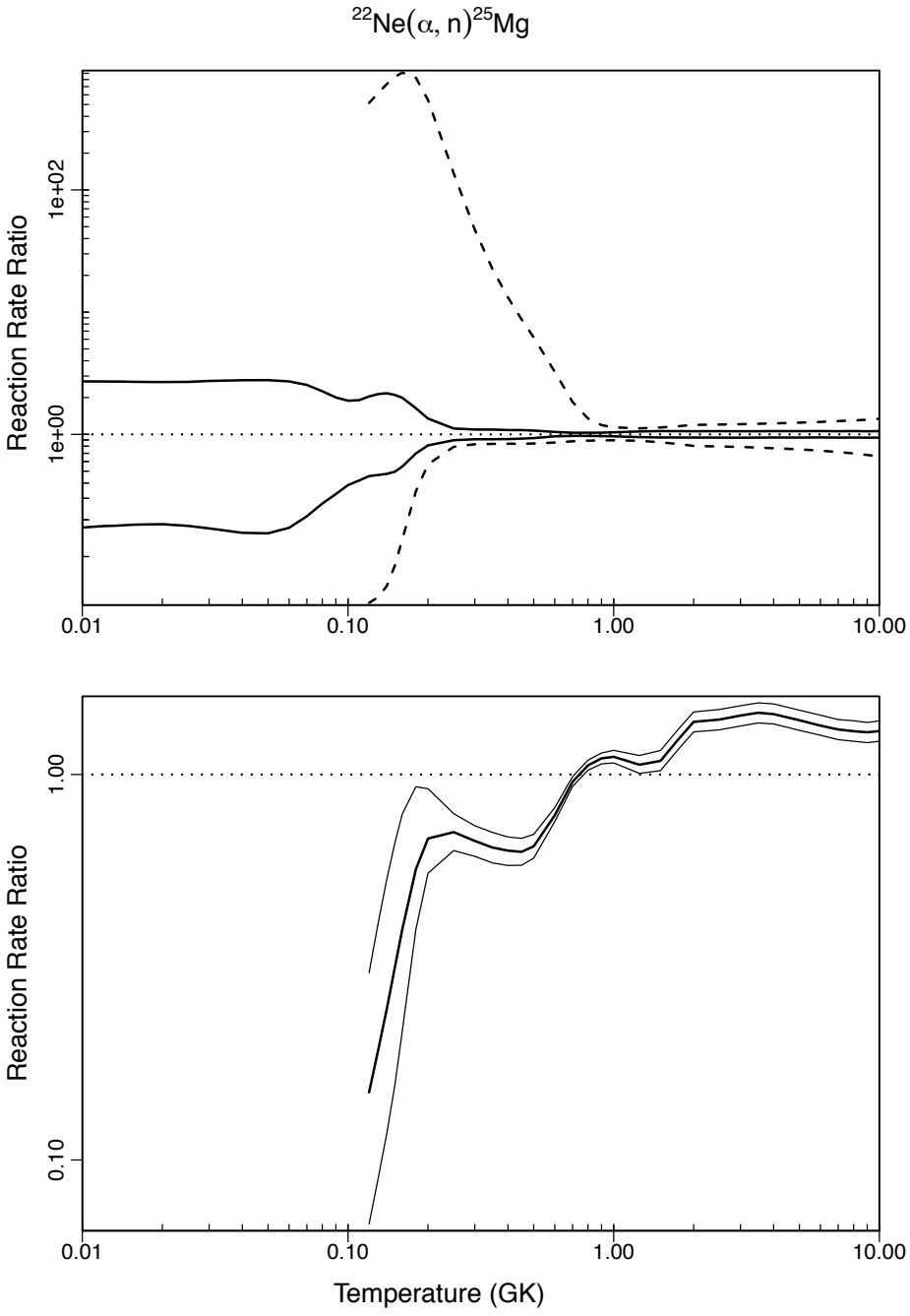

Figure 7.9: The uncertainty bands for the ^{22}Ne(α,n)^{25}Mg reaction in comparison to those presented by the NACRE compilation [Ang99]. See Fig. 7.3 for a description of the plotted lines.

GK, with a slight dip at $T \approx 0.15$ GK arising from the present $E_x = 11154$ keV result.

A further comparison can be made between the Monte Carlo reaction rates prior to and following the experiment discussed in Sec. 5. This comparison is made in Fig. 7.11. The upper panel of the figure shows approximately equal uncertainties. This is expected because only the upper limit resonance at $E_r^{\text{lab}} \approx 630$ keV is removed in the present result. The new statistical method of calculating upper limits reduces their impact on reaction rates, resulting in only a small reduction in uncertainty shown at $T \approx 0.15$ GK when the resonance is removed. The lower panel in Fig. 7.11 shows a slight dip in reaction rate at $T \approx 0.15$ GK that was observed in Fig. 7.10, arising from the removal of the $E_r^{\text{lab}} \approx 630$ keV resonance upper limit.

7.4.5 Influence of 832 keV Resonance Assignments

The resonance at $E_r = 832$ keV was assumed to be the same state as that seen in the measurements of ^{22}Ne(α,γ)^{25}Mg. This state has been assumed to be a $J^\pi = 2^+$ state, with a width of that measured by Jaeger *et al*. [Jae01b]. The other possibility is that these two resonance are, indeed, corresponding to separate states as Koehler suggests [KÖ2]. See Sec. 7.4.1 for more discussion. Figure 7.12 shows the effect of assuming two distinct resonances on the ^{22}Ne(α,γ)^{26}Mg reaction rate. In separating these resonances, the only excited state that is corresponds to the $E_r^{\text{lab}} = 832$ keV resonance in energy is at $E_x = 11326.13(54)$ keV (compared with $E_x = 11319(2)$ measured by Jaeger *et al*.) [Jae01b]. This state has a measured total width of $\Gamma = 428(86)$ compared to the width of $\Gamma = 250(170)$ measured by Jaeger *et al*. [Jae01b]. The weighted average of these widths was used in the present calculation. This state also has $J^\pi = 1^-$, where Ref. [Jae01b] assume a spin-parity of 2^+ from the Giesen *et al*. [Gie93] assignment of $J^\pi = (1^-)2^+$. In the present calculation, $J^\pi = 1^-$ has been assigned to this resonance. The transfer measurement of Giesen *et al*. [Gie93] could have observed a doublet corresponding to the ^{22}Ne(α, γ)^{26}Mg and ^{22}Ne(α, n)^{25}Mg resonances.

The results of assuming two distinct resonances at $E_r^{\text{lab}} = 830$ keV is shown in Fig. 7.12. The top panel shows that the rate uncertainties obtained when assuming a single state (solid lines) are comparable to those resulting from separating the states into a doublet (dashed line). The smaller uncertainties for two resonances at low temperatures arise from taking a weighted average of the resonance width. A weighted average will reduce uncertainties in the width, resulting in smaller

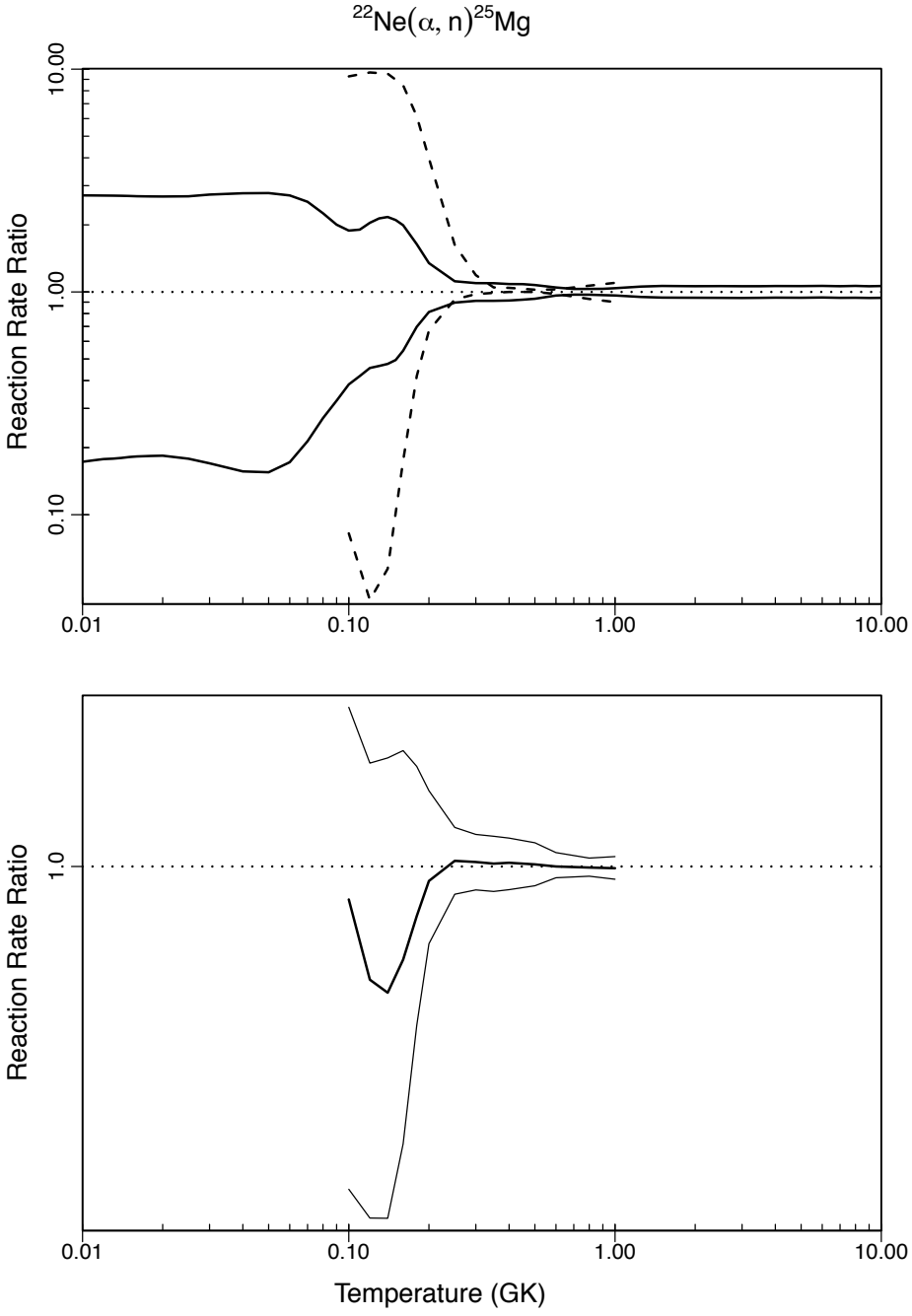

Figure 7.10: Reaction rate comparison with the rates presented by Jaeger *et al*. [Jae01b]. See Fig. 7.3 for a description of the plotted lines.

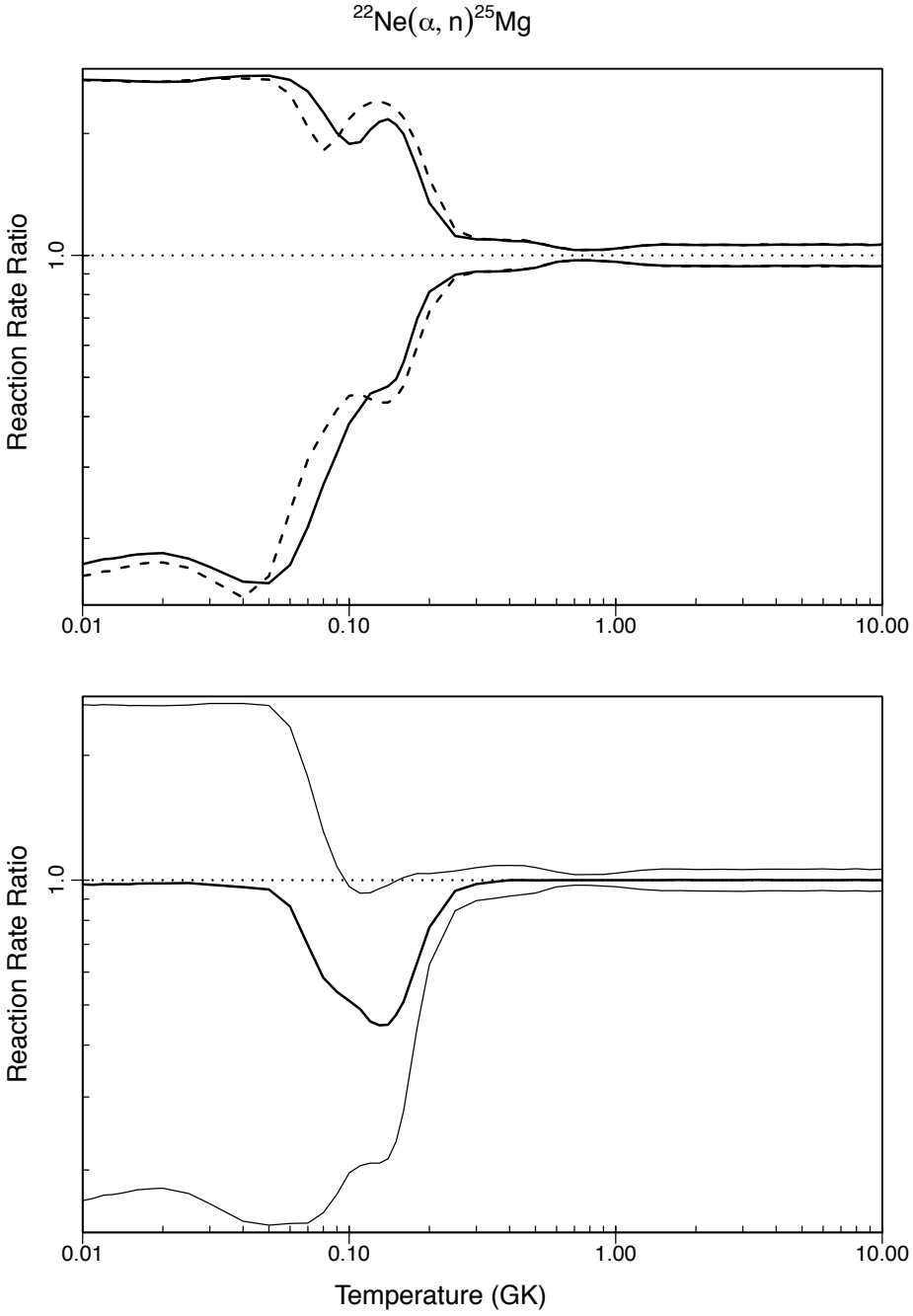

Figure 7.11: Comparison with rates obtained prior to the recent ^{26}Mg$(\gamma,\gamma)^{26}$Mg measurement. See Fig. 7.3 for a description of the plotted lines.

uncertainties in the wide resonance reaction rate from that state. The lower panel shows that a single resonance at $E_r^{\rm lab} = 830$ keV produces a slightly higher strength at $T = 0.2$ GK. This is because the partial widths calculated in this case are slightly larger than if the resonance is assumed to be a doublet. To remove ambiguities in the parameters of this resonance, direct measurements of both the ^{22}Ne$(\alpha, \mathrm{n})^{25}$Mg and the ^{22}Ne$(\alpha, \gamma)^{26}$Mg reactions with precise energy calibrations should be performed.

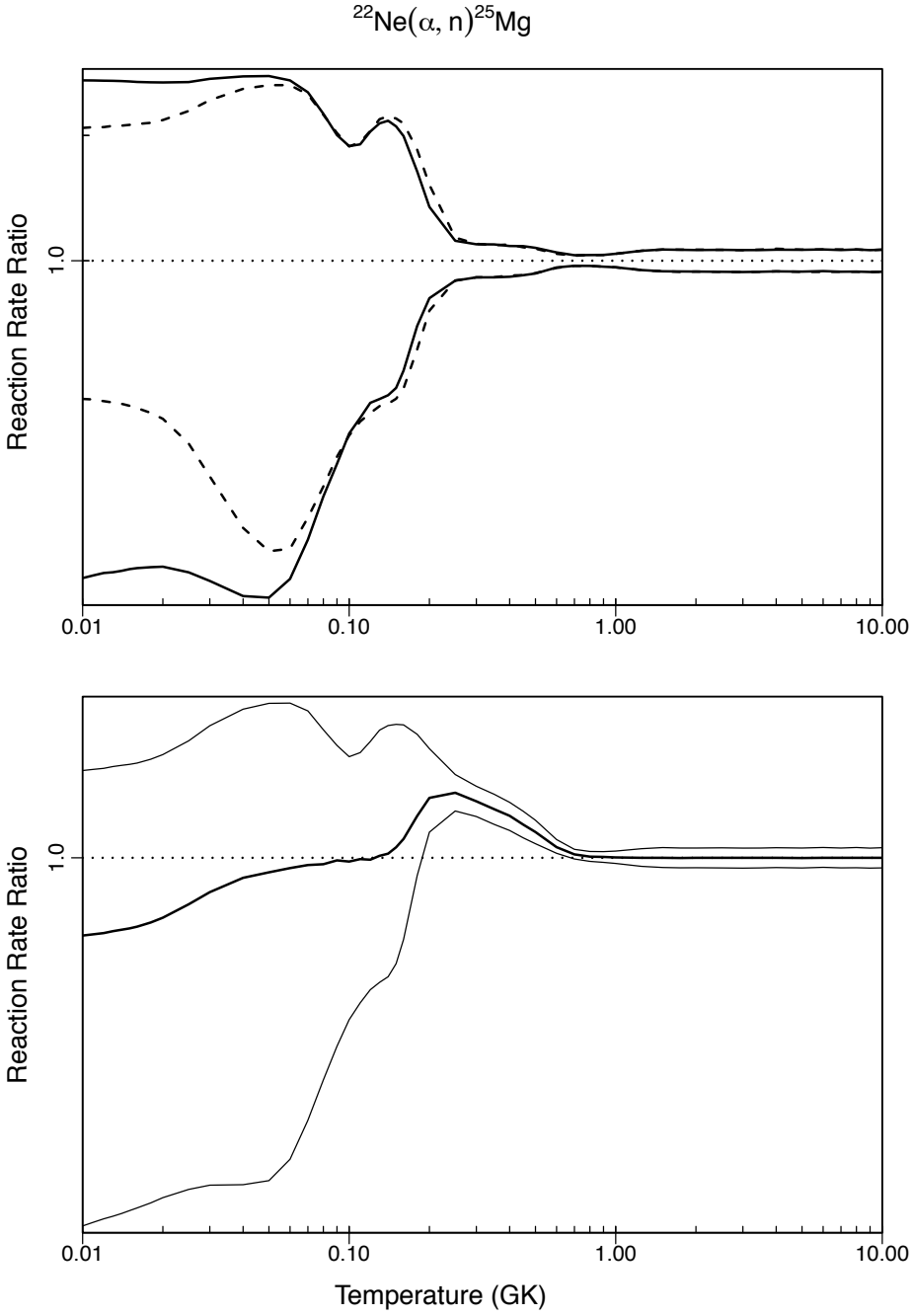

Figure 7.12: The effect of separating the 832 keV resonance into two resonances on the reaction rate. The solid lines represent the present reaction rate, where a single state is assumed to be responsible for the two resonances. Dashed lines represent the case assuming two distinct resonances. In the lower panel, the ratio of present rates to the doublet rates are displayed. A ratio above unity means that the single state assumption produced higher rates than that of a doublet. See Fig. 7.3 for a description of the plotted lines.

8 Conclusions

For over half a century, the s-process has been associated with the production of many elements heavier than iron. The s-process consists of the slow capture of neutrons followed by β-decay on seed nuclei to produce nuclei up to the most massive stable nucleus, ^{209}Bi. Models of the s-process show [Kae90] that there must be two contributions to the s-process: the main component, occurring over relatively long time periods for a limited proportion of seed nuclei, and the weak component, involving a more efficient neutron exposure operating for a short period of time. The main s-process component produces nuclei up to a cut-off mass of $A = 209$, while the weak component is responsible for the enhancement of nuclear abundances at $A < 90$. The stellar environments responsible for the main and weak s-process components are AGB stars and massive stars, respectively.

The ^{22}Ne$(\alpha, \mathrm{n})^{25}$Mg neutron producing reaction is important both in AGB stars and in massive stars. In massive stars, it is the main source of s-process neutrons during the core helium burning stage, with the possibility of producing an extra flux of neutrons during the carbon burning stage. In AGB stars, the ^{13}C$(\alpha$,n$)^{13}$N reaction is the main s-process neutron source, with the ^{22}Ne$(\alpha, \mathrm{n})^{25}$Mg reaction mainly affecting branchings in the s-process path leading to enrichment in some elements [Gar06]. It has also been postulated that the ^{22}Ne$(\alpha, \mathrm{n})^{25}$Mg reaction could be the main neutron source in metal poor AGB stars with masses larger than $M = 5M_{\odot}$ [Lug08].

In order to address some of the astrophysical questions regarding the s-process in these environments, the ^{22}Ne$(\alpha, \mathrm{n})^{25}$Mg reaction and its competing ^{22}Ne$(\alpha, \gamma)^{26}$Mg reaction have been studied in the present work. In Ch. 2, a new Monte Carlo method of propagating reaction rate uncertainties was developed. The new method provides, for the first time, statistically meaningful reaction rates (in which the coverage probability can be quantified). Treatment of upper limits in resonance parameters was improved to provide a statistically meaningful calculation of reaction rates arising from

unobserved resonances.

In Ch. 5, an experiment to measure the spin-parities of several excited states in the ^{26}Mg compound nucleus for the ^{22}Ne$(\alpha,\mathrm{n})^{25}$Mg and ^{22}Ne$(\alpha,\gamma)^{26}$Mg reactions was described. The measurement consisted of exciting the ground state of ^{26}Mg with an intense photon beam through the reaction ^{26}Mg$(\gamma,\gamma)^{26}$Mg . The measurement improved our knowledge of the resonance parameters significantly. Perhaps the most important result of the ^{26}Mg$(\gamma,\gamma)^{26}$Mg experiment was the unnatural spin-parity determination for the state associated with the previously suggested $E_r^{\mathrm{lab}} = 633$ keV resonance. This resonance had been the subject of numerous experimental searches, and has finally been shown here not to contribute to the rates of the ^{22}Ne+α reactions.

Calculations of the reaction rates for ^{22}Ne$(\alpha,\mathrm{n})^{25}$Mg and ^{22}Ne$(\alpha,\gamma)^{26}$Mg in Ch. 7 show a significant reduction in reaction rate uncertainties. However, it was shown that the reactions are still uncertain in important aspects. The $E_r^{\mathrm{lab}} = 830$ keV resonance quantum numbers and energy must be resolved in both reactions to determine if a doublet exists at this energy. Furthermore, the ^{22}Ne$(\alpha,\gamma)^{26}$Mg reaction, which is lacking in direct experimental data, should be explored at energies between $E_r = 800$ and 2000 keV. Resonances below these energies should be measured indirectly through α-particle transfer measurements. Ambiguities in current experimental data at low energies must be resolved.

One of the main sources of uncertainty in measuring reactions directly is the target stoichiometry. In Ch. 6, a novel method was developed to determine the stoichiometry of targets produced by implanting ^{22}Ne into an aluminium substrate, which was used to calculate the ^{22}Ne(p,γ)^{23}Na resonance strength at $E_r^{\mathrm{lab}} = 479$ keV with significant improvements in uncertainty. This low energy resonance is now available for determining the stoichiometry of implanted targets to be used in direct ^{22}Ne$(\alpha,\mathrm{n})^{25}$Mg and ^{22}Ne$(\alpha,\gamma)^{26}$Mg resonance strength measurements, reducing uncertainties in these measurements considerably.

Given the results presented in this work, the next step will be to perform model calculations of AGB stars and massive stars to determine the influence of the new reaction rates on the s-process. The present results are expected to reduce uncertainties in s-nuclei production yields and will, therefore, improve stellar models. As the uncertainty in nuclear input to stellar models improves, our understanding of the way stars burn will, one day, be understood.

A Statistical Distributions

A brief review of statistical distributions relevant to the present work is provided. These distributions were found in Sec. 2.2 to best describe the probability density functions of nuclear input quantities for reaction rate calculations.

The expectation value and variance of a parameter, x are given by

$$E[x] = \int_{-\infty}^{\infty} x f(x) dx, \qquad V[x] = \int_{-\infty}^{\infty} (x - E[x])^2 f(x) dx \tag{A.1}$$

where $f(x)$ is the (normalised) probability density function. The cumulative distribution, which is useful for finding the quantiles (or percentiles) of a distribution and for calculating the Anderson-Darling statistic in Sec. 2.2.3, is defined by

$$F(x) = \int_{-\infty}^{x} f(x') dx' \tag{A.2}$$

If $f(x)$ is correctly normalised, the median of x, for example, corresponds the point at which the cumulative distribution reaches 0.5.

A.1 Gaussian Distribution

The *Gaussian distribution* is the most commonly used statistical distribution because of its simplicity and ease of calculation. The probability density function of a normally (Gaussian) distributed variable x is given by

$$f(x) = \frac{1}{\sigma\sqrt{2\pi}} e^{-(x-\mu)^2/(2\sigma^2)} \tag{A.3}$$

where the parameters μ and σ refer to the mean and standard deviation, respectively. For a Gaussian distribution, the expectation value and variance are

$$E[x] = \mu, \qquad V[x] = \sigma^2 \tag{A.4}$$

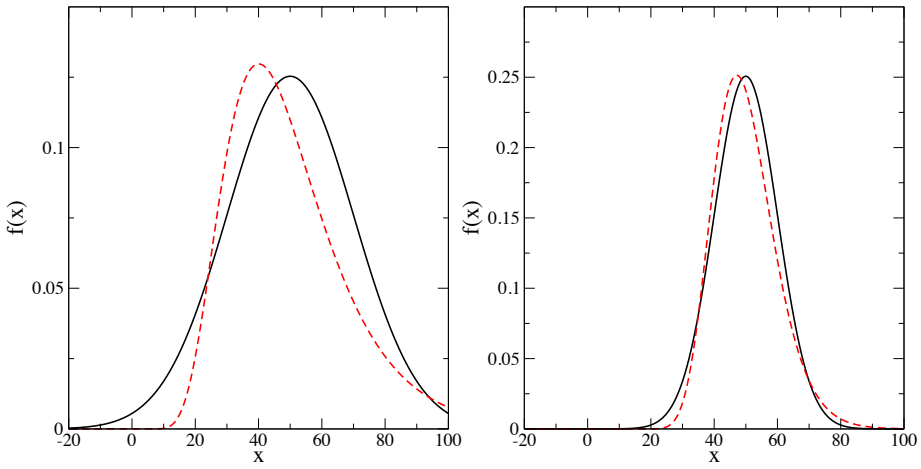

Figure A.1: Comparison of lognormal (dashed line) and Gaussian (solid line) distributions for two specific cases. In case (a), the uncertainty is fairly large in comparison to the mean value ($E[x] = 50$ and $V[x] = 20^2$), and there is little agreement between the distributions (note also that the Gaussian extends visibly to negative values). Case (b), for $E[x] = 50$ and $V[x] = 10^2$, the distributions are very similar.

A.2 Lognormal Distribution

If the natural logarithm of a variable is normally distributed, then the variable will follow a *log-normal distribution*:

$$f(x) = \frac{1}{\sigma x \sqrt{2\pi}} e^{-(\ln x - \mu)^2/(2\sigma)^2} \tag{A.5}$$

The parameters of the lognormal distribution, μ and σ, are not the same quantities as for the Gaussian distribution. They do not represent the mean and standard deviation of the variable, x, but of $\ln x$. The expectation value and variance are given by

$$E[x] = e^{(2\mu+\sigma^2)/2}, \qquad V[x] = e^{(2\mu+\sigma^2)/2}\left[e^{\sigma^2}\right] \tag{A.6}$$

It is worth noting that the lognormal distribution will approach a Gaussian as the parameter σ becomes small in comparison to μ. An example of this is shown in Fig. A.1. This feature of the lognormal distribution is useful for describing reaction rate probability distributions at high temperatures, which tend towards a Gaussian shape. See Sec. 2.2.3 for more details.

A.3 Chi-squared Distribution

The standard normal distribution is defined as a normal distribution with $\mu = 0$ and $\sigma = 1$. The sum of the squares of k standard normal distributions is distributed according to a *chi-squared distribution* with k degrees of freedom.

The case in which the degrees of freedom is unity is defined as,

$$f(x) = \frac{1}{\sqrt{2\pi x}} e^{-x/2} \tag{A.7}$$

Note that there are no defining parameters to the distribution. However, the variable x can be defined as the ratio of a quantity to its mean value, i.e., $x \equiv y/\langle y \rangle$. The expectation value and variance are given by

$$E[x] = k = 1, \qquad V[x] = 2k = 2 \tag{A.8}$$

B Reaction Rate Calculations

B.1 Excitation Energies

The excitation energies for all observed excited states are taken as the weighted average of energies observed in Refs. [Wei76, KÖ2, Jae01b, Uga07, Wol89, Gla86, Dro93, Mos76], as well as from the present results from the ^{26}Mg$(\gamma,\gamma)^{26}$Mg experiment in chapter 5. The states are matched as closely as possible between experiments by looking at resonance parameters such as partial widths and quantum numbers as discussed in the main text. Tables B.3 and B.1 list the energies obtained.

(α,pγ)	(p,p$'$)	(n,γ)	(α,γ),(α,n)	(α,n)	(α,n)	(γ,γ)	Weighted Average
[Gla86]	[Mos76]	[KÖ2]	[Wol89]	[Jae01b]	[Dro93]		
	11114(3)	11112.192(84)					11112.164(77)
	11156(3)	11153.387(86)				11153.84 (29)	11153.392(76)
		11162.937(92)					11162.949(91)
	11171(3)	11169.31(17)					11169.34(13)
		11171.06(16)					11171.07(15)
		11183.06(18)					11183.06(18)
		11189.21(10)					11189.21(10)
11191(2)							11191(2)
							11194.5(2)
		11243.19(11)					11243.22(10)
		11274.11(11)					11274.11(11)
		11280.04(12)					11279.90(10)
		11285.60(12)					11285.60(12)
		11286.34(12)					11286.38(11)
		11289.03(43)					11289.15(25)
		11296.09(13)					11295.99(13)
		11310.50(49)					11310.50(49)
			11315(5)	11319(2)			11318.1(21)
		11326.13(54)					11326.13(54)
11329(2)		11328.17(14)					11328.19(14)
		11329.12(54)					11329.12(54)
		11336.91(56)					11336.91(56)
		11343.96(16)					11343.93(15)
		11344.82(16)					11344.82(16)
							11362.0(6)

continued from previous page

(α,pγ)	(p,p′)	(n,γ)	(α,γ),(α,n)	(α,n)	(α,n)	(γ,γ)	Weighted Average
[Gla86]	[Mos76]	[KÖ2]	[Wol89]	[Jae01b]	[Dro93]		
							11364.9(6)
							11372.5(6)
		11392.55(17)					11392.56(16)
							11425.40(70)
		11440.92(20)		11441(2)			11440.83(19)
11457(2)							11457(2)
		11465.40(22)		11461(2)			11465.23(21)
							11499.4(8)
				11506(2)			11508.1(9)
				11526(2)			11526(2)
							11540.8(9)
11570(2)							11570(2)
							11586(1)
			11626(10)	11630(2)			11630(2)
			11655(10)				11655(10)
				11748(8)			11748(8)
			11795(10)	11787(3)			11787(3)
			11801(6)				11801(6)
			11828(3)	11828(2)			11828(2)
					11863(3)		11863(3)
			11880(5)		11880(3)		11880(3)
			11895(5)		11891(3)		11891(3)
			11912(3)		11910(3)		11910(3)
			11953(3)		11951(3)		11951(3)
			12051(3)		12052(3)		12052(3)
			12116(8)		12115(4)		12115(4)
			12139(3)		12141(3)		12141(3)
			12184(8)		12184(7)		12184(7)
			12273(8)		12265(8)		12265(8)
			12343(5)		12346(7)		12346(7)
					12435(8)		12435(8)
					12551(13)		12551(13)

Table B.1: Table of excitation energies above the neutron threshold

Energy (keV)	(α,pγ)	(n,γ)	(^{6}Li,d)	(α,γ),(α,n)	(α,n)	(γ,γ)	Assignment
	[Gla86]	[KÖ2]	[Gie93]	[Wol89]	[Jae01b]		
11112.164(77)		2^+					2^+
11153.392(76)		1^-				1^+	1^+
11162.949(91)		2^+					2^+
11169.34(13)		3^+					3^+
11171.07(15)		(2^+)					(2^+)
11183.06(18)		(1^-)					(1^-)
11189.21(10)		3^+					3^+
11191(2)	$(3^-$-$6^+)$						$(3^-$-$6^+)$
11194.5(2)		2^+					2^+
11243.22(10)		$2^{(-)}$					$2^{(-)}$
11274.11(11)		$(2)^+$					$(2)^+$
11279.90(10)		4^-					4^-
11285.60(12)		1^-					1^-
11286.38(11)		(2^+)					(2^+)
11289.15(25)		(2^-)					(2^-)
11295.99(13)		(3^-)					(3^-)
11310.50(49)		(1^-)					(1^-)
11318.1(21)			$(1^-)2^+$		2^+		2^+
11326.13(54)		(1^-)					(1^-)
11328.19(14)	$(3^+$-$7^+)$	1^-					$(1^-,2^+)$
11329.12(54)		(1^-)					(1^-)
11336.91(56)		(1^-)					(1^-)
11343.93(15)		(4^-)					(4^-)
11344.82(16)		(2^+)					(2^+)
11362.0(6)							
11364.9(6)							
11372.5(6)							
11392.56(16)		$5^{(+)}$					$5^{(+)}$
11425.40(70)							
11440.83(19)		4^+			1^-		4^+
11457(2)			$(1^-,2^+)3^-$				$(1^-,2^+)3^-$
11465.23(21)		5^-			1^-		5^-
11499.4(8)							
11508.1(9)					1^-		1^-
11526(2)					1^-		1^-
11540.8(9)							
11570(2)	$(4^+$-$7^+)$						$(4^+$-$7^+)$
11586(1)				$1^-,2^+,3^-$	2^+		2^+

continued from previous page

Energy (keV)	(α,pγ)	(n,γ)	(^{6}Li,d)	(α,γ),(α,n)	(α,n)	(γ,γ)	Assignment
	[Gla86]	[KÖ2]	[Gie93]	[Wol89]	[Jae01b]		
11863(3)							
11880(3)							
11891(3)				1^-,2^+,3^-			1^-,2^+,3^-
11910(3)				1^-,2^+			1^-,2^+
11951(3)				2^+,3^-,4^+			2^+,3^-,4^+
12052(3)				2^+,3^-			2^+,3^-
12115(4)				(0^+)			(0^+)
12141(3)							
12184(7)				(0^+)			(0^+)
12265(8)				(0^+)			(0^+)
12346(7)				0^+			0^+
12435(8)							
12551(13)							

Table B.2: Spin-parity assignments for states in ^{26}Mg. Italic numbers are taken from Ref. [Wei76]

B.2 Calculating Upper Limits

Upper limits for resonances in the ^{22}Ne(α,γ)^{26}Mg reaction were calculated from Fig. 7a in Ref. [Wol89]. That figure plots the cross section of the reaction versus the α-particle energy. The cross section was calculated using a wide resonance approximation:

$$\frac{I_\gamma(E_{\rm eff})}{I_{el}(\theta_{\rm lab})} = [l_\alpha d\Omega \sigma_R(\theta_{\rm lab})]^{-1}\, l_\gamma \varepsilon_\gamma(b=0)\sigma(E_{\rm eff}) \tag{B.1}$$

where I_γ is the intensity of γ-rays measured in the detector; I_{el} is the number of elastically scattered α-particles; l_α and l_γ are the effective target lengths for the α-particle and γ-ray, respectively; $d\Omega$ is the solid angle of the γ-ray detector; σ_R is the elastic scattering cross section; ε_γ is the γ-ray detection efficiency and $\sigma(E_{\rm eff})$ is the cross section for the reaction. We will assume that the detector efficiency is approximately constant in this region, and will assume constant l_γ.

All of the states in this region are much narrower than the 50 keV thick target used by Wolke *et al.*, as shown in Tab. 7.1. Therefore, this cross section curve can be treated as a thick target yield in

(γ,γ)	(α,pγ)	(p,p$'$)	(n$_t$,γ)	(^{6}Li,d)	(^{6}Li,d)	(γ,γ)	Resulting Assignment
[Ber69]	[Gla86]	[Mos76]	[Wal92]	[Gie93]	[Uga07]		
10647 (2)		10644(3)				10647.36(18)	10647.35(18)
	10650(2)						10650(3)
		10678(3)					10678(3)
			10681.9(3)				10681.9(3)
	10695(2)	10689(3)		10694(20)			10693.2(16)
	10709(2)	10702(3)					10707(3)
		10715(3)	10718.75(90)				10718.75(9)
		10726(3)					10726(3)
		10744(3)	10745.98(12)				10745.98(12)
	10766(2)	10769(3)					10767(3)
			10805.9(4)		10808(20)	10805.86(16)	10805.87(15)
		10824(3)					10824(3)
		10881(3)					10881(3)
		10893(3)					10893(3)
		10915(3)					10915(3)
		10927(3)					10927(3)
	10943(2)						10943(2)
		10950(3)			10953(25)	10949.09(15)	10949.09(15)
		10978(3)					10978(3)
		10998(3)					10998(3)
	11010(2)	11017(3)					11012(3)
		11048(3)					11048(3)
		11084(3)					11084(3)

Table B.3: Table of excitation energies below the neutron threshold

the low energy region. In the thick target approximation, the yield of a resonant reaction is given by:

$$Y_{\max} = \frac{\lambda_r^2}{2}\frac{\omega\gamma}{\varepsilon_r} \tag{B.2}$$

where λ_r is the deBroglie wavelength at the resonance energy, E_r; $\omega\gamma$ is the resonance strength and ε_r is the effective stopping power. In order to calculate the upper limits, a 4^{th} order polynomial stopping power correction for energies away from our normalisation point at 832 keV was calculated with `SRIM` [Zie04], so the upper limit resonance strength could be obtained using:

$$\omega\gamma_{UL} = N\frac{2}{\lambda_r^2}C_r Y \tag{B.3}$$

where N is a normalisation factor found from the 832 keV resonance and C_r is the stopping power correction. Once an upper limit for the resonance strength was found, the upper limit for the α-particle partial width was obtained from Eq. (2.16). The total widths and quantum numbers of the resonances

Excitation Energy (keV)	(γ,γ) [Ber69]	$(\alpha,p\gamma)$ [Gla86]	(n_t,γ) [Wal92]	$(^6Li,d)$ [Uga07]	(γ,γ)	Resulting Assignment
10646(2)	1^+				1^+	1^+
10650(3)		$(4^-\text{-}7^-)$				$(4^-\text{-}7^-)$
10678(3)						
10681.9(3)						
10693.2(16)		$(3^+\text{-}7^+)$		Natural		(4^+)
10707(3)		$(2^+\text{-}6^+)$				$(2^+\text{-}6^+)$
10718.75(9)						
10726(3)						
10745.98(12)						
10767(3)		$(1^+\text{-}4^+)$				$(1^+\text{-}4^+)$
10805.9(4)			$(0^+\text{-}4^+)$	Natural	1^-	1^-
10824(3)						
10881(3)						
10893(3)						
10915(3)						
10927(3)						
10943(2)		$(4^\pm\text{-}7^\pm)$				$(4^\pm\text{-}7^\pm)$
10949.09(15)				Natural	1^-	1^-
10978(3)						
10998(3)						
11012(3)		$(2^+\text{-}6^+)$				$(2^+\text{-}6^+)$
11048(3)						
11084(3)						

Table B.4: Spin-parity assignments below the neutron threshold

are taken from Ref. [KÖ2]. The reference resonance used was that at $E_\alpha = 828$ keV. `DataThief`© [Tum] was used to extract the cross sections of the resonances and upper limit points. The upper limit points in Ref. [Wol89] were at an approximately constant level, so a single upper limit cross section of $\sigma = 2.5 \times 10^{-4}$ μb was adopted. Upper limit resonance strengths were obtained, and Eq. (2.16) could be used to find the upper limit for Γ_α.

Another method of calculating upper limit partial widths is to consider the spectroscopic factors of the states in question. The partial width of a state was defined in Eq. (2.18).A conservative upper limit can be calculated by assuming a spectroscopic factor and single-particle reduced width of unity, giving us an upper limit defined as:

$$\Gamma_{\text{UL}} = 2\frac{\hbar^2}{\mu R^2}P \tag{B.4}$$

The penetration factor was calculated numerically from coulomb wave-functions.

The upper limits in this work were taken as the smaller of the values from the two methods.

E_{lab} (keV)	J^π	(α,γ) Upper Limit Γ_α (eV)			(α,n) Upper Limit Γ_α (eV)		
		From Wolke	Assuming $C^2S\theta = 1$	Adopted	From Jaeger	Assuming $C^2S\theta = 1$	Adopted
587.90	2	7.22E-07	7.73E-09	7.73E-09	6.57E-09	7.73E-09	6.57E-09
647.93	2	8.11E-07	8.74E-08	8.74E-08	7.38E-09	8.74E-08	7.38E-09
657.53	2	8.25E-07	1.25E-07	1.25E-07	7.50E-09	1.25E-07	7.50E-09
671.70	2	8.45E-07	2.08E-07	2.08E-07	7.69E-09	2.08E-07	7.69E-09
742.81	2	9.46E-07	2.16E-06	9.46E-07	8.61E-09	2.16E-06	8.61E-09
779.32	2	9.97E-07	6.32E-06	9.97E-07	9.07E-09	6.32E-06	9.07E-09
786.17	4	5.59E-07	9.16E-08	9.16E-08	5.09E-09	9.16E-08	5.09E-09
792.90	1	1.69E-06	3.54E-05	1.69E-06	1.54E-08	3.54E-05	1.54E-08
793.83	2	1.02E-06	9.49E-06	1.02E-06	9.25E-09	9.49E-06	9.25E-09
797.10	2	1.02E-06	1.04E-05	1.02E-06	9.29E-09	1.04E-05	9.29E-09
805.19	3	7.37E-07	1.86E-06	7.37E-07	6.71E-09	1.86E-06	6.71E-09
822.64	1	1.81E-06	1.32E-04	1.81E-06	1.60E-08	7.83E-05	1.60E-08
840.81	1	1.80E-06	1.24E-04	1.80E-06	1.23E-07	1.24E-04	1.23E-07
843.24	1	1.81E-06	1.32E-04	1.81E-06	1.24E-07	1.32E-04	1.24E-07
844.35	1	1.81E-06	1.36E-04	1.81E-06	1.24E-07	1.36E-04	1.24E-07
853.55	1	1.83E-06	1.71E-04	1.83E-06	1.25E-07	1.71E-04	1.25E-07
861.86	2	1.11E-06	5.52E-05	1.11E-06	7.58E-08	5.52E-05	7.58E-08
862.91	4	6.16E-07	7.10E-07	6.16E-07	4.22E-08	7.10E-07	4.22E-08
919.34	5	5.37E-07	1.51E-07	1.51E-07	3.68E-08	1.51E-07	3.68E-08

Table B.5: Upper limit calculations for ^{22}Ne $+\alpha$. Resonance energies are in the laboratory frame.

The estimation of upper limits in the ^{22}Ne$(\alpha, \mathrm{n})^{25}$Mg reaction utilised Fig. 1 in Ref. [Jae01b], and followed the same technique as outlined above.

C ^{22}Ne Targets

Targets were produced for measuring the ^{22}Ne$(\alpha,\gamma)^{26}$Mg and ^{22}Ne$(\alpha,\mathrm{n})^{25}$Mg reactions directly. The targets were produced using the implantation procedure described in Sec. 4.4 for a $\Delta E = 30$ keV targets for α-particles at $E_\alpha \approx 600$ keV. For a target stoichiometry of Ne:Ta$= 1:2$, the implantation parameters were calculated to be:

Parameter	Value
Required Dose	0.25 C
Implantation Energy	65 keV for Ta 50 keV for Cu 40 keV for Ni

Table C.1: Implantation parameters used to produce ^{22}Ne targets. The target thickness desired was $\Delta E = 30$ keV for $E_\alpha \approx 600$ keV α-paricles.

A total of six targets were produced in this manner: three with tantalum backings, two with nickel backings, and a single copper backing target. Detector efficiencies were not well determined for a number of the targets, leading to ambiguities in the target stoichiometries. These targets should be reanalysed before use in a ^{22}Ne$(\alpha,\mathrm{n})^{25}$Mg or ^{22}Ne$(\alpha,\gamma)^{26}$Mg measurement.

Using the determined strength of $\omega\gamma = 0.524(51)$ for the ^{22}Ne(p,γ)^{23}Na resonance at $E_r^{\mathrm{lab}} = 479$ keV (Sec. 6), each target was analysed by measuring the resonance yield curve. The obtained stoichiometries are shown in Tab. C.2.

Target	Stoichiometry N_{Ne}/N_b
Tantalum 1	0.107 (13)
Nickel 2	0.111 (13)
Tantalum 3	0.374 (43)
Tantalum 4	0.398 (93)

Table C.2: Stoichiometries obtained for the implanted ^{22}Ne targets described in Tab. C.1.

BIBLIOGRAPHY

[Ago03] S. Agostinelli et al., "Geant4 - a simulation toolkit", Nucl. Inst. and Meth. A **506**, 250 (2003), (Geant4 Collaboration).

[Ang99] C. Angulo et al., "A compilation of charged-particle induced thermonuclear reaction rates.", Nucl. Phys. A **656**, 3 (1999).

[Arn96] D. Arnett, *Supernovae and nucleosynthesis. an investigation of the history of matter, from the Big Bang to the present*, Princeton University Press, 1996.

[AS91] F. Ajzenberg-Selove, "Energy levels of light nuclei A = 13-15", Nuclear Physics A **523**, 1 (1991).

[Bee89] H. Beer and R. L. Macklin, "Measurement of the Rb-85 and Rb-87 capture cross sections for s-process studies", Astro. Phys. J. **339**, 962 (1989).

[Ber69] B. L. Berman, R. L. van Hemert, and C. D. Bowman, "Threshold photoneutron cross section for ^{26}Mg and a source of stellar neutrons.", Phys. Rev. Lett. **23**, 386 (1969).

[Ber84] U. E. P. Berg, K. Ackermann, K. Bangert, C. Blsing, W. Naatz, R. Stock, K. Wienhard, M. K. Brussel, T. E. Chapuran, and B. H. Wildenthal, "Bound state M1 transitions in sd-shell nuclei", Phys. Lett. B **140**, 191 (1984).

[Bie53] L. C. Biedenharn and M. E. Rose, "Theory of Angular Correlation of Nuclear Radiations", Rev. Mod. Phys. **25**, 729 (1953).

[Bol80] H. Bolotin, "Experimental determinations of directional-correlation solid-angle attenuation factors for Ge(Li) γ-ray detectors: comparison of experimental and calculated values", Nuclear Instruments and Methods **178**, 237 (1980).

[Boo96] J. Boone and A. Chavez, "Comparison of x-ray cross sections for diagnostic and therapeutic medical physics", Medical Physics **23**, 1997 (1996).

[Bow74] W. Bowman and K. MacMurdo, "Radioactive-decay gammas: ordered by energy and nuclide", Name: At. Data Nucl. Data Tables, v. 13, no. 2-3, pp. 89-292 (1974).

[Bre36] G. Breit and E. Wigner, "Capture of Slow Neutrons", Phys. Rev. **49**, 519 (1936).

[Bro07] E. Browne and J. Tuli, "Nuclear Data Sheets for A = 137", Nucl. Data Sheets **108**, 2173 (2007).

[Bur57] E. M. Burbidge, G. R. Burbidge, W. A. Fowler, and F. Hoyle, "Synthesis of the Elements in Stars", Rev. Mod. Phys. **29**, 547 (1957).

[Cam04] J. A. Cameron and B. Singh, "Nuclear Data Sheets for A=40", Nucl. Data Sheets **102**, 293 (2004).

[Car96] T. S. Carman, V. Litveninko, J. Madey, C. Neuman, B. Norum, P. G. O'Shea, N. R. Roberson, C. Y. Scarlett, E. Schreiber, and H. R. Weller, "The TUNL-FELL inverse Compton γ-ray source as a nuclear physics facility", Nucl. Inst. Meth. A **378**, 1 (1996).

[Car10] S. Carson, C. Iliadis, J. Cesaratto, A. Champagne, L. Downen, M. Ivanovic, J. Kelley, R. Longland, J. R. Newton, G. Rusev, and A. P. Tonchev, "Ratio of germanium detector peak efficiencies at photon energies of 4.4 and 11.7MeV: Experiment versus simulation", Nucl. Inst. and Meth. A **In Press, Corrected Proof**, (2010).

[Cou08] R. D. Cousins, J. T. Linnemann, and J. Tucker, "Evaluation of three methods for calculating statistical significance when incorporating a systematic uncertainty into a test of the background-only hypothesis for a Poisson process", Nucl. Inst. and Meth. A **595**, 480 (2008).

[Cra89] G. M. Crawley, C. Djalali, N. Marty, M. Morlet, A. Willis, N. Anantaraman, B. A. Brown, and A. Galonsky, "Isovector and isoscalar spin-flip excitations in even-even s-d shell nuclei excited by inelastic proton scattering", Phys. Rev. C **39**, 311 (1989).

[Deb79] K. Debertin and U. Schtzig, "Coincidence summing corrections in Ge(Li)-spectrometry at low source-to-detector distances", Nucl. Inst. and Meth. **158**, 471 (1979).

[Dra94] J. M. Drake, E. G. Bilpuch, G. E. Mitchell, and J. F. Shriner, Jr., "Detailed-balance tests of time-reversal invariance with interfering charged-particle resonances", Phys. Rev. C **49**, 411 (1994).

[Dro91] H. W. Drotleff, A. Denker, J. W. Hammer, H. Knee, S. Küchler, D. Streit, C. Rolfs, and H. P. Trautvetter, "New ^{22}Ne(γ,n)^{25}Mg-resonances at very low energies relevant for the astrophysical s-process", Z. Phys. A **338**, 367 (1991).

[Dro93] H. W. Drotleff, A. Denker, H. Knee, M. Soine, G. Wolf, J. W. Hammer, U. Greife, C. Rolfs, and H. P. Trautvetter, "Reaction rates of the s-process neutron sources ^{22}Ne(α, n)^{25}Mg and ^{13}C(α, n)^{16}O", Astrophys. J. **414**, 735 (1993).

[Du 71] Z. B. Du Toit, P. R. de Kock, and W. L. Mouton, "Resonance strengths, branching ratios and mean lifetimes of nuclear energy levels in ^{23}Na", Z. Phys. **246**, 170 (1971).

[End90] P. M. Endt, "Energy levels of A = 21-44 nuclei (VII)", Nucl. Phys. A **521**, 1 (1990).

[End98] P. M. Endt, "Supplement to energy levels of A = 21-44 nuclei (VII)", Nucl. Phys. A **633**, 1 (1998).

[Gar06] D. A. García-Hernández, P. García-Lario, B. Plez, F. D'Antona, A. Manchado, and J. M. Trigo-Rodríguez, "Rubidium-Rich Asymptotic Giant Branch Stars", Science **314**, 1751

(2006).

[Geh77] R. Gehrke, R. Helmer, and R. Greenwood, "Precise relative γ-ray intensities for calibration of Ge semiconductor detectors", Nucl. Inst. and Meth. **147**, 405 (1977).

[Gie93] U. Giesen, C. P. Browne, J. Grres, S. Graff, C. Iliadis, H. P. Trautvetter, M. Wiescher, W. Harms, K. L. Kratz, B. Pfeiffer, R. E. Azuma, M. Buckby, and J. D. King, "The astrophysical implications of low-energy resonances in ^{22}Ne+α", Nucl. Phys. A **561**, 95 (1993).

[Gla86] F. Glatz, S. Norbert, E. Bitterwolf, A. Burkard, F. Heidinger, T. Kern, R. Lehmann, H. Röpke, J. Siefert, C. Schneider, and B. H. Wildenthal, "High-spin states in ^{26}Mg", Z. Phys. A **324**, 187 (1986).

[Hab04] H. Habing and H. Olofsson, *Asymptotic giant branch stars*, Springer, 2004.

[Har91] V. Harms, K.-L. Kratz, and M. Wiescher, "Properties of ^{22}Ne(α,n)^{25}Mg resonances", Phys. Rev. C **43**, 2849 (1991).

[Hel03] R. G. Helmer, J. C. Hardy, V. E. Iacob, M. Sanchez-Vega, R. G. Neilson, and J. Nelson, "The use of Monte Carlo calculations in the determination of a Ge detector efficiency curve", Nucl. Inst. and Meth. A **511**, 360 (2003).

[Ili90] C. Iliadis, T. Schange, C. Rolfs, U. Schröder, E. Somorjai, H. P. Trautvetter, K. Wolke, P. M. Endt, S. W. Kikstra, A. E. Champagne, M. Arnould, and G. Paulus, "Low-energy resonances in ^{25}Mg(p,γ)^{26}Al, ^{26}Mg(p,γ)^{27}Al and ^{27}Al(p,γ)^{28}Si", Nucl. Phys. A **512**, 509 (1990).

[Ili97] C. Iliadis, "Proton single-particle reduced widths for unbound states", Nucl. Phys. A **618**, 166 (1997).

[Ili07] C. Iliadis, *Nuclear physics of stars*, Wiley-VCH, 2007.

[Ili10] C. Iliadis et al., "Charged-Particle Thermonuclear Reaction Rates: III. Nuclear Physics Input", Submitted to Nucl. Phys. A (2010).

[Imb05] G. Imbriani et al., "S-factor of ^{14}N(p,γ)^{15}O at astrophysical energies", Euro. Phys. J. A **25**, 455 (2005).

[Jac98] J. Jackson, *Classical Electrodynamics*, volume 3, Wiley, 1998.

[Jae01a] M. Jaeger, *Die Einfangreaktion ^{22}Ne(α,n)^{25}Mg - die Hauptneutronenquelle in massiven Sternen*, Ph.D. thesis, Universität Stuttgart, 2001.

[Jae01b] M. Jaeger, R. Kunz, A. Mayer, J. W. Hammer, G. Staudt, K. L. Kratz, and B. Pfeiffer, "^{22}Ne(α,n)^{25}Mg: The Key Neutron Source in Massive Stars", Phys. Rev. Lett. **87**, 202501

(2001).

[JJ91] R. Juvet Jr, G. Allmaier, and E. Schmid, "Counting metal oxide monolayers on a metal surface using plasma desorption mass spectrometry", Anal. Chem. **63**, 2352 (1991).

[Jun99] H. Junde, "Nuclear Data Sheets for A = 56", Nucl. Data Sheets **86**, 315 (1999).

[KÖ2] P. E. Köhler, "Constraints on the ^{22}Ne(α,n)^{25}Mg s-process neutron source from analysis of ^{nat}Mg+n total and ^{25}Mg(n,γ) cross sections", Phys. Rev. C **66**, 055805 (2002).

[Kae90] F. Kaeppeler, R. Gallino, M. Busso, G. Picchio, and C. M. Raiteri, "S-process nucleosynthesis - Classical approach and asymptotic giant branch models for low-mass stars", Astro. Phys. J **354**, 630 (1990).

[Kar06] A. I. Karakas, M. A. Lugaro, M. Wiescher, J. Görres, and C. Ugalde, "The Uncertainties in the ^{22}Ne+α-Capture Reaction Rates and the Production of the Heavy Magnesium Isotopes in Asymptotic Giant Branch Stars of Intermediate Mass", Astrophys. J. **643**, 471 (2006).

[Kei77] J. Keinonen, M. Riihonen, and A. Anttila, "Absolute resonance strengths in the ^{20,21,22}Ne(p, γ)^{21,22,23}Na and ^{21}Ne(p, p$_1\gamma$)^{21}Ne reactions", Phys. Rev. C **15**, 579 (1977).

[Kim03] I. Kim, C. Park, and H. Choi, "Absolute calibration of ^{60}Co by using sum-peak method and an HPGe detector", Appl. Rad. and Iso. **58**, 227 (2003).

[Kle29] O. Klein and T. Nishina, "Über die Streuung von Strahlung durch freie Elektronen nach der neuen relativistischen Quantendynamik von Dirac", Z. Phys. A **52**, 853 (1929).

[Kno89] G. F. Knoll, *Radiation Detection and Measurement*, Wiley, 1989.

[Lit97] V. N. Litvinenko et al., "Gamma-Ray Production in a Storage Ring Free-Electron Laser", Phys. Rev. Lett. **78**, 4569 (1997).

[Lon06] R. Longland, C. Iliadis, A. E. Champagne, C. Fox, and J. R. Newton, "Nuclear astrophysics studies at the LENA facility: The γ-ray detection system", Nucl. Inst. and Meth. A **566**, 452 (2006).

[Lon10] R. Longland et al., "Charged-Particle Thermonuclear Reaction Rates: I. Monte Carlo Method and Statistical Distributions", Submitted to Nucl. Phys. A (2010).

[Lug08] M. Lugaro and M. van Raai, "New discoveries and challenges for the s-process in AGB stars", Jour. of Phys. G **35**, 014007 (2008).

[Mar07] M. Martin, "Nuclear Data Sheets for A = 208", Nucl. Data Sheets **108**, 1583 (2007).

[Mau82] B. Maurel, G. Amsel, and J. Nadai, "Depth profiling with narrow resonances of nuclear reactions: Theory and experimental use", Nucl. Inst. and Meth. **197**, 1 (1982).

[McC75] G. J. McCallum and G. E. Coote, "Influence of source-detector distance on relative intensity and angular correlation measurements with Ge(Li) spectrometers", Nucl. Inst. and Meth. **130**, 189 (1975).

[McG91] V. A. McGlone and P. B. Johnson, "Deconvolution of resonance reaction yield curves by a nonlinear least squares method", Nucl. Inst. and Meth. B **61**, 201 (1991).

[Mey73] M. A. Meyer and J. J. A. Smit, "The energy levels of ^{23}Na", Nucl. Phys. A **205**, 177 (1973).

[Mos76] C. E. Moss, "Excitation energies of levels in ^{23}Na, ^{24}Mg and ^{26}Mg", Nucl. Phys. A **269**, 429 (1976).

[Nar00] I. Narsky, "Estimation of upper limits using a Poisson statistic", Nucl. Inst. and Meth. A **450**, 444 (2000).

[Nas90] J. Nash, *Compact numerical methods for computers: linear algebra and function minimisation*, CRC Press, 1990.

[Nel65] J. Nelder and R. Mead, "A simplex method for function minimization", The Computer Journal **7**, 308 (1965).

[New08] J. R. Newton, R. Longland, and C. Iliadis, "Matching of experimental and statistical-model thermonuclear reaction rates at high temperatures", Phys. Rev. C **78**, 025805 (2008).

[New10a] J. R. Newton, *Hydrogen Burning of ^{17}O*, Ph.D. thesis, University of North Carolina at Chapel Hill, 2010.

[New10b] J. R. Newton, C. Iliadis, A. E. Champagne, J. M. Cesaratto, S. Daigle, and R. Longland, "Measurement of ^{17}O(p,γ)^{18}F between the narrow resonances at $E_r^{\rm lab} = 193$ and 519 keV", Phys. Rev. C **81**, 045801 (2010).

[Pez08] R. P. Pezzi, C. Krug, P. L. Grande, E. B. O. da Rosa, G. Schiwietz, and I. J. R. Baumvol, "Analytical energy loss distribution for accurate high resolution depth profiling using medium energy ion scattering", Appl. Phys. Lett. **92**, 164102 (2008).

[Pig05] M. Pignatari, R. Gallino, F. Käppeler, and M. Wiescher, "Effects of uncertainties of the ^{22}Ne(α, n)^{25}Mg and ^{13}C(α, n)^{16}O reaction rates in the s-process yields", Nucl. Phys. A **758**, 541 (2005).

[Pii71] M. Piiparinen, A. Anttila, and M. Viitasalo, "A study of the excited states of ^{23}Na from the ^{22}Ne(p, γ)^{23}Na reaction", Z. Phys. **247**, 400 (1971).

[Por56] C. E. Porter and R. G. Thomas, "Fluctuations of Nuclear Reaction Widths", Phys. Rev. **104**, 483 (1956).

[Pow98] D. C. Powell, C. Iliadis, A. E. Champagne, S. E. Hale, V. Y. Hansper, R. A. Surman, and

K. D. Veal, "Low-energy resonance strengths for proton capture on Mg and Al nuclei", Nucl. Phys. A **644**, 263 (1998).

[Pre07] W. Press, S. Teukolsky, W. Vetterling, and B. Flannery, *Numerical recipes: the art of scientific computing*, Cambridge Univ Pr, 2007.

[Rau01] T. Rauscher and F.-K. Thielemann, "Tables Of Nuclear Cross Sections And Reaction Rates: An Addendum To The Paper "Astrophysical Reaction Rates From Statistical Model Calculations"", At. Data Nucl. Data Tables **79**, 47 (2001).

[Rol75] C. Rolfs and W. S. Rodney, "Hydrogen burning of ^{17}O in the CNO cycle", Nucl. Phys. A **250**, 295 (1975).

[Sch09] R. Schwengner, A. Wagner, Y. Fujita, G. Rusev, M. Erhard, D. D. Frenne, E. Grosse, A. R. Junghans, K. Kosev, and K. D. Schilling, "Dipole transition strengths in ^{26}Mg", Phys. Rev. C **79**, 037303 (2009).

[Sem90] T. M. Semkow, G. Mehmood, P. P. Parekh, and M. Virgil, "Coincidence summing in γ-ray spectroscopy", Nucl. Inst. and Meth. A **290**, 437 (1990).

[The00] L. The, M. F. El Eid, and B. S. Meyer, "A New Study of s-Process Nucleosynthesis in Massive Stars", Astro. Phys. J **533**, 998 (2000).

[Tho99] W. J. Thompson and C. Iliadis, "Error analysis for resonant thermonuclear reaction rates", Nucl. Phys. A **647**, 259 (1999).

[Tra99] R. Tramontano and V. R. Vanin, "Mixing activity-calibrated and uncalibrated γ-ray sources in efficiency calibration", Appl. Rad. and Iso. **51**, 323 (1999).

[Tum] B. Tummers, "Datathief III", www.datathief.org.

[Uga07] C. Ugalde et al., "Experimental evidence for a natural parity state in ^{26}Mg and its impact on the production of neutrons for the s-process", Phys. Rev. C **76**, 025802 (2007).

[Wal92] T. A. Walkiewicz, S. Raman, E. T. Jurney, J. W. Starner, and J. E. Lynn, "Thermal-neutron capture by magnesium isotopes", Phys. Rev. C **45**, 1597 (1992).

[Wei76] H. Weigmann, R. L. Macklin, and J. A. Harvey, "Isobaric analog impurities from neutron capture and transmission by magnesium", Phys. Rev. C **14**, 1328 (1976).

[Wel] H. Weller, "The HIγS Facility", http://www.tunl.duke.edu/higs/.

[Wel09] H. R. Weller, M. W. Ahmed, H. Gao, W. Tornow, Y. K. Wu, M. Gai, and R. Miskimen, "Research opportunities at the upgraded HIγS facility", Prog. Part. Nucl. Phys. **62**, 257 (2009).

[Wol89] K. Wolke, H. W. Becker, C. Rolfs, U. Schröder, H. P. Trautvetter, V. Harms, K. L. Kratz, J. W. Hammer, M. Wiescher, and A. Wöhr, "Helium burning of ^{22}Ne.", Z. Phys. A **334**, 491 (1989).

[Woo03] S. E. Woosley, A. Heger, T. Rauscher, and R. D. Hoffman, "Nuclear data needs for the study of nucleosynthesis in massive stars", Nucl. Phys. A **718**, 3 (2003).

[Yat63] M. J. L. Yates, "Angular correlation attenuation coefficients for photopeaks measured with NaI crystals", Nucl. Inst. and Meth. **23**, 152 (1963).

[Zhu07] Y. Zhu, "Upper limit for Poisson variable incorporating systematic uncertainties by Bayesian approach", Nucl. Inst. and Meth. A **578**, 322 (2007).

[Zie04] J. Ziegler, "SRIM-2003", Nucl. Inst. and Meth. B **219**, 1027 (2004).

[Zin05] E. Zinner, L. R. Nittler, P. Hoppe, R. Gallino, O. Straniero, and C. M. O. . Alexander, "Oxygen, magnesium and chromium isotopic ratios of presolar spinel grains", Geochim. Cosmochim. Acta. **69**, 4149 (2005).